Plasma Physics Reports, Vol. 31, No. 2, 2005, pp. 104–109. Translated from Fizika Plazmy, Vol. 31, No. 2, 2005, pp. 126–132.

Behavior of the Fast Neutrals Generated during a Disruption in the T-11M Tokamak

A. M. Belov, A. I. Markin, A. G. Alekseev, and S. V. Mirnov

Troitsk Institute for Innovation and Fusion Research, Troitsk, Moscow oblast, 142190 Russia

Received April 22, 2004; in final form, June 8, 2004

Abstract—Results are presented from experimental studies of the generation of high-energy neutrals during a major disruption in the T-11M tokamak. Fast-neutral fluxes from the plasma, magnetic perturbations, and the neutral-hydrogen and impurity radiation from the plasma core are measured simultaneously in the course of disruption. A high (~1 μs) temporal resolution of the recording system (the characteristic disruption time being about 100 μs) makes it possible to thoroughly investigate the time behavior of the processes that occur during a disruption. © *2005 Pleiades Publishing, Inc.*

1. INTRODUCTION

The generation of fast (with energies far exceeding the plasma temperature) neutrals during major disruptions was first observed in early tokamaks [1] and is still attracting interest of physicists (see, e.g., [2, 3]). Evidently, two successive processes underlie this phenomenon: first, the acceleration of ions in electric fields generated during a disruption and, second, the charge exchange of fast ions with neutrals arriving from the tokamak wall during a disruption (i.e., the conversion of the accelerated ions into fast neutrals).

Note that fast electrons (which may be expected to be generated by analogy to ions) either are not observed at all or are detected only in the initial phase of disruption by observing accompanying effects, such as radiation bursts in the GHz frequency range (see, e.g., [4]).

An example of such a burst at a frequency of 1 GHz is given in Fig. 1.[1] The figure also shows a negative voltage pulse U_p, which serves as an indicator of a major disruption (the signal is saturated at a level of −10 to −15 V). It can be seen that the radiation burst (an indicator of fast electrons [4]) first closely follows the U_p signal and then is suddenly cut off. The latter effect may be associated with the onset of MHD turbulence or with the arrival of impurities from the wall. Thus, in the fast phase of disruption, which is of most interest to us, runaway electrons are in fact absent. Note that, in large tokamaks, fast electrons sometimes appear again in the current-decay phase, when the plasma is already cooled. In this case, their appearance merely indicates the onset of the final phase of a major disruption.

Hence, the study of the behavior of fast ions and neutrals escaping from the plasma column is one of a few ways of obtaining information about the process of plasma column destruction in all of the disruption phases.

In our experiments in the T-11M tokamak, fast-neutral fluxes from the plasma, magnetic perturbations, and neutral-hydrogen and impurity radiation from the plasma core were simultaneously measured in the course of disruption. A high (~1 μs) time resolution of the recording system (the characteristic disruption time being about 100 μs) allowed us to thoroughly investigate the time behavior of the processes that occur during a disruption.

2. EXPERIMENT

The experiments were carried out in the T-11M tokamak with R = 0.7 m, a = 0.2 m, B_T = 1 T, I_p = 70–100 kA, T_i = 100–150 eV, T_e = 300–450 eV, and n_e =

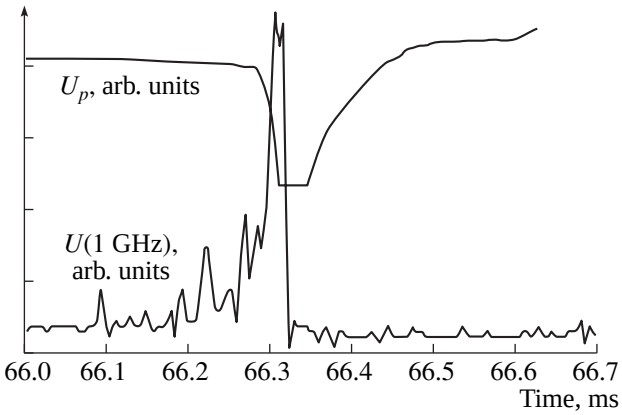

Fig. 1. Negative voltage pulse U_p and the waveform of the plasma radiation intensity at a frequency of 1 GHz [4] during a disruption in the T-11M tokamak (shot no. 9181).

[1] We thank V.I. Poznyak for providing us with the data presented in Fig. 1.

1063-780X/05/3102-0104$26.00 © 2005 Pleiades Publishing, Inc.

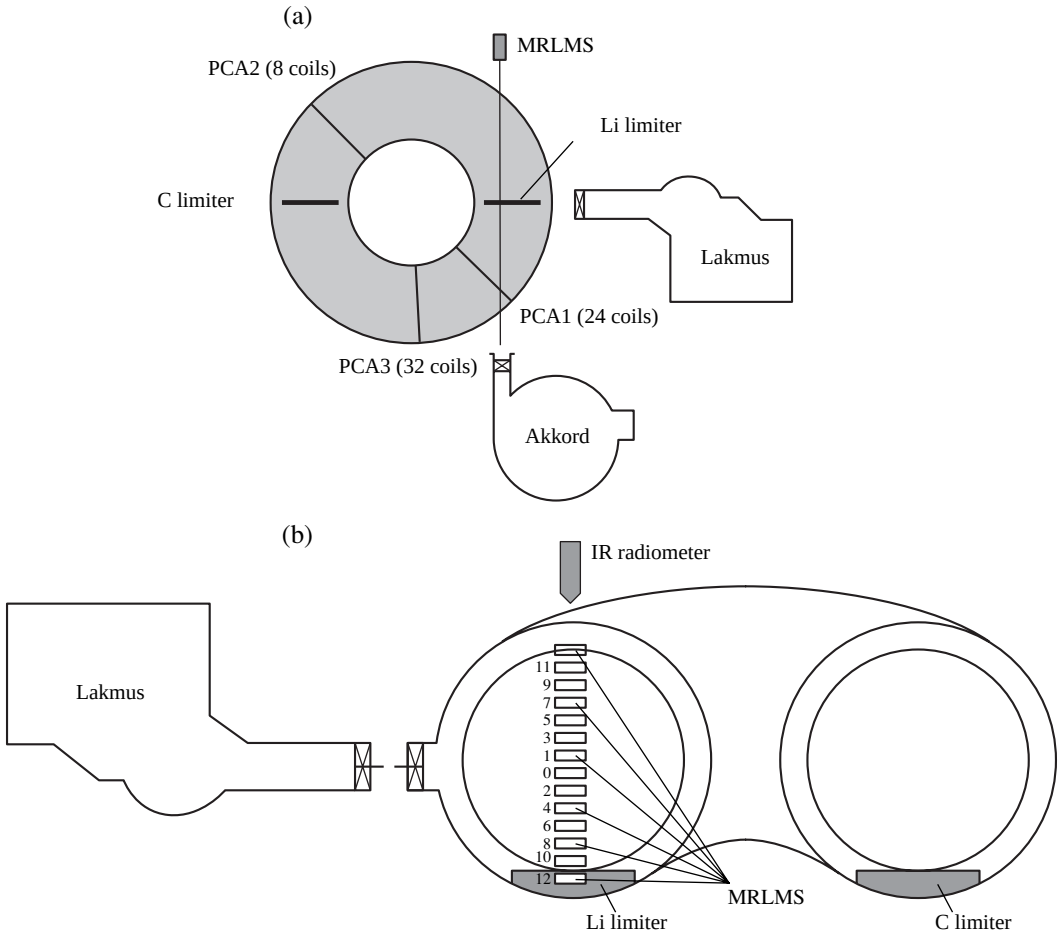

Fig. 2. Arrangement of the recording system: (a) the positions of the PCAs (PCA1, PCA2, and PCA3), the Lakmus and Akkord NPAs, and the MRLMS and (b) the observational diagram of the Lakmus NPA, the MRLMS channels, and the IR radiometer.

1.3×10^{19} or 1.9×10^{19} m^{-3} in a regime with a Li limiter. The isotopic composition of the hydrogen–deuterium plasma was n_H/n_D = 10–12%. The arrangement of the recording system is shown in Fig. 2.

The flux of charge-exchange neutrals escaping from the T-11M tokamak in the radial direction across the toroidal magnetic field (transverse neutrals) were measured by a Lakmus charge-exchange neutral particle analyzer (NPA) [5] (Fig. 3). The Lakmus NPA was located in front of the lithium limiter in the equatorial plane of the tokamak and measured the energy distribution of deuterium atoms in the energy range of 0.2–2 keV with a pulse counting rate of up to 1 MHz. Deuterium atoms were separated by applying a magnetic or electric field. VEU-6 vacuum multiplier tubes were used as a detector. The maximal solid angle of the NPA collimator was 3×10^{-4} sr, and the viewing field at the plasma axis was 5 × 5 cm. In parallel to the main (count) mode, the neutral fluxes in the NPA channels were also measured in the current mode. For this purpose, *RC* integrating circuits with $\tau_{RC} \approx 8$ μs were installed at the outputs of the NPA channels.

When measuring the particle flux with a microsecond time resolution, it is necessary to take into account the time during which the neutrals move from the emitting plasma region to the NPA detector. This time is defined as

$$t_i = L_i \sqrt{\frac{m_D}{2E_i}},$$

where i is the number of the NPA channel, L_i is the distance from the emitting plasma region to the ith NPA detector, m_D is the deuteron mass, and E_i is the energy of a particle detected by the ith NPA channel. Strictly speaking, the distance L_i is different for different channels; however, for the third and fifth channels, which detect particles with energies of E_3 = 640 eV and E_5 = 1477 eV (it is these channels the data from which are considered in this paper), the distances differ by no more than 10 cm and can be assumed to be L = 140 cm for both channels. Hence, the neutrals are detected by the NPA and the fast data acquisition system with a time delay of Δt = 5.7 μs for the third channel and Δt = 3.7 μs for the fifth channel.

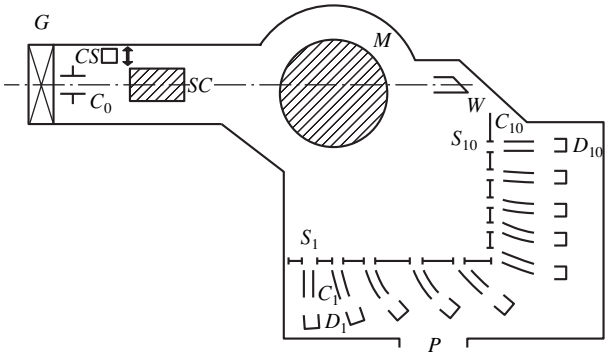

Fig. 3. Schematic of the Lakmus NPA installed in the T-11M tokamak [5]: (*G*) gate, (C_0) clearing capacitor, (*CS*) calibration system, (*SC*) stripping chamber, (*M*) magnet, (*W*) window, (S_1–S_{10}) windows for deflected particles, (C_1–C_{10}) calibrating capacitors, (D_1–D_{10}) diode amplifiers, and (*P*) pump duct.

The radiation from the plasma column was measured with the help of a multichannel radiation loss measurement system (MRLMS) consisting of sixteen AXUV photodiodes with a time resolution of no worse than 2 μs [6]. The AXUV diodes had a nearly constant sensitivity in the 100- to 5000-eV photon energy range and a somewhat lower (by a factor of 3–4) sensitivity in the visible range. Since the intensity of the tokamak plasma radiation was maximal in the ultraviolet (UV) and soft X-ray (SXR) regions, these diodes could serve as a fast bolometer. The area viewed by an MRLMS channel was 5×2.6 cm^2. The plasma column was observed in the direction parallel to the toroidal axis of the tokamak in the cross section where a rail-type lithium limiter (the main source of lithium incoming to the plasma) was installed (Fig. 2). In contrast to a conventional transverse observational scheme, our scheme allowed us to avoid errors that are inherent to the Abel procedure when applying it to an asymmetric radiation source (as is the case under the disruption conditions). It was expected that, during the first 30–50 μs after the impurity injection, when the impurities had not yet diffused appreciably along the torus, the photodiodes would receive the radiation from local (with respect to *r*) regions lying on vertical chords in their viewing fields (rather than the radiation averaged over the chords in the vicinity of the lithium limiter). Note that, according to calculations, the time it takes for a lithium ion to make one complete turn around the torus is about 100 μs under our experimental conditions.

Magnetohydrodynamic (MHD) measurements were performed with MHD diagnostic coils [7]. In the experiments, we used three pick-up coil arrays (PCA1, PCA2, and PCA3) with 24, 32, and 8 coils positioned in three poloidal cross sections of the tokamak ($\varphi = 45°$, 88°, and 180°, respectively). The cross section with $\varphi = 0°$ corresponded to the position of the Li limiter. In each PCA, the coils were arranged equidistantly along the poloidal circumference of the torus and detected the poloidal component of the magnetic field. The upper operating frequency of PCA1 and PCA3 was determined by the time constant of the protecting stainless-steel tubes (with a wall thickness of $\delta = 0.3$ mm) in which the coils were placed ($\tau_{tb} \approx 2$ μs).

In addition to the above measurements, we also measured SXR ($h\nu > 2000$ eV) emission from the plasma core with a time resolution of about 30 μs. The power deposited in the limiter was measured by an IR detector with a time resolution of about 0.5 ms. The data acquisition system provided the simultaneous recording of 72 signals with a time resolution from 1 to 20 μs.

Figures 4 and 5 show the time behavior of the main plasma parameters during a typical T-11M major disruption: the discharge current ΔI_p, the Shafranov shift ΔR, the distribution of the magnetic perturbations B_θ over the poloidal angle θ, the distribution of the integrated plasma radiation intensity along a vertical chord (the MRLMS signals; see Fig. 2), and the time-integrated ($\tau_{RC} \sim 8$ μs) NPA signals for energies of $E_3 = 640$ eV and $E_5 = 1477$ eV.

An analysis of the results obtained by processing 18 similar T-11M discharges with major disruptions shows that, in some discharges, the flux of neutrals with intermediate energies ($E \cong 5T_i$) increases substantially against the background level 100–200 μs before the disruption (Fig. 5). This coincides in time with the fast thermal quench and is accompanied by a more intense plasma–wall interaction (Figs. 4, 5). The disruption (i.e., the generation of a positive current pulse ΔI_p and a negative pulse U_p; see Fig. 1) is accompanied by intense bursts of neutrals with energies $E \cong 5T_i$–$15T_i$. The latter effect has always been regarded as an indicator of the transverse acceleration of primary ions during a disruption [1–3]. Note that the beginning of the neutral burst coincides in time with the reconnection of the outer modes of helical magnetic perturbations B_θ (from $m/n = 2/1$ to (3–4)/1) in the current rise phase. This means that the transverse acceleration of the primary ions is probably caused by the outer magnetic reconnection acting as a generator of a turbulent electric field.

However, the picture appears to be even more intricate. Recent studies in the MAST tokamak [2] showed that internal magnetic reconnections can result in the efficient longitudinal acceleration of ions. In classical tokamaks, internal reconnections precede a major disruption (fast thermal quench). Hence, it may be expected that, by the instant of outer reconnections, a large number of longitudinally accelerated ions will be accumulated at the axis of the plasma column. Since the major disruption in classical tokamaks is accompanied by the onset of turbulence at the axis of the plasma column and by the penetration of impurities into this region from the periphery [8], the scattering of fast ions

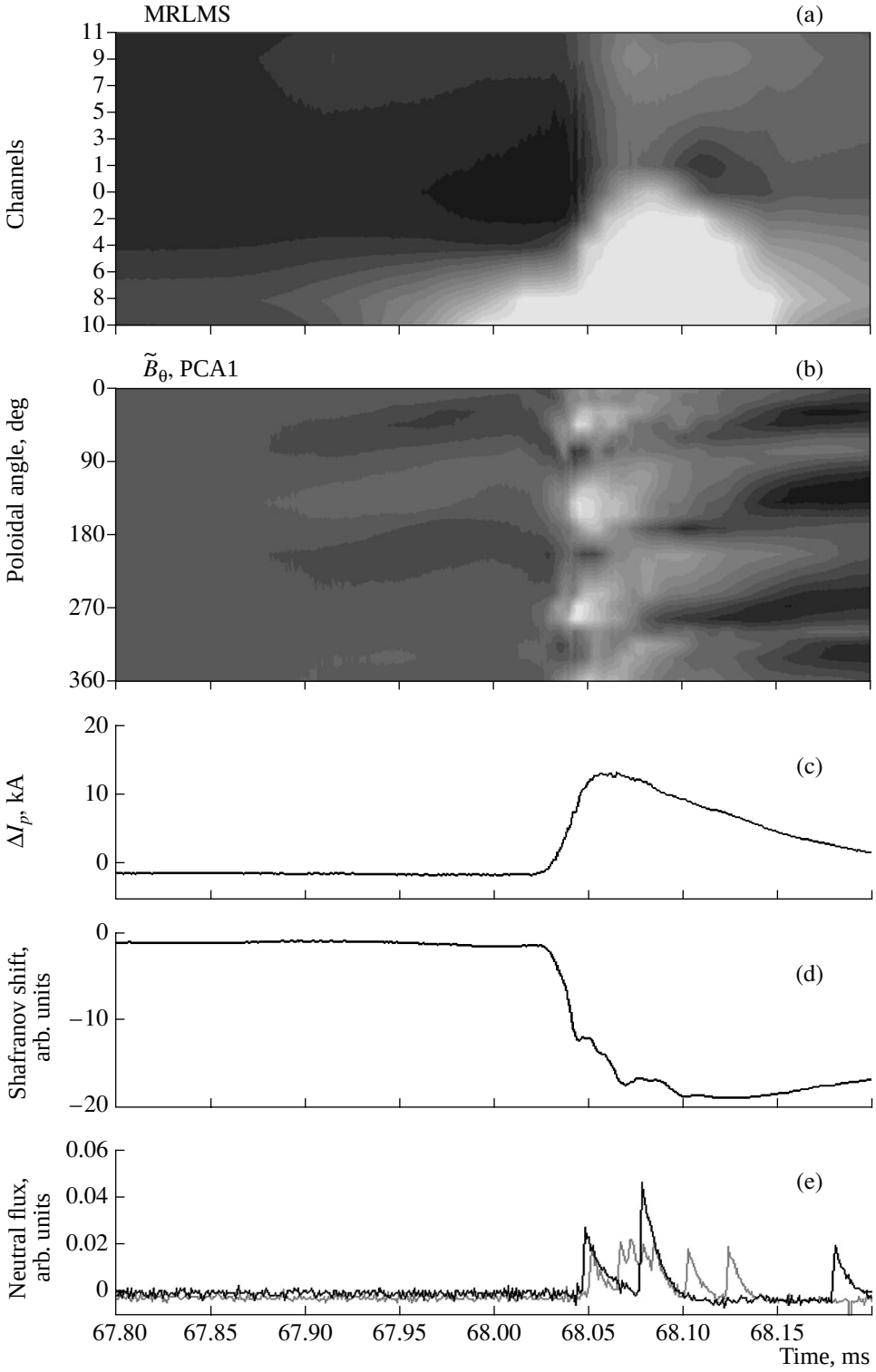

Fig. 4. Time behavior of the main plasma parameters during a typical major disruption in T-11M: (a) propagation of impurity radiation along the vertical chord near the Li limiter, (b) time evolution of MHD perturbations, (c) waveform of the plasma current, (d) variations in the Shafranov shift, and (e) time-integrated ($\tau_{RC} \sim 8$ μs) NPA signals for energies of $E_3 = 640$ eV and $E_5 = 1477$ eV.

by turbulent fluctuations leads to their isotropization. This, in turn, can result in the appearance of an additional transverse flux of high-energy neutrals from the plasma core after a short delay time.

The behavior of impurities (lithium) can be inferred from the character of the MRLMS signal. Figure 5 shows the time evolution of impurity radiation during a typical major disruption, the waveform of the plasma

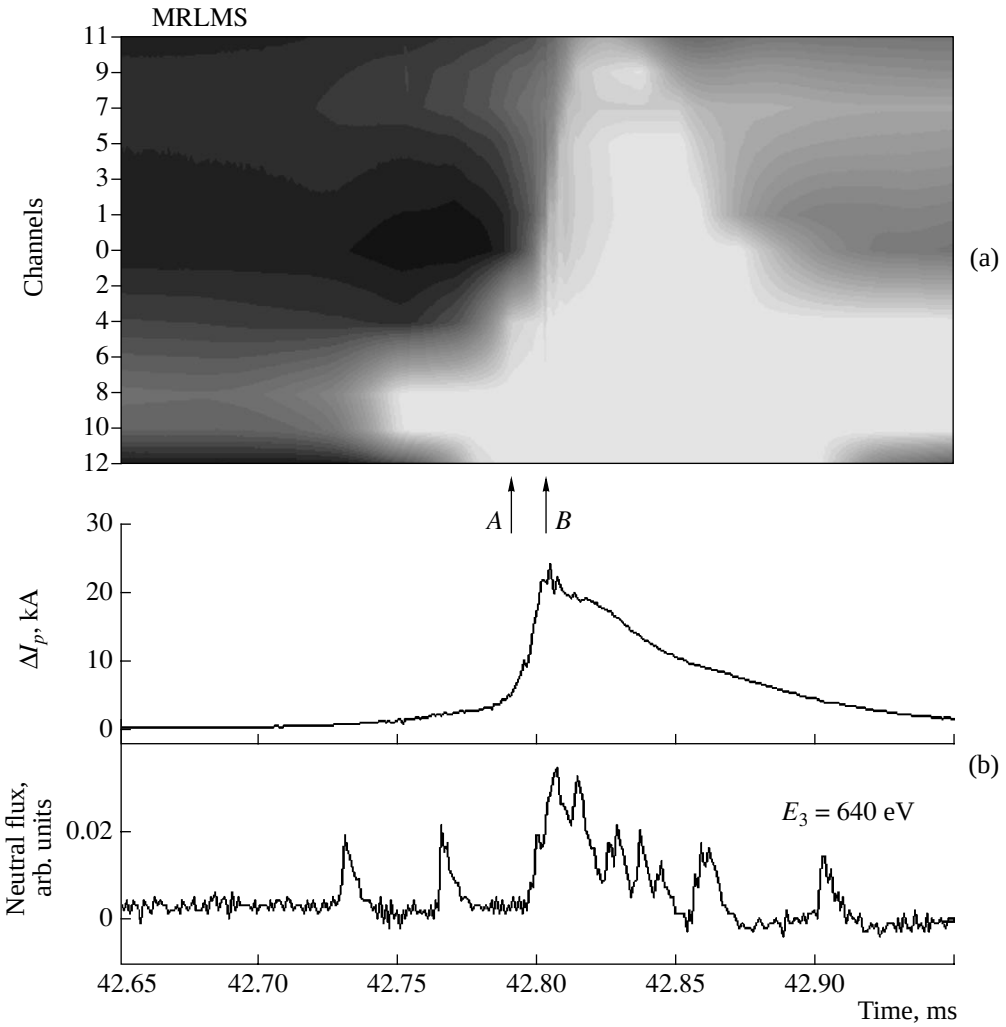

Fig. 5. Time evolution of (a) the impurity radiation intensity (the MRLMS signals) and (b) the plasma current ΔI_p and the Lakmus NPA signal for E_3 = 640 eV.

current ΔI_p, and the behavior of the 640-eV neutral flux measured by the Lakmus NPA. One can see that the radiation from the plasma core passes through two characteristic phases, namely, the fast (*A*) and slow (*B*) phases. In the fast phase, the radiation burst appears almost simultaneously (within 1 μs) both at the plasma periphery and in the plasma core. The slow phase can be interpreted as the propagation of the emitting particles into the plasma core with a velocity of up to 5 km/s. This may be associated with the flux of impurities from the limiter toward the plasma axis [8]. It can be supposed that the fast phase of radiation is related to the generation of fast neutrals in the course of outer magnetic reconnection at the plasma periphery.

If this were so, then the NPA signal would coincide (to within the time during which a particle moves from the plasma axis to the NPA) with the time derivative of the MRLMS signal from the plasma core. Figure 6 compares this derivative and the NPA signals for E_5 = 1477 eV and E_3 = 640 eV. The fact that these signals are similar to one another is a qualitative argument in favor of our model. Hence, it may be expected that the peaks of the radiation intensity of impurity ions from the plasma core will appear in the descending order of the ion charge (from the upper to lower ionization states), in contrast to the normal order (from the lower to upper ionization states) during breakdown and ionization. Indeed, this effect is sometimes observed experimentally during major disruptions [9] and is widely used to determine the energies of impurity ions in the course of their charge exchange with a neutral beam. This method may also be used to measure the ion temperature from the Doppler broadening of the impurity lines during a disruption. We note that, in Fig. 6, another interesting effect can be seen: the neutral flux with energies of E_5 = 1477 eV is delayed with respect to that with E_3 = 640 eV. This discrepancy between the experimental results and the predictions of the simple transit-time model may be regarded as an argument in favor of the above assumption about different ion acceleration

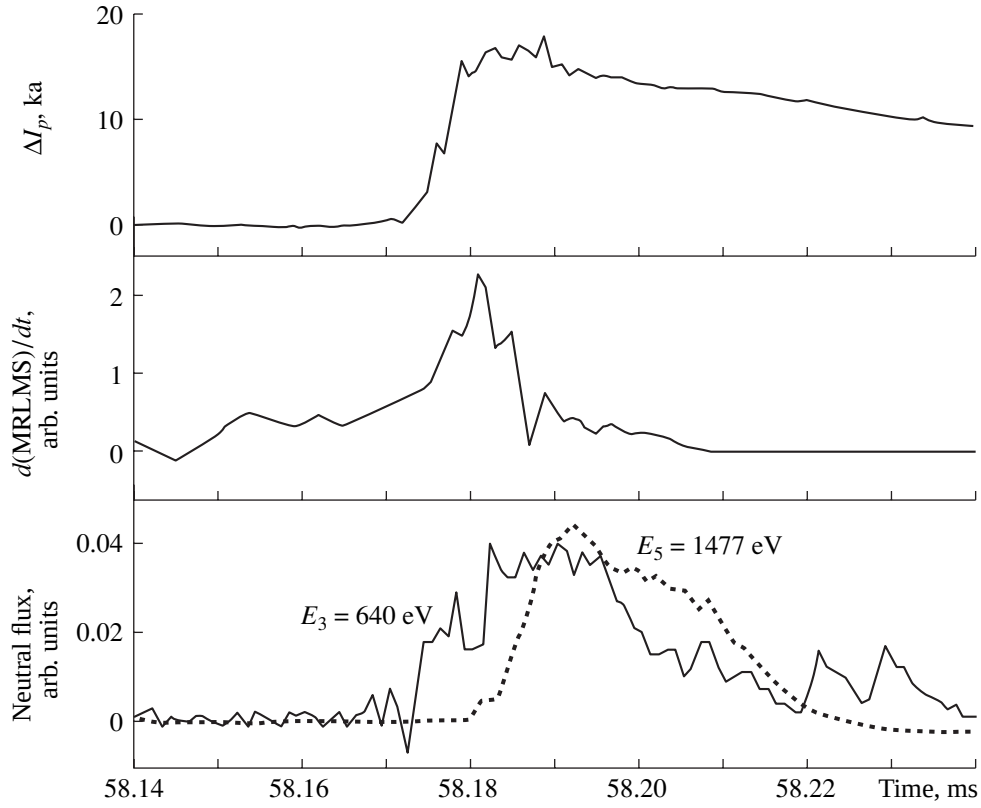

Fig. 6. Waveforms of the plasma current ΔI_p, the derivative of the central MRLMS signal (channel no. 1), and the intensities of the neutral fluxes with energies of E_3 = 640 eV and E_5 = 1477 eV. The waveforms of the neutral fluxes are shifted to the left by the time during which a particle moves from the plasma axis to the NPA detector: Δt = 5.7 μs for the third channel and Δt = 3.7 μs for the fifth channel.

mechanisms in the plasma core and at the plasma periphery.

3. CONCLUSIONS

(i) The time at which fast neutrals are detected by the NPA almost coincides with the spontaneous transition of an MHD perturbation from the $m = 2$ to the $m = 3$ or 4 mode. This allows us to suggest that the energy source of fast neutrals is the magnetic reconnection accompanying a major disruption.

(ii) The appearance of a radiation burst from the central region of the plasma column is probably due to the penetration of fast neutrals (a fraction of the total flux that is geometrically symmetric to the outward flux measured by the NPA) into the plasma core.

REFERENCES

1. L. A. Artsimovitch, V. V. Afrosimov, I. P. Gladkovsky, *et al.*, in *Proceedings of the 2nd International Conference on Plasma Physics and Controlled Nuclear Fusion Research, Culham, 1995* (IAEA, Vienna, 1996), Vol. II, p. 595.
2. P. Helander, L.-G. Eriksson, R. J. Akers, *et al.*, Phys. Rev. Lett. **89**, 235002 (2002).
3. A. V. Bortnikov, N. N. Brevnov, Yu. V. Gott, and V. A. Shurygin, Fiz. Plazmy **21**, 672 (1995) [Plasma Phys. Rep. **21**, 634 (1995)].
4. S. V. Mirnov, A. M. Belov, I. N. Makashin, *et al.*, in *Proceedings of the 16th International Conference on Fusion Energy, Montreal, 1996* (IAEA, Vienna, 1997), Vol. 1, p. 763.
5. A. I. Kislyakov, A. V. Krasil'nikov, M. P. Petrov, and A. N. Romannikov, Preprint No. 4460/7, Kurchatov Inst. of Atomic Energy (TsNIIatominform, Moscow, 1987).
6. A. Alekseyev, G. Perov, A. Kurnosov, *et al.*, Plasma Devices Oper. **7**, 139 (1999).
7. A. M. Belov and I. N. Makashin, Fiz. Plazmy **30**, 195 (2004) [Plasma Phys. Rep. **30**, 173 (2004)].
8. A. M. Belov, S. V. Mirnov, A. G. Alekseyev, and I. N. Makashin, in *Proceedings of the 27th EPS Conference on Controlled Fusion and Plasma Physics, Budapest, 2000*, ECA **24B**, 596 (2000).
9. N. N. Brevnov, Yu. V. Gott, and V. A. Shurygin, in *Proceedings of XXX Zvenigorod Conference on Plasma Physics and Controlled Nuclear Fusion, Zvenigorod, 2003*, Abstracts of Papers, p. 85.

Translated by N.F. Larionova

Plasma Physics Reports, Vol. 31, No. 2, 2005, pp. 110–122. Translated from Fizika Plazmy, Vol. 31, No. 2, 2005, pp. 133–145.

MAGNETIC CONFINEMENT SYSTEMS

MHD Stabilization by the Magnetic Hill at a Small Rotational Transform

A. A. Skovoroda

Nuclear Fusion Institute, Russian Research Centre Kurchatov Institute, pl. Kurchatova 1, Moscow, 123182 Russia

Received April 22, 2004

Abstract—The effect of very small rotational transform on the plasma stability in three-dimensional closed magnetic configurations with closed magnetic field lines, stabilized by the magnetic hill (i.e., by the plasma compressibility), is considered using ideal MHD theory. It is shown that, for infinitely small values of the rotational transform, the Suydam–Mercier criterion predicts the onset of acoustic instability with a finite growth rate, provided that the Bernstein–Kadomtsev criterion is satisfied. Consequently, for a vanishingly small rotational transform, the limiting transition from the Suydam–Mercier criterion to the Bernstein–Kadomtsev criterion is impossible. Taking into account the finite Larmor radius allows this limiting transition to be made. The Bernstein–Kadomtsev criterion ensures MHD stability at rotational transform values below a certain critical value determined by the ratio of the ion Larmor radius to the plasma minor radius. Under experimental conditions, this critical value is larger than that expected to be produced by the actual magnetic perturbations. © *2005 Pleiades Publishing, Inc.*

1. INTRODUCTION

In most magnetic confinement systems, the MHD stability of a hot plasma is ensured by the magnetic well and/or magnetic shear. It is also known, however, that MHD stabilization by plasma compressibility is possible in configurations with a magnetic hill and without a rotational transform [1–3]. Examples of such configurations can be found, e.g., in [4–6].

In toroidal systems without a rotational transform and magnetic well, a necessary and sufficient condition for the stability of flute oscillations (those with a zero longitudinal wavenumber, $k_\parallel = 0$) is given by the Bernstein–Kadomtsev (BK) criterion [1–3]

$$\nabla p \cdot \nabla U + \frac{\gamma_0 p (\nabla U)^2}{U} \geq 0. \quad (1)$$

Here, p is the equilibrium plasma pressure, γ_0 is the adiabatic index, and $U = \oint \frac{dl}{B}$ = const is the label of the equilibrium magnetic surface. For configurations with a magnetic hill, we have $\nabla U \cdot \nabla p < 0$, and there exists a neutrally stable decreasing pressure profile $p \sim U^{-\gamma_0}$. In practice, such pressure profiles are achieved with toroidal magnetic divertors in which the magnetic well/hill U has a singularity at the separatrix. There are sound reasons to suggest that the plasma relaxes to a state with a neutrally stable pressure profile in a self-consistent fashion [7].

Since the assumption that the magnetic field lines are closed is a theoretical idealization, the question naturally arises of how the presence of a small rotational transform will affect the plasma stability under the BK criterion. The answer might seem obvious: the plasma will be unstable. Indeed, for a nonzero rotational transform, the fundamental Suydam–Mercier (SM) criterion predicts the onset of strong MHD instabilities in configurations with a magnetic hill and small shear. The objective of the present paper is to investigate the question of the actual range of applicability of the BK criterion.

To answer this question, it is necessary to understand the relation between two fundamental criteria for ideal MHD stability: the SM and BK criteria. In [8], it was shown that, when BK condition (1) is satisfied and the SM criterion fails to hold because of the smallness of the magnetic shear, the instability growth rates become appreciably slower. The reason for this is that the instability changes from one type to another: in the expression for the instability growth rate, the Alfvén speed is replaced with the acoustic speed. It is presumably this circumstance that can explain, e.g., the observed positive features in the behavior of the plasma in small-aspect-ratio tokamaks. In [9], in which the studies were carried out for cylindrical geometry, it was pointed out that the acoustic instability occurs at a very small rotational transform. In ideal MHD theory, this instability is found to grow fairly rapidly even at arbitrarily small values of the rotational transform μ because of a decrease in the wavelength of the perturbations (or, equivalently an increase in the mode number, $m \sim \mu^{-1} \longrightarrow \infty$).

In the present paper, the results of [9] are extended to three-dimensional configurations such as toroidal

1063-780X/05/3102-0110$26.00

mirror systems [10]. It is shown that, in the one-fluid ideal MHD approximation, a continuous transition from the SM to the BK criterion in the limit of zero rotational transform is impossible.

In order to make this limiting transition possible, it is necessary to take into account the finite Larmor radius (FLR) of the ions. For the displacement of the magnetic field line making one turn in the toroidal direction around the circumference of the torus to be less than the ion Larmor radius ρ_i, the rotational transform should satisfy the condition $\mu \sim \rho_i/a \ll 1$, where a is the plasma minor radius. In the ideal MHD approximation, the modes for which $m\rho_i/a = k_\perp\rho_i \sim 1$ are unstable. It is well known, however, that, because of the FLR effects, such small-scale MHD modes are, as a rule, stable.

In what follows, FLR effects will be incorporated into the ideal ballooning equations, which will then be solved in order to determine the critical value of the rotational transform below which the BK criterion guarantees MHD plasma stability.

2. STABILITY AT $\mu \longrightarrow 0$

We begin this section with the familiar equations for local ideal ballooning modes in toroidal confinement systems of arbitrary geometry (see, e.g., [11], Eqs. (6.137) and (6.138)):

$$-\rho\omega^2\frac{k_\perp^2}{k_b^2}\xi = \mathbf{B}\cdot\nabla\left(\frac{k_\perp^2}{k_b^2}\mathbf{B}\cdot\nabla\xi\right) + 2\frac{(\mathbf{B}\times\boldsymbol{\kappa})\cdot\mathbf{k}_\perp}{Bk_b}$$

$$\times\left\{p'\xi + \frac{\gamma_0 pB^2}{\gamma_0 p + B^2}\left(\mathbf{B}\cdot\nabla\frac{\tau}{B^2} - 2\frac{[\mathbf{B}\times\boldsymbol{\kappa}]\cdot\mathbf{k}_\perp}{Bk_b}\xi\right)\right\}, \quad (2)$$

$$-\rho\omega^2\tau$$

$$= \mathbf{B}\cdot\nabla\left\{\frac{\gamma_0 pB^2}{\gamma_0 p + B^2}\left(\mathbf{B}\cdot\nabla\frac{\tau}{B^2} - 2\frac{[\mathbf{B}\times\boldsymbol{\kappa}]\cdot\mathbf{k}_\perp}{Bk_b}\xi\right)\right\}.$$

Here, ξ and τ are, respectively, the plasma displacement components normal to the magnetic surface and along the magnetic field line; $\boldsymbol{\kappa} = \left(\frac{\mathbf{B}}{B}\cdot\nabla\right)\frac{\mathbf{B}}{B} = \nabla_\perp(p + B^2/2)/B^2$ is the curvature vector of the magnetic field line; $\mathbf{k}_\perp = \nabla_\perp S$ is the normal component of the wave vector (see Appendix 1); $k_b = \left(\frac{\mathbf{B}}{B}\times\nabla a\right)\cdot\mathbf{k}_\perp$ is the azimuthal component of the wave vector; a is the label (radius) of the magnetic surface; ρ is the mass density; ω is the frequency; and the prime denotes the derivative with respect to a. We introduce the notation $R^{-1} = (\mathbf{B}\times\boldsymbol{\kappa})\cdot\mathbf{k}_\perp/Bk_b$ and take into account the expression for the divergence of the displacement vector $X = \nabla\cdot\boldsymbol{\xi}$, $X = \frac{B^2}{\gamma_0 p + B^2}\left(\mathbf{B}\cdot\nabla\frac{\tau}{B^2} - 2\frac{(\mathbf{B}\times\boldsymbol{\kappa})\cdot\mathbf{k}_\perp}{Bk_b}\xi\right)$ [11] to rewrite Eqs. (2) as

$$\left[\mathbf{B}\cdot\nabla\left(\frac{k_\perp^2}{k_b^2}\mathbf{B}\cdot\nabla\right) + \frac{2p'}{R} + \rho\omega^2\frac{k_\perp^2}{k_b^2}\right]\xi = -\frac{2\gamma_0 pX}{R},$$
$$\left[\mathbf{B}\cdot\nabla\left(\frac{c_s^2}{\omega^2B^2}\mathbf{B}\cdot\nabla\right) + \frac{\gamma_0 p + B^2}{B^2}\right]X = -\frac{2\xi}{R}, \quad (3)$$

where $c_s = \sqrt{\gamma_0 p/\rho}$ is the speed of sound. According to Eqs. (3), we always have $\omega \neq 0$ provided that $\nabla\cdot\boldsymbol{\xi} \neq 0$. Note that Eqs. (2) and (3) are valid for arbitrary values of the rotational transform, in particular, at zero value.

It is convenient to analyze Eqs. (3) in magnetic flux coordinates (a, β, ζ) with straightened field lines (SFLs). Such coordinates can be introduced through the representations of the magnetic field with SFLs for currentless confinement systems in terms of the flux and of the current (see, e.g., [11]):

$$2\pi\mathbf{B} = \Phi'[\nabla a\times\nabla\beta],$$
$$2\pi\mathbf{B} = F\nabla\zeta - \nu\nabla a. \quad (4)$$

Here, Φ and $F(a)$ are the toroidal magnetic flux and the external azimuthal current; $\beta = \theta - \mu\zeta$, with θ and ζ being the azimuthal and toroidal angular (Boozer) coordinates, which vary within the range 0–2π; $\mu = -\Psi'/\Phi'$ is the rotational transform; Ψ is the external poloidal magnetic flux; and ν is a periodic function of the coordinates θ and ζ, which is determined by the equation $(\nabla\times\mathbf{B})\times\mathbf{B} = \nabla p$, namely,

$$\mathbf{B}\cdot\nabla\nu = -2\pi p' - F'\mathbf{B}\cdot\nabla\zeta. \quad (5)$$

In the coordinates so chosen, we have

$$\frac{k_\perp^2}{k_b^2} = \frac{\Phi'^2}{4\pi^2B^2}A^2, \quad \mathbf{B}\cdot\nabla = \frac{2\pi B^2}{F}\frac{\partial}{\partial\zeta},$$

$$A^2 = \left[|\nabla\beta|^2 + 2\left(\frac{\partial S/\partial a}{\partial S/\partial\beta}\right)(\nabla a\cdot\nabla\beta) + \left(\frac{\partial S/\partial a}{\partial S/\partial\beta}\right)^2|\nabla a|^2\right],$$

and Eqs. (3) take the form

$$\left[\frac{\partial}{\partial\zeta}A^2\frac{\partial}{\partial\zeta} + \frac{2F^2p'}{\Phi'^2B^2R} + \frac{A^2F^2\omega^2}{4\pi^2B^2c_A^2}\right]\xi = -\frac{2F^2\gamma_0 p}{\Phi'^2B^2R}X,$$
$$\left[\frac{\partial^2}{\partial\zeta^2} + \frac{F^2\omega^2}{4\pi^2B^2c_s^2}\left(1 + \frac{\gamma_0 p}{B^2}\right)\right]X = -\frac{F^2\omega^2}{2\pi^2B^2c_s^2R}\xi, \quad (6)$$

where $c_A = \sqrt{B^2/\rho}$ is the Alfvén speed. We also present the form that Eq. (5) assumes in the flux coordinates:

$$\frac{\partial \nu}{\partial \zeta} = -F' - \frac{Fp'}{B^2}. \quad (7)$$

Note that the coordinate β labels the magnetic field line: the derivatives in Eqs. (6) and (7) are taken at $\beta = \text{const}$.

If the equations involve the rotational transform, then they, as a rule, also involve the shear, $\mu' \neq 0$. Consequently, Eqs. (6) can contain secular terms of the form $\nabla\beta = \nabla\theta - \mu\nabla\zeta - \mu'\zeta\nabla a$, which enter, e.g., into the quantity A. It turns out, however, that the main conclusions regarding the stability behavior at $\mu \longrightarrow 0$ can be drawn by considering a simpler shearless case, $\mu = \text{const} \ll 1$. The general case with a nonzero shear is considered in Appendix 2.

In the shearless case, Eqs. (6) do not contain secular terms and we can employ a simple technique of expanding in Fourier series. Since the displacement of the magnetic field line is a periodic function of the coordinate θ, we can expand ξ in a Fourier series in the azimuthal coordinate:

$$\xi = \sum_{m=-\infty}^{\infty} \xi_m(\zeta) e^{-im\theta} = \sum_{m=-\infty}^{\infty} \xi_m(\zeta) e^{-im(\beta+\mu\zeta)} = \sum_{m=-\infty}^{\infty} \bar{\xi}_m(\zeta) e^{-im\beta}. \quad (8)$$

Here, the function $\bar{\xi}_m(\zeta) = \xi_m(\zeta)\exp(-im\mu\zeta)$, in contrast to the function $\xi_m(\zeta)$, is nonperiodic at irrational values of μ. In turn, expanding the periodic function $\xi_m(\zeta)$ in a Fourier series, $\xi_m(\zeta) = \sum_{n=-\infty}^{\infty} \xi_{mn} e^{in\zeta}$, and taking the integral Fourier transform of the function $\bar{\xi}_m(\zeta)$ yields a discrete spectrum of the latter function, which is characterized by the dimensionless longitudinal wavenumbers

$$k_{zn} = n - \mu m. \quad (9)$$

Let us consider perturbations with $m \gg 1$. In [9], it was shown that, for small μ values (i.e., when the magnetic field lines are unclosed only slightly), the most dangerous perturbations are those localized predominantly in the azimuthal direction. Hence, assuming that $\partial S/\partial\beta \gg a\partial S/\partial a$ in Eqs. (6) and using Fourier series expansion (8) for X, we arrive at equations for the Fourier components $\bar{\xi}_m(\zeta)$ and $\bar{X}_m(\zeta)$. These equations have the same form as Eqs. (6), but they are simpler because $A \sim |\nabla\beta|^2$. For clarity, we will work in the notation adopted in Eqs. (6).

We will consider many-period toroidal mirror systems with closed magnetic field lines and without a magnetic well [10]. For such systems, Eqs. (6) can be solved by an asymptotic procedure [12]. This possibility stems from the fact that the characteristic longitudinal scale of variation of the amplitude of the ballooning modes differs substantially from the spatial scale on which the geometric parameters of the equilibrium magnetic field vary. We call such ballooning perturbations *quasi-flute* perturbations [9, 13].

We introduce the "fast" (ζ) and "slow" ($z = \varepsilon\zeta$, where $\varepsilon \ll 1$) coordinates. In the representation $\xi = \xi_0(\zeta, z) + \varepsilon\xi_1(\zeta, z) + \varepsilon^2\xi_2(\zeta, z)$ of the displacement ξ, we single out the periodic part in accordance with the condition $\xi_i(\zeta, z) = \xi_i(\zeta + 2\pi, z)$ (see, e.g., [14]). The periodic part in the corresponding representation of the displacement vector X is singled out in the same manner. Here, the role of the small quantity ε is played by the quantities μ and N^{-1}, where N is the number of periods of the toroidal confinement system. In fact, this averaging procedure serves to filter all the harmonics out of spectrum (9) except for those with small mode numbers n.

To zero order in ε, we obtain from Eqs. (6) the equations

$$\frac{\partial}{\partial\zeta} A^2 \frac{\partial\xi_0}{\partial\zeta} = 0, \quad \frac{\partial^2 X_0}{\partial\zeta^2} = 0. \quad (10)$$

Taking into account the fact that the functions ξ_0 and X_0 are periodic in the fast coordinate ζ, we arrive at a solution to Eqs. (10) in the form $\xi_0(\zeta, z) = \xi_0(z)$ and $X_0(\zeta, z) = X_0(z)$.

To first order, we obtain from Eqs. (6) the equations

$$\frac{\partial}{\partial\zeta}\left[A^2\left(\frac{\partial\xi_1}{\partial\zeta} + \frac{\partial\xi_0}{\partial z}\right)\right] = 0, \quad \frac{\partial}{\partial\zeta}\left(\frac{\partial X_1}{\partial\zeta} + \frac{\partial X_0}{\partial z}\right) = 0. \quad (11)$$

With allowance for the periodicity of the functions ξ_1 and X_1, we obtain the following solution to Eqs. (11):

$$\frac{\partial\xi_1}{\partial\zeta} = \frac{d\xi_0}{dz}\left(\frac{2\pi A^{-2}}{\oint A^{-2} d\zeta} - 1\right), \quad \frac{\partial X_1}{\partial\zeta} = 0. \quad (12)$$

Here, the integration is carried out along the magnetic field line over *one* turn in the toroidal direction around the entire circumference of the torus. For this reason, the integral in the first of Eqs. (12) depends on the azimuthal coordinate of the initial point on the magnetic field line. We will ignore this dependence, however, because doing so is justified by the smallness of the rotational transform and the isometry property used in [10] to construct the magnetic configurations of toroidal mirror systems.

In the second approximation, we take into account Eqs. (12) to transform Eqs. (6) to

$$\begin{aligned}
&\frac{\partial}{\partial\zeta}A^2\left(\frac{\partial\xi_2}{\partial\zeta}+\frac{\partial\xi_1}{\partial z}\right)+2\pi\frac{\partial}{\partial z}\frac{1}{\oint A^{-2}d\zeta}\frac{\partial\xi_0}{\partial z}\\
&+\left(\frac{2F^2p'}{\Phi'^2B^2R}+\frac{A^2F^2\omega^2}{4\pi^2B^2c_A^2}\right)\xi_0+\frac{2F^2\gamma_0 p}{\Phi'^2B^2R}X_0=0,\\
&\frac{\partial^2X_2}{\partial\zeta^2}+\frac{\partial^2X_0}{\partial z^2}+\frac{F^2\omega^2}{4\pi^2B^2c_s^2}\left(1+\frac{\gamma_0 p}{B^2}\right)X_0\\
&+\frac{F^2\omega^2}{2\pi^2B^2c_s^2R}\xi_0=0.
\end{aligned}\tag{13}$$

With the periodicity of the functions ξ_2 and X_2 in mind, we obtain the solution

$$\begin{aligned}
&\frac{4\pi^2}{\oint A^{-2}d\zeta}\frac{\partial^2\xi_0}{\partial z^2}+\left(\frac{2F^2p'}{\Phi'^2}\oint\frac{d\zeta}{B^2R}+\frac{F^2\omega^2}{4\pi^2}\oint\frac{A^2d\zeta}{B^2c_A^2}\right)\xi_0\\
&+\frac{2F^2\gamma_0 pX_0}{\Phi'^2}\oint\frac{d\zeta}{B^2R}=0,\\
&2\pi\frac{\partial^2X_0}{\partial z^2}+\frac{F^2\omega^2X_0}{4\pi^2c_s^2}\oint\left(1+\frac{\gamma_0 p}{B^2}\right)\frac{d\zeta}{B^2}\\
&+\frac{F^2\omega^2\xi_0}{2\pi^2c_s^2}\oint\frac{d\zeta}{B^2R}=0.
\end{aligned}\tag{14}$$

In relationship (14), we switch from the frequency ω to the growth rate γ, $\omega^2 = -\gamma^2$. As a result, taking the Fourier transformation $\xi_0(z) = \int\xi_0(k_z)e^{ik_zz}dk_z$ (and the analogous transformation for X_0), we arrive at the dispersion relation

$$U_0+\frac{U_1}{1+\dfrac{k_z^2}{k_{zs}^2}}+k_{zA}^2+k_z^2=0.\tag{15}$$

Here, we have introduced conventional notation for the terms describing the magnetic well/hill, U_0, and plasma compressibility, U_1 (see Appendices 2, 3),

$$\begin{aligned}
U_0&=-\frac{F^2p'}{2\pi^2\Phi'^2}\oint\frac{d\zeta}{B^2R}\oint A^{-2}d\zeta,\\
U_1&=\frac{F^2\gamma_0 p}{\pi^2\Phi'^2}\left(\oint\frac{d\zeta}{B^2R}\right)^2\frac{\oint A^{-2}d\zeta}{\oint\left(1+\dfrac{\gamma_0 p}{B^2}\right)\dfrac{d\zeta}{B^2}},
\end{aligned}\tag{16}$$

and those describing the characteristic acoustic and Alfvén wavenumbers, k_{zs} and k_{zA} [8, 15],

$$\begin{aligned}
k_{zs}^2&=\frac{\gamma^2F^2}{8\pi^3c_s^2}\oint\left(1+\frac{\gamma_0 p}{B^2}\right)\frac{d\zeta}{B^2},\\
k_{zA}^2&=\frac{\gamma^2F^2}{16\pi^4}\oint\frac{A^2d\zeta}{B^2c_A^2}\oint A^{-2}d\zeta.
\end{aligned}\tag{17}$$

Ignoring the term k_{zA}^2 in dispersion relation (15) in comparison to k_{zs}^2 ($k_{zA}^2 \ll k_{zs}^2$ for small β values) and taking into account the inequality $U_0 + U_1 \geq 0$ (which means that BK condition (1) holds) yields

$$k_{zs}^2=-\frac{k_z^2(U_0+k_z^2)}{(k_z^2+U_0+U_1)}.\tag{18}$$

Dispersion relation (18) implies that the conditions for the onset of acoustic instability are satisfied (i.e., the growth rate is positive) when

$$0<k_z^2<-U_0.\tag{19}$$

Recall that we are investigating the stability of a system with a magnetic hill, $U_0 < 0$. Since, in accordance with spectrum (9), we have $k_z^2 = (n - \mu m)^2$, we can rewrite instability criterion (19) as

$$0<(n-\mu m)^2<-U_0.\tag{20}$$

For closed magnetic field lines ($\mu = 0$), the flute oscillations ($n = 0$) are stable. They can become unstable only above the instability threshold for ballooning modes in terms of β values (the parameter β is minimum for $n = 1$):

$$-U_0>1.\tag{21}$$

For any arbitrarily small value of the rotational transform, $\mu \ll 1$, there always exists a large mode number $m \gg 1$ such that $\mu \sim n/m \ll 1$ and an instability for which there is essentially no threshold becomes possible. The maximum wavenumber (which corresponds to the maximum growth rate) of this instability,

$$k_{zs_{\max}}^2=(\sqrt{U_1}-\sqrt{U_0+U_1}),\tag{22}$$

occurs at large mode numbers m such that

$$(n-\mu m)^2=\sqrt{U_0+U_1}(\sqrt{U_1}-\sqrt{U_0+U_1}).\tag{23}$$

The result just obtained agrees with the conclusions of [9].

Hence, at arbitrarily small values of the rotational transform μ, the plasma stability depends upon the restrictions on the azimuthal wavenumber. In ideal MHD theory, there are no such restrictions and, consequently, a continuous transition from the SM to the BK

criterion is impossible. The restrictions in question are naturally introduced by the FLR effects, which are ignored in the ideal MHD approximation.

3. STABILITY AT $\mu \longrightarrow 0$ WITH ALLOWANCE FOR THE FINITE LARMOR RADIUS

We begin by writing the equations for small-scale ideal modes with allowance for FLR effects (see Appendix 1):

$$\left[\mathbf{B}\cdot\nabla\left(\frac{k_\perp^2}{k_b^2}\mathbf{B}\cdot\nabla\right)+\frac{2p'}{R}+\rho\omega\left(\omega-\omega^*+\frac{3}{2}\omega_R\right)\frac{k_\perp^2}{k_b^2}\right]\xi = -\frac{2\gamma_0 pX}{R},$$
$$\left[\mathbf{B}\cdot\nabla\left(\frac{c_s^2}{\omega(\omega-\omega_M)B^2}\mathbf{B}\cdot\nabla\right)+\frac{\gamma_0 p+B^2}{B^2}\right]X = -\frac{2\xi}{R}\left(1-\frac{\omega^*}{\omega}\right). \quad (24)$$

Equations (24) are valid for small values of $k_\perp\rho_i$. They differ from Eqs. (3) in that the terms with ω^2 are supplemented with the diamagnetic drift frequency $\omega^* = \frac{k_b p'}{\omega_{ci}\rho}$ and magnetic drift frequency $\omega_M = \omega_B + \omega_R$. Here, $\omega_R = \frac{p}{\omega_{ci}\rho}\frac{k_b}{R}$ and $\omega_B = \frac{p}{\omega_{ci}\rho}\frac{k_b}{R_B}$, with $\frac{1}{R_B} = \frac{\mathbf{k}_\perp\cdot(\mathbf{B}\times\nabla B)}{k_b B^2}$ and ω_{ci} being the ion gyrofrequency. Under the BK condition, all drift frequencies are of the same order of magnitude.

We first consider a local dispersion relation that can be derived from Eqs. (24) in the quasiclassical approximation, in which the perturbations are represented as

$$X,\xi = C_{1,2}\exp\left(i\int k_\parallel dl\right), \quad (25)$$

where $C_{1,2}$ are functions slowly varying along the magnetic field lines. The relationship between the functions C_1 and C_2 follows from the second of Eqs. (24),

$$C_1 = -\frac{2(\omega-\omega^*)(\omega-\omega_M)}{[\omega(\omega-\omega_M)(1+\gamma_0 p/B^2)-c_s^2k_\parallel^2]R}C_2, \quad (26)$$

and the sought local dispersion relation can be obtained by substituting relationship (26) into the first of Eqs. (24),

$$\omega\left(\omega-\omega^*+\frac{3}{2}\omega_R\right) = k_\parallel^2 V_A^2 + \frac{2k_b^2}{k_\perp^2R^2}\left(-\frac{p'R}{\rho}+\frac{2(\omega-\omega^*)(\omega-\omega_M)c_s^2}{\omega(\omega-\omega_M)(1+\gamma_0 p/B^2)-c_s^2k_\parallel^2}\right). \quad (27)$$

Let us compare dispersion relation (27), which was derived in the hydrodynamic approximation, to an analogous equation derived by Mikhailovskii [16] for a longitudinally uniform curvilinear magnetic field in the kinetic approximation. For an isotropic isothermal plasma with a uniform temperature at low β values, this equation takes the form

$$\sum_{e,i}\frac{\omega_p^2 M}{k_\perp^2 T}\left(1-\frac{\omega^*}{\omega}\right)\left\langle 1-J_0^2(z)-\frac{\omega_d}{\omega}J_0^2+\frac{\omega_\Delta}{\omega}\left(\frac{4J_0J_1}{z}-1\right)-\frac{\left(J_0\omega_d-\frac{2J_1}{z}\omega_\Delta\right)^2}{\omega(\omega-\omega_d-k_\parallel V_\parallel)}\right\rangle-\frac{k_\parallel^2c^2}{\omega^2} = 0, \quad (28)$$

where J_0 and J_1 are Bessel functions of the argument $z = k_\perp V_\perp/\omega_c$, the angular brackets $\langle\ \rangle$ indicate integration over velocities with a Maxwellian distribution function, $\omega_d = \frac{k_b V_\perp^2 B'}{2\omega_c B} + \frac{k_b V_\parallel^2}{\omega_c R}$, $\omega_\Delta = \frac{k_B V_\perp^2}{2\omega_c}\left(\frac{B'}{B}-\frac{1}{R}\right)$, and ω_p is the plasma frequency. Note that, unlike Eq. (27), Eq. (28) is valid for arbitrary values of $k_\perp\rho_i$.

Since we have $z_e \ll 1$ for electrons, we can use power-series expansions of the Bessel functions to obtain

$$\frac{\omega_{pi}^2 M_i}{k_\perp^2 T}\left(1-\frac{\omega^*}{\omega}\right)\langle I\rangle+\frac{2k_b\omega_{pi}^2}{k_\perp^2\omega_{ci}\omega R}\left(1+\frac{\omega^*}{\omega}\right)-\frac{k_\parallel^2c^2}{\omega^2} = 0,$$
$$I = 1-J_0^2(z_i)-\frac{\omega_{di}}{\omega}J_0^2+\frac{\omega_{\Delta i}}{\omega}\left(\frac{4J_0J_1}{z_i}-1\right)-\frac{\left(J_0\omega_{di}-\frac{2J_1}{z_i}\omega_{\Delta i}\right)^2}{\omega(\omega-\omega_{di}-k_\parallel V_\parallel)}, \quad (29)$$

where we have ignored the compressibility of the electron gas, $k_\parallel V_{Te}/\omega \gg 1$. As can be seen, the sole contri-

bution of the electrons is to the term that contains the curvature and describes the instability growth.

We consider Eq. (29) in the limit $z_i \ll 1$ in order to make a limiting transition to hydrodynamic dispersion relation (27). Again using power-series expansions of the Bessel functions, we find

$$I = -\frac{\omega_{di}-\omega_{\Delta i}}{\omega} - \frac{(\omega_{di}-\omega_{\Delta i})^2}{\omega(\omega-\omega_{\Delta i}-k_\parallel V_\parallel)} + \frac{z_i^2}{2}\left(1+\frac{\omega_{di}-\omega_{\Delta i}}{\omega}-\frac{\omega_{\Delta i}}{2\omega}+\frac{(\omega_{di}-\omega_{\Delta i})(\omega_{di}-\omega_{\Delta i}/2)}{\omega(\omega-\omega_{di}-k_\parallel V_\parallel)}\right). \quad (30)$$

Averaging the first term in expression (30) with allowance for the electron contribution to Eq. (29) leads to the expression $\frac{4\omega_{pi}^2 k_b^2 p'}{\omega_{ci}^2 k_\perp^2 \omega^2 R\rho}$ for the term describing the instability growth in the dispersion relation. Recall that the total plasma pressure is equal to $2p$, where $p = p_i = p_e$. Averaging the second term in expression (30) leads to an expression that can be represented with sufficient accuracy (by appropriately adjusting the value of the adiabatic index γ_0) as $-\frac{4\omega_{pi}^2 k_b^2}{\omega_{ci}^2 k_\perp^2 \omega^2 R^2}\frac{(\omega-\omega^*)(\omega-\omega_M)c_s^2}{\omega(\omega-\omega_M)-c_s^2 k_\parallel^2}$. Averaging the third term in which the quantity ω_Δ and the last summand are ignored leads to the expression $\frac{\omega_{pi}^2(\omega-\omega^*)\left(\omega+\frac{3}{2}\omega_R\right)}{\omega_{ci}^2\omega^2}$. One can readily verify that inserting these three expressions into dispersion relation (29) yields dispersion relation (27).

An analysis of the local dispersion relation shows that, under the BK condition, $D^{-1} = p'R/(2\gamma_0 p) < 1$, and for $k_\parallel = 0$, it has only nonzero real roots. The imaginary part of the roots is nonzero only for $k_\parallel$ values larger than that given by the equality $k_{\parallel l}^2 = C\omega^{*2}/c_s^2$, where the quantity C is on the order of unity. The figure shows how C generally depends on the extent to which the BK criterion is satisfied, $D > 1$. Hence, the zero in inequalities (19) should be replaced with a certain finite quantity corresponding to a nonzero rotational transform below which instability occurs under the BK condition.

The general dispersion relation can be derived from Eqs. (24) in the same way as that in Section 2 for the shearless case,

$$\omega(\omega-\langle\omega^*-1.5\omega_R\rangle) = k_z^2\langle\omega_A^2\rangle + U_0 + \frac{U_1(\omega-\langle\omega^*\rangle)(\omega-\langle\omega_M\rangle)}{\omega(\omega-\langle\omega_M\rangle)-k_z^2\langle\omega_s^2\rangle}, \quad (31)$$

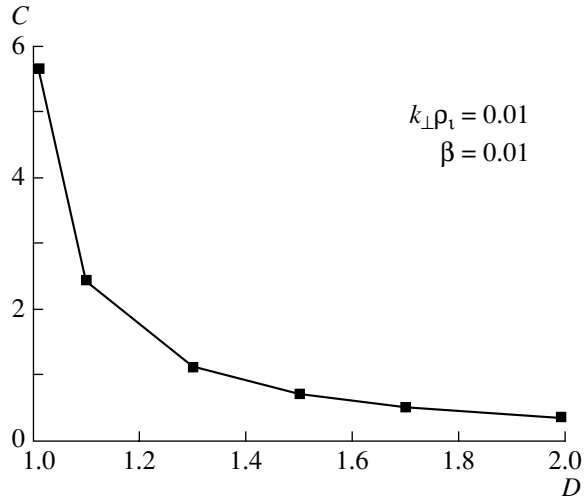

Dependence of C on D.

where we have introduced the following notation for the averaged frequencies:

$$\langle\omega_A^2\rangle = 16\pi^4 F^{-2}\left(\oint\frac{A^2 d\zeta}{B^2 c_A^2}\oint A^{-2}d\zeta\right)^{-1},$$
$$\langle\omega_s^2\rangle = 8\pi^3 F^{-2}c_s^2\left(\oint\left(1+\frac{\gamma_0 p}{B^2}\right)\frac{d\zeta}{B^2}\right)^{-1},$$
$$\langle\omega_M\rangle = \oint\omega_M d\zeta/2\pi, \quad \langle\omega^*\rangle = \oint\frac{\omega^* d\zeta}{B^2 R}/\oint\frac{d\zeta}{B^2 R}, \quad (32)$$
$$\langle\omega^*-1.5\omega_R\rangle = \oint\frac{(\omega^*-1.5\omega_R)A^2 d\zeta}{B^2 c_A^2}/\oint\frac{A^2 d\zeta}{B^2 c_A^2}.$$

Dispersion relation (31) has the same structure as local dispersion relation (27). Under the BK condition, $U_0 + U_1 > 0$, and for $k_z = 0$, it has only nonzero real roots. In this case, the roots can be imaginary (i.e., the instability can occur) only when $k_z^2 > k_{zl}^2$. The bifurcation point for the solution to dispersion relation (31) is easy to calculate numerically. As far as an analytic estimate of the value of k_{zl}^2 is concerned, it can be derived from dispersion relation (31) by ignoring all the terms except for those with U_0 and U_1. Thus, under the condition $(U_0 + U_1)/U_1 < 1$, we obtain

$$k_{zl}^2 \sim \frac{U_1\langle\omega^*\rangle^2}{4(U_0+U_1)\langle\omega_s^2\rangle}. \quad (33)$$

Since, for a nonzero rotational transform, we have $k_z^2 = (n-\mu m)^2$, the instability under the BK condition can occur only when

$$(n-\mu m)^2 > \frac{U_1\langle\omega^*\rangle^2}{4(U_0+U_1)\langle\omega_s^2\rangle}. \quad (34)$$

For $n = 0$, the instability is impossible up to rotational transform values of about

$$\mu_l \sim \sqrt{\frac{U_1\langle\omega^*\rangle^2}{4(U_0+U_1)\langle\omega_s^2\rangle m^2}} \approx \frac{\rho_i R_1}{a^2}, \qquad (35)$$

where R_1 is the characteristic major radius of the toroidal mirror system. For $n \neq 0$, formula (35) gives a lower estimate for the rotational transform. We can see that, even when the rotational transform is fairly large, the BK condition also is a sufficient condition for the stability of quasi-flute oscillations in a plasma with hot ions confined in a large-aspect-ratio device.

4. CONCLUSIONS

The above analysis confirms the conclusions of [9] on the impossibility of a limiting transition from the SM criterion to the BK criterion when the rotational transform approaches zero. Under the BK condition, the SM criterion predicts the onset of an acoustic instability with a finite growth rate when the extent to which the magnetic field lines are unclosed is vanishingly small. Taking into account the finite ion Larmor radius allows this limiting transition to be made. The BK criterion ensures MHD stability at rotational transform values below a certain critical value determined by the ratio of the ion Larmor radius to the plasma minor radius. Under experimental conditions, this critical value is far larger than the one expected to be produced by actual magnetic perturbations. In toroidal mirror systems, the plasma with hot electrons and cold ions is more sensitive to magnetic perturbations than the plasma with hot ions.

ACKNOWLEDGMENTS

This work was supported in part by the RF Program for State Support of Leading Scientific Schools (project no. NSh-2024.2003.2) and the Russian Foundation for Basic Research (project no. 03-02-16768).

APPENDIX 1

Derivation of the Equations for Ideal Ballooning Modes with Allowance for the Finite Larmor Radius

The FLR is taken into account as follows. The equations of fluid motion (see Eqs. (A1.1) below) are supplemented with the ion magnetic viscosity tensor [17, 18] $\overleftrightarrow{\pi} = -\frac{p_i}{4\omega_{ci}}\{(\overleftrightarrow{P}\times\mathbf{b}) + Tr\}$, which contains the tensor $\overleftrightarrow{P} = 3\mathbf{b}\otimes(\mathbf{b}\times(\nabla\times\mathbf{V}_\perp)) + 6\mathbf{b}\otimes(\mathbf{b}\cdot\nabla)\mathbf{V} + (\nabla\otimes\mathbf{V} + Tr)$ and in which $\mathbf{b} = \mathbf{B}/B$ and the symbol $\otimes$ stands for the tensor product. It is also necessary to account for the diamagnetic ion drift velocity $\mathbf{V}_D = \frac{\mathbf{B}\times\nabla p_i}{\rho\omega_{ci}B}$. The invariant form of the magnetic viscosity tensor that was presented in [17] is convenient for deriving the general equations. For simplicity, we consider a plasma with uniform temperature (i.e., without heat fluxes) and assume that the plasma is dominated by the *ion* pressure (so the subscript in the pressure will be dropped). Thus, the equations of fluid motion have the form

$$\begin{aligned} Mn\frac{d\mathbf{V}}{dt} &= -\nabla p + \mathbf{j}\times\mathbf{B} - \nabla\cdot\overleftrightarrow{\pi}, \\ \frac{\partial n}{\partial t} + \nabla\cdot(n\mathbf{V}) &= 0, \quad \frac{d}{dt}(pn^{-\gamma_0}) = 0. \end{aligned} \qquad (A1.1)$$

Here, the velocity is equal to $\mathbf{V} = \mathbf{V}_D - i\omega\boldsymbol{\xi}_\perp - i\omega\boldsymbol{\xi}_\parallel$, where $\boldsymbol{\xi}_\perp = \frac{i}{\omega}\frac{\tilde{\mathbf{E}}\times\mathbf{B}}{B^2}$, $\boldsymbol{\xi}_\parallel = \frac{i}{\omega}\frac{\mathbf{B}(\mathbf{B}\cdot\tilde{\mathbf{V}})}{B^2}$, and the tilde marks the perturbed quantities. The use of the adiabatic equation (the third of Eqs. (A1.1)) in place of the heat balance equation is a fairly good approximation (provided that the γ_0 value is chosen appropriately), which makes it possible to reveal the main changes in the ideal MHD equations. Note that, once the diamagnetic drift velocity is taken into account, the procedure of linearizing Eqs. (A1.1) should be performed with allowance for the steady-state fluid velocity $\mathbf{V}_{D0}$. The perturbed magnetic field is given by the relationship

$$\tilde{\mathbf{B}} = \nabla\times(\boldsymbol{\xi}_\perp\times\mathbf{B}). \qquad (A1.2)$$

The perturbations $\boldsymbol{\xi}$ whose wavelengths in the direction transverse to the magnetic field $\mathbf{B}$ are short and those in the longitudinal direction are long can be conveniently considered in the eikonal approximation

$$\boldsymbol{\xi} = \hat{\boldsymbol{\xi}}(\mathbf{r})\exp\left(\frac{i}{\varepsilon}S(\mathbf{r}) - i\omega t\right), \qquad (A1.3)$$

where $\mathbf{k}_\perp = \nabla_\perp S$ and $\mathbf{k}_\perp\cdot\mathbf{B} = 0$. The parameter $\varepsilon \ll 1$ reflects the fact that the perturbations are small-scale, $|\mathbf{B}\times\nabla\ln\tilde{f}| \gg |\mathbf{B}\times\nabla\ln f|$, $|\mathbf{B}\cdot\nabla\tilde{f}| \ll |\mathbf{B}\times\nabla\tilde{f}|$. The magnetoacoustic perturbations are ignored; this corresponds to the condition $\mathbf{k}_\perp\cdot\hat{\boldsymbol{\xi}} = 0$, which leads to the representation [11]

$$\hat{\boldsymbol{\xi}}_\perp = \frac{\mathbf{k}_\perp\times\mathbf{B}}{k_b B}\xi, \qquad (A1.4)$$

where ξ is the component of the displacement vector $\hat{\boldsymbol{\xi}}$ that is normal to the magnetic surface and $k_b = \left(\frac{\mathbf{B}}{B}\times\nabla a\right)\cdot\mathbf{k}_\perp$. Note that $\mathbf{B}\cdot\nabla\frac{k_b}{B} = 0$ [11].

The first of Eqs. (3) is derived by linearizing the current-continuity equation $\nabla\cdot\mathbf{j} = 0$ in the following way

[15]. Representing the current as a sum of the longitudinal and transverse components, $\mathbf{j} = \alpha\mathbf{B} + \mathbf{j}_\perp$, where

$$\mathbf{j}_\perp = \mathbf{j}_{\perp 1} + \mathbf{j}_{\perp 2} + \mathbf{j}_{\perp 3}$$
$$= (\mathbf{B}\times\nabla p)/B^2 + (\mathbf{B}\times\rho d\mathbf{V}/dt)/B^2 + (\mathbf{B}\times\nabla\cdot\overleftrightarrow{\pi})/B^2,$$

yields

$$\mathbf{B}\cdot\nabla\tilde{\alpha} + \tilde{\mathbf{B}}\cdot\nabla\alpha + \nabla\cdot\tilde{\mathbf{j}}_\perp = 0. \quad \text{(A1.5)}$$

By virtue of the small scales of the perturbations under consideration, the expression for the divergence of the current component $\tilde{\mathbf{j}}_{\perp 1} = \frac{\mathbf{B}\times\nabla\tilde{p}}{B^2} + \frac{\tilde{\mathbf{B}}\times\nabla p}{B^2} - 2\frac{(\mathbf{B}\times\nabla p)}{B^2}\frac{\tilde{\mathbf{B}}\cdot\mathbf{B}}{B^2}$ can be simplified to

$$\nabla\cdot\tilde{\mathbf{j}}_{\perp 1} = \nabla\tilde{p}\cdot\left(\nabla\times\frac{\mathbf{B}}{B^2}\right) + \frac{\nabla p\cdot(\nabla\times\tilde{\mathbf{B}})}{B^2} - 2\frac{(\mathbf{B}\times\nabla p)\cdot\nabla(\tilde{\mathbf{B}}\cdot\mathbf{B})}{B^4}. \quad \text{(A1.6)}$$

Using the relationships $\nabla\times\frac{\mathbf{B}}{B^2} = \frac{\alpha\mathbf{B}}{B^2} + 2\frac{\mathbf{B}\times\boldsymbol{\kappa}}{B^2} - \frac{p'}{B^2}\frac{\mathbf{B}\times\nabla a}{B^2}$ and $\nabla p\cdot(\nabla\times\tilde{\mathbf{B}}) \approx \nabla p\cdot\frac{\mathbf{B}\times\nabla\tilde{p}}{B^2}$ and replacing the quantity $\nabla(\mathbf{B}\cdot\tilde{\mathbf{B}})$ in the last term of Eq. (A1.6) by $-\nabla\tilde{p}$ (that this replacement can be made is a consequence the perturbed equilibrium equation; see, e.g., [15]) leads to the relationship

$$\nabla\cdot\tilde{\mathbf{j}}_{\perp 1} = 2\nabla\tilde{p}\cdot\frac{\mathbf{B}\times\boldsymbol{\kappa}}{B^2}. \quad \text{(A1.7)}$$

With representation (A1.4), the divergence of the vector $\tilde{\mathbf{j}}_{\perp 2} = (\mathbf{B}\times\rho d\tilde{\mathbf{V}}/dt)/B^2$ is described by the expression

$$\nabla\cdot\tilde{\mathbf{j}}_{\perp 2} = -\frac{i\omega(\omega - 2\omega^*)\rho k_\perp^2\xi}{Bk_b}, \quad \text{(A1.8)}$$

where the diamagnetic drift frequency is equal to $\omega^* = k_b p'/(\omega_{ci}\rho)$. The presence of the factor 2 multiplying the diamagnetic drift frequency in expression (A1.8) should not lead to confusion because, in the resulting equation, it will be canceled by the same factor, stemming from the contribution of the term with the viscosity. In fact, using the expression for the viscosity tensor reduces the term with the divergence of $\tilde{\mathbf{j}}_{\perp 3}$ to

$$\nabla\cdot\tilde{\mathbf{j}}_{\perp 3} = -\frac{i\omega\left(\omega^* + \frac{3}{2}\omega_R\right)\rho k_\perp^2\xi}{Bk_b}, \quad \text{(A1.9)}$$

where the magnetic drift frequency is equal to $\omega_R = \frac{p}{\omega_{ci}\rho}\frac{k_b}{R}$ because it takes into account the curvature of the magnetic field lines.

In order to derive the expression for $\mathbf{B}\cdot\nabla\tilde{\alpha}$, where $\tilde{\alpha} = \mathbf{B}\cdot(\nabla\times\tilde{\mathbf{B}})/B^2$, it is necessary to substitute relationship (A1.4) and the relationships $\mathbf{k}_\perp = \nabla_\perp S$ and $\mathbf{B}\cdot\nabla\frac{k_b}{B} = 0$ into expression (A1.2). Doing this yields

$$\tilde{\mathbf{B}} = \frac{\mathbf{B}\cdot\nabla\xi}{Bk_b}[\mathbf{k}_\perp\times\mathbf{B}] + \xi\left[\mathbf{k}_\perp\times\nabla_\perp\left(\frac{B}{k_b}\right)\right]. \quad \text{(A1.10)}$$

Relationship (A1.10) makes it possible to represent $\tilde{\alpha}$ in the form $\tilde{\alpha} = -i\frac{k_\perp^2}{B^2}\frac{B}{k_b}\mathbf{B}\cdot\nabla\xi$ and, accordingly, to obtain

$$\mathbf{B}\cdot\nabla\tilde{\alpha} = -i\mathbf{B}\cdot\nabla\left(\frac{k_\perp^2}{B^2}\frac{B}{k_b}\mathbf{B}\cdot\nabla\xi\right). \quad \text{(A1.11)}$$

Since the term $\tilde{\mathbf{B}}\cdot\nabla\alpha$ in expression (A1.5) can be ignored (see, e.g., [15]), the only thing that remains to be done in deriving the sought equation is to express the perturbed pressure $\tilde{p}$ in terms of the transverse displacement ξ and the divergence of the displacement vector $X = \frac{i}{\omega}\nabla\cdot\tilde{\mathbf{V}}$. This expression can be obtained by linearizing the last of Eqs. (A1.1). Taking into account the second of Eqs. (A1.1) gives

$$-i\omega\tilde{p} + \mathbf{V}_{D0}\cdot\nabla\tilde{p} + \tilde{\mathbf{V}}_D\cdot\nabla p - i\omega(\boldsymbol{\xi}_\perp\cdot\nabla p) - i\omega\gamma_0 pX = 0, \quad \text{(A1.12)}$$

where the finite divergence of the steady-state fluid velocity is ignored. The second and third terms in expression (A1.12) cancel one another, thus yielding

$$\tilde{p} = -\xi p' - \gamma_0 pX. \quad \text{(A1.13)}$$

Substituting all these relationships into Eq. (A1.5) and multiplying by B/k_b leads to the first equation for ideal ballooning modes with allowance for the FLR:

$$\left[\mathbf{B}\cdot\nabla\left(\frac{k_\perp^2}{k_b^2}\mathbf{B}\cdot\nabla\right) + \frac{2p'}{R} + \rho\omega\left(\omega - \omega^* + \frac{3}{2}\omega_R\right)\frac{k_\perp^2}{k_b^2}\right]\xi = -\frac{2\gamma_0 pX}{R}. \quad \text{(A1.14)}$$

The second equation, which relates the divergence of the displacement vector to its transverse component, can be derived from the longitudinal component of the equation of motion. For this, it is necessary to know the

expression for the divergence of the perturbed diamagnetic velocity:

$$\nabla \cdot \tilde{\mathbf{V}}_D \approx \frac{1}{en}\nabla \cdot \tilde{\mathbf{j}}_{\perp 1} \approx -i\omega^* \frac{2\xi}{R}. \quad \text{(A1.15)}$$

The expression for the divergence of $\boldsymbol{\xi}_\perp$ can also be written in a form analogous to expression (A1.15). Representing $\nabla \cdot \boldsymbol{\xi}_\perp$ as

$$\begin{aligned}\nabla \cdot \boldsymbol{\xi}_\perp &= \nabla \cdot \left(\frac{\mathbf{B} \times (\boldsymbol{\xi}_\perp \times \mathbf{B})}{B^2}\right) \\ &= B^2 \boldsymbol{\xi}_\perp \cdot \nabla\left(\frac{1}{B^2}\right) - \frac{\boldsymbol{\xi}_\perp \cdot \nabla p}{B^2} - \frac{\mathbf{B} \cdot \tilde{\mathbf{B}}}{B^2} \\ &= -2\boldsymbol{\xi}_\perp \cdot \boldsymbol{\kappa} + \frac{\boldsymbol{\xi}_\perp \cdot \nabla p}{B^2} - \frac{\mathbf{B} \cdot \tilde{\mathbf{B}}}{B^2}\end{aligned}$$

and making, with an accuracy sufficient for the derivation, the replacement $\frac{\boldsymbol{\xi}_\perp \cdot \nabla p}{B^2} - \frac{\mathbf{B} \cdot \tilde{\mathbf{B}}}{B^2} \sim -\frac{\gamma_0 p}{B^2}(\nabla \cdot \boldsymbol{\xi}_\perp + \nabla \cdot \boldsymbol{\xi}_\parallel)$ yields

$$\nabla \cdot \boldsymbol{\xi}_\perp = -\frac{2\xi}{R\left(1 + \frac{\gamma_0 p}{B^2}\right)} - \frac{\frac{\gamma_0 p}{B^2}}{\left(1 + \frac{\gamma_0 p}{B^2}\right)} \nabla \cdot \boldsymbol{\xi}_\parallel. \quad \text{(A1.16)}$$

Using relationships (A1.15) and (A1.16) puts the divergence of the displacement into the form

$$\begin{aligned}X = &\left(-\frac{2\xi}{R}\left(1 - \frac{\omega^*}{\omega}\right) + \mathbf{B} \cdot \nabla\left(\frac{\mathbf{B} \cdot \boldsymbol{\xi}_\parallel}{B^2}\right)\right) \\ &\times \left(1 + \frac{\gamma_0 p}{B^2}\right)^{-1}.\end{aligned} \quad \text{(A1.17)}$$

Taking the scalar product of the equation of motion with $\mathbf{B}$ and linearizing the resulting equation gives

$$\begin{aligned}-\rho\omega^2(\mathbf{B} \cdot \boldsymbol{\xi}_\parallel) + \mathbf{B} \cdot (\rho(\mathbf{V}_{D0} \cdot \nabla)\tilde{\mathbf{V}} + \nabla \cdot \overleftrightarrow{\tilde{\pi}}) \\ + \mathbf{B} \cdot \nabla \tilde{p} + \tilde{\mathbf{B}} \cdot \nabla p = 0.\end{aligned} \quad \text{(A1.18)}$$

With allowance for relationships (A1.13) and (A1.2), the last two terms here are transformed as $\mathbf{B} \cdot \nabla \tilde{p} + \tilde{\mathbf{B}} \cdot \nabla p = -\gamma_0 p \mathbf{B} \cdot \nabla X$. It can be shown that the second term in Eq. (A1.18) can be reduced to

$$\mathbf{B} \cdot (\rho(\mathbf{V}_{D0} \cdot \nabla)\tilde{\mathbf{V}} + \nabla \cdot \overleftrightarrow{\tilde{\pi}}) = \rho\omega_M \omega(\mathbf{B} \cdot \boldsymbol{\xi}_\parallel), \quad \text{(A1.19)}$$

where ω_M is the total magnetic drift frequency: $\omega_M = \omega_B + \omega_R = \frac{p}{\omega_{ci}\rho}\frac{\mathbf{k}_\perp \cdot (\mathbf{B} \times \nabla B)}{B^2} + \frac{p}{\omega_{ci}\rho}\frac{k_b}{R}$. The component of the divergence of the viscosity tensor along the magnetic field direction has the form (see, e.g., [17]):

$$\begin{aligned}&\mathbf{b} \cdot (\nabla \cdot \overleftrightarrow{\tilde{\pi}}) \\ &= \frac{1}{\omega_{ci}}(\nabla \times \tilde{\mathbf{V}}_\perp)\left(-\nabla p + p\frac{\nabla B}{B} + p\boldsymbol{\kappa}\right).\end{aligned} \quad \text{(A1.20)}$$

Introducing the notation $\boldsymbol{\xi} = \boldsymbol{\xi}_\perp + \boldsymbol{\xi}_\parallel$ and using the relationship $(\nabla \times \tilde{\mathbf{V}}_\perp) = \omega(\mathbf{k}_\perp \times \boldsymbol{\xi})$ gives

$$\mathbf{B} \cdot (\nabla \cdot \overleftrightarrow{\tilde{\pi}}) = \rho\omega(\omega_M - \omega^*)(\mathbf{B} \cdot \boldsymbol{\xi}_\parallel). \quad \text{(A1.21)}$$

Taking into account the relationship $\mathbf{B} \cdot (\mathbf{V}_{D0} \cdot \nabla)\tilde{\mathbf{V}} = \omega\omega^*(\mathbf{B} \cdot \boldsymbol{\xi}_\parallel)$ leads to relationship (A1.19). As a result, with relationship (A1.18), the longitudinal displacement can be represented as

$$\mathbf{B} \cdot \boldsymbol{\xi}_\parallel = -\frac{c_s^2}{\omega(\omega - \omega_M)}\mathbf{B} \cdot \nabla X. \quad \text{(A1.22)}$$

Inserting representation (A1.22) into expression (A1.17) leads to the second equation for ideal ballooning modes with allowance for the FLR:

$$\begin{aligned}&\left[\mathbf{B} \cdot \nabla\left(\frac{c_s^2}{\omega(\omega - \omega_M)B^2}\mathbf{B} \cdot \nabla\right) + \frac{\gamma_0 p + B^2}{B^2}\right]X \\ &= -\frac{2\xi}{R}\left(1 - \frac{\omega^*}{\omega}\right).\end{aligned} \quad \text{(A1.23)}$$

Ignoring the drift frequencies in Eqs. (A1.14) and (A1.23) reduces them to the familiar equations for the ideal ballooning modes. The equations derived are valid for any values of the rotational transform and of the shear, in particular, for a zero rotational transform.

APPENDIX 2

Stability at $\mu, \mu' \longrightarrow 0$

When the shear is finite (nonzero), Eqs. (6) contains secular terms. Consequently, it is necessary to use a special ballooning representation [19–21]. We employ here a somewhat modified representation, namely,

$$\begin{aligned}\xi = &\sum_{m=-\infty}^{\infty} \lim_{N\to\infty} \frac{1}{2N+1} \sum_{n=-N}^{N} \bar{\xi}_m(\zeta - 2\pi n) \\ &\times \exp(im(\beta + 2\pi n\mu)).\end{aligned} \quad \text{(A2.1)}$$

In the limit $\mu = 0$, representation (A2.1) yields a periodic solution, characteristic of closed magnetic field lines. The slight difference between representation (A2.1) and the widely used ballooning representation [19–21] lies precisely in the fact that the former permits a transition to the limit at hand.

The choice of the form (A2.1) for the ballooning representation can be clarified with the following con-

siderations. Expansion (8) leads to discrete spectrum (9) of the function $\bar{\xi}_m(\zeta)$. This indicates that, for small values of the rotational transform, the function $\bar{\xi}_m(\zeta)$ is *almost periodic* and, consequently, can be approximated (at $N \gg 1$) by a trigonometric polynomial [22]

$$\bar{\xi}_m(\zeta) = \lim_{T\to\infty}\sum_{n=-N}^{N} e^{ik_n\zeta}\frac{1}{2T}\int_{-T}^{T}\bar{\xi}_m(\eta)e^{-ik_n\eta}d\eta. \quad \text{(A2.2)}$$

Substituting polynomial (A2.2) into expansion (8) and approximating the series $\sum_{n=-N}^{N} e^{in(\zeta-\eta)} = 2\pi\sum_{k=-N}^{N}\delta(\zeta-\eta-2\pi k)$ by δ functions, we arrive at representation (A2.1). Here, $\bar{\xi}_m$ is an aperiodic function of ζ over an infinite interval $-\infty < \zeta < \infty$; in the limit $\bar{\xi}_m \longrightarrow \infty$, it approaches zero, $|\zeta| \longrightarrow 0$.

Using ballooning representation (A2.1) and singling out the secular terms in explicit form, $\nabla\beta = \mathbf{M} - \mu'\zeta\nabla a$, we obtain equations analogous to Eqs. (6):

$$\left[\frac{\partial}{\partial\zeta}A^2\frac{\partial}{\partial\zeta} + \frac{2F^2p'}{\Phi'^2B^2R_0} + \frac{A^2F^2\omega^2}{4\pi^2B^2c_A^2}\right]\xi + \frac{2F^2\gamma_0 p}{\Phi'^2B^2R_0}X$$
$$= -\frac{\mu' zF}{\Phi'}\frac{\partial\alpha}{\partial\zeta}\left(\xi + \frac{\gamma_0 p}{p'}X\right),$$
$$\left[\frac{\partial^2}{\partial\zeta^2} + \frac{F^2\omega^2}{4\pi^2B^2c_s^2}\left(1+\frac{\gamma_0 p}{B^2}\right)\right]X + \frac{F^2\omega^2}{2\pi^2B^2c_s^2R_0}\xi \quad \text{(A2.3)}$$
$$= -\frac{\mu' zF\Phi'\omega^2}{4\pi^2p'c_s^2}\frac{\partial\alpha}{\partial\zeta}\xi,$$

where

$$A^2 = M^2 - 2\mu' z(\mathbf{M}\cdot\nabla a) + (\mu' z)^2|\nabla a|^2,$$
$$\alpha = \mathbf{j}\cdot\mathbf{B}/B^2 = \Phi'^{-1}\partial\nu/\partial\beta,$$
$$\frac{1}{R_0} = -\frac{\Phi'}{2\pi}\frac{(\mathbf{B}\times\mathbf{M})\cdot\boldsymbol{\kappa}}{B^2},$$
$$\frac{1}{R} = \frac{1}{R_0} + \frac{\Phi'\mu' z}{2\pi}\frac{(\mathbf{B}\times\nabla a)\cdot\boldsymbol{\kappa}}{B^2},$$
$$p'\frac{(\mathbf{B}\times\nabla a)\cdot\boldsymbol{\kappa}}{B^4} = \frac{2\pi p'}{\Phi'}\frac{1}{B^3}\frac{\partial B}{\partial\beta} = \frac{2\pi}{F\Phi'}\frac{\partial^2\nu}{\partial\zeta\partial\beta},$$

and a new notation is again avoided. In deriving Eqs. (A2.3), we have used the derivative of equilibrium equation (7) with respect to β and also the relationship $\nabla\beta = \mathbf{M} - \mu' z\nabla a$, where z is the slow coordinate.

We apply the same averaging procedure as in Section 2. Without going into the details of the derivation, we immediately write out the resulting equation:

$$4\pi^2\frac{\partial}{\partial z}\frac{1}{\oint A^{-2}d\zeta}\frac{\partial\xi_0}{\partial z}$$
$$+\left(\frac{2F^2p'}{\Phi'^2}\oint\frac{d\zeta}{B^2R_0} - \frac{F^2\gamma^2}{4\pi^2}\oint\frac{A^2d\zeta}{B^2c_A^2}\right)\xi_0$$
$$+\frac{2F^2\gamma_0 p}{\Phi'^2}\frac{\left(\oint\frac{d\zeta}{B^2R_0}\right)^2}{\oint\left(1+\frac{\gamma_0 p}{B^2}\right)\frac{d\zeta}{B^2}} \quad \text{(A2.4)}$$
$$\times(e^y\int\xi_0e^{-y}dy - e^{-y}\int\xi_0e^y dy) = 0,$$

where $y = z\frac{F\gamma}{(2\pi)^{3/2}c_s}\sqrt{\oint\left(1+\frac{\gamma_0 p}{B^2}\right)\frac{d\zeta}{B^2}}$. In order to simplify the analytic solution of Eq. (A2.4), we replace the integral terms containing A^2 with approximate expressions in which the dependence of z is explicitly taken into account:

$$\left(\oint A^{-2}d\bar{\zeta}\right)^{-1} \approx \frac{2\pi F}{\Phi'^2}\left(\oint\frac{|\nabla a|^2dl}{B}\right)^{-1}$$
$$\times\left(1+\frac{\mu'^2\Phi'^2}{4\pi^2}z^2\oint\frac{|\nabla a|^2dl}{B}\left(\oint\frac{Bdl}{|\nabla a|^2}\right)^{-1}\right),$$
$$\oint\frac{A^2d\zeta}{B^2c_A^2} \approx \frac{8\pi^3\rho}{F\Phi'^2}\left(\oint\frac{dl}{|\nabla a|^2B}\right) \quad \text{(A2.5)}$$
$$\times\left(1+\frac{\mu'^2\Phi'^2}{4\pi^2}z^2\oint\frac{|\nabla a|^2dl}{B^3}\left(\oint\frac{dl}{B|\nabla a|^2}\right)^{-1}\right).$$

Expressions (A2.5) are derived as follows. The sequence of operations of (i) taking the vector product of the second of representations (4) of the magnetic field in terms of the current with ∇a, (ii) substituting the first of representations (4) of the magnetic field in terms of the flux into the resulting expression, and (iii) taking its scalar product with $\nabla\beta$ yields the relationship

$$A^{-2} = \frac{1}{|\nabla\beta|^2} = \frac{|\nabla a|^2}{\left(\frac{F}{\Phi'\sqrt{g}} + (g^{12})^2\right)}, \quad \text{(A2.6)}$$

where $g^{12} = \nabla a\cdot\nabla\beta$ is the element of the metric tensor and $\sqrt{g} = F\Phi'/2\pi^2B^2$ is its Jacobian. We express the element g^{12} in terms of the so-called *local* shear $S = \frac{(\mathbf{B}\times\nabla a)\cdot(\nabla\times(\mathbf{B}\times\nabla a))}{|\nabla a|^4}$. To obtain the sought-for

equation, we take the vector product of the second of representations (4) of the magnetic field in terms of the current with ∇a and substitute the result into the expression for S:

$$\mathbf{B}\cdot\nabla\left(\frac{g^{12}}{|\nabla a|^2}\right) = -\frac{4\pi^2}{\Phi'}S + \frac{\mu}{F}\mathbf{B}\cdot\nabla\nu + \frac{\mu'}{\sqrt{g}}. \quad \text{(A2.7)}$$

We can see that the quantity S averaged over the magnetic surface is related to the shear μ' of the magnetic field lines. It is for this reason that we have introduced the term local shear. For μ = const, the averaged local shear is equal to zero and, moreover, its maximum value is, as a rule, small. Consequently, the right-hand side of Eq. (A2.7) is dominated by the second term. However, for small values of the rotational transform, this second term is also small; therefore, we are justified in ignoring the element g^{12} of the metric tensor in relationship (A2.6). As a result, in accordance with the asymptotic behavior of A^2 at large and small z values, we arrive at approximate expressions (A2.5).

Taking into account expressions (A2.5), we convert Eqs. (A2.4) into the form

$$\begin{aligned}&\frac{\partial}{\partial z}(1+C_1^2z^2)\frac{\partial\xi_0}{\partial z}\\ &-\frac{\gamma^2\rho}{4\pi^2}(1+C_2^2z^2)\oint\frac{dl}{B|\nabla a|^2}\oint\frac{|\nabla a|^2dl}{B}\xi_0\\ &+\frac{F}{4\pi^3}\oint\frac{d\zeta}{B^2R_0}\oint\frac{|\nabla a|^2dl}{B}\\ &\times\left[p'\xi_0+\frac{\gamma_0 p\oint\frac{d\zeta}{B^2R_0}}{\oint\left(1+\frac{\gamma_0 p}{B^2}\right)\frac{d\zeta}{B^2}}(e^y\int\xi_0e^{-y}dy-e^{-y}\int\xi_0e^ydy)\right]=0,\end{aligned} \quad \text{(A2.8)}$$

$$C_1^2 = \frac{\mu'^2\Phi'^2}{4\pi^2}\oint\frac{|\nabla a|^2dl}{B}\left(\oint\frac{Bdl}{|\nabla a|^2}\right)^{-1},$$

$$C_2^2 = \frac{\mu'^2\Phi'^2}{4\pi^2}\oint\frac{|\nabla a|^2dl}{B^3}\left(\oint\frac{dl}{B|\nabla a|^2}\right)^{-1}.$$

We apply the Fourier transformation and introduce notation (16) and (17) to reduce Eq. (A2.8) to

$$\begin{aligned}&C_1^2\frac{d}{dk_z}\left(k_z^2+\left(\frac{C_2}{C_1}\right)^2k_{zA}^2\right)\frac{d\xi_0}{dk_z}\\ &-\left(U_0+\frac{U_1}{1+\frac{k_z^2}{k_{zs}^2}}+k_{zA}^2\right)\xi_0-k_z^2\xi_0 = 0.\end{aligned} \quad \text{(A2.9)}$$

At this point, we should say a few words about the boundary conditions with which to solve Eq. (A2.9). Taking into account the fact that flute oscillations with $k_z = 0$ are suppressed by the plasma compressibility (the Kadomtsev condition $U_0 + U_1 \geq 0$ is satisfied), we are considering the displacements $X(k_z = 0) = 0$ of an incompressible plasma. In this case, the second of Eqs. (14) yields the first boundary condition

$$\xi_0(k_z = 0) = 0. \quad \text{(A2.10)}$$

The second boundary condition has the form

$$\xi_0(k_z) \longrightarrow 0 \quad \text{for} \quad k_z \longrightarrow \infty. \quad \text{(A2.11)}$$

Since Eq. (A2.9) essentially coincides with Eq. (3.1) from [8], the dispersion relation may be derived in a general way, i.e., by matching the solutions obtained for different ranges of the wavenumber k_z, namely, the Alfvén range, the acoustic range, and the range of its infinite values (the characteristic values of the wavenumber are given by expressions (17)). But here we use the smallness of the shear, $C_1^2 \ll 1$. Making the replacement $y = \xi_0\sqrt{k_z^2+\left(\frac{C_2}{C_1}\right)^2k_{zA}^2}$, we reduce Eq. (A2.9) to the standard form of a differential equation with a small coefficient in front of the highest order derivative:

$$\begin{aligned}&C_1^2\frac{d^2y}{dk_z^2}-F(k_z)y = 0,\\ &F = \frac{1}{k_z^2+\left(\frac{C_2}{C_1}\right)^2k_{zA}^2}\\ &\times\left(k_z^2+k_{zA}^2+U_0+\frac{U_1}{\frac{k_z^2}{k_{zs}^2}+1}+\frac{C_2^2}{\frac{k_z^2}{k_{zA}^2}+\left(\frac{C_2}{C_1}\right)^2}\right).\end{aligned} \quad \text{(A2.12)}$$

Note that, under BK condition (1), $U_0 + U_1 \geq 0$, we have $F(k_z = 0) > 0$. We also have $F(k_z \longrightarrow \infty) = 1$. Since the magnetic well is absent, $U_0 < 0$, there exists a maximum growth rate (a maximum value of k_{zs}^2) below which the function F vanishes at two points, k_{z1}^2 and k_{z2}^2. In Eq. (A2.12), we ignore the Alfvén wavenumber k_{zA}^2 (because we have $k_{zA} \ll k_{zs}$ for small beta values) and the last term in parentheses. As a result, for $k_{zs}^2 \ll (\sqrt{U_1} - \sqrt{U_0+U_1})^2$ (cf. expression (22)), we obtain

$$\begin{aligned}k_{z1}^2 &= -\frac{U_0+k_{zs}^2}{2}-\sqrt{\left(\frac{U_0+k_{zs}^2}{2}\right)^2-k_{zs}^2(U_0+U_1)},\\ k_{z2}^2 &= -\frac{U_0+k_{zs}^2}{2}+\sqrt{\left(\frac{U_0+k_{zs}^2}{2}\right)^2-k_{zs}^2(U_0+U_1)}.\end{aligned} \quad \text{(A2.13)}$$

Using the familiar asymptotic solutions to Eq. (A2.12) in the ranges $k_{z1} \le k_z \le k_{z2}$, $k_z < k_{z1}$, and $k_z > k_{z2}$ and also boundary conditions (A2.10) and (A2.11), we obtain the dispersion relation

$$\tan\left(C_1^{-1}\int\limits_{k_{z1}}^{k_{z2}}\sqrt{-F}dk_z + \frac{\pi}{4}\right) = \frac{1-\exp\left(C_1^{-1}\int\limits_{0}^{k_{z1}}\sqrt{F}dk_z\right)}{1+\exp\left(C_1^{-1}\int\limits_{0}^{k_{z1}}\sqrt{F}dk_z\right)}, \quad \text{(A2.14)}$$

or, in another form,

$$C_1^{-1}\int\limits_{k_{z1}}^{k_{z2}}\sqrt{-F}dk_z = \arctan\left(\frac{1-\exp\left(C_1^{-1}\int\limits_{0}^{k_{z1}}\sqrt{F}dk_z\right)}{1+\exp\left(C_1^{-1}\int\limits_{0}^{k_{z1}}\sqrt{F}dk_z\right)}\right) - \frac{\pi}{4} + j\pi. \quad \text{(A2.15)}$$

Here, $j = 1, 2, 3, \ldots$. Noting that the growth rates are maximum at minimum values of j, we arrive at the maximum growth rate determined by relationship (23).

We thus have obtained the same results as those in the absence of shear.

APPENDIX 3

Expressions for $\oint\frac{d\zeta}{B^2R}$ *and* $\oint\left(1+\frac{\gamma_0 p}{B^2}\right)\frac{d\zeta}{B^2}$

In order to calculate the quantity $\frac{1}{R} = -\frac{\Phi'}{2\pi}\frac{(\mathbf{B}\times\nabla\beta)\cdot\boldsymbol{\kappa}}{B^2}$, we use the general expression for the curvature, $\boldsymbol{\kappa} = -\frac{\mathbf{B}}{B}\times\left(\nabla\times\frac{\mathbf{B}}{B}\right)$, and equilibrium equation (7). Carrying out the transformations

$$\frac{(\mathbf{B}\times\nabla\beta)\cdot\boldsymbol{\kappa}}{B^4} = -\frac{\sqrt{g}(\mathbf{B}\times\nabla\beta)\cdot\left(\mathbf{B}\times\left(\nabla\times\frac{\mathbf{B}}{B}\right)\right)}{(\sqrt{g}B^2)B^3}$$

$$= -\frac{4\pi^2}{F\Phi'}\frac{\sqrt{g}\nabla\beta\cdot\left(\nabla\times\frac{\mathbf{B}}{B}\right)}{B}$$

$$= -\frac{2\pi}{F\Phi'}\frac{\sqrt{g}}{B^2}\nabla\beta\cdot\left(F'(\nabla a\times\nabla\zeta) - (\nabla\nu\times\nabla a) - F\frac{\nabla B\times\nabla\zeta}{B} + \nu\frac{\nabla B\times\nabla a}{B}\right) \quad \text{(A3.1)}$$

$$= \frac{2\pi}{F\Phi'}\frac{1}{B^2}\left(F' + \frac{\partial\nu}{\partial\zeta} - \frac{F}{B}\frac{\partial B}{\partial a} - \frac{\nu}{B}\frac{\partial B}{\partial\zeta}\right)$$

$$= \frac{2\pi}{F\Phi'}\left[\frac{1}{B^2}\left(F' + \frac{1}{2}\frac{\partial\nu}{\partial\zeta} - \frac{F}{B}\frac{\partial B}{\partial a}\right) + \frac{1}{2}\frac{\partial(\nu/B^2)}{\partial\zeta}\right]$$

$$= \frac{\pi}{F\Phi'}\left(\left[\frac{\partial(F/B^2)}{\partial a} - \frac{Fp'}{B^4}\right] + \frac{\partial(\nu/B^2)}{\partial\zeta}\right)$$

and using the notation $U = \oint dl/B$, we obtain

$$\oint\frac{d\zeta}{B^2R} = -\frac{\pi}{F}\left(U' - p'\oint\frac{dl}{B^3}\right),$$
$$\oint\left(1+\frac{\gamma_0 p}{B^2}\right)\frac{d\zeta}{B^2} = \frac{2\pi}{F}\left(U + \gamma_0 p\oint\frac{dl}{B^3}\right). \quad \text{(A3.2)}$$

Recall that we are analyzing an isometric toroidal mirror system for which the above contour integrals along the magnetic field line in one turn in the toroidal direction around the circumference of the torus are independent of the azimuthal coordinate of the initial point of integration.

REFERENCES

1. I. B. Bernstein, E. A. Frieman, M. D. Kruskal, and R. M. Kulsrud, Proc. R. Soc. London A **244**, 17 (1958).
2. B. B. Kadomtsev, in *Plasma Physics and the Problem of Controlled Thermonuclear Reactions*, Ed. by M. A. Leontovich (Izd. Akad. Nauk SSSR, Moscow, 1958; Pergamon Press, New York, 1960), Vol. 4.
3. V. V. Arsenin, E. D. Dlougach, V. M. Kulygin, *et al.*, Trans. Fusion Sci. Technol. **43** (1T), 17 (2003).
4. A. I. Morozov, V. P. Pastukhov, and A. Yu. Sokolov, in *Proceedings of the Workshop on D–^{3}He Based Reactor Studies, Moscow, 1991*, Paper 1C1.
5. A. Hasegava, L. Chen, and M. E. Mauel, Nucl. Fusion **30**, 2405 (1990).
6. V. V. Arsenin, E. D. Dlougach, V. M. Kulygin, *et al.*, Nucl. Fusion **41**, 945 (2001).
7. V. P. Pastukhov and N. V. Chudin, Fiz. Plazmy **27**, 963 (2001) [Plasma Phys. Rep. **27**, 907 (2001)].
8. A. B. Mikhailovskii and A. Skovoroda, Plasma Phys. Controlled Fusion **44**, 2033 (2002).
9. A. V. Zvonkov and A. A. Skovoroda, Fiz. Plazmy **30**, 269 (2004) [Plasma Phys. Rep. **30**, 241 (2004)].

10. A. V. Zvonkov, A. Yu. Kuyanov, J. Nuehrenberg, *et al.*, Fiz. Plazmy **28**, 822 (2002) [Plasma Phys. Rep. **28**, 756 (2002)].
11. V. D. Pustovitov and V. D. Shafranov, in *Reviews of Plasma Physics*, Ed. by B. B. Kadomtsev (Énergoatomizdat, Moscow, 1987; Consultants Bureau, New York, 1990), Vol. 15.
12. N. N. Bogolyubov and Yu. A. Mitropol'skii, *Asymptotic Methods in the Theory of Nonlinear Oscillations* (Nauka, Moscow, 1974; Gordon & Breach, New York, 1962).
13. V. V. Ilgisonis, Fiz. Plazmy **14**, 529 (1988) [Sov. J. Plasma Phys. **14**, 309 (1988)].
14. L. J. Zheng and M. Tessarotto, Phys. Plasmas **1**, 2956 (1994).
15. A. B. Mikhailovskii, *Instabilities in a Confined Plasma* (IOP, Bristol, 1998).
16. A. B. Mikhailovskii, *Electromagnetic Instabilities in a Nonuniform Plasma* (Énergoatomizdat, Moscow, 1991), p. 300.
17. V. I. Ilgisonis, Fiz. Plazmy **16**, 1046 (1990) [Sov. J. Plasma Phys. **16**, 607 (1990)].
18. A. B. Mikhailovskii, *Theory of Plasma Instabilities* (Atomizdat, Moscow, 1971; Consultants Bureau, New York, 1974).
19. J. W. Connor, R. J. Hastie, and J. B. Taylor, Phys. Rev. Lett. **40**, 396 (1978).
20. M. S. Chance, R. L. Dewar, E. A. Frieman, *et al.*, Nucl. Fusion Suppl. **1**, 677 (1979).
21. O. P. Pogutse and É. I. Yurchenko, in *Reviews of Plasma Physics*, Ed. by M. A. Leontovich and B. B. Kadomtsev (Atomizdat, Moscow, 1982; Consultants Bureau, New York, 1986), Vol. 11.
22. B. M. Levin and V. V. Zhikov, *Almost-Periodic Functions and Differential Equations* (Izd. MGU, Moscow, 1978).

Translated by O.E. Khadin

Plasma Physics Reports, Vol. 31, No. 2, 2005, pp. 123–132. Translated from Fizika Plazmy, Vol. 31, No. 2, 2005, pp. 146–156.

PLASMA KINETICS

Quantum Corrections to the Particle Distribution Function and Reaction Rates in Dense Media

A. N. Starostin*, A. G. Leonov, Yu. V. Petrushevich*, and Vl. K. Rerikh***

**Troitsk Institute for Innovation and Fusion Research, Troitsk, Moscow oblast, 142190 Russia*

***Moscow Institute of Physics and Technology, Institutskiĭ pr. 9, Dolgoprudnyĭ, Moscow oblast, 141700 Russia*

Received May 19, 2004; in final form, June 18, 2004

Abstract—Quantum mechanics predicts the existence of power-law tails in the momentum distribution function of particles in dense media even under conditions of thermodynamic equilibrium. The generalized expressions allowing for the effect of the medium density show that quantum corrections lead to a sharp increase in the reaction rates of threshold exothermic processes (such as fusion and chemical reactions and vibrational–translational relaxation). The accompanying modification of the distribution function changes the wings of the emission and absorption lines. The profiles of the absorption lines in dense gaseous media are shown to be asymmetric with respect to the line center. © *2005 Pleiades Publishing, Inc.*

1. INTRODUCTION

Because of frequent particle collisions, a kinetic description of dense gases and plasmas should be based on the generalized energy and momentum distribution function $f(E, \mathbf{p}, r, t)$, where E and $\mathbf{p}$ are the particle energy and momentum [1]. For an ideal gas (i.e., in the case of a low gas density) under conditions of thermodynamic equilibrium, the particles obey a Maxwellian distribution over momenta. Because of the finite lifetime of the excited energy states, the tails of the momentum distribution function in dense collisional media are substantially larger than those of the exponentially decaying Maxwellian distribution. Quantum uncertainty in the particle energy also contributes to these non-Maxwellian tails. As a result, the tails of the distribution function acquire a power-law form.

The effect of quantum uncertainty on the velocity distribution function was first pointed out by Kardanoff and Baym [2] in 1932. They calculated the leading nonvanishing term in the expansion of the distribution function in series in Planck's constant $\hbar$. The resulting correction to the temperature led to a Maxwellian velocity distribution function with the effective temperature

$$T_{\text{eff}} = T + \frac{\hbar^2}{12 m_i T^2}\left\langle\left(\frac{\partial U}{\partial q_i}\right)\right\rangle, \quad (1)$$

where U is the particle interaction energy and m_i and q_i are the mass and coordinate of a particle of the ith species. As was first noted in [3], due to quantum effects, the equilibrium momentum distribution function differs from a Maxwellian one and has power-law tails.

The kinetic equation for the generalized distribution function of the particles in an external field has the form

$$\frac{\partial f}{\partial t} + \mathbf{v}\cdot\nabla f - \mathbf{F}\frac{\partial f}{\partial \mathbf{p}} = \mathrm{St}\{f\}. \quad (2)$$

This equation can be solved using the well-known two-term approximation

$$f(E, \mathbf{p}, r, t) = f_0(E, \varepsilon, \mathbf{r}, t) + f_1(E, \varepsilon, \mathbf{r}, t)\frac{\mathbf{p}}{p}, \quad (3)$$

where ε is the particle kinetic energy, $f_0(E, \varepsilon, \mathbf{r}, t)$ is the spherical part of the distribution function, and $f_1(E, \varepsilon, \mathbf{r}, t)$ describes weak anisotropy caused by the external force (for example, for electrons in an external electric field, this force determines the current density). The kinetic coefficients (such as the drift velocity and diffusion coefficient) are calculated using the spherical part of the generalized distribution function.

In [1], the spherical part of the generalized particle distribution function was represented in the form

$$f_0(E, \varepsilon) = \delta_\gamma(E - \varepsilon)n(E). \quad (4)$$

In the simplest cases, such a representation enables one to obtain explicit expressions for this spherical part.

For an ideal gas, $\delta_\gamma(E - \varepsilon)$ is a Dirac delta function and, for a nonideal gas, it is a Lorentzian function [3, 4],

$$\delta_\gamma(E - \varepsilon) = \frac{1}{\pi}\frac{\mathrm{Im}\,\Sigma^R(E, \varepsilon)}{(E - \varepsilon - \mathrm{Re}\,\Sigma^R(E, \varepsilon))^2 + (\mathrm{Im}\,\Sigma^R(E, \varepsilon))^2}, \quad (5)$$

where $n(E)$ is the occupation number and $\Sigma^R(E, \varepsilon)$ is the retarded mass operator. Thus, the imaginary part of the mass operator determines the width of the Lorentzian function, whereas its real part determines the shift of

the resonance. By denoting $\gamma(E, \varepsilon) = \mathrm{Im}\Sigma^R(E, \varepsilon)$ and $\Delta(E, \varepsilon) = \mathrm{Re}\Sigma^R(E, \varepsilon)$, it is possible to reduce expression (5) to

$$\delta_\gamma(E-\varepsilon) = \frac{1}{\pi}\frac{\gamma(E,\varepsilon)}{(E-\varepsilon-\Delta(E,\varepsilon))^2+\gamma(E,\varepsilon)^2}. \quad (6)$$

There is a relation between the shapes of the spectral line wings and the tails of the particle momentum distribution function. Indeed, the line profile is determined by the convolution of Lorentzians (6) and by averaging over the velocities of he emitting (absorbing) atoms. In the resonance, the particle energy is a sum of the kinetic energy of the center of mass and the internal energy of the particle state.

The asymptotic behavior of the momentum distribution function can be expressed via the imaginary part of the retarded mass operator $\mathrm{Im}\Sigma^R(E, \mathbf{p}) \equiv \gamma(E, \mathbf{p})$:

$$f(\varepsilon) = \int_{-\infty}^{\infty}\frac{\gamma(E,\varepsilon)}{\varepsilon^2}n(E)\frac{dE}{\pi}. \quad (7)$$

Note that, in the absence of an external field, the distribution function is spherically symmetric and the index 0 can be omitted. For the Lorentz gas of electrons in plasma, the following approximate formula was obtained in [4]:

$$\gamma(E,\varepsilon) = \frac{\hbar N\sigma_{\mathrm{tot}}(\varepsilon)}{\varepsilon^2}\sqrt{\frac{2E}{m_e}}. \quad (8)$$

Here, N is the gas density, $\sigma_{\mathrm{tot}}(\varepsilon)$ is the total cross section for electron scattering by the gas atoms (ions), and m_e is the electron mass. From Eqs. (7) and (8), one can obtain the quantum correction to the distribution function related to the Coulomb interaction:

$$f(\varepsilon) = \frac{2\hbar Ne^4}{\varepsilon^4}\sqrt{\frac{2}{m_e}}\int_0^\infty\sqrt{E}n(E)dE. \quad (9)$$

It was shown in [3] that, for the unscreened Coulomb interaction, $f(\mathbf{p}) \sim \hbar N/p^8$. The power-law tails of the distribution function can significantly affect the rates of nonresonant fusion reactions. On a qualitative level, the emergence of such tails can be explained by the fact that, due to the interaction of a particle with the surrounding medium, its motion is spatially limited as compared to a free particle. According to the uncertainty principle, such a spatial limitation enlarges the phase volume of a particle in momentum space.

For the spectral line profile, an analogue of non-Maxwellian tails of the momentum distribution function is the Lorentzian asymptote of the line wings against the background of the central Doppler core. However, in contrast to the conventional interpretation of the spectral line profiles, the presence of a power-law tail in the momentum distribution function is of fundamentally quantum nature since, in classical statistics, the equilibrium particle distribution remains Maxwellian for any gas density because of the commutativity of the kinetic and potential energies.

The spherical part of a nonequilibrium distribution function formed under the action of an external force also has a power-law tail but with a different power index. Along with the change in the reaction rates (as is the case with an equilibrium distribution function), this also leads to a change in kinetic transport coefficients. In the case of a nonequilibrium distribution function, the occupation numbers should be calculated in accordance with the specific conditions of the problem under study.

The spectral intensity of radiation is determined by the distribution function of photons over frequencies. At low temperatures, when the equivalent linewidth exceeds the temperature, $\hbar\Delta\omega_e \geq T$, the line shape differs significantly from the Planck formula and the radiation intensity can substantially exceed the Planck intensity. Resonance radiation transfer in dense gas media was studied in [5, 6] both theoretically and experimentally. In [5], equations for resonant radiation transfer were derived in terms of the generalized spectral intensity $J(\omega, \mathbf{k})$, where the frequency ω and the wave vector $\mathbf{k}$ are independent variables.

The conventional theory of resonant radiation transfer, which was developed for the case of low gas densities, is inapplicable at very high pressures, because, in this case, the permittivity ε can differ substantially from unity and the photon mean free path becomes comparable to the radiation wavelength. When the photon mean free path with respect to the absorption in the center of the resonance line becomes comparable to the radiation wavelength (for sodium vapor, this occurs at gas densities of $N \geq 10^{17}$ cm^{-3}), the theory has to be modified. It can easily be shown that, in a dense medium, a photon is a rather "bad" quasi-particle for which the dispersion relation $(\varepsilon')^{1/2}\omega = ck$ is not satisfied (here, c is the speed of light in vacuum and k is the wavenumber). In this case, the problem of resonant radiation transfer can be resolved using an equation for the Fourier components of the correlation functions of the electromagnetic field. Such an equation can be formulated in terms of the Green's kinetic functions. This allows one to introduce the generalized spectral intensity of radiation $J(\omega, \mathbf{k})$, where the frequency ω and the wave vector $\mathbf{k}$ are independent variables. In the general case, $J(\omega, \mathbf{k})$ is not necessarily positive and only some of its moments (i.e., integrals over k with different weighting functions) have physical meaning. The spectral radiation intensity J_ω—a measurable quantity that is dealt with in the conventional transfer theory—is related to $J(\omega, \mathbf{k})$ by the relation

$$J_\omega(\mathbf{\Omega}) = \frac{2c^2}{\omega}\int_0^\infty kJ(\omega,\mathbf{k})\frac{k^2dk}{(2\pi)^5}, \quad (10)$$

where $\mathbf{\Omega}$ is the unit vector directed along $\mathbf{k}$.

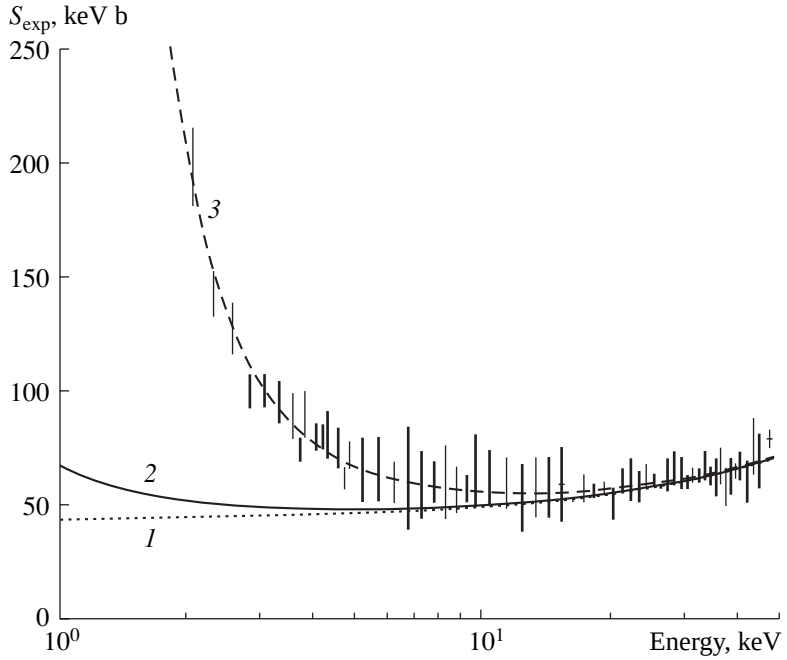

Fig. 1. Astrophysical factor in the cross section for the fusion reaction of deuterons as a function of the particle energy in the center-of-mass frame (the figure is taken from [8]). The experimental results are shown by the vertical bars. The theoretical dependences are obtained for bare deuterium nuclei (curve *1*) and for nuclei screened by the free electrons of the target metal at U_e = (*2*) 28 and (*3*) 309 eV.

The generalized transfer theory shows that, in the line center, the intensity of radiation emitted from a nonuniformly heated medium is by many orders of magnitude higher than the radiation intensity predicted by the conventional theory of resonant radiation transfer. Another consequence of the generalized transfer theory is the feasibility of obtaining (under definite conditions) anomalously high radiation intensity on the far red wing of a spectral line; this effect is determined by the Boltzmann spectral factor arising in the expression for the intensity of spontaneous emission from a thermodynamically equilibrium medium.

2. REACTION RATES

The rates of nonresonant reactions (in particular, fusion reactions) are determined by the energy of the interacting particles in the center-of-mass frame. At moderate temperatures, the main contribution to fusion reactions is made by the particles with energies a few times higher than the plasma temperature [7].

Recent experiments [8, 9] showed that, at low energies, the measured dependence of the rates of nonresonant fusion reactions on the particle energy differs from that predicted by theory. Figure 1 (taken from [8]) shows the measured energy dependence of the astrophysical factor in the cross section for a fusion reaction occurring in the interaction of a deuteron beam with deuterons imbedded into the crystal lattice of the target metal. It was found that the reaction rate in the range of low energies (<5 keV) of the beam particles was much higher than the calculated one. To explain this effect, a hypothesis about the screening of the target ions by an electron cloud was proposed in [8]. The theoretical dependences of the astrophysical factor obtained in [8] for bare and screened (with different screening potentials) deuterium nuclei are shown in Fig. 1. For a screening potential of 28 eV, which is quite reasonable under the given conditions, the theoretical curve disagrees with the experimental one. It can be seen that agreement between them in the range of low beam energies can be achieved only if the screening potential were 309 eV, which is nonrealistic under these experimental conditions. Obviously, the current theoretical models must be refined in order to adequately interpret the experimental results.

In [4, 10], it was shown that quantum corrections lead to a significant deviation of the distribution function from a Maxwellian one. The resulting power-law tails of the distribution function affect the reaction rates with the participation of these particles, thus leading to a nonexponential temperature dependence of the cross sections for inelastic processes.

In this study, we examine how quantum corrections to the distribution function influence fusion reactions under actual experimental conditions, calculate the rates of the interaction reactions between the beam and target particles, and compare them to the results of measurements performed in [8, 9].

The reaction rate K of particles of species a and b can be found from the collision integral in Eq. (2). In the general case, the problem is reduced to the calculation of

$$\begin{aligned} n_a n_b K &= C\int_0^\infty dE_a \int d\mathbf{p}_a \int_0^\infty dE_b \int d\mathbf{p}_b \int d\omega \int dq q^2 n(E_a) \\ &\times (1 \mp n(E_a'))\delta\gamma_a(E_a - \varepsilon_a, \varepsilon_a) n(E_b)(1 \mp n(E_b')) \\ &\times \delta\gamma_b(E_b - \varepsilon_b, \varepsilon_b)\delta\gamma_a'(E_a' - \varepsilon_{p_a - q}, \varepsilon_{p_a - q}) \\ &\times \delta\gamma_b'(E_b' - \varepsilon_{p_b + q}, \varepsilon_{p_b + q})\sigma(\varepsilon_p)\sqrt{\frac{2\varepsilon_p}{\mu}}, \end{aligned} \tag{11}$$

where E_a and p_a are the energy and momentum of an a-species particle; $E_a' = E_a + Q_a - \omega$, $E_b' = E_b + \omega + Q_b$, ε_p is the particle kinetic energy in the center-of-mass frame; μ is the reduced mass of the colliding particles; C is a normalization constant, which is determined by comparing with the results of calculations performed for a low density and high temperature;

$$\varepsilon_p = \frac{p^2}{2\mu}, \quad \mathbf{p} = \frac{m_b\mathbf{p}_a - m_a\mathbf{p}_b}{m_a + m_b}.$$

In Eq. (11), the minus and plus signs refer to fermions and bosons, respectively.

For endothermic reactions ($Q_a < 0$), the factors $(1 \mp n(E'))$ are exponentially small. This means that, for the concerned mechanism for intensifying fusion reactions by the power-law tails of the distribution function to operate, the plasma temperature should not be too low because the colliding particles are already ionized and the ionization rate is an exponential function of the temperature. In a solid matrix, ionization occurs due to the presence of conduction electrons.

For exothermic reactions ($Q_a > 0$) in the nondegenerate case, $n(E')$ is much less than unity and thus can be ignored. The particle occupation numbers $n(E)$ depend on the system statistics. For deuteron reactions, in which we are interested here, the Bose statistics is valid:

$$n(E) = [\exp\{(E - \mu)/T\} - 1]^{-1}. \tag{12}$$

For a nonideal plasma, the dependence of the distribution function on the kinetic energy ε is described by a Lorentzian:

$$\delta\gamma(E - \varepsilon, \varepsilon) = \frac{\gamma(E, \varepsilon)/\pi}{(E - \varepsilon - \Delta(E, \varepsilon))^2 + \gamma^2}. \tag{13}$$

The linewidth is determined by the relation [10]

$$\gamma_a(E_a, \varepsilon_a) = \hbar N \sigma_a V_a, \quad \sigma_a = \frac{\pi e^4}{\varepsilon_a^2}, \quad V_a = \sqrt{\frac{2\varepsilon_a}{m_a}}, \tag{14}$$

where N is the density of the scattering particles.

When passing to an ideal plasma (e.g., by decreasing the plasma density), the parameter $\gamma(E, \varepsilon)$ tends to zero and the function $\delta\gamma(E - \varepsilon, \varepsilon)$ tends to a δ function.

In the center-of-mass frame, the reaction cross section as a function of the kinetic energy ε_p can be represented in the form

$$\sigma_1(\varepsilon_p) = \frac{S(\varepsilon_p)}{\varepsilon_p}\exp\{-2\pi\eta(\varepsilon_p)\}, \tag{15}$$

where $\eta(\varepsilon_p) = \dfrac{Z_1 Z_2 e^2}{\hbar v}$ is the Sommerfeld parameter. The astrophysical factor $S(\varepsilon_p)$ varies slightly with energy. The influence of the potential U_e (which arises due to the screening of an atom by electrons) on the reaction cross section can be taken into account by adding it to the collision energy:

$$\sigma(\varepsilon_p) = \sigma_1(\varepsilon_p + U_e). \tag{16}$$

The reaction rates were calculated numerically under conditions close to the experimental ones: the particle density was $n_a = 5 \times 10^{23}$ cm^{-3} and the masses of the interacting particles were $m_a = m_b = 2$ amu. We considered a reaction between the a-species target particles and b-species incident particles. In expression (14) for the linewidth, the value of N was taken to be equal to the density of the scattering ions in a metal matrix.

Taking into account the high multiplicity of integral (11), it was calculated using the Monte Carlo method. The distribution function over kinetic energies corresponded to a particle temperature of $T = 2.44 \times 10^{-2}$ eV. The energy of the b-species (beam) particles was also specified.

Note that, for a monoenergetic particle beam, the computation of the reaction rate by formula (11) can be reduced to calculating a simpler integral:

$$\begin{aligned} n_a K' &= C\int_0^\infty dE_a \int d\mathbf{p}_a \int n(E_a) a(E_a - \varepsilon_a, \varepsilon_a)\sqrt{\frac{2\varepsilon_p}{\mu}}\sigma(\varepsilon_p), \end{aligned} \tag{17}$$

where $a(E - \varepsilon, \varepsilon)$ stands for Lorentzian (13). For an ideal plasma, the influence of the wings of the Lorentzian function can be ignored and the expression for the reaction rate simplifies to

$$\begin{aligned} n_a K_2 &= C\int_0^\infty dE_a \int d\mathbf{p}_a \int n(E_a)\delta(E_a - \varepsilon_a)\sqrt{\frac{2\varepsilon_p}{\mu}}\sigma(\varepsilon_p) \\ &\sim \int_0^\infty d\varepsilon_a n(\varepsilon_a)\varepsilon_p\sigma(\varepsilon_p). \end{aligned} \tag{18}$$

Table 1

E_b, keV	K_1	K_2	K_3	K	K/K_1
15	4.38×10^4	4.045×10^4	7.393×10^4	4.38×10^4	1.00×10^0
10	4.073×10^3	3.762×10^3	6.877×10^3	4.11×10^3	1.01×10^0
5	1.711×10^1	1.580×10^1	2.892×10^1	1.77×10^1	1.03×10^0
2	2.615×10^{-4}	2.421×10^{-4}	4.487×10^{-4}	2.85×10^{-4}	1.09×10^0
1.8	5.038×10^{-5}	7.223×10^{-5}	1.344×10^{-4}	5.62×10^{-5}	1.12×10^0
1.5	2.339×10^{-6}	3.850×10^{-6}	7.343×10^{-6}	3.34×10^{-6}	1.43×10^0
1.2	3.613×10^{-8}	7.474×10^{-8}	2.265×10^{-7}	7.84×10^{-7}	2.17×10^1
1	8.252×10^{-10}	7.711×10^{-10}	5.678×10^{-8}	2.82×10^{-7}	3.42×10^2

Table 2

E_b, keV	K_1	K_2	K_3	K_3/K_1
15	4.474×10^4	4.133×10^4	7.552×10^4	1.6879937
10	4.237×10^3	3.914×10^3	7.152×10^3	1.6880552
5	1.911×10^1	1.766×10^1	3.232×10^1	1.69143
2	4.059×10^{-4}	5.370×10^{-4}	9.931×10^{-4}	2.4466201
1.8	8.433×10^{-5}	1.184×10^{-4}	2.197×10^{-4}	2.6056397
1.5	4.605×10^{-6}	7.336×10^{-6}	1.383×10^{-5}	3.0034846
1.2	9.315×10^{-8}	1.819×10^{-7}	4.320×10^{-7}	4.6383085
1	2.863×10^{-9}	6.951×10^{-9}	7.386×10^{-8}	25.801192

By comparing the results of calculations by formulas (18) and (11), one can estimate the effect of the tails of the distribution function on the reaction cross section. Moreover, these results may also be compared to the calculations of the reaction rate by the formula $K_1 = \sigma v$ using expression (15). This allows one to estimate the factor $S(\varepsilon_p)$ and the difference between of theoretical and experimental results.

To estimate the effect of the tails of the distribution function on the rate of reaction (17), it is necessary to take into account the deviations of the distribution function from a Maxwellian one. It was shown in [4] that quantum corrections lead to the appearance of power-law tails in the distribution function over kinetic energies:

$$f(\varepsilon) = C'\int_0^\infty dE_a n(E_a) a(E_a - \varepsilon_a, \varepsilon_a) \sim \exp\left\{-\frac{\varepsilon_a}{T}\right\} + \frac{C_a(T)}{\varepsilon_p^4}. \quad (19)$$

Substituting this expression in formula (17), we calculate the reaction rate with allowance for the deviation of the distribution function over kinetic energies from Maxwellian:

$$K_3 = C_3\int_0^\infty d\varepsilon_a f(\varepsilon_a)\sqrt{\frac{2\varepsilon_a\varepsilon_p}{\mu}}\sigma(\varepsilon_p). \quad (20)$$

The results of these calculations are presented in Table 1.

These results allow us to conclude that the reaction rates calculated using different models are in good agreement for beam energies higher than 2 keV. In the 1- to 2-keV energy range, the K_1 and K_2 values are still close to one another, whereas the reaction rate K is much higher than these values. We also note satisfactory agreement between the K and K_3 values. Therefore, we can conclude that the reaction rates can be quite satisfactorily estimated by formula (17). The results of these calculations show that the tails of the momentum distribution function significantly contribute to the reaction rates. The last column of Table 1 shows the ratio between the reaction rate K calculated by formula (11) and that calculated for an ideal plasma.

It is of interest to consider the effect of screening on the reaction rate with allowance for the influence of non-Maxwellian tails of the distribution function. For this purpose, we performed calculations for a screening

potential of U_e = 28 eV, which was taken into account in accordance with formula (16). Such a value of the screening potential is quite realistic under the experimental conditions of [8]. The results of calculations are presented in Table 2.

In these calculations, we did not use general expression (11) because a fairly accurate estimate can be obtained using Eq. (17). The results obtained show that the influence of a realistic screening potential is weak, which agrees with the results of [8, 9]. It can be seen, however, that quantum corrections greatly increase the calculated value of the reaction rate in the range of low (from 1 to 2 keV) beam energies.

3. DETAILED BALANCE OF THE ABSORPTION AND EMISSION OF RESONANT RADIATION

The effects that were observed in experiments on the interaction of radiation with dense media (see the Introduction) cannot be explained by the conventional theory of resonant radiation transfer [11]. These effects can manifest themselves in measuring thermal emission from a dense medium. The intensity of this radiation can be calculated using the generalized spectral intensity $J(\omega, k, \mathbf{\Omega}, \mathbf{r})$. In the steady-state case, the function $J(\omega, k, \mathbf{\Omega}, \mathbf{r})$ should satisfy the kinetic equation

$$\mathbf{\Omega} \cdot \nabla J = -k_\omega J + \tilde{\varepsilon}(\omega, k, \mathbf{\Omega}, \mathbf{r}). \tag{21}$$

Here, k_ω is the absorption coefficient,

$$\begin{aligned} k_\omega &= \frac{\omega^2 \varepsilon''(\omega, k)}{c^2 k} \\ &= \frac{4}{3}(g_2/g_1)\frac{(\pi d\omega)^2}{\hbar c^2 k} a(\omega, k) \\ &\times \{\tilde{N}_1 - (g_1/g_2)\tilde{N}_2 \exp[-\hbar(\omega - \omega_0)/T]\}, \end{aligned} \tag{22}$$

and $\tilde{\varepsilon}$ is the generalized spontaneous spectral emissivity,

$$\begin{aligned} \tilde{\varepsilon} &= \frac{4}{3}\frac{d^2\omega^3\hbar\omega}{\hbar c^2 k}\frac{\omega^2\varepsilon''}{\left|\omega^2\varepsilon - c^2k^2\right|^2}(2\pi)^3 a(\omega, k)\tilde{N}_2 \\ &\times \exp[-\hbar(\omega - \omega_0)/T], \end{aligned} \tag{23}$$

where $a(\omega, k)$ is the generalized line profile; $\varepsilon(\omega, \mathbf{k}) = \varepsilon'(\omega, \mathbf{k}) + i\varepsilon''(\omega, \mathbf{k})$ is the complex permittivity of the medium (with $\varepsilon'(\omega, \mathbf{k})$ and $\varepsilon''(\omega, \mathbf{k})$ being its real and imaginary parts, respectively); T is the temperature of an equilibrium medium in energy units; $g_{1,2}$ are the statistical weights of the ground and excited states; $\tilde{N}_{1,2}$ are their effective populations, which obey a Boltzmann distribution under equilibrium conditions or, in a nonequilibrium state, can be found from the kinetic equations given in [5]; and d is the matrix element of the dipole moment operator for the $2 \longrightarrow 1$ transition.

Ignoring spatial dispersion (in this case, $a(\omega, k) \approx a(\omega)$ and $\int a(\omega)d\omega = 1$) and integrating expression (23) over k, we obtain the following explicit expression for the spectral intensity of spontaneous emission from an optically thick medium:

$$\begin{aligned} \varepsilon_\omega &= (1/4\pi)\hbar\omega A_0\left(\frac{\omega}{\omega_0}\right)^3 \mathrm{Re}(\sqrt{\varepsilon})a(\omega)\tilde{N}_2 \\ &\times \exp[-\hbar(\omega - \omega_0)/T], \end{aligned} \tag{24}$$

where A_0 is the probability of spontaneous emission in vacuum.

In the general case, Eq. (21) is insufficient to uniquely describe the spectral intensity J_ω, defined by formula (10). Thus, in addition to the first-order partial differential equation (21), the function $J(\omega, k, \mathbf{\Omega}, \mathbf{r})$ should also satisfy a nonuniform wave equation, which, in the steady-state case, has the form

$$\begin{aligned} \left[-\frac{c^2}{2}\Delta + 2(c^2k^2 - \omega^2\varepsilon')\right]J &= \frac{8\pi\hbar\omega^4\varepsilon''}{\left|\omega^2\varepsilon - c^2k^2\right|^2} \\ \times \frac{2(c^2k^2 - \omega^2\varepsilon')}{\{(N_1/N_2)(g_2/g_1)\exp[-\hbar(\omega - \omega_0)/T] - 1\}}&. \end{aligned} \tag{25}$$

To close the set of Eqs. (21) and (25), it is necessary to supplement them with equations for the populations N_i. In the limit $N_2 \ll N_1 \approx N$ and with allowance for the total redistribution over frequencies in a dense medium, we obtain the following equation for N_2:

$$\begin{aligned} &\frac{2}{3}\frac{d}{\hbar}^2\frac{g_2}{g_1}\int\frac{d\omega d\mathbf{\Omega}k^2dk}{(2\pi)^3}J(\omega, k, \mathbf{\Omega}, \mathbf{r})a(\omega, k)\tilde{N}_1 \\ &-\frac{8}{3}\frac{d}{\hbar}^2\int\frac{d\omega k^2dk}{\pi}\frac{\omega^4\varepsilon''(\omega, k)}{\left|\omega^2\varepsilon - c^2k^2\right|^2}a(\omega, k) \\ &\times \exp\left(-\frac{\hbar(\omega - \omega_0)}{T}\right)\tilde{N}_2 \\ &-W\left(\tilde{N}_2 - \tilde{N}_1\frac{g_2}{g_1}\exp\left(-\frac{\hbar\omega_0}{T}\right)\right) = 0. \end{aligned} \tag{26}$$

The first term in Eq. (26) corresponds to photoabsorption, the second is responsible for the spontaneous decay of the excited atoms, and the third describes the collisional exchange between states 1 and 2 with a probability W.

The exponential factor $\exp[-\hbar(\omega - \omega_0)/T]$ in expressions (22)–(26) is related to the generalization of the conventional theory of radiation transfer [12, 13] to the case of broad lines, which are characteristic of dense media. This factor was first derived in [5] within the frame of the Keldysh theory using kinetic Green's functions [14, 15].

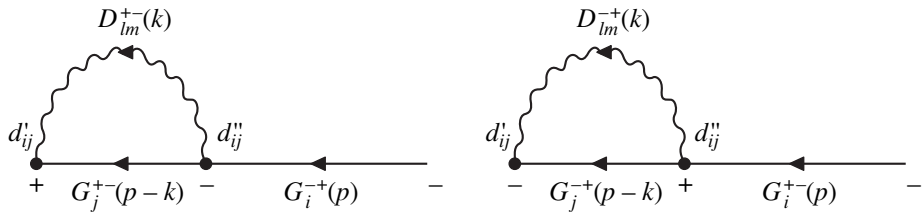

Fig. 2. Diagrams of atomic emission and absorption.

As was shown in [5], the spectral intensity of spontaneous emission ε_ω obtained by integrating the equations for radiation transfer over the wave vectors **k** can be written in the form

$$\varepsilon_\omega = \frac{1}{4\pi}\hbar\omega A_0\left(\frac{\omega^3}{\omega_0^3}\right)n_\omega\tilde{N}_2(\omega). \quad (27)$$

Here, A_0 is the probability of spontaneous emission in vacuum; $n_\omega = \mathrm{Re}\sqrt{\varepsilon}$ is the refractive index of the resonance medium (note that, in [5], Eq. (25) was derived without allowance for spatial dispersion); and $\tilde{N}_2(\omega)$ is the effective spectral population of the upper level,

$$\tilde{N}_2(\omega) = \tilde{N}_2 a(\omega)\exp[-\hbar(\omega-\omega_0)/T], \quad (28)$$

where $a(\omega)$ is the spectral line profile ($\int a(\omega)d\omega = 1$) and $\tilde{N}_2$ is the effective population of the excited state. Under equilibrium conditions, from formulas (27) and (28), we obtain the spectral Boltzmann distribution

$$\tilde{N}_2(\omega) = \frac{g_2}{g_1}N_1 a(\omega)\exp[-\hbar\omega/T], \quad (29)$$

where g_i is the statistical weight of the ith state ($i = 1, 2$ for a two-level atom) and N_1 is the total population of the lower state. Note that a formula for a low-density medium (similar to expression (28)) was earlier derived in [16] from the principle of detailed balance, according to which, in equilibrium, the spectral intensity of radiation is described by the Planck formula

$$J_\omega = \frac{\hbar\omega^3}{4\pi^3 c^2}\frac{1}{\exp[\hbar\omega/T]-1}, \quad (30)$$

In the conventional theory of radiation transfer, the principle of detailed balance leads to expression (30) with a fixed transition frequency ω_0. For large detunings from the resonance ($\Delta = \omega - \omega_0 \approx T/\hbar$), expressions (28) and (29) differ appreciably from the corresponding formulas used in the conventional theory of resonant radiation transfer [12, 17, 18].

After publications [5, 6], formulas similar to expression (28) were derived by R. More (private communication) in a clearer way. He considered the balance between the emission and absorption of a moving atom and took into account conservation of the energy and momentum of the emitting and absorbing atoms with allowance for the change in their kinetic energy after transitions from the ground to excited state and vice versa (actually, this corresponds to taking into account the Doppler effect).

An adequate technique for describing resonant radiation transfer in dense media is the method of nonequilibrium Green's functions, which was developed in [14] and applied in [5] to the problems under consideration.

Let us consider the Keldysh diagram (Fig. 2) for the emission from an atom in the ith state, whose spectral and kinetic properties are described by the kinetic Green's function $G_i^{-+}(p)$ (see the notation in [15]), where $p = (\mathbf{p}, \omega)$. Here, the solid lines correspond to the Green's functions of "dressed" particles and the transition into the ground state j is described by the matrix element $(d_l)_{ij}$ of the dipole moment with the projection l. The generation of a photon with a 4-momentum $k = (\mathbf{k}, \omega)$ is denoted by the wavy line, which corresponds to the Green's function $D_{lm}^{+-}(k)$ of a transverse photon in a resonance medium.

The diagrams in Fig. 2 are described by the formulas (see [15])

$$iM_{em} = \int iG_i^{-+}(p)G_j^{+-}(p-k)d_{ij}^l iD_{lm}^{+-}(k)d_{ij}^m\frac{d^4k}{(2\pi)^4},$$
$$iM_{\mathrm{abs}} = \int iG_i^{+-}(p)G_j^{-+}(p-k)d_{ij}^l iD_{lm}^{-+}(k)d_{ij}^m\frac{d^4k}{(2\pi)^4}. \quad (31)$$

Under conditions of thermodynamic equilibrium, the Green's functions in formula (31) are

$$iG_i^{-+}(p) = \frac{1}{\exp[(\omega-\mu_a)/T]+1}a_i(\omega-\omega_i-E(\mathbf{p})), \quad (32)$$

where μ_a is the atomic chemical potential and $a_i(\omega)$ is spectral profile of the ith state with an excitation energy ω_i and a translational energy $E(p)$. For simplicity, Planck's constant here is set equal to unity. The occupa-

tion numbers $n_a(\omega)$ of the atomic states in Eq. (31) are assumed to obey a Fermi distribution,

$$a_i = \frac{\gamma_i(\omega, \mathbf{p})}{\pi[(\omega - \omega_i - E(\mathbf{p}) - \Delta_i(\omega, \mathbf{p})^2 + \gamma_i^2(\omega, \mathbf{p}))]}, \quad (33)$$

where γ_i is the width of the ith state and Δ_i is its shift due to the interaction of the atom with the medium and radiation (these quantities are described by the imaginary and real parts of the retarded operator $\Sigma_i^R(\omega, \mathbf{p})$, respectively; cf. (5)). The Green's function of a transverse photon in a resonance medium is described by the expression

$$iD_{lm}^{+-}(k) = \left(\delta_{lm} - \frac{k_i k_j}{k^2}\right)(1 + n_R(\omega_k))\frac{8\pi\omega_k^4\varepsilon''(\omega_k, \mathbf{k})}{\left|\omega_k^2\varepsilon(\omega_k, \mathbf{k}) - c^2k^2\right|^2}, \quad (34)$$

where $n_R(\omega_k) = 1/(\exp[\omega_k/T_R] - 1)$ are the Bose occupation numbers for radiation with a temperature T_R, which, in the general case, does not coincide with the medium temperature T.

It follows from the detailed balance of emission and absorption that, in the general case, the atomic occupation numbers obey a two-temperature distribution with the temperature T and the excitation temperature T_{ex} (the radiation temperature T_R is assumed to be equal to the translational temperature T):

$$n_i(\mathbf{p}, \varepsilon) = \frac{1}{\exp\left\{\frac{\varepsilon + E(p)}{T}\right\}\exp\left\{\frac{\omega_i - \mu_a}{T_{ex}}\right\} + 1}. \quad (35)$$

In the nondegenerate case ($\exp[-\mu_a/T_{ex}] \gg 1$) with allowance for the generalized formula (35), we find that the atomic emission rate is

$$M_{em}^{i\to j} \sim N_i^* \exp\left[-\frac{E(\mathbf{p} - \mathbf{k})}{T}\right] \times \exp\left[-\frac{\omega_k - \omega_0}{T}\right](1 + n_R), \quad (36)$$

where $N_i^* \sim \exp\left\{-\frac{\omega_i - \mu_a}{T_{ex}}\right\}$ is the density of the excited atoms. For the absorption rate, we obtain

$$M_{abs}^{j\to i} \sim \exp\left\{\frac{E(\mathbf{p} - \mathbf{k})}{T}\right\}N_i^* \exp\left\{\frac{\omega_0}{T}\right\}n_R. \quad (37)$$

The occupation number of the ground state N_j^* is equal to $N_j^* \sim \exp\left\{-\frac{\omega_j - \mu_a}{T_{ex}}\right\}$; hence, without allowance for degeneracy, we have $N_j^*/N_i^* = \exp\left\{\frac{\omega_0}{T_{ex}}\right\}$.

Note that, in conventional notation, the power indexes in formulas (36) and (37) will contain Planck's constant $\hbar$.

4. ASYMMETRY OF THE COEFFICIENT OF RESONANT RADIATION ABSORPTION

It follows from Eq. (28) that, strictly speaking, even under equilibrium conditions, the total effective populations $\tilde{N}_2$ do not obey a Boltzmann distribution and coincide with the true populations only for a narrow line with $\hbar\Gamma \ll T$, where Γ is the line width.

For a broad line (see [5, 6, 19–21] for details) due to the presence of the exponential factor, the intensity of the far wing of the line can greatly exceed the intensity predicted by the conventional theory. The bulk of the radiation energy can be emitted within the nonresonant red wing rather than within the central resonant part of the line (in this case, an additional lower frequency maximum in the emission spectrum of the line can even appear [20, 21]). Indeed, we experimentally observed such maxima when studying thermal emission from a thermal tube filled with sodium vapor at temperatures of 800–1100 K (see Fig. 3). Note that the vapor density at these temperatures reaches $\sim 8 \times 10^{16}$ to 4×10^{18} cm^{-3}. The measurement results agree qualitatively with the results of calculations of the radiation emitted from a nonuniform vapor layer. Moreover, it was found experimentally that the radiation intensity in the IR region was higher by several (up to four) orders of magnitude than that calculated by the classical theory. This result also agrees with the predictions of the generalized theory of radiation transfer [5, 6, 19–21]. It should be noted, however, that the mechanism for radiation absorption in the far wing of the line is quite understandable up to approximately 0.7 μm. In this wavelength range, absorption is primarily determined by the Van der Waals interaction between the excited sodium atoms and the buffer gas (there is good correlation between the radiation intensity and the polarizability of the buffer gas—argon or helium—in this spectral range). In the wavelength range around 2 μm, the question about the absorption mechanism still remains open (see [6]).

Ignoring corrections for stimulated emission ($\tilde{N}_i \ll N_j$), we obtain the following expression for the absorption coefficient:

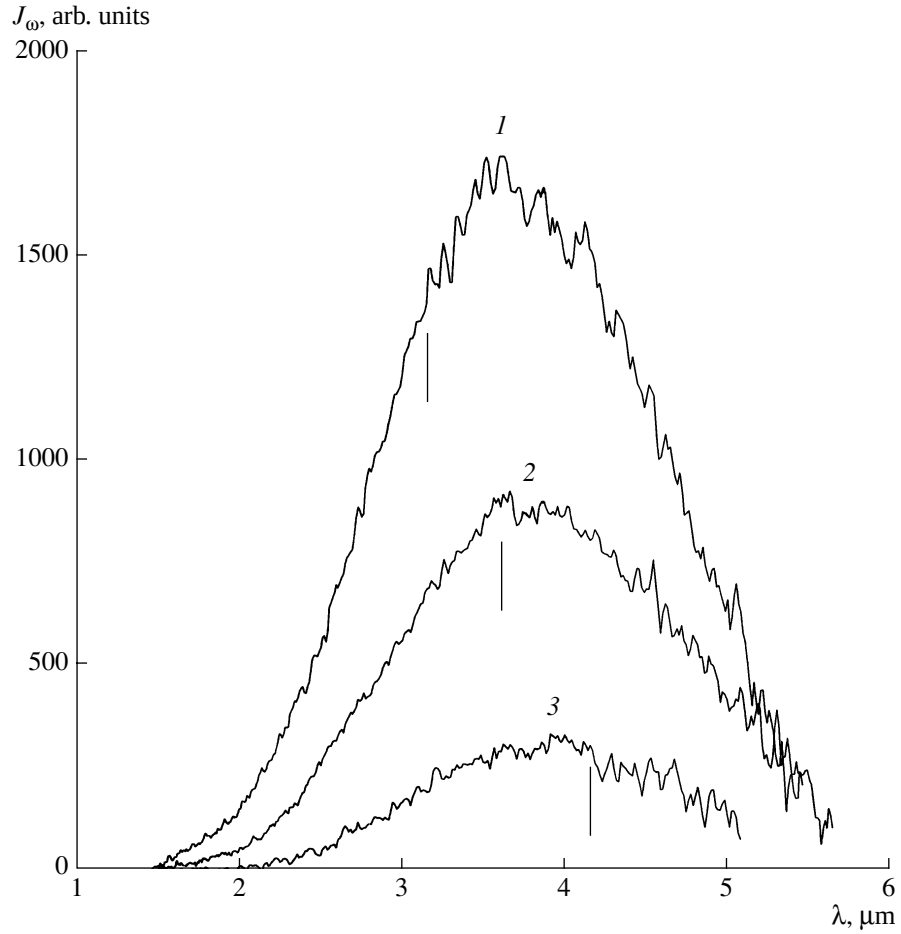

Fig. 3. IR spectrum of thermal emission from sodium vapor at temperatures in the thermal tube center of T = (*1*) 1080, (*2*) 950, and (*3*) 830 K. The vertical lines show the calculated positions of the spectral maxima.

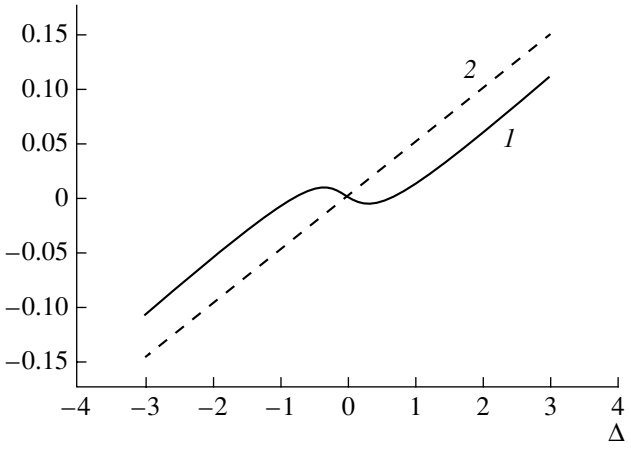

Fig. 4. Asymmetry of the absorption coefficient in units of the average value of $\dfrac{k(\omega_0-\Delta)-k(\omega_0+\Delta)}{k(\omega_0-\Delta)+k(\omega_0-\Delta)}$ vs. detuning Δ for $\hbar\omega_0/T = 20$, $\mu/T = -20$, $\gamma_1/T = 3.26\times10^{-5}$, $\gamma_2/T = 1.81\times10^{-3}$, and two gas densities: n = (*1*) 10^{21} and (*2*) 10^{19} cm^{-3}.

$$k(\omega) = \frac{2\pi\hbar\omega}{c}\frac{d^2}{3}\int\frac{dEd\mathbf{p}}{(2\pi)^4}G_i^{+-}(\mathbf{p}+\mathbf{k})G_j^{-+}(\mathbf{p}). \quad (38)$$

Then, using Eqs. (32) and (33) and returning to the conventional notation, we have

$$k(\omega) = \hbar\frac{\lambda^2}{4}A_0\int\frac{dEd\mathbf{p}}{(2\pi)^3}n(E)(1-n(E+\hbar\omega)) \times a_j(E-\varepsilon_p-E_j)a_i(E-\varepsilon_{\mathbf{p}+\hbar\mathbf{k}}-E_i+\hbar\omega). \quad (39)$$

To find the widths of the spectral profiles of the *i*th and *j*th states, we can use estimates like $\gamma_j(E, \mathbf{p}) = \hbar n\sigma_g(p)/2\sqrt{2E/M}$. Here, σ_g is the cross section for gas-kinetic scattering (e.g., by a heavy buffer gas with a density n) and M is the mass of the resonance atom. Then, we have

$$\gamma_i(E+\hbar\omega, \mathbf{p}+\hbar\mathbf{k}) = \gamma_j(E+\hbar\omega, \mathbf{p}+\hbar\mathbf{k}) + \frac{\hbar N_p\pi d_{ij}^2}{\hbar|\mathbf{V}+\hbar\mathbf{k}/M|}\sqrt{\frac{2(E+\hbar\omega)}{M}}, \quad (40)$$

where the second term describes the additional broadening of the *i*th state due to resonant excitation exchange.

Figure 4 illustrates the total asymmetry of the absorption coefficient. The asymmetry is caused by the efficient resonance at high values of the particle momentum $\varepsilon_p = \hbar(\omega - \omega_0)$. An additional asymmetry is also introduced by the dependence of the effective width of the *i*th state on the frequency ω (see Eq. (40)).

ACKNOWLEDGMENTS

We are grateful to P. Quarrati for his continuing interest in this work. A.N. Starostin is also grateful to R. More and T. Kato for fruitful cooperation. This study was supported in part by the Russian Foundation for Basic Research (project nos. 04-02-16775, 03-02-06590, and 02-02-17153) and the RF Presidential Program for State Support of Leading Scientific Schools (project nos. MK-1565.2003.02, 338.2003.02, and NSh-1257.2003.2).

REFERENCES

1. L. P. Kadanoff and G. Baym, *Quantum Statistical Mechanics: Green's Function Methods in Equilibrium and Nonequilibrium Problems* (Benjamin, New York, 1962; Mir, Moscow, 1964).
2. E. Wigner, Phys. Rev. **40**, 749 (1932).
3. V. M. Galitskiĭ and V. V. Yakimets, Zh. Éksp. Teor. Fiz. **51**, 957 (1966) [Sov. Phys. JETP **24**, 637 (1967)].
4. A. N. Starostin, A. N. Mironov, N. L. Aleksandrov, *et al.*, Physica A (Amsterdam) **305**, 287 (2002).
5. Yu. K. Zemtsov, A. Yu. Sechin, and A. N. Starostin, Zh. Éksp. Teor. Fiz. **110**, 1654 (1996) [JETP **83**, 909 (1996)].
6. A. G. Leonov, A. A. Rudenko, A. N. Starostin, *et al.*, Zh. Éksp. Teor. Fiz. **122**, 282 (2002) [JETP **95**, 242 (2002)].
7. L. A. Artsimovich, *Controlled Thermonuclear Reactions* (Fizmatgiz, Moscow, 1961; Gordon & Breach, New York, 1964).
8. F. Raiola, P. Migliardi, G. Gyurky, *et al.*, Eur. Phys. J. A **13**, 377 (2002).
9. F. Raiola, P. Migliardi, P. Gang, *et al.*, Phys. Lett. **547**, 193 (2002).
10. A. N. Starostin, V. I. Savchenko, and N. J. Fish, Phys. Lett. A **274**, 64 (2000).
11. L. M. Biberman, Zh. Éksp. Teor. Fiz. **17**, 416 (1947); T. Holstein, Phys. Rev. **72**, 1212 (1947).
12. L. M. Biberman, V. S. Vorob'ev, and I. T. Yakubov, *Kinetics of Nonequilibrium Low-Temperature Plasmas* (Nauka, Moscow, 1982; Consultants Bureau, New York, 1987).
13. D. Mihalas, *Stellar Atmospheres* (Freeman, San Francisco, 1978; Mir, Moscow, 1982).
14. L. V. Keldysh, Zh. Éksp. Teor. Fiz. **47**, 1515 (1964) [Sov. Phys. JETP **20**, 1018 (1964)].
15. E. M. Lifshitz and L. P. Pitaevskiĭ, *Physical Kinetics* (Nauka, Moscow, 1979; Pergamon, Oxford, 1981).
16. A. Phelps, Rep. No. 110 (JILA Information Center, Univ. of Colorado, Boulder, CO, 1972); G. York and A. Gallagher, Rep. No. 114 (JILA Information Center, Univ. of Colorado, Boulder, CO, 1974).
17. T. Holstein, Phys. Rev. **72**, 1212 (1947).
18. V. V. Ivanov, *Radiative Transport and Spectra of Celestial Bodies* (Nauka, Moscow, 1969).
19. A. Yu. Sechin, A. N. Starostin, Yu. K. Zemtsov, *et al.*, J. Quant. Spectrosc. Radiat. Transf. **58**, 887 (1997).
20. Yu. K. Zemtsov, Yu. A. Sechin, A. N. Starostin, *et al.*, Pis'ma Zh. Éksp. Teor. Fiz. **65**, 807 (1997) [JETP Lett. **65**, 839 (1997)].
21. Yu. K. Zemtsov, Yu. A. Sechin, A. N. Starostin, *et al.*, Zh. Éksp. Teor. Fiz. **114**, 135 (1998) [JETP **87**, 76 (1998)].

Translated by N.N. Ustinovskiĭ

Plasma Physics Reports, Vol. 31, No. 2, 2005, pp. 133–146. Translated from Fizika Plazmy, Vol. 31, No. 2, 2005, pp. 157–171.

DUSTY PLASMA

Self-Consistent Quasineutral Dust Structures

V. N. Tsytovich

Prokhorov Institute of General Physics, Russian Academy of Sciences, ul. Vavilova 38, Moscow, 119991 Russia

Received November 11, 2003; in final form, December 29, 2003

Abstract—Distributions of the dusty plasma parameters (electron, ion, and dust densities; dust grain charge; and ion drift velocity) in quasineutral dust structures whose dimensions are much greater than the mean free path of the ions in their interactions with neutral particles are calculated numerically under conditions such that ionization sources are located outside the structures. Planar, cylindrical, and spherical structures are investigated. It is shown that static equilibrium structures are governed by a single (basic) parameter: the electrostatic potential drop between the center of the structure and its boundary. It is found that the maximum value of the basic parameter (in energy units) does not exceed the electron temperature. The basic parameter also determines the total number of dust grains in the structure and the power of external ionization sources that are necessary to sustain this structure. The fact that the basic parameter varies within a limited range allows one to consider all the possible structures with a given dimensionality (planar, cylindrical, and spherical). © *2005 Pleiades Publishing, Inc.*

1. INTRODUCTION: FORMULATION OF THE PROBLEM

At present, much experimental and theoretical effort is being expended in order to search for and analyze equilibrium structures in dusty plasmas [1–3], such as compact dust bunches, dust voids, and dust vortices. A theoretical analysis of these structures is needed both to explain experimental observations and to predict the results of future experiments. According to a general theoretical concept, an initially homogeneous dusty plasma is unstable against fragmentation into dust bunches (in which dust is accumulated) and dust voids (which contain no dust) [4]. Therefore, the study of possible equilibrium dust structures is of general interest. Observations and estimates have shown that the lifetime of the dust structures is long enough for the balance of all the forces acting on the structure components, as well as for the balance of the plasma flows and the local equilibrium charge of the dust grains, to be established. As a rule, the size of the structure is greater than both the ion–dust and ion–neutral mean free paths The ion–dust mean free path is usually less than or on the order of the ion–neutral one (the ratio between them depends strongly on the gas pressure). So far, in the theory of such equilibrium structures, only a few particular limiting cases have been analyzed in which the structure size is much less [5, 6] or much greater [7, 8] than the ion–neutral mean free path. However, a complete analysis of possible equilibrium structures has not yet been performed (the calculations have been carried out only for particular parameters close to the available observational data).

The aim of the present study is to partially fill this gap for the case where the structure size is much greater than both of the above mean free paths and under the conditions such that (i) the plasma is quasineutral and (ii) the ionization sources sustaining the structure are located outside it. The second condition requires additional explanation. By virtue of the strong absorption of the plasma particles by the dust (the structure size is assumed to be larger than the electron–dust and ion–dust mean free paths), equilibrium structures can exist only if this absorption is balanced by ionization inside the structure or there are external plasma flows toward the structure. Spherical structures [8] and planar structures [9] were considered under the conditions such that ionization sources were located both inside and outside the structure. The source intensity was assumed to be proportional to the local electron density, whose spatial distribution corresponded to a self-consistent solution to a complete nonlinear problem. Such a formulation of the problem for numerical calculations is close to the experimental conditions in which ionization is produced by an external microwave field; in this case, the ionization rate is proportional to the electron density.

This study is partially motivated by the fact that, in microgravity experiments, it is difficult to create dust structures without a central void [9]. In [8, 9], conditions were determined under which the dust void was not formed at the center of the structure. It was shown that, if the chamber wall is at the floating potential, then a void adjacent to the wall must exist outside the structure. It was also shown that, under certain circumstances, dust convection can arise, which can hinder the formation of a structure without a central void. Eventually, experiments were performed in which the central void was eliminated (see [9]). Note that experimental difficulties in achieving a state without a central void are essentially similar to those in obtaining such a state in numerical simulations [8, 9]. On the whole, these simulations fairly correctly (both qualitatively and

1063-780X/05/3102-0133$26.00

quantitatively) describe the experimental results; namely, states without a central void arise in numerical simulations within quite a narrow range of gas pressures and degrees of ionization (microwave power).

It follows from the results of [8, 9] that the situation can change radically when other types of ionization sources are used. The properties of the near-wall void [8, 9], which contains no dust, differ radically from the known properties of dust-free gas discharges, because such voids are bounded by the chamber wall on the outer side and by the dust structure on the inner side. The dust structure determines the intensities of the particle fluxes, the electric field strength, and the electron and ion densities on its boundary. In this case, the ion flow in the near-wall void must change its direction: it must be directed outward in the wall region and inward near the dust structure. In [8, 9], no equilibrium states in which the ion flow in the near-wall void does not change its direction were found. This indicates that, if there is an ionization source outside the dust structure and if this source is concentrated, e.g., in the wall region, then it will be able to provide ion flows directed toward both the wall and the structure.

To create an equilibrium structure, it is not necessary that the ionization source be located inside the structure: it is sufficient to provide an ion flux onto the surface of the structure. The plasma flows can be produced either by ionization sources located outside the structure or by some other methods that do not need to be specified if the distribution of the parameters is to be considered only inside the structure. This distribution determines the plasma flux that is necessary to compensate for plasma absorption in the structure. The structures can be self-sustained because they themselves can induce plasma flows that are necessary to sustain the structure. Such a situation frequently occurs in practice, because each of the dust grains, being a sink for the plasma, generates a plasma flux onto its surface. All the grains constituting the structure create a plasma flux onto its surface. Here, we analyze just this situation, in which the ionization sources are located outside the structure, and consider the distributions of the parameters only inside the structure. The properties of the external region can be different in the presence of a wall that is at the floating potential and in the presence of an external electric field or another ionization source. Such "gas discharges" outside the structure have nothing to do with a glow discharge or a conventional microwave discharge because their parameters are completely determined by the dust structure. The distributions of the parameters inside the structure are also completely determined by the dust and, as calculations show, do not depend on the external conditions, which can only determine the structure size (the size of the structure is defined as the distance from the center of the structure to the point at which the dust density vanishes) and the plasma flux that is necessary to sustain the structure. In this paper, such structures (which may be called free-boundary structures) are analyzed by solving a self-consistent set of nonlinear balance equations numerically. It is shown that such equilibrium structures can indeed exist in a wide range of parameters, without being influenced by the effects related to the excitation of dust convection. Here, we do not consider methods for creating the necessary external plasma flux, although there are a number of experimental schemes for the excitation of such discharges under microgravity conditions. It is clear that schemes with external ionization will have advantages from the standpoint of creating plasma crystals under microgravity conditions; at the same time, such discharges will differ qualitatively from conventional laboratory gas discharges.

In solving equilibrium equations for dust structures with allowance for the above assumptions, we will also assume that there is a certain symmetry in the system, namely, the distributions of the parameters in the structures depend on a single coordinate; i.e., we will consider planar, cylindrical, and spherical structures. In this paper, we will show that planar, cylindrical, and spherical compact dust structures are governed by a single (basic) parameter and can exist only within a limited range of this parameter. As a basic parameter, we can use one of the following parameters, which are uniquely related to one another: the electrostatic potential drop between the center of the dust structure and its boundary, the total number of dust grains in the structure, or the total plasma flux that is necessary to sustain the structure. The range in which the basic parameter governing an equilibrium structure can vary is limited; this allows one to consider all of the possible equilibrium structures and the distributions of the dust density, the grain charge, the ion and electron densities, and the ion and diffusive fluxes in them.

The results of this study can be of interest for laboratory experiments in which self-sustained planar dust structures have already been observed [3] and experiments that are planned to be performed in spherical [3] and long cylindrical [9] chambers. Astrophysical interest in such structures is motivated by the fact that no external forces are necessary for their origin because they are spontaneous self-organizing structures. Moreover, the formulations of the problem of possible equilibrium dust structures and the problem of possible equilibrium spherical structures arising in the presence of pressure and gravitation (e.g., stars) are close to one another (note that the latter structures too can exist only within a limited parameter range). Of course, equilibrium dust structures are much more complicated because, besides the electron and ion pressure, the friction on dust, the processes of dust charging, and the convective and diffusive plasma circulation play an important role in them. In a sense, spherical dust structures may be called dusty stars or dusty planets. Some estimates are given below, but a detailed astrophysical analysis of such structures requires special consideration in the relevant literature and, thus, is not presented here. The main difference between astrophysical and

laboratory structures lies in the fact that, in the former, the ratio of the dust grain size to the Debye screening length is much smaller and that the electron and ion temperatures are close to one another. The difference in the degree of ionization is of minor importance because, in dust–molecular clouds, it is only one order of magnitude lower than in laboratory plasmas. In laboratory plasmas, the ion temperature is about two orders of magnitude lower than the electron temperature. Therefore, in this study, we perform calculations for two cases: one corresponds to conditions typical of laboratory plasmas, and the other corresponds to a typical astrophysical plasma. As a typical example of laboratory plasma, we consider argon plasma. In this case, the ratio of the grain size a to the Debye screening length λ_D is taken to be ≈ 0.1 and the temperature ratio is $\tau = T_i/T_e \approx 0.02$. As a typical example of astrophysical plasma, we consider a hydrogen plasma with $\tau = 1$ and $a/\lambda_D \approx 10^{-7}$. The dimensionless equations used below contain the latter ratio only under the logarithm sign and are applicable to both laboratory and astrophysical plasmas.

In this study, we also ignore electron–electron, electron–ion, and ion–ion collisions as compared to electron–dust and ion–dust collisions, which are more intense by approximately a factor of $Z_d P_H$ (here, Z_d is the grain charge normalized to the electron charge and P_H is the ratio between the dust and ion space charge densities). Therefore, the condition of applicability of our model is a sufficiently large dust grain charge. Note that the presence of charged dust makes diffusion nonambipolar, and the presence of an electric field in the structures does not contradict the quasineutrality condition because the spatial derivatives of the electric field are sufficiently small.

We recall that, in dissipative systems, the electric fields related to the finite mobility of the system components are always present. The structures under consideration can be classified as self-organized dissipative structures.

2. BALANCE EQUATIONS

In deriving the balance equations, we assume that all the quantities depend on a single coordinate: this is the coordinate y for planar structures, the distance ρ from the cylinder axis for cylindrical structures, and the radius r for spherical structures. To generalize the notation, we introduce the dimensionless coordinate

$$x = \{y, \rho, r\}\frac{\tau}{\lambda_{in}}, \quad (1)$$

where $\lambda_{in} = 1/(n_n\sigma)$ is the ion–neutral mean free path (as a rule, σ is determined by the charge-exchange cross section), with n_n being the density of neutral particles. For the sake of convenience, we introduced the parameter τ in normalization (1) because, with this normalization, most of the balance equations in the case where ion–neutral collisions and the friction of ions on dust are dominant have the same form as in the opposite limit, in which ions–dust collisions prevail. To normalize the ion and electron densities (n_i and n_e) and introduce the Havnes parameter P (it is different from P_H), we use the following expression for the critical density

$$n_{\rm cr} = n_0\lambda_{id}/\lambda_{in}, \quad (2)$$

where n_0 is the ion density far from structure and $\lambda_{id} = T_i/(4\pi n_0 e^2 a)$ is the coefficient in the mean free path of ions with respect to absorption by dust, λ_{id}/P. Note that this critical density is independent of n_0. Thus, for the normalized ion density n, normalized electron density n_e, and Havnes parameter P, we have

$$n = \frac{n_i}{n_{\rm cr}}; \quad n_e \longrightarrow \frac{n_e}{n_{\rm cr}}; \quad P = \frac{Z_d n_d}{n_{\rm cr}}. \quad (3)$$

In these variables, the quasineutrality condition takes the form

$$P = n - n_e. \quad (4)$$

We also introduce the dimensionless electric field E, dimensionless dust grain charge z, and dimensionless ion drift velocity u:

$$E = \frac{eE\lambda_{in}}{T_i}, \quad z = \frac{Z_d e^2}{aT_e}, \quad u = \frac{v_i}{\sqrt{2}v_{Ti}}, \quad (5)$$

where $v_{Ti} = \sqrt{\frac{T_i}{m_i}}$.

We also make some additional assumptions that are not of fundamental importance and are confirmed a posteriori by the results of our calculations. First, we assume that the ion flow in dust structures is subsonic (the Mach number is much smaller than unity, $M = \sqrt{2\tau}u \ll 1$) and the electron flow velocity is much lower than the electron thermal velocity. The friction force and the electron inertia force are assumed to be negligibly small as compared to the electron pressure force, so the electrons adiabatically follow the ions. As a result, no currents are generated inside the structure and there is only a plasma flow characterized by the ion drift velocity. Therefore, we can use the following equilibrium condition for the electrons:

$$-\frac{1}{n_e}\frac{dn_e}{dx} - E = 0. \quad (6)$$

For the ions, it is also necessary to take into account the forces related to friction on dust and neutrals:

$$-\frac{\tau}{n}\frac{dn}{dx} + E - \alpha_{\rm dr}(z, u, \tau)uzP - uf(|u|) = 0, \quad (7)$$

where the function $f(|u|)$ describes the nonlinearity of the ion mobility in collisions with neutrals (when the

mobility can be approximated by a linear function, we have $f(|u|) = 1$). It is well known that, at $u \gg 1$, the mobility is proportional to $\sqrt{|E|}$; therefore, to a good accuracy, the above nonlinearity can be approximated by the function $f(|u|) \approx 1 + \alpha_N|u|$, where the coefficient of nonlinear friction α_N is close to unity. Here, we will assume that $\alpha_N = 1$.

The smallness of the parameter $1/Z_d \ll 1$ is also used in the force balance equation for dust, in which the dust pressure force is on the order of $T_n/(T_eZ_d)$ (under laboratory conditions, this parameter is small not only due to the smallness of the parameter $1/Z_d \ll 1$, but also due to the smallness of $T_n/T_e \ll 1$):

$$E = \alpha_{dr}(z, u, \tau)nzu. \tag{8}$$

The total ion flux Φ is assumed to be equal to the sum of the convective flux nu and the diffusive flux. The expression for the dimensionless flux Φ has the form

$$\Phi = nu - \frac{\tau}{3}\frac{dn}{dx}, \tag{9}$$

where the second term describes the diffusive flux. The normalization of the total flux follows directly from Eq. (9). Finally, the continuity equation for the flux Φ has the form

$$\frac{d\Phi}{dx} + \frac{s}{x}\Phi = -\alpha_{ch}(z, u, \tau)nP, \tag{10}$$

where $s = 0$ for planar structures, $s = 1$ for cylindrical structures, and $s = 2$ for spherical structures and the coefficient $\alpha_{ch}(z, u, \tau)$ describes the absorption of ions by dust. The dust grain charge can be found from the balance equation for electron and ion fluxes absorbed by a dust grain:

$$\exp(-z) = \alpha_{ch}(z, u, \tau)2\sqrt{\pi}z\sqrt{\frac{m_e}{\tau m_i}}. \tag{11}$$

The grain charge depends on the sorts of gas (through the ion mass m_i in Eq. (11)). The procedure of calculating the grain charge is substantially simplified when the calculation begins from the center of the structure, i.e., when Eq. (11) is used to find the grain charge at the center of the structure and the change of the charge is then determined from the equation for dz/dx, which is obtained from Eq. (11) by differentiation with respect to x. By combining the above equations, we obtain a set of equations for the first spatial derivatives of the electron and ion densities, ion flux, ion drift velocity, and grain charge. These equations are then used to calculate equilibrium structures numerically. Here, we do not write out these equations because they are simply derived from the above balance equations. The expressions for the drag coefficient $\alpha_{dr}(z, u, \tau)$ and charging coefficient $\alpha_{ch}(z, u, \tau)$ with allowance for the ion absorption and ion scattering by dust have the form

$$\begin{aligned}\alpha_{dr}(z, u, \tau) &= \frac{\exp(-u^2)\tau}{4z\sqrt{\pi}u^2}\left(2 + \frac{\tau}{z} + 2u^2\frac{\tau}{z}\right) \\ &+ \ln\Lambda\left[\frac{\mathrm{erf}(u)}{2u^2} - \frac{\exp(-u^2)}{\sqrt{\pi}u^2}\right] \\ &+ \left[\frac{\tau}{4u^3z}\left(2u^2 + 2\frac{\tau}{z}u^2 + 2u^4\frac{\tau}{z} + \frac{2\tau}{z}\right)\right], \\ \alpha_{ch}(z, u, \tau) &= \frac{\mathrm{erf}(u)}{4u}\left(-1 - \frac{\tau}{2z} + \frac{\tau u^2}{2z}\right) \\ &+ \frac{\tau}{4z\sqrt{\pi}}\exp(-u^2),\end{aligned} \tag{12}$$

where $\ln\Lambda$ is the effective Coulomb logarithm, which takes into account both the contribution related to the charging of the dust grains (see [10]) and the contribution from the large-angle scattering of ions by them (see [11]).

3. RESTRICTIONS ON THE PARAMETERS OF EQUILIBRIUM STRUCTURES

It is expedient to begin numerical calculations from the center of the structure, which is below denoted as $x = \{y, \rho, r\} = 0$: this is the central plane $y = 0$ for planar structures, the central axis $\rho = 0$ for cylindrical structures, and the center $r = 0$ for spherical structures. We can find asymptotic solutions to the above balance equations at $x \longrightarrow 0$. In this limit, the ion drift velocity should tend to zero. At $u = 0$, the drag coefficient $\alpha_{dr}^{(0)}(z, \tau) = \alpha_{dr}(z, 0, \tau)$ and the charging coefficient $\alpha_{ch}^{(0)}(z, \tau) = \alpha_{ch}(z, 0, \tau)$ have the form

$$\begin{aligned}\alpha_{ch}^{(0)}(z, \tau) &= \frac{1}{2\sqrt{\pi}}\left(1 + \frac{\tau}{z}\right), \\ \alpha_{dr}^{(0)}(z, \tau) &= \frac{2}{3\sqrt{\pi}}\left(\ln\Lambda + \frac{\tau}{z} + 2\frac{\tau^2}{z^2}\right).\end{aligned} \tag{13}$$

The ion density $n(0)$ at the center of the structure can serve as the basic parameter of the structure. From the asymptotic expression at $x \longrightarrow 0$, we have $u \longrightarrow u^{(0)}x$ and, from the condition that the diffusive flux vanishes at the center of structure, $dn/dx \longrightarrow 0$, we obtain the relationship between the central electron density $n_e(0)$ and the central ion density $n(0)$. These relationships can be written using the maximum possible and minimum possible values of the central ion density, $n_{max}(z, \tau)$ and $n_{min}(z, \tau)$, which can be obtained from the following two inequalities:

$$u^{(0)} < 0, \quad n_e(0) > 0. \tag{14}$$

The first of these inequalities indicates that, near the center of the structure, the ion flow is directed toward the center; hence, a dusty void cannot be formed there (the ion flow directed toward the center ensures the confinement of dust in the structure). The second inequality is quite obvious. We write out the expressions for $u^{(0)}$ and $n_e(0)$ in a form from which inequalities (14) can be directly seen:

$$u^{(0)}(z,\tau) = -\frac{1}{2\tau}\frac{n(0)-n_{\min}(z,\tau)}{n_{\max}(z,\tau)-n_{\min}(z,\tau)},$$
$$n_e(0)(z,\tau) = n_{\min}(z,\tau)\frac{n_{\max}(z,\tau)-n(0)}{n_{\max}(z,\tau)-n_{\min}(z,\tau)}, \quad (15)$$

where

$$n_{\min}(z,\tau) = \frac{1}{z\alpha_{\rm dr}^{(0)}(z,\tau)},\ n_{\max}(z,\tau) = \frac{s+1}{2\tau\alpha_{\rm ch}^{(0)}(z,\tau)}. \quad (16)$$

We recall that $s = 0$ for planar structures, $s = 1$ for cylindrical structures, and $s = 2$ for spherical structures. The grain charge at the center can be found from the charging equation

$$\exp(-z) = \frac{2\sqrt{\pi}\alpha_{\rm ch}^{(0)}(z,\tau)}{\sqrt{\tau m_i/m_e}}\frac{zn(0)}{n_e(0)(z,\tau)}, \quad (17)$$

which should be solved numerically as an algebraic equation for each sort of gas (the sort of gas determines the mass of a singly ionized ion) within the above interval of the possible values of the parameter $n(0)$:

$$n_{\min}(z,\tau) < n(0) < n_{\max}(z,\tau). \quad (18)$$

Equation (17) yields the value of the grain charge $z(0)$ at the center of the structure, and inequalities (18) should be satisfied for $z = z(0)$.

At $x \longrightarrow 0$, the total flux is equal to the convective flux:

$$\Phi \longrightarrow n(0)u^{(0)}(z(0),\tau)x. \quad (19)$$

These expressions are sufficient to solve the above complete set of equations for n, n_e, u, Φ, and z, starting from a coordinate very close to $x = 0$ and using the above asymptotic expressions. Such a procedure, in which calculations begin, e.g., from $x = 0.001$ (as is done in this paper), rather than exactly from the center, allows one to find solutions with a correct asymptote at the center of the structure.

The results of our study show that it is sufficient to vary a single parameter, namely, $n(0)$, within the limits determined by inequalities (18). The final point of numerical calculations is determined by the condition that the dust density and the parameter P vanish at this point. This point determines the structure size $x^{\rm str}$. The parameter $n(0)$ is uniquely related to the total electrostatic potential drop between the center of the structure and its boundary; hence, the structure can be characterized by this potential drop. The central ion density $n(0)$ is also uniquely related to the total number of grains in the structure N and the total power Q required to sustain the structure. The parameter N is equal to

$$N = \int_0^{x^{\rm str}} \frac{P}{z}dV, \quad (20)$$

where $dV = dy$ for planar structures (in this case, Eq. (20) determines the number of dust grains per unit area), $dV = 2\pi\rho d\rho$ for cylindrical structures (in this case, Eq. (20) determines the number of dust grains per unit length along the cylinder axis), and $dV = 4\pi r^2 dr$ for spherical structures (in this case, Eq. (20) determines the total number of dust grains in the structure). Note that, in Eq. (20) the number N is in dimensionless units, but it can easily be written in dimensional units (see Section 7, devoted to the discussion of the results obtained).

An important parameter of the structure is the total power Q absorbed by dust. This parameter determines the external plasma sources that are necessary to sustain the structure:

$$Q = \int_0^{x^{\rm str}} \alpha_{\rm ch}(u,z,\tau)Pn dV. \quad (21)$$

4. RESULTS FROM THE NUMERICAL SOLUTION OF THE EQUILIBRIUM EQUATIONS FOR DUST STRUCTURES

When solving the balance equations numerically, it was found that there are computational problems related to the use of exact expressions (12) for $\alpha_{\rm dr}(z,u,\tau)$ and $\alpha_{\rm dr}(z,u,\tau)$ at the center of the structure, because, at the center, $u \longrightarrow 0$ and expressions (12) contain u^3 in the denominator. Hence, it is necessary to determine the limit of the ratio of the two small quantities that tend to zero in both the numerator and denominator of the corresponding expressions. In fact, the resolving of the uncertainty at $u \longrightarrow 0$ leads to analytic expressions (13). Therefore, expressions (13) (rather than exact expressions (12)) were used in the vicinity of the center until u became about 0.1. These solutions were then joined to solutions that were obtained using exact expressions (12) at larger values of x, the final values of the parameters in the central region being used as the initial values of the parameters in this "outer" region. The numerical results presented below give the total distributions of the parameters in the structure, including both the central and peripheral regions. Our calculations show that $u \approx 1$–4 at the boundary of the structure; hence, it is necessary to use the exact expressions for $\alpha_{\rm dr}(z,u,\tau)$ and $\alpha_{\rm dr}(z,u,\tau)$ and to take into account the nonlinearity of ion friction on the neutral gas. On the other hand, the Mach number M at the boundary of the structure is

fairly small; this justifies the assumptions made in deriving the equilibrium equations.

The results of our numerical calculations show that the structures under study possess the following qualitative features:

(i) Solutions to Eq. (17) for the grain charge $z(0)$ at the center of the structure exist in the range that is somewhat narrower than that determined by inequalities (18). This is quite natural because, at the upper boundary of parameter range (18), the central electron density vanishes and the dust does not acquire electric charge. The extent to which the range of existence of dust structures is narrowed is not great; nevertheless, it is appreciable and the narrowing takes place at both the upper and lower boundaries of range (18). This narrower range of $n(0)$, in which equilibrium structures can exist, should be found separately for each sort of gas (which is characterized by the ratio m_i/m_e), for each value of τ, and for each type of structure (planar, cylindrical, or spherical).

(ii) It can be seen from inequalities (18) that, in laboratory plasmas, where $\tau \ll 1$, the maximum ion density at the center of the structure is fairly large. Even with allowance for the narrowing of range (18), the central ion density reaches a value of about 50–80, whereas the minimum value of the ion density at the center of the structure is on the order of or less than unity.

(iii) In astrophysical plasmas, where $\tau \approx 1$ but the Coulomb logarithm is large, the minimum value of the central ion density can be much less than unity, whereas its maximum value is on the order of unity.

(iv) For all the $n(0)$ values for which solutions to Eq. (17) exist, the structures are characterized by a monotonic decrease (down to zero) in the Havnes parameter P from the center to the periphery. The point at which the Havnes parameter vanishes is further referred to as the structure size x^{str}.

(v) The size of a structure monotonically increases with increasing $n(0)$. The maximum possible structure size corresponds to the maximum possible value of $n(0)$.

(vi) The electrostatic potential drop $\Delta\phi$ between the center of the structure and its boundary increases with increasing $n(0)$ and, at the maximum possible value of $n(0)$, reaches its maximum value on the order of or less than T_e/e.

(vii) The ion drift velocity increases toward the periphery, reaching a value of about $u \approx 2$–10 for structures with the maximum potential drop.

(viii) The difference between n and P decreases with increasing potential drop. In structures with the maximal potential drop, almost all the electrons are attached to dust and, for $\tau \ll 1$ (laboratory plasma), the Havnes parameter P at the center of the structures reaches fairly large values (about 50–80). In this case, the parameter P_H is always close to unity.

(ix) The dimensionless dust grain charge z usually increases toward the periphery of the structure; however, in some cases, the spatial derivative of the grain charge can change its sign.

(x) In most cases, the electron density is low (on the order of unity both at the center of the structure and at its periphery). The ion density decreases toward the periphery and, at the boundary of the structure, is equal to the electron density.

(xi) Distributions of all the parameters in the structures are smooth and are not influenced by the effects related to the excitation of dust convection.

(xii) The dimensionless number of dust grains in the structure increases with increasing $n(0)$ (or, equivalently, with increasing potential drop between the center of the structure and its boundary), reaching a maximum value of about 2 to 4 for structures with the maximal potential drop.

(xiii) The total power of the external ionization sources increases with increasing structure size (or the potential drop) and reaches its maximum value for structures with the maximal potential drop.

(xiv) As a basic parameter of the structure, one can use the total power of the external ionization sources, the total number of dust grains in the structure, or the potential drop between the center of the structure and its boundary.

The distributions of the parameters in all types of structures are qualitatively the same; however, the ranges within which the potential drop, the structure size, the total number of dust grains, and the plasma flux absorbed by the structure can vary are different. Therefore, we will first describe the results obtained for planar structures for two typical cases: (a) for parameters characteristic of laboratory plasmas and (b) for the expected parameters of astrophysical plasmas. We will then describe the basic quantitative differences between cylindrical and spherical structures, on the one hand, and planar structures, on the other, and will present some plots for structures with the maximum possible values of the potential drop, the number of the confined dust grains, the structure size, and the plasma flux that is required to balance the absorption of plasma by dust in these structures. All the results are given in a dimensionless form. The relationships between dimensional and dimensionless parameters are presented in Section 7.

5. PLANAR STRUCTURES

5.1. Laboratory Plasma

The calculations were performed for an argon of plasma with $\tau = 0.02$ and $\ln\Lambda = 3$. Under these conditions, the upper limit in inequalities (18) is equal to $n_{max} = 88.6$; however, it follows from the charging equation that $n(0)$ is smaller than ≈ 74. The lower limit in inequalities (18) contains the grain charge z; this limit can only be determined by solving Eq. (17) and is approximately equal to 0.4. The calculations were per-

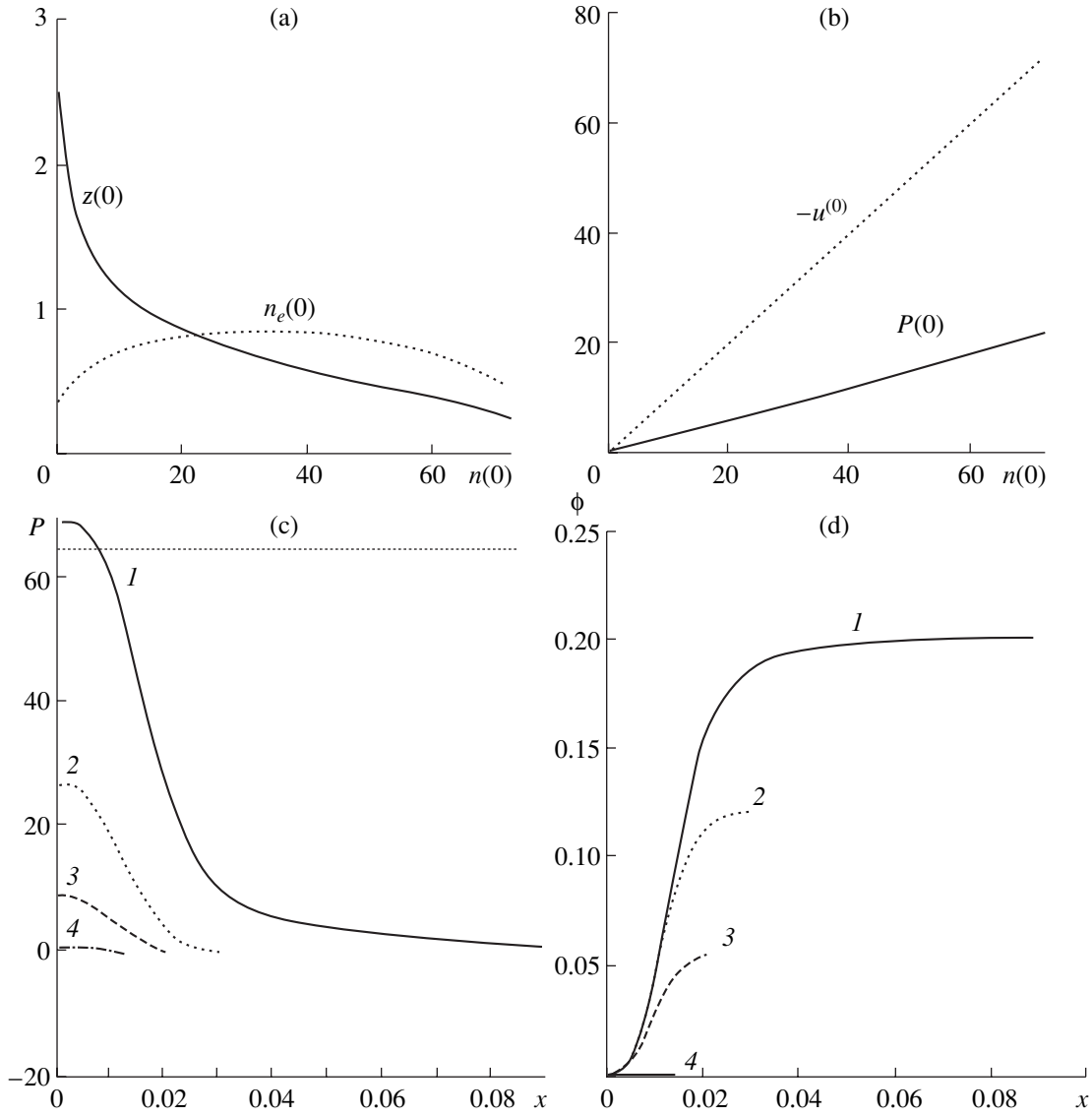

Fig. 1. (a) The grain charge $z(0)$ and the electron density $n_e(0)$ and (b) the first derivative of the ion drift velocity $u^{(0)}$ and the Havnes parameter $P(0)$ at the center of a planar structure as functions of $n(0)$ for an argon plasma with $\tau = 0.02$ and $\ln\Lambda = 3$. (c) The Havnes parameter P and (d) the dimensionless electrostatic potential $\phi \equiv e\phi^{ac}/T_e$ as functions of the distance from the center of the structure for different values of the ratio $n(0)/n_{max}$: (*1*) 0.8, (*2*) 0.4, (*3*) 0.1, and (*4*) 0.02.

formed within the range $0.6 < n(0) < 72.6$. Figures 1a and 1b show the main parameters at the center of the structure as functions of $n(0)$. It can be seen that, throughout the entire range of the parameter $n(0)$, the electron density is close to unity, whereas the dust grain charge decreases and tends to zero as the maximum value of $n(0)$ is approached, thus defining the range of existence of the structures. At the same time, the spatial derivative $u^{(0)}$ of the ion drift velocity at the center and the Havnes parameter $P(0)$ rapidly increase with increasing $n(0)$. The structure size increases from values close to zero up to $x^{str} = 0.112$ for the maximum possible value of $n(0)$. Figures 1c and 1d show the Havnes parameter and the dimensionless electrostatic potential $\phi \equiv e\phi^{ac}/T_e$ (here, ϕ^{ac} is the dimensional potential) inside the structure as functions of the distance from the center of the structure for different values of the ratio $n(0)/n_{max}$: (*1*) 0.8, (*2*) 0.4, (*3*) 0.1, and (*4*) 0.02. In the subsequent figures, we will also qualitatively examine how the distributions of the parameters change as the basic parameter of the structure varies (no anomalies in the distributions were observed; hence, for intermediate values of the basic parameter, the distributions can be interpolated using the plots presented below).

It can be seen that the Havnes parameter and the potential drop are maximum for structures with the maximum value of $n(0)$. Each of the curves in Figs. 1c,

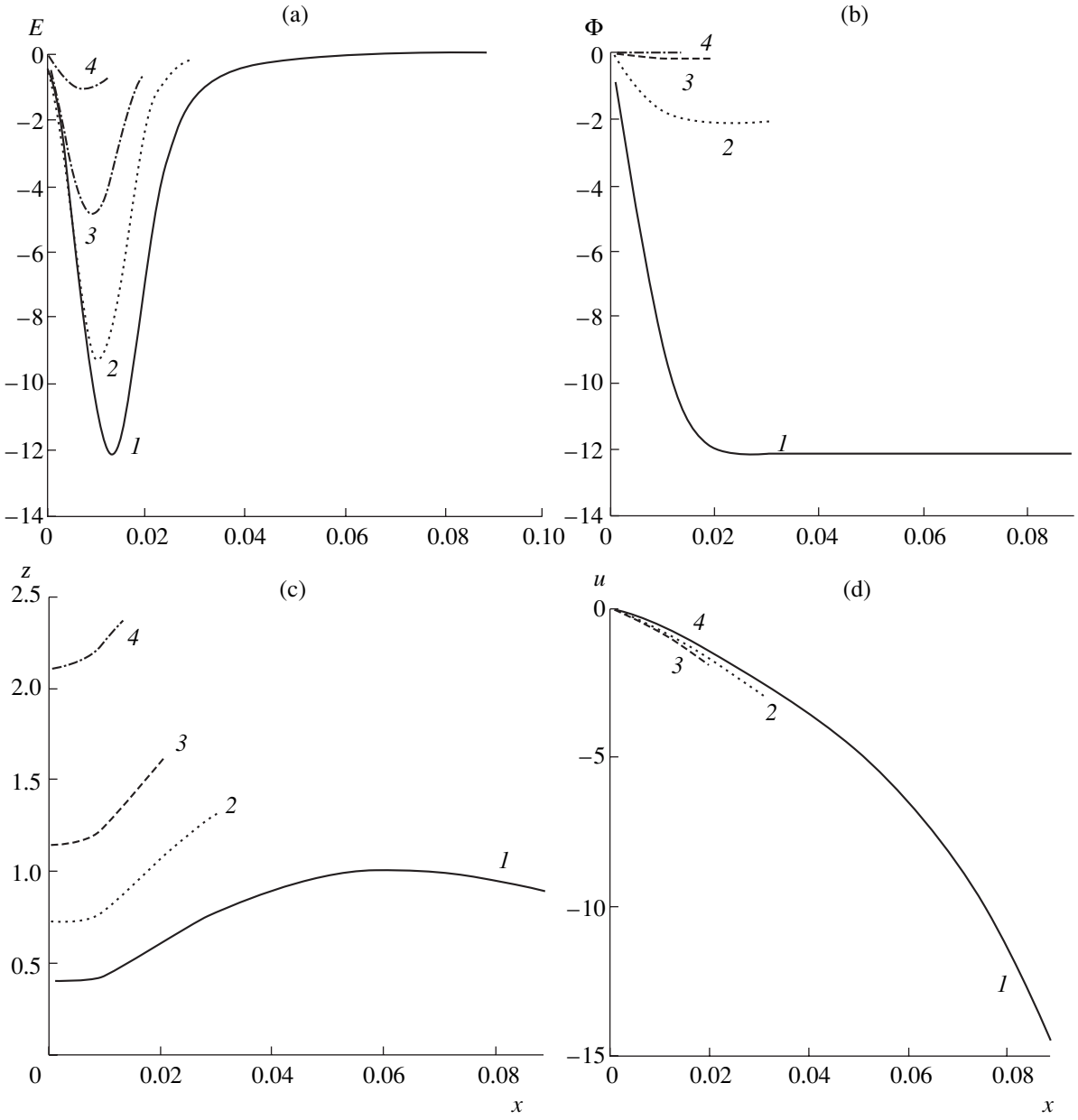

Fig. 2. (a) Electric field E, (b) total ion flux Φ, (c) grain charge z, and (d) ion drift velocity as functions of the distance from the center of a planar structure for an argon plasma with $\tau = 0.02$ and $\ln\Lambda = 3$ at the same values of $n(0)/n_{max}$ as in Fig. 1.

1d, and 2 ends at the point with the coordinate equal to the corresponding structure size x^{str}. Figure 2a shows the distribution of the electric field in the structure. It is seen that the spatial derivative of the electric field changes its sign; this corresponds to the change of the sign of the polarization charge. Note that, in this case, the quasineutrality condition is not disturbed, because the corresponding space charge density is small by virtue of the smallness of the parameter presented in Section 7 (in dimensionless units, this space charge density is much less than unity). Figures 2b–2d show the distributions of the total ion flux; the grain charge; and the ion drift velocity, which monotonically increases with increasing $n(0)$. The structures with the above four values of the central ion density are characterized by the following values of the total number of dust grains N and the power Q that is required to sustain the structure: (*1*) $N = 2.145$ and $Q = 11.242$, (*2*) $N = 0.434$ and $Q = 1.951$, (*3*) $N = 0.018$ and $Q = 0.023$, and (*4*) $N = 2.8 \times 10^{-3}$ and $Q = 1.7 \times 10^{-3}$. For a structure with $n(0)$ close to its maximum value, we have $N = 4.264$ and $Q = 18.334$. The electron density slightly increases with distance from the center but always remains lower than or on the order of unity. Figures 3a and 3b show the distributions of the ion and electron densities, the Havnes parameter, and the ion flux for a structure with an inter-

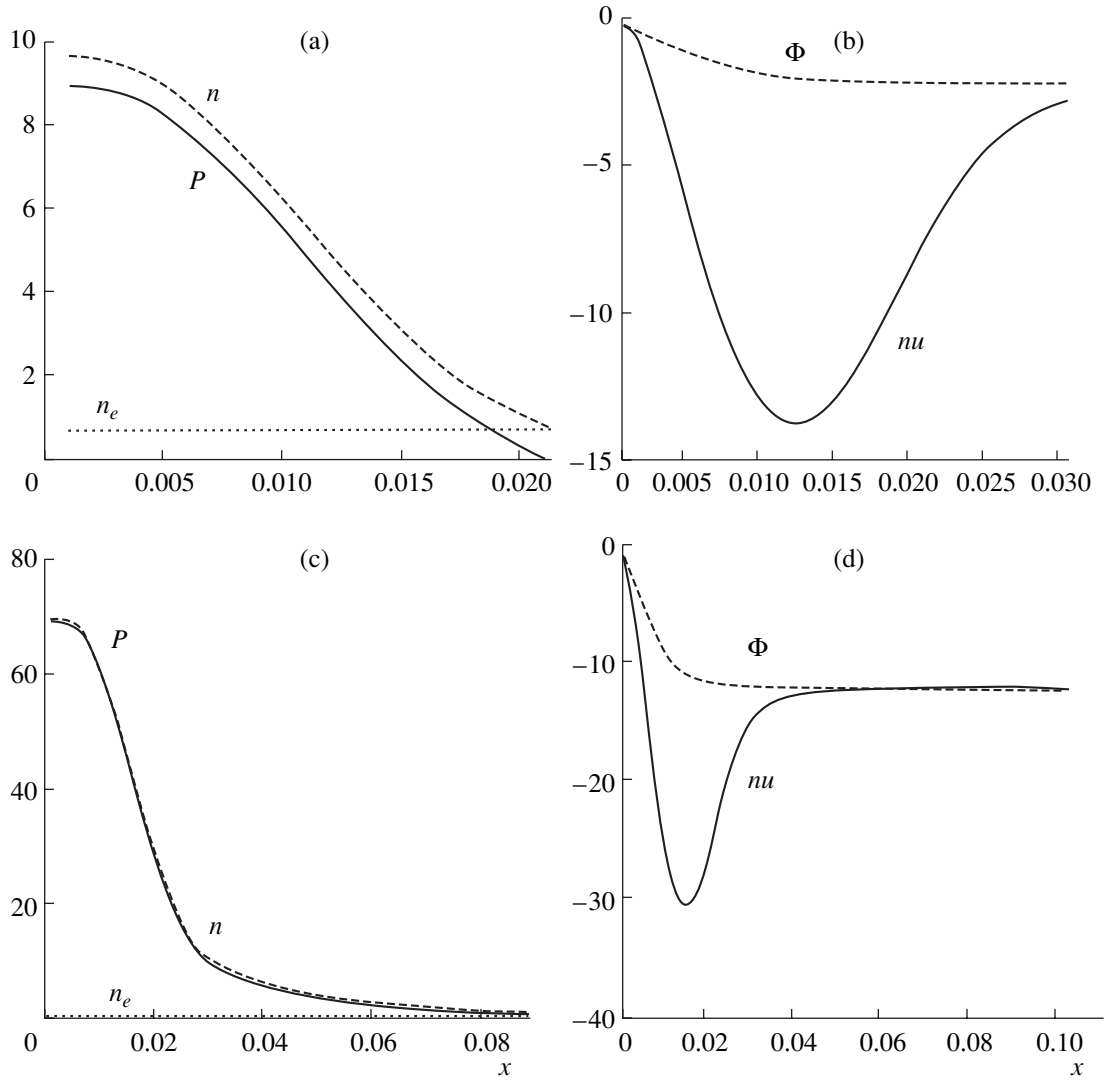

Fig. 3. Distributions of (a, c) the ion and electron densities (n and n_e) and the Havnes parameter P and (b, d) the total and convective ion fluxes (Φ and nu) in planar structures with (a, b) an intermediate central ion density ($n(0) = 27.6$) and (c, d) the maximal central ion density ($n(0) = 69.6$) for an argon plasma with $\tau = 0.02$ and $\ln\Lambda = 3$.

mediate (between $n_{\min}$ and $n_{\max}$) value of the central ion density, $n(0) = 27.6$. It can be seen that, in this structure, the ion density is much greater than the electron density and the convective flux is larger than the total flux (the diffusive flux is directed opposite to the convective flux and partially cancels it). Figures 3c and 3d show the distributions of the same parameters in a structure with the central ion density close to its maximum value, $n(0) = 69.6$.

5.2. Astrophysical Plasma

Calculations were performed for a hydrogen plasma with $\tau = 1$ and $\ln\Lambda = 18.4$. It follows from the charging equation that the maximum value of the central ion density is $n(0) \approx 0.61$. The minimum value is approximately equal to $n(0) = 0.05$. The calculations were performed within the range $0.06 < n(0) < 0.60$. The structure size is equal to $x^{\text{str}} = 0.215$ at $n(0) = 0.06$ and increases to 0.868 with increasing $n(0)$. Within the admissible range of the central ion density, the total number of dust grains in the structure, the power required to sustain the structure, and the potential drop vary in the ranges $4.26 \times 10^{-4} < N < 0.28$, $2.58 \times 10^{-5} < Q < 0.082$, and $0.037 < \phi < 1.285$, respectively. Figures 4a and 4b show the grain charge, the electron density, the spatial derivative of the ion drift velocity, and the Havnes parameter at the center of the structure as functions of $n(0)$. It can be seen that the derivative of the drift velocity increases with increasing $n(0)$ but not as rapidly as in the case of a laboratory plasma. The Havnes parameter also increases but does not reach such large values as in the laboratory plasma. Figures 4c and 4d show the distributions of the electric potential and the Havnes parameter.

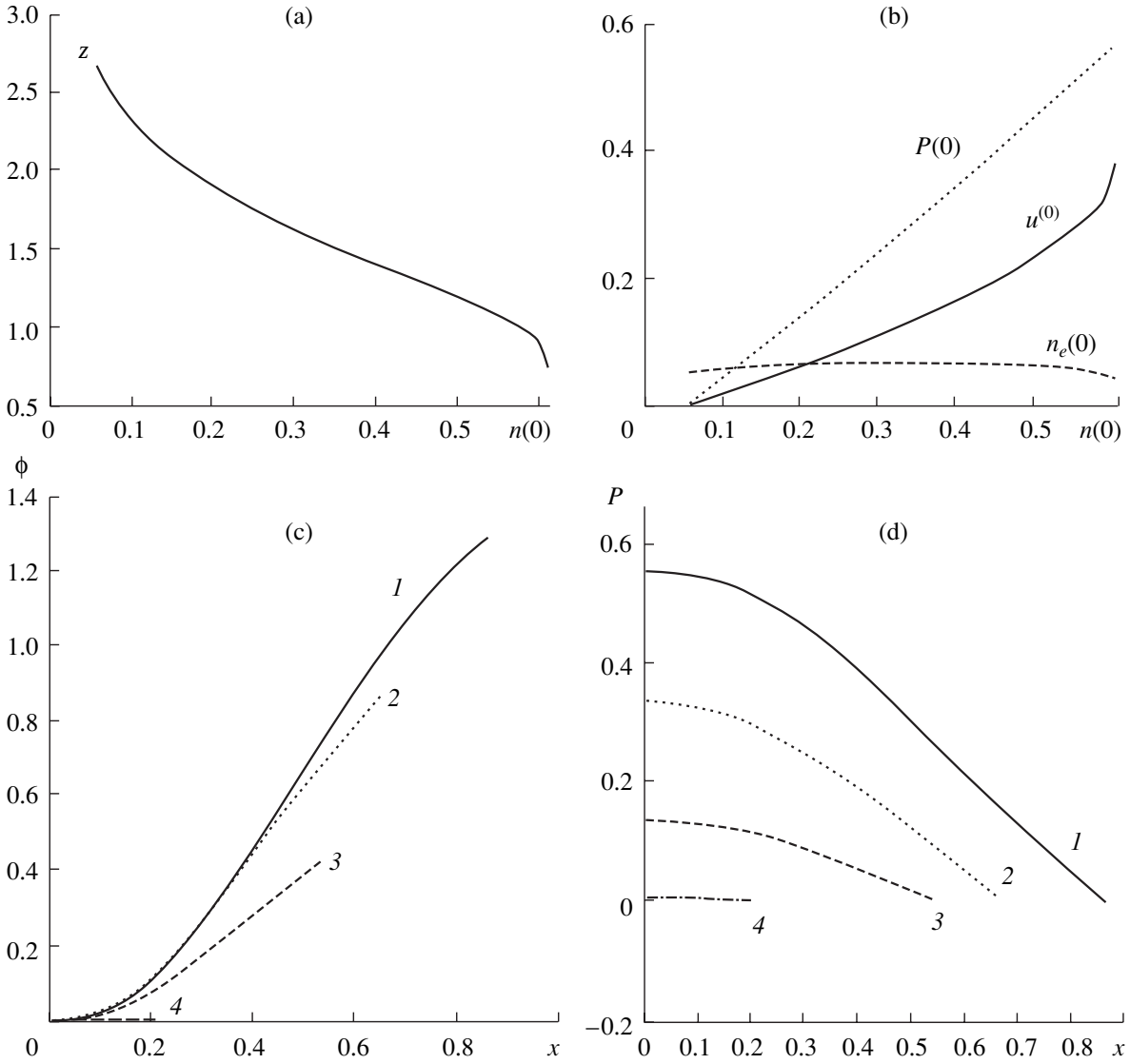

Fig. 4. (a) The grain charge $z(0)$ and the electron density $n_e(0)$ and (b) the first derivative of the ion drift velocity $u^{(0)}$ and the Havnes parameter $P(0)$ at the center of a planar structure as functions of $n(0)$ for parameters typical of astrophysical plasmas (hydrogen plasma with $\tau = 1$ and $\ln\Lambda = 18.4$), and (c) the dimensionless electrostatic potential ϕ and (d) the Havnes parameter P as functions of the distance from the center of the structure for different values of $n(0)$: (*1*) 0.6, (*2*) 0.4, (*3*) 0.2, and (*4*) 0.06.

It follows from these distributions that the maximum value of the potentials is larger than in the laboratory plasma and the profile of the Havnes parameter is not as flattened as in the laboratory plasma (curves *1*, *2*, *3*, and *4* correspond to $n(0) = 0.6$, 0.4, 0.2, and 0.06, respectively). Figure 5 shows the distributions of the parameters in a structure corresponding to an intermediate value of the central ion density, $n(0) = 0.4$. It can be seen that the electron and ion densities become equal to one another at the boundary of the structure, the grain charge and the absolute value of the ion drift velocity increase toward the periphery, and the convective flux is appreciably greater than the total flux (the diffusive flux is directed opposite to the convective flux and partially cancels it).

6. CYLINDRICAL AND SPHERICAL STRUCTURES

6.1. Cylindrical Structures under Typical Laboratory Conditions

We performed calculations for the same conditions as for planar structures, i.e., for an argon plasma with $\tau = 0.02$ and $\ln\Lambda = 3$. It was found that the range of $n(0)$ values at which compact cylindrical structures can exist is wider than for planar structures: $0.4 < n(0) < 142$. The corresponding ranges of the other parameters are $0 < \rho^{str} < 0.082$, $0 < N < 1.014$, $0 < Q < 4.171$, $0 < P(0) < 141$, and $0 < \Delta\phi < 1.5$ (note that, in this case, N and Q are the number of grains per unit length and the power absorbed by dust per unit length, respectively). Figure 6

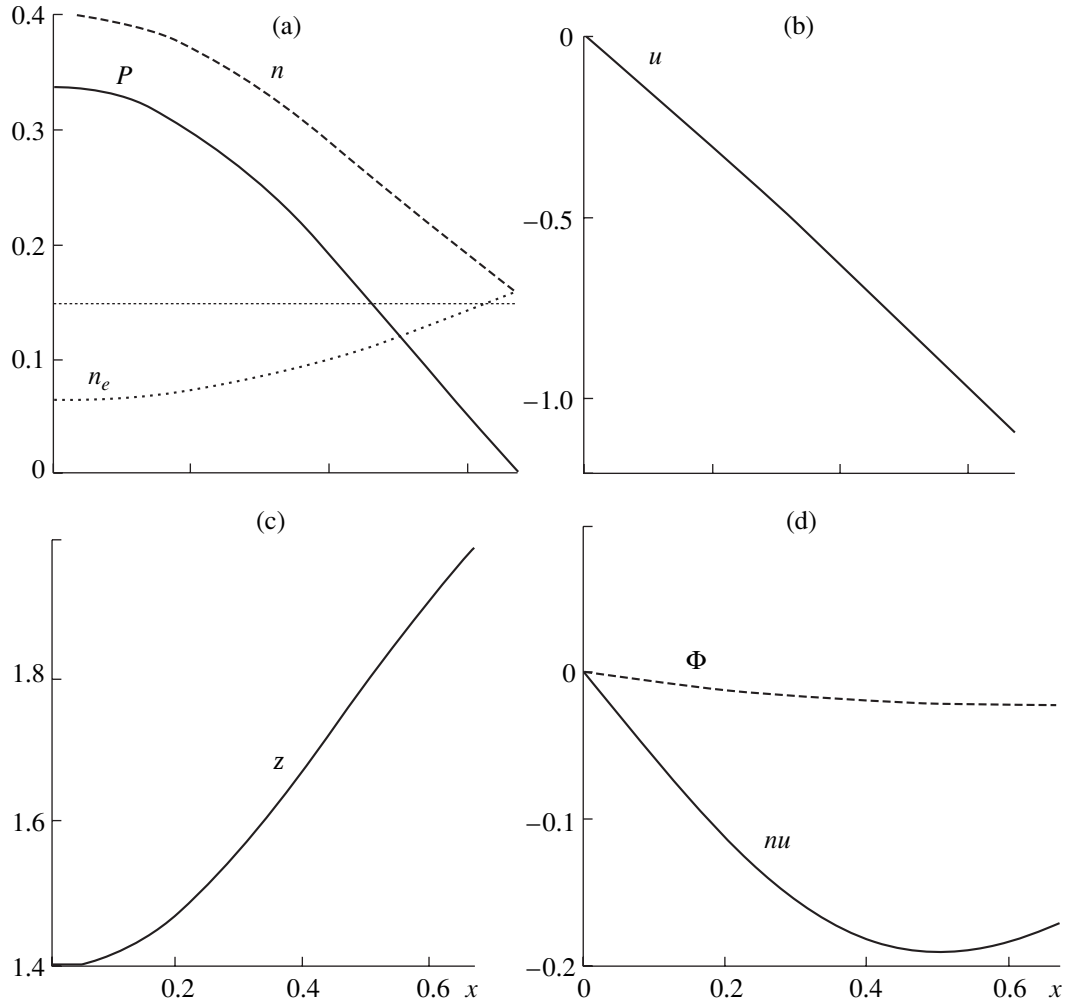

Fig. 5. Distributions of (a) n, n_e, and P; (b) u; (c) z; and (d) Φ and nu in a planar structure with an intermediate central ion density ($n(0) = 0.4$) for parameters typical of astrophysical plasmas (hydrogen plasma with $\tau = 1$ and $\ln\Lambda = 18.4$).

presents some results for $n(0)$ = (*1*) 142, (*2*) 116.4, (*3*) 76.4, (*4*) 12.4, (*5*) 4.4, and (*6*) 0.4.

6.2. Cylindrical Structures under Typical Astrophysical Conditions

We performed calculations for the same conditions as for planar structures, i.e., for a hydrogen plasma with $\tau = 1$ and $\ln\Lambda = 18.4$. It was found that the range of $n(0)$ values at which compact cylindrical structures can exist is wider than for planar structures: $0.05 < n(0) < 1$. The corresponding ranges of the other parameters are $0 < \rho^{str} < 0.753$, $0 < N < 0.787$, $0 < Q < 0.33$, and $0 < P(0) < 1$. Figure 7 presents some results for $n(0)$ = (*1*) 0.99, (*2*) 0.59, (*3*) 0.39, (*4*) 0.19, and (*5*) 0.09.

6.3. Spherical Structures under Typical Laboratory Conditions

We performed calculations for the same conditions as for planar and cylindrical structures, i.e., for an argon plasma with $\tau = 0.02$ and $\ln\Lambda = 3$. It was found that the range of $n(0)$ values at which compact spherical structures can exist is wider than for planar and cylindrical structures: $0.4 < n(0) < 202$. The corresponding ranges of the other parameters are $0 < r^{str} < 0.054$, $0 < N < 0.051$, $0 < Q < 0.187$, and $0 < P(0) < 201$ (note that, in this case, N and Q are the total number of grains in the structure and the total power absorbed by dust, respectively).

6.4. Spherical Structures under Typical Astrophysical Conditions

We performed calculations for the same conditions as for planar and cylindrical structures, i.e., for a hydrogen plasma with $\tau = 1$ and $\ln\Lambda = 18.4$. It was found that the range of $n(0)$ values at which compact spherical structures can exist is wider than for planar and cylindrical structures: $0.5 < n(0) < 1.19$. The corresponding ranges of the other parameters are $0 < r^{str} < 0.765$,

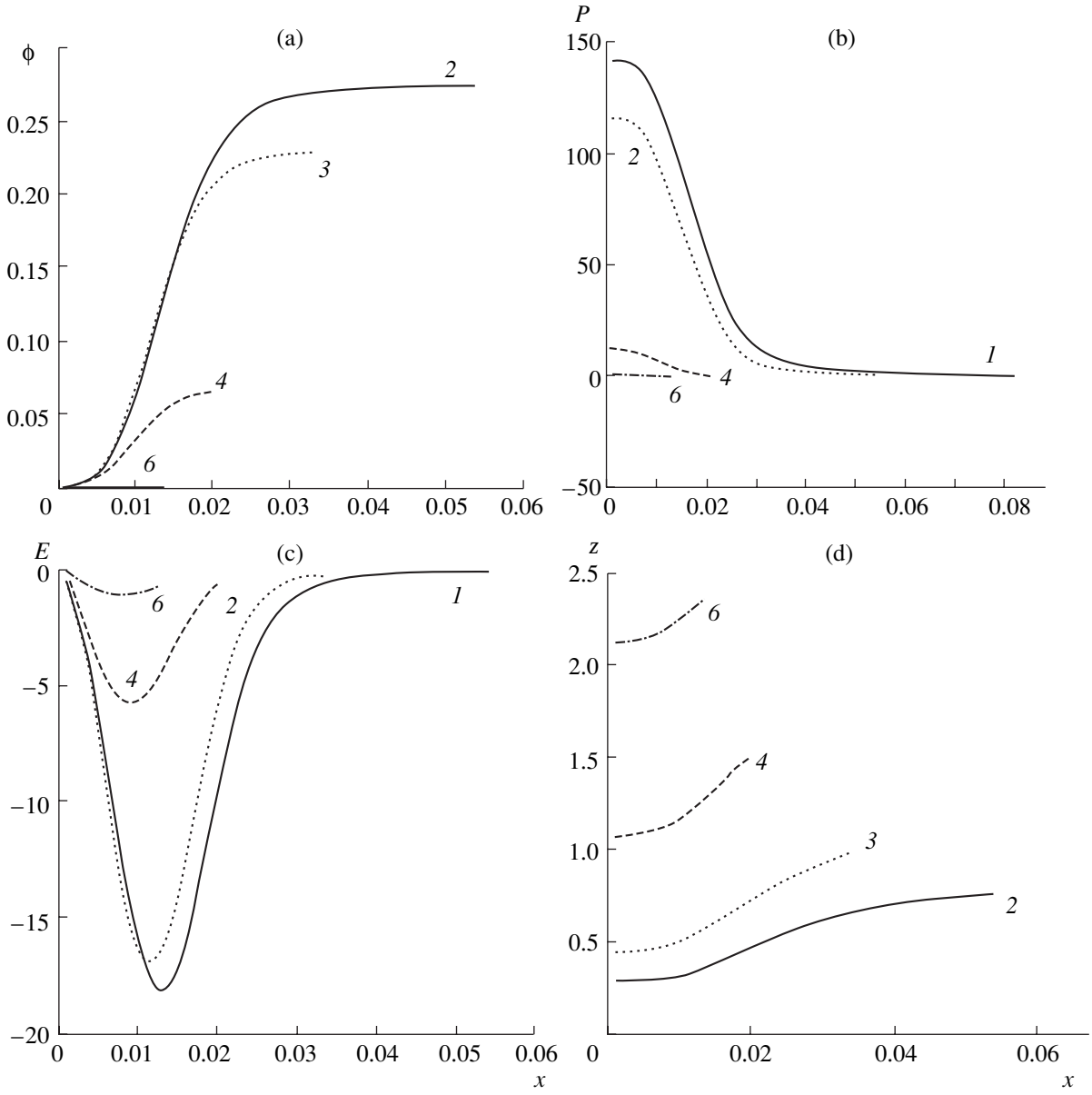

Fig. 6. Distributions of (a) Φ, (b) *P*, (c) *E*, and (d) *z* in a cylindrical structure for an argon plasma with $\tau = 0.02$ and $\ln\Lambda = 3$ at different values of $n(0)$: (*1*) 142, (*2*) 116.4, (*3*) 76.4, (*4*) 12.4, (*5*) 4.4, and (*6*) 0.4.

$0 < N < 0.959$, $0 < Q < 0.403$, $0 < P(0) < 1.18$, and $0 < \Delta\phi < 1.73$.

7. DISCUSSION

The main qualitative results of our calculations have already been discussed above. Here, we will only emphasize some points that are important for future experiments:

(i) The main feature of cylindrical and spherical structures is that these structures can exist in a wider parameter range than planar structures and that the potential drop between the center of the structure and its boundary is greater in them. Therefore, experiments with cylindrical or spherical geometry are more advantageous as compared to those with planar (or nearly planar) geometry.

(ii) Previous calculations performed for the case of spatially uniform ionization [9], as well as experiments carried out in a nearly planar geometry [3], showed that the creation of compact structures at the center of the chamber encounters some difficulties. An important point of those investigations was that ionization was spatially uniform. In [3], compact structures arose only when the degree of ionization at the center of the chamber was small enough; otherwise, a fairly large dust void was observed at the center. A plasma–dust crystal was formed only in the wall region both in ground-

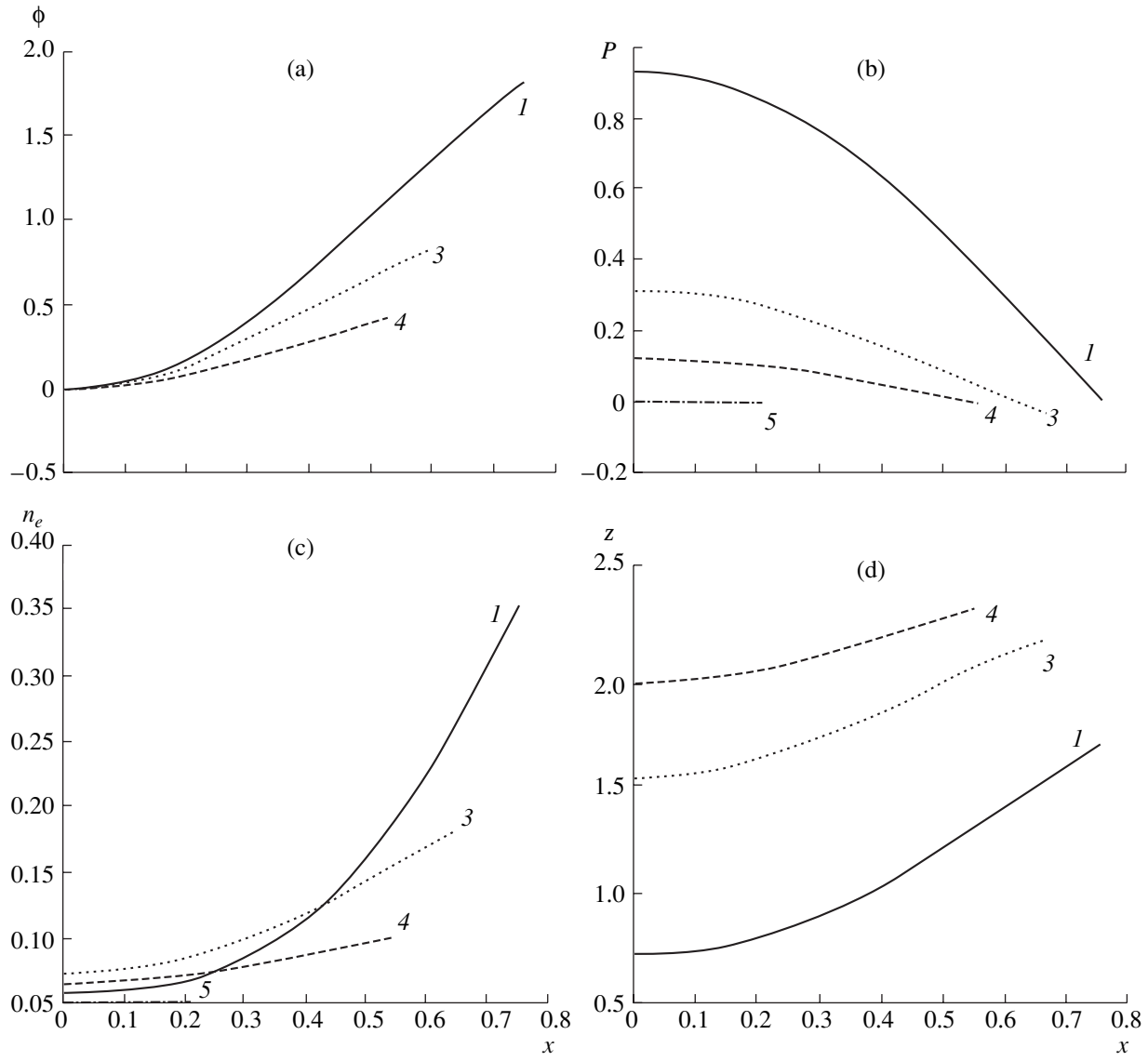

Fig. 7. Distributions of (a) Φ, (b) *P*, (c) n_e, and (d) *z* in a cylindrical structure for parameters typical of astrophysical plasmas (hydrogen plasma with $\tau = 1$ and $\ln\Lambda = 18.4$) at different values of $n(0)$: (*1*) 0.99, (*2*) 0.59, (*3*) 0.39, (*4*) 0.19, and (*5*) 0.09.

based experiments and under microgravity conditions onboard the International Space Station [3]. In theory [9], a criterion was found for the degree of ionization that is necessary for the existence of compact structures under microgravity conditions, assuming that ionization was spatially uniform (as in the experiment of [3]). When crystals are formed under microgravity conditions, the gravitational force is small, but there is a fairly large ion drag force near the wall, where plasma–dust crystals have been observed. Therefore, the main experimental problem is to avoid the occurrence of voids at the center of the chamber and to create there a dust structure that can crystallize as the temperature is reduced. The results of the present study allows us to offer a scheme for the future experiments in which compact dust structures at the center of the chamber are easier to produce. In the above calculations, the ionization rate was assumed to be zero within the structure and the power absorbed by the structure was delivered from plasma sources located outside it. It was found that, under these conditions, dust structures can easily be created within a rather wide parameter range, especially in laboratory experiments (or in experiments onboard the International Space Station) in which the ion-to-electron temperature ratio is small. Thus, to form a compact structure, it is expedient to use spatially nonuniform ionization sources operating at the chamber periphery. For this purpose, one can use, e.g., ionizing fields with a much higher frequency than that used in current experiments, in which the wavelength of the microwave field substantially exceeds the device

dimensions and, as a result, ionization is spatially uniform.

(iii) As was shown above, the electric field in the structures under study is nonuniform and, accordingly, the space charge is nonzero. The use of the quasineutrality condition is justified only in a first approximation, when the space charge plays a minor role. The corresponding criterion, which follows directly from Poisson's equation, has the form

$$a \ll \lambda_{in} x^{\mathrm{str}}, \tag{22}$$

where x^{str} is the size of the structure (in units of λ_{in}/τ). In this criterion, it is necessary to use the x^{str} values that were obtained above numerically (they are usually on the order of unity). Thus, the results of the present study are only applicable to the case of sufficiently small dust grains.

(iv) To apply the results of the above numerical calculations to experiments, it is necessary to keep in mind the normalization used in this study. As regards the dimensionless quantities N and Q, we will present here their relationships with the dimensional quantities: the number of dust grains per unit area $N_{1\mathrm{D}}$ and the power absorbed by dust per unit area $Q_{1\mathrm{D}}$ for planar structures, the number of dust grains per unit length $N_{2\mathrm{D}}$ and the power absorbed by dust per unit length $Q_{2\mathrm{D}}$ for cylindrical structures, and the total number of dust grains $N_{3\mathrm{D}}$ and the total absorbed power $Q_{3\mathrm{D}}$ for spherical structures:

$$N_{1\mathrm{D}} = \frac{N}{4\pi a^2 \tau}; \quad Q_{1\mathrm{D}} = Q\frac{n_0\sqrt{2}v_{Ti}\tau\lambda_{Di}^2}{\lambda_{in}a}, \tag{23}$$

$$N_{2\mathrm{D}} = N\frac{\lambda_{in}}{4\pi a^2\tau^2}; \quad Q_{2\mathrm{D}} = Q\frac{n_0\sqrt{2}v_{Ti}\lambda_{Di}^2}{\tau a}, \tag{24}$$

$$N_{3\mathrm{D}} = N\frac{\lambda_{in}^2}{4\pi a^2\tau^3}; \quad Q_{3\mathrm{D}} = Q\frac{n_0\sqrt{2}v_{Ti}\lambda_{in}\lambda_{Di}^2}{\tau^2 a}. \tag{25}$$

For example, according to Eqs. (23), a planar structure with the maximum possible value of N will contain 2.132×10^8 grains per cm^2.

(v) In contrast to conventional discharges, the electric field and the electron density in dust structures are too low to produce additional ionization. Here, the main role is played by the absorption of electrons by dust, which substantially reduces the electron density. Thus, in structures with the maximum possible value of N, the electric field reaches its maximal value and the electron density is almost two orders of magnitude (or more) lower than the ion density, whereas in structures with small N, the electric field is much lower. As a result, an additional flux that is produced by the self-consistent field of a quasineutral dust structure is smaller than the external flux. We recall that the ionization rate within the structure is proportional to the electron density, which is relatively low in structures with large N, in which almost all the electrons are attached to dust grains.

As for astrophysical applications, the above calculations can serve only as preliminary estimates of the possibility of spontaneous formation of dusty stars and planets (for dust–molecular clouds, rough estimates yield the structure mass on the order of the planetary mass). A series of additional studies must be performed to confirm these estimates. First of all, it is necessary to develop a theory of dust structures for the case where dust grains have different sizes and obey a certain size distribution (observations show that the grain size distribution is often described by a power-law function). It is also necessary to consider the problems of stability of such structures, to study their small oscillations, and to investigate the possibility of the excitation of dust convection in them. It is now quite possible to formulate these problems, but their solution requires an adequate astrophysical analysis and a large amount of numerical calculations.

ACKNOWLEDGMENTS

This study was supported by the INTAS–RFBR grant no. 02-02-16439.

REFERENCES

1. G. Morfill, H. Thomas, and U. Konopka, Phys. Rev. Lett. **83**, 1598 (1999).
2. D. Samsonov and J. Goree, Phys. Rev. E **59**, 1047 (1999).
3. F. Nefedov, G. Morfill, V. Fortov, *et al.*, New J. Phys. **5**, 33 (2003).
4. G. E. Morfill and V. N. Tsytovich, Fiz. Plazmy **26**, 727 (2000) [Plasma Phys. Rep. **26**, 682 (2000)].
5. V. N. Tsytovich, Comments Mod. Phys., Part C **1**, 1 (2000).
6. V. N. Tsytovich, Fiz. Plazmy **26**, 712 (2000) [Plasma Phys. Rep. **26**, 668 (2000)].
7. V. Tsytovich, S. Vladimirov, G. Morfill, and J. Goree, Phys. Rev. E **63**, 056609 (2001).
8. G. Morfill and V. Tsytovich, Phys. Plasmas **9**, 4 (2002).
9. V. Tsytovich, G. Morfill, U. Konopka, and H. Thomas, New J. Phys. **5**, 66 (2003).
10. V. Tsytovich and U. de Angelis, Phys. Plasmas **8**, 1141 (2001).
11. S. Khrapak, A. Ivlev, G. Morfill, and H. Thomas, in *Proceedings of the Third International Conference on the Physics of Dusty Plasmas, Durban, 2002*, AIP Conf. Proc. **649**, 341 (2002).

Translated by A.S. Sakharov

Plasma Physics Reports, Vol. 31, No. 2, 2005, pp. 147–166. Translated from Fizika Plazmy, Vol. 31, No. 2, 2005, pp. 172–191.

PLASMA OSCILLATIONS AND WAVES

Theory of Slow Waves in Transversely Nonuniform Plasma Waveguides

M. V. Kuzelev, R. V. Romanov, and A. A. Rukhadze

Prokhorov Institute of General Physics, Russian Academy of Sciences, ul. Vavilova 38, Moscow, 119991 Russia

Received November 27, 2003; in final form, May 12, 2004

Abstract—A general method is developed for a numerical analysis of the frequency spectra of internal, internal–surface, and surface slow waves in a waveguide with transverse plasma density variations. For waveguides with a piecewise constant plasma filling, the spectra of slow waves are thoroughly examined in the limits of an infinitely weak and an infinitely strong external magnetic field. For a smooth plasma density profile, the frequency spectrum of long-wavelength surface waves remains unchanged, but a slow damping rate appears that is caused by the conversion of the surface waves into internal plasma waves at the plasma resonance point. As for short-wavelength internal waves, they are strongly damped by this effect. It is pointed out that, for annular plasma geometry, which is of interest from the experimental point of view, the spectrum of the surface waves depends weakly on the magnetic field strength in the waveguide. © *2005 Pleiades Publishing, Inc.*

1. INTRODUCTION. BASIC MATHEMATICAL ASSUMPTIONS

In studies of plasma-filled waveguides, a great deal of attention is traditionally devoted to waves whose phase velocities are lower than the speed of light in vacuum. Investigation of slow plasma waves is important for solving many challenging problems in plasma physics, plasma electronics, electrodynamics of electron beams, and some other branches of physics. The properties of slow plasma waves depend on the transverse distribution of the plasma over the waveguide, the strength of the external magnetic field, and the character of interfaces between plasmas of different densities and between plasmas and other media. Slow plasma waves are usually classified on the basis of the structure of their electromagnetic fields into internal waves, internal–surface waves, and surface waves. They are also classified according to their dispersion relations into waves with a normal and an anomalous dispersion. Slow plasma waves have very different properties in weak and strong external magnetic fields. Surface waves localized near the plasma boundary are commonly treated as a special type of surface waves. In what follows, all the above types of waves are investigated for different transverse plasma density profiles in the limits of an infinitely weak and an infinitely strong external magnetic field as well as in the very important particular case of a weak (but finite) external magnetic field.

We consider a waveguide with a circular cross section that is filled with a plasma whose dielectric tensor has the form [1]

$$\varepsilon_{i,j}(r) = \begin{pmatrix} \varepsilon_\perp(r) & 0 & 0 \\ 0 & \varepsilon_\perp(r) & 0 \\ 0 & 0 & \varepsilon_\parallel(r) \end{pmatrix}; \quad i, j = r, \varphi, z, \quad (1)$$

where r, φ, and z are cylindrical coordinates (such that the z axis is the symmetry axis of the waveguide). For a plasma in an infinitely strong external magnetic field, we have $\varepsilon_\perp(r) = 1$ and

$$\varepsilon_\parallel(r) = \varepsilon(r) = 1 - \frac{\omega_p^2(r)}{\omega^2}, \quad (2)$$

where $\omega_p(r)$ is the radius-dependent electron plasma frequency. For a zero external magnetic field, the transverse dielectric function of the plasma has the form

$$\varepsilon_\perp(r) = \varepsilon(r) = 1 - \frac{\omega_p^2(r)}{\omega^2}, \quad (3)$$

and the longitudinal dielectric function is again given by formula (2).

The components E_z, E_r, and B_φ of the electromagnetic field of a symmetric E wave in the waveguide under consideration satisfy the set of equations [1]

$$k_z B_\varphi = \frac{\omega}{c}\varepsilon_\perp E_r,$$

$$\frac{1}{r}\frac{d}{dr}(rB_\varphi) = -i\frac{\omega}{c}\varepsilon_\parallel E_z, \quad (4)$$

$$ik_z E_r - \frac{dE_z}{dr} = i\frac{\omega}{c}B_\varphi,$$

1063-780X/05/3102-0147$26.00 © 2005 Pleiades Publishing, Inc.

where ω is the frequency of the wave and k_z is its longitudinal wavenumber. Eliminating the components E_r and B_φ in Eqs. (4), we obtain a single equation for E_z. In the limit of an infinitely strong external magnetic field, this equation has the form

$$\frac{d}{dr}\left(r\frac{dE_z}{dr}\right) - r\chi_0^2\varepsilon(r)E_z \equiv -\hat{L}_r^\infty E_z = 0. \quad (5)$$

For a zero external magnetic field, the equation is

$$\frac{d}{dr}\left(r\frac{\varepsilon(r)}{\chi^2}\frac{dE_z}{dr}\right) - r\varepsilon(r)E_z \equiv -\hat{L}_r^0 E_z = 0. \quad (6)$$

Here,

$$\chi_0^2 = k_z^2 - \frac{\omega^2}{c^2}, \quad \chi^2 = k_z^2 - \frac{\omega^2}{c^2}\varepsilon(r) = \chi_0^2 + \frac{\omega_p^2(r)}{c^2}, \quad (7)$$

and $\hat{L}_r^\infty$ and $\hat{L}_r^0$ are the differential operators on the left-hand sides of Eqs. (5) and (6).

Equations (5) and (6) are supplemented with the standard boundary conditions:

$$\frac{dE_z}{dr}(0) = 0, \quad E_z(R) = 0, \quad (8)$$

where R is the waveguide radius. The first of conditions (8) implies that the electromagnetic field components E_r and B_φ vanish at the waveguide axis and is equivalent to the requirement for the field to be finite at the axis, $|E_z(0)| < \infty$.

For further analysis, it is necessary to specify the quadratic forms $(\hat{L}_r^\alpha E_z, E_z)$ ($\alpha = \infty, 0$), which are obtained by multiplying Eqs. (5) and (6) by $E_z(r)$ and by integrating the resulting equations by parts over r from zero to R [2] with allowance for boundary conditions (8). For an infinitely strong external magnetic field, the quadratic form is given by the expression

$$(\hat{L}_r^\infty E_z, E_z) = \int_0^R \left(\left|\frac{dE_z}{dr}\right|^2 + \chi_0^2\varepsilon(r)|E_z|^2\right)r\,dr, \quad (9)$$

and for a zero external magnetic field, it is given by the expression

$$(\hat{L}_r^0 E_z, E_z) = \int_0^R \left(\frac{1}{\chi^2}\left|\frac{dE_z}{dr}\right|^2 + |E_z|^2\right)\varepsilon(r)r\,dr. \quad (10)$$

The boundary-value problem given by Eq. (5) and boundary conditions (8) and that given by Eq. (6) and the same boundary conditions are eigenvalue problems. The eigenvalues are the functions $\omega = \omega(k_z)$, which determine the frequency spectra of the eigenmodes in the plasma waveguides under investigation. The relationships

$$(\hat{L}_r^\alpha E_z, E_z) = 0, \quad \alpha = \infty, 0 \quad (11)$$

can be regarded as dispersion relations for determining the eigenfrequencies $\omega = \omega(k_z)$. In order to write dispersion relations (11) in explicit form, we must know continuous solutions to differential equations (5) and (6) that satisfy boundary conditions (8). Simple explicit forms of dispersion relations (11) in the case of a piecewise constant radial plasma density profile will be presented below.

Note that the problem given by Eq. (5) and boundary conditions (8) and that given by Eq. (6) and the same boundary conditions are not equivalent to the Sturm–Liouville problem in its classical formulation [2, 3]. In fact, in the Sturm–Liouville problem, with boundary conditions of form (8) or even with more general boundary conditions, the differential equation has the form

$$\hat{L}_r U \equiv -\frac{d}{dr}\left(p(r)\frac{dU}{dr}\right) + q(r)U = \lambda U, \quad 0 < r < R, \quad (12)$$

where λ is the eigenvalue and $U(r)$ is the eigenfunction. Moreover, the conditions $p(r) \geq p_0 > 0$ and $q(r) \geq 0$ must necessarily be satisfied on the radial interval $0 < r < R$. In contrast to Eq. (12), Eqs. (5) and (6) are nonlinear in the eigenvalue (frequency), which enters into them through quantities (7) and the dielectric function $\varepsilon(r)$. In turn, the dielectric function can vanish at certain points of the interval $0 < r < R$. For those eigensolutions to the problem given by Eq. (6) and boundary conditions (8) on which our attention is focused, it is important that there be points at which $\varepsilon(r) = 0$. As for the boundary-value problem given by Eq. (5) and boundary conditions (8), it in fact reduces to a conventional eigenvalue problem.

2. SOME FEATURES OF SLOW PLASMA WAVES AND METHODS FOR THEIR INVESTIGATION

We assume that the function $\omega_p(r)$ is a piecewise continuous function on the closed interval $[0, R]$ and that it satisfies the inequalities

$$0 \leq \omega_{\min} \leq \omega_p(r) \leq \omega_{\max}. \quad (13)$$

In what follows, we will focus on low-frequency slow plasma waves whose frequency and wavenumber ranges are given by the conditions

$$\omega \leq k_z c, \quad \omega \leq \omega_{\max}. \quad (14)$$

To be specific, we assume that $\omega > 0$. Let us determine what restrictions are imposed by expressions (9) and (10) for the quadratic form on the frequencies of low-frequency slow waves, i.e., what solutions to dispersion relations (11) are possible under conditions (14) and

what solutions are certainly impossible. To do this, we take into account the following inequalities and assertions, which follow from expression (3) and conditions (13) and (14):

(i) $\chi_0^2 > 0$ and $\chi^2 > 0$;

(ii) if $\omega \in (0, \omega_{min})$, then $\varepsilon(r) < 0$ for all $r \in [0, R]$; and

(iii) for $\omega \in (\omega_{min}, \omega_{max})$, there are finite intervals along the r direction in which the dielectric function $\varepsilon(r)$ has different signs.

For an infinitely strong external magnetic field, the first term in the integrand in expression (9) is positive and the second term either is negative or necessarily changes sign. This structure of the integrand makes it possible in principle to satisfy the equality $(\hat{L}_r^{\infty} E_z, E_z) = 0$ for any frequency ω over the range from 0 to ω_{max}. Consequently, the frequency range of slow plasma waves that can exist in an infinitely strong external magnetic field is given by the inequalities $0 \le \omega < \omega_{max}$.

For a zero external magnetic field, the integrand in expression (10) and the dielectric function $\varepsilon(r)$ are of the same sign. Therefore, in the absence of an external magnetic field, low-frequency slow plasma waves in the frequency range $0 \le \omega < \omega_{min}$, over which the dielectric function $\varepsilon(r)$ does not change sign, cannot exist. In this case, the only possible slow plasma waves are those whose frequencies lie in the range $\omega_{min} < \omega < \omega_{max}$. This, however, does not imply that such waves are indeed possible.

If the function $\omega_p(r)$ is not a piecewise constant function, then the problem given by Eq. (5) and boundary conditions (8) and that given by Eq. (6) and the same boundary conditions cannot be solved analytically. An approximate method for solving these problems can be as follows [4, 5]: For arbitrary values of ω and k_z, the solutions to Eqs. (5) and (6) cannot simultaneously satisfy both of boundary conditions (8). We fix a certain value of k_z and solve the Cauchy problem for Eqs. (5) and (6) with the following initial conditions at $r = 0$:

$$\frac{dE_z}{dr}(0) = 0, \quad E_z(0) = \text{const}.$$

The value of the constant in the second condition is unimportant because Eqs. (5) and (6) and boundary conditions (8) are linear and homogeneous. When solving the Cauchy problem, the frequency ω is adjusted to satisfy the second of boundary conditions (8). The frequency (or frequencies, if there are several waves) adjusted in such a manner is the sought-for eigenfrequency $\omega = \omega(k_z)$, and the corresponding solutions to Eqs. (5) and (6) are the sought-for eigenfunctions. The correctness of the solutions obtained by this method can be checked by substituting them into the integrals in expressions (9) or (10): if the solutions are correct, then the integrals should vanish.

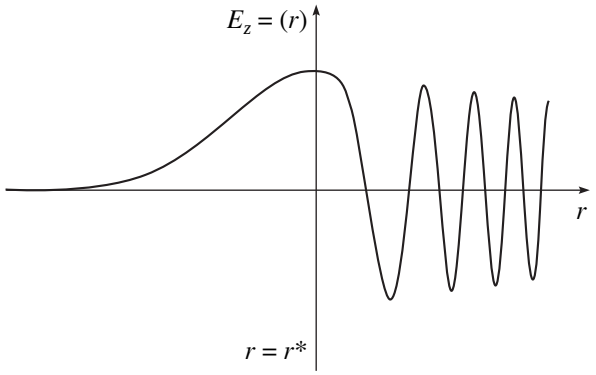

Fig. 1. Field structure of an internal–surface wave.

Equation (5) is fairly easy to solve numerically. Physically, this stems from the fact that slow plasma waves in a fully magnetized waveguide are actually internal–surface waves. For the waveguide regions determined by the inequality $\omega_p(r) > \omega$, Eq. (5) has the form

$$(rE_z')' + r\sigma(r)E_z = 0, \quad \text{with} \quad \sigma > 0.$$

Here, it is assumed that inequalities (14) are satisfied. The solution to this equation is expressed in terms of oscillating functions (such as Bessel and Neumann functions of the real argument [3]). In other words, the solution describes a standing internal wave or an internal wave running in the radial direction. For waveguide regions in which $\omega_p(r) < \omega$, the form of Eq. (5) differs from that in the previous case:

$$(rE_z')' - r\sigma(r)E_z = 0, \quad \text{with} \quad \sigma > 0.$$

The solution to this equation is expressed in terms of monotonic functions (such as first- and second-kind modified Bessel functions of the real argument [3]) and thus describes a surface wave that is damped in the radial direction. Figure 1 illustrates the characteristic structure of the solution $E_z(r)$ to Eq. (5). In the region $r < r^*$, the function $E_z(r)$ describes a surface wave, and, for $r > r^*$, it describes an internal wave. Here, $r = r^* = r^*(\omega)$ is the solution to the equation $\omega_p(r) = \omega$. This partially internal nature of the waves described by the solution to Eq. (5) indicates that the problem given by Eq. (5) and boundary conditions (8) has an infinite number of eigenvalues and eigenfunctions. Each solution to this problem describes an eigenmode of a plasma waveguide in an infinitely strong external magnetic field. Such waves are commonly denoted as E_{ls}, where l is the azimuthal wavenumber (here, we are considering only symmetric waves with $l = 0$) and $s = 1, 2, \ldots$ is the radial wavenumber [6, 7], which characterizes the number of oscillations (i.e., the number of zeros) of

the function $E_z(r)$ in the closed interval [0, R] (see Fig. 1).

Equation (6) is more difficult to solve because it has a singularity at the radius $r = r^*$, at which $\varepsilon(r) = 0$, i.e., $\omega = \omega_p(r)$. Let us rewrite Eq. (6) in a form convenient for qualitative analysis of its solutions:

$$\frac{d^2E_z}{dr^2} + \left[\frac{\chi^2}{\varepsilon}\frac{d}{dr}\left(\frac{\varepsilon}{\chi^2}\right) + \frac{1}{r}\right]\frac{dE_z}{dr} - \chi^2 E_z = 0. \qquad (15)$$

Under inequalities (14) (and by virtue of the inequality $\chi^2 > 0$), the solution to Eq. (6) on both sides of the surface $r = r^*$ is expressed in terms of monotonic functions, which indicates that it describes a surface plasma wave. It is the singularity $\varepsilon(r) = 0$ with which is associated the very existence of surface waves in a waveguide with an unmagnetized plasma inhomogeneous in the r direction. At $r = r^*$, there is a "layer" of resonant electrons whose oscillations constitute the essence of the wave motion in a surface wave. The relationship $\omega = \omega_p(r)$ is the plasma resonance condition. At the resonant surface, the electromagnetic field component E_z has a singularity, the component B_φ is continuous, and the component E_r undergoes a jump.

Let us examine the qualitative behavior of the field of a surface wave in an unmagnetized plasma waveguide near a surface of radius r^*, at which transverse dielectric function (3) vanishes. In the vicinity of this surface (whose radius is assumed to be nonzero), we can retain only the lowest order terms in Eq. (15) to obtain

$$\frac{1}{U}\frac{dU}{dr} = -\frac{1}{\varepsilon}\frac{d\varepsilon}{dr}, \quad U = \frac{dE_z}{dr}. \qquad (16)$$

Integrating this equation yields [5]

$$\frac{dE_z}{dr} = \frac{C}{\varepsilon(r)} \approx C\frac{\omega_p(r)}{[\omega - \omega_p(r)]},$$

$$E_r = -i\frac{k_z}{\chi^2}\frac{dE_z}{dr} \approx -iC\frac{k_z^{-1}\omega_p(r)}{[\omega - \omega_p(r)]}, \qquad (17)$$

$$B_\varphi = -i\varepsilon\frac{\omega}{c\chi^2}\frac{dE_z}{dr} \approx -iC\frac{k_z^{-1}\omega_p(r)}{k_z c},$$

where C is an arbitrary constant. The last two of relationships (17) were derived using Eqs. (4). In the vicinity of the resonant surface of radius r^*, we represent the plasma electron frequency as $\omega_p(r) = \omega_p(r^*) + \omega_p'(r^*)(r - r^*)$; in this case, the first of relationships (17) yields the following representation near the resonant radius r^*:

$$E_z(r \approx r^*) \approx -C\frac{\omega_p(r^*)}{\omega_p'(r^*)}\ln|r - r^*| + \text{const}. \qquad (18)$$

It can be seen that, as $r \longrightarrow r^*$, the field component E_z diverges logarithmically and the component E_r has a nonremovable discontinuity. Note that the presence of a singularity in one of the solutions at the surface $r = r^*$ at which $p(r) = 0$ is a general property of equations of form (12). Usually, the point $r = r^*$ is a boundary point of the closed interval on which the Sturm–Liouville problem for Eq. (12) is solved [2, 3]. In the case under analysis, the singular point lies within the interval of integration.

If we substitute asymptotic expression (18) into quadratic form (10) and take into account the relationship $\varepsilon(r) \sim r - r^*$, which holds in the vicinity of the surface of radius r^*, then we arrive at a diverging integral. This circumstance indicates that, when considering waves in an unmagnetized plasma waveguide, the frequency ω should be regarded as complex. The only exception is the case of a piecewise constant function $\omega_p(r)$; it is this case that will be investigated in detail below. However, even when the plasma density is not piecewise constant, the frequency ω can be assumed to be real under certain conditions and asymptotic formula (18) can then be applied. In this case, the integrals should be understood in terms of the Cauchy principal value. This point will be discussed in more detail in the final section of our paper.

3. INTERNAL PLASMA WAVES IN THE ABSENCE OF AN EXTERNAL MAGNETIC FIELD

Along with solutions corresponding to surface waves (which will be thoroughly analyzed below), the problem given by Eq. (6) and boundary conditions (8) has solutions describing internal plasma waves in an unmagnetized plasma waveguide. In fact, let us assume that, in a certain region G_0 that is continuous in the r direction, the plasma density is constant, i.e., $\omega_p(r) = \omega_{p0} = \text{const}$ for $r \in G_0$. If we set $\omega = \omega_{p0}$, then we can see that, in the region G_0, Eq. (6) is identically satisfied for $E_z(r) = \tilde{E}_z(r)$, where $\tilde{E}_z(r)$ is an arbitrary function. Outside the region G_0, Eq. (6) is satisfied by the function $E_z(r) \equiv 0$. If we have $\tilde{E}_z = 0$ at the boundaries of G_0, then the function $E_z(r)$ is continuous over the closed interval [0, R] and satisfies boundary conditions (8). Thus, for the problem given by Eq. (6) and boundary conditions (8), we have constructed the solution that determines the structure of the simplest internal plasma waves in an unmagnetized plasma waveguide. The dispersion of such waves is described by the formula $\omega = \omega_{p0}$.

Any smooth function $\omega_p(r)$ can be approximated by a piecewise constant function. Specifically, for $r \in G_j$ ($j = 1, 2, \ldots$), we can write $\omega_p(r) = \omega_{pj} = \text{const}$, where G_j are nonoverlapping continuous subintervals of the closed interval [0, R]. It has been shown above that, for a piecewise constant function $\omega_p(r)$, there exist internal

waves whose eigenfrequencies and eigenfunctions are given by the relationships

$$\omega = \omega_{pj},$$

$$E_z(r) = \begin{cases} \text{arbitrary function for } r \in G_j, \\ \text{identical null for } r \notin G_j, \end{cases} \quad (19)$$

where j = 1, 2, ….

Taking the limit $|G_j| \longrightarrow 0$, $j = 1, 2, \ldots$ in relationships (19), we obtain the expressions

$$\omega = \omega_p(r), \quad E_z(r) = \tilde{\delta}(r - r^*), \quad (20)$$

which determine the frequencies and the field of the waves in a plasma waveguide in a zero external magnetic field. Such waves can be called local internal waves. In expressions (20), $\tilde{\delta}(x)$ is an arbitrary function that is nonzero only at the point $x = 0$, e.g., the Dirac δ function.

4. DISPERSION RELATIONS FOR DETERMINING THE SPECTRA OF WAVES IN A WAVEGUIDE WITH A PIECEWISE CONSTANT PLASMA FILLING

In order to investigate the simplest internal–surface, surface, and internal waves, we consider a waveguide in which the piecewise constant plasma filling is specified by the formulas

$$\omega_p(r) = \begin{cases} \omega_{p1} = \text{const}_1, & 0 \le r < r_p, \\ \omega_{p2} = \text{const}_2, & r_p \le r < R. \end{cases} \quad (21)$$

For a piecewise constant function $\varepsilon(r)$, Eqs. (5) and (6) are solved separately for the regions $r < r_p$ and $r > r_p$ and then the solutions obtained are matched at $r = r_p$. One of the matching conditions follows from the continuity of the function $E_z(r)$, and the other is obtained by integrating Eqs. (5) and (6) over r in the vicinity of the point $r = r_p$. For an infinitely strong external magnetic field, the conditions for matching the solutions have the form

$$\{E_z\}_{r_p} = 0, \quad \left\{\frac{dE_z}{dr}\right\}_{r_p} = 0. \quad (22)$$

For an infinitely weak external magnetic field, the matching conditions are

$$\{E_z\}_{r_p} = 0, \quad \left\{\frac{\varepsilon}{\chi^2}\frac{dE_z}{dr}\right\}_{r_p} = 0. \quad (23)$$

Solving Eqs. (5) and (6) in the regions $r < r_p$ and $r > r_p$ and substituting the solutions obtained into boundary conditions (8) and (22) or into boundary conditions (8) and (23), we arrive at dispersion relations for determining the frequency spectra of waves in the waveguide under consideration. For an infinitely strong external magnetic field, the dispersion relation has the form [8]

$$\kappa_1 \frac{I_1(\kappa_1 r_p)}{I_0(\kappa_1 r_p)} = \kappa_2 \frac{I_1(\kappa_2 r_p)K_0(\kappa_2 R) + K_1(\kappa_2 r_p)I_0(\kappa_2 R)}{I_0(\kappa_2 r_p)K_0(\kappa_2 R) - K_0(\kappa_2 r_p)I_0(\kappa_2 R)}, \quad (24)$$

$$\kappa_{1,2}^2 = \chi_0^2 \varepsilon_{1,2}.$$

and, for a zero external magnetic field, the dispersion relation is [8]

$$\frac{\varepsilon_1}{\chi_1}\frac{I_1(\chi_1 r_p)}{I_0(\chi_1 r_p)} = \frac{\varepsilon_2}{\chi_2}\frac{I_1(\chi_2 r_p)K_0(\chi_2 R) + K_1(\chi_2 r_p)I_0(\chi_2 R)}{I_0(\chi_2 r_p)K_0(\chi_2 R) - K_0(\chi_2 r_p)I_0(\chi_2 R)}, \quad (25)$$

$$\chi_{1,2}^2 = k_z^2 - \frac{\omega^2}{c^2}\varepsilon_{1,2}.$$

Here, $\varepsilon_{1,2} = 1 - \omega_{p1,2}^2/\omega^2$ and $I_l(x)$ and $K_l(x)$ are lth-order modified Bessel functions of the first and the second kind, respectively.

Dispersion relations (24) and (25) can also be derived by appropriately transforming quadratic forms (11) in the following way. For a piecewise constant plasma filling, the continuous solutions to Eqs. (5) and (6) that satisfy boundary conditions (8) have the form

$$E_z(r) = \begin{cases} I_0(q_1 r), & r < r_p, \\ I_0(q_1 r_p)\dfrac{I_0(q_2 r)K_0(q_2 R) - K_0(q_2 r)I_0(q_2 R)}{I_0(q_2 r_p)K_0(q_2 R) - K_0(q_2 r_p)I_0(q_2 R)}, & \\ r_p < r < R, & \end{cases} \quad (26)$$

where $q_{1,2}^2 = \kappa_{1,2}^2$ for an infinitely strong external magnetic field and $q_{1,2}^2 = \chi_{1,2}^2$ for a zero external magnetic field. Substituting functions (26) into quadratic forms (9) and (10), performing simple but rather laborious integration, and equating the results to zero yields dispersion relations (24) and (25). Of course, these dispersion relations are much easier to derive by inserting functions (26) into the second relationships in matching conditions (22) and (23). However, the method of matching solutions is effective only for a piecewise constant function $\varepsilon(r)$. As for dispersion relations (11), they are meaningful for arbitrary dielectric functions. Moreover, for a zero external magnetic field, a dispersion relation of form (11) is more general than a dispersion relation of form (25). In fact, when deriving solution (26) in the region where $\varepsilon(r)$ is constant, we

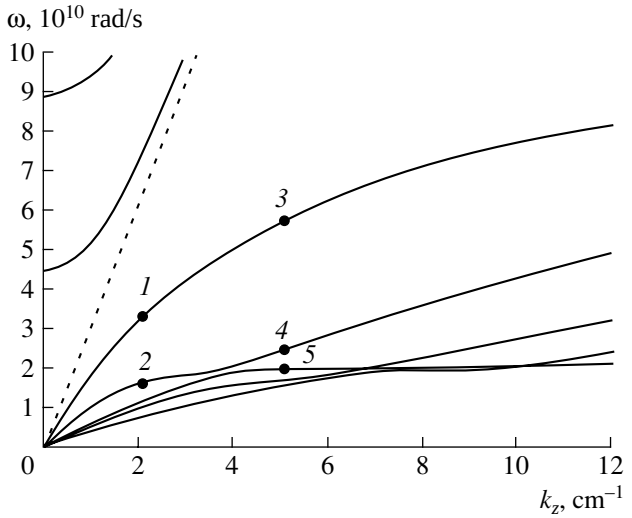

Fig. 2. Dispersion curves of the internal–surface and internal waves in a plasma waveguide in an infinitely strong external magnetic field.

divided Eq. (6) by $\varepsilon(r)$ and thereby excluded from consideration internal waves for which $\varepsilon(r) = 0$.

5. SPECTRA OF WAVES IN A WAVEGUIDE WITH A PIECEWISE CONSTANT PLASMA FILLING IN AN INFINITELY STRONG EXTERNAL MAGNETIC FIELD

Now, we consider solutions to dispersion relations (24) and (25). Figure 2 shows the dispersion curves for a plasma waveguide in an infinitely strong external magnetic field. The curves were calculated by solving dispersion relation (24) numerically for the following parameter values: $R = 2$ cm, $r_p = 1$ cm, $\omega_{p1} = 10 \times 10^{10}$ rad/s, and $\omega_{p2} = 2 \times 10^{10}$ rad/s. In this case, we have $\omega_{\max} = \omega_{p1}$ and $\omega_{\min} = \omega_{p2}$ (see conditions (13)). In this and similar subsequent figures, the frequency is expressed in units of 10^{10} rad/s, the wavenumber being given in units of cm^{-1}. The dashed line in the figures is used to represent the "light" straight line $\omega = k_z c$. Figure 2 displays the dispersion curves of slow plasma waves with the highest frequencies (see five branches below the line $\omega = k_z c$). The figure also shows the dispersion curves of the electromagnetic waves that were captured by the relevant numerical calculations (see two branches above the light straight line). The plasma waves are seen to fall into two groups: those whose frequencies approach the frequency ω_{p1} as $k_z \longrightarrow \infty$ and those whose frequencies approach ω_{p2} as $k_z \longrightarrow \infty$. This follows from the fact that, in the short-wavelength limit, the coupling between the neighboring plasma species is weak.

The waves whose frequencies and wavenumbers are marked by the points in the dispersion curves in Fig. 2 can be described as follows. Points *1* and *3* refer to an E_{01} wave belonging to a group of waves whose frequencies approach the frequency ω_{p1} as $k_z \longrightarrow \infty$. Since $\omega_{1,3} > \omega_{p2}$, the eigenfunctions corresponding to points *1* and *3* describe an internal wave in the region $r < r_p$ and a surface wave in the region $r_p < r < R$. Points *2* and *5* refer to an E_{01} wave belonging to a group of waves whose frequencies approach the frequency ω_{p2} as $k_z \longrightarrow \infty$. Since $\omega_{2,5} < \omega_{p2}$, the eigenfunctions corresponding to points *2* and *5* describe a purely internal wave. Finally, point *4* refers to an E_{02} wave belonging to a group of waves whose frequencies approach the frequency ω_{p1} as $k_z \longrightarrow \infty$. Since $\omega_4 > \omega_{p2}$, the eigenfunction corresponding to point *4* describes an internal wave in the region $r < r_p$ and a surface wave in the region $r_p < r < R$.

The frequency spectra and eigenfunctions of waves in a waveguide with a piecewise constant plasma filling in an infinitely strong external magnetic field are fairly simple in structure. We touch on this point merely in order to make our description more complete (see [8] for details). In particular, if the positions of the higher and lower density plasma species are interchanged, i.e., if $\omega_{p1} < \omega_{p2}$, then we arrive at approximately the same pattern of dispersion curves as shown in Fig. 2. For a homogeneous plasma filling such that $\omega_{p1} = \omega_{p2} = \omega_{p0}$ and $\varepsilon_1 = \varepsilon_2 = \varepsilon_0 = 1 - \omega_{p0}^2/\omega^2$, dispersion relation (24) reduces to a much simpler form:

$$I_0(\kappa_0 R) = 0, \quad \kappa_0^2 = \chi_0^2 \varepsilon_0.$$

The solution to this dispersion relation is determined from the relationship $\kappa_0^2 R^2 + \mu_{0s}^2 = 0$, where μ_{0s} are the roots of the Bessel function, $J_0(x) = 0$. In the frequency range given by inequalities (14), these solutions describe the spectra of an infinite number of slow internal plasma waves, and, in the frequency range given by inequalities opposite to inequalities (14), they describe the spectra of electromagnetic waves.

6. SPECTRA OF WAVES IN A WAVEGUIDE WITH A PIECEWISE CONSTANT PLASMA FILLING IN A ZERO EXTERNAL MAGNETIC FIELD

Here, we consider dispersion relation (25), which determines the eigenfrequencies of a plasma waveguide in the absence of an external magnetic field. It is easy to see that, in the frequency range given by inequalities (14) and in the limit $k_z \longrightarrow \infty$, dispersion relation (25) reduces to the equation

$$\varepsilon_1 + \varepsilon_2 = 0. \tag{27}$$

The solution to this equation,

$$\omega = \sqrt{\frac{\omega_{p1}^2 + \omega_{p2}^2}{2}}, \tag{28}$$

describes how the dispersion curve of the only surface wave in the waveguide under consideration behaves in the short-wavelength range. In the opposite (long-wavelength) limit, $k_z \longrightarrow \infty$, dispersion relation (25) is difficult to investigate analytically. However, a qualitatively correct behavior of the frequencies of plasma waves in the range given by inequalities (14) can be derived in the potential approximation, which is valid under the condition

$$\omega_{\max} \ll c/R. \tag{29}$$

Under this condition, and in the limit $k_z \longrightarrow 0$, dispersion relation (25) has the form

$$\frac{1}{2}\varepsilon_1 k_z^2 r_p^2 \ln\frac{R}{r_p} + \varepsilon_2 = 0. \tag{30}$$

The only solution to dispersion relation (30),

$$\begin{aligned}\omega &= \omega_{p2}\left[1 + \frac{1}{2}\left(1 - \frac{\omega_{p1}^2}{\omega_{p2}^2}\right)k_z^2 r_p^2 \ln\frac{R}{r_p}\right]^{-1/2} \\ &\approx \omega_{p2}\left[1 - \frac{1}{4}\left(1 - \frac{\omega_{p1}^2}{\omega_{p2}^2}\right)k_z^2 r_p^2 \ln\frac{R}{r_p}\right],\end{aligned} \tag{31}$$

determines the long-wavelength asymptotic behavior of the only surface wave in a plasma waveguide in a zero external magnetic field.

When the inequality $\omega_{p2} < \omega_{p1}$ is satisfied (an important point here is that the electron plasma frequencies are numbered in accordance with formulas (21)), frequency (31) increases with k_z and, as $k_z \longrightarrow \infty$, approaches solution (28) from below. For $\omega_{p1} < \omega_{p2}$, frequency (31) decreases with increasing k_z (this indicates that the dispersion of the surface wave is anomalous, in contrast to the case $\omega_{p2} < \omega_{p1}$, in which the wave dispersion is normal) and approaches solution (28) from above as $k_z \longrightarrow \infty$. Note that, for $\omega_{p2} = \omega_{p1} = \omega_{p0}$, formula (31) becomes $\omega = \omega_{p0}$. It is clear that the latter relation corresponds to an internal wave because, at a constant electron plasma frequency, there is no surface of radius r at which a surface wave structure can be localized. On the other hand, if we set $\omega_{p2} = \omega_{p1} = \omega_{p0}$ and $\omega = \omega_{p0}$ in formula (26), then we arrive at a solution typical of a surface wave, i.e., that in which the derivative dE_z/dr is discontinuous at $r = r_p$. This, however, does not cause confusion because, for $\omega_p(r) = \omega_{p0} = \text{const}$, Eq. (6) with $\varepsilon \equiv 0$ (i.e., with $\omega = \omega_{p0}$) is satisfied by any function $E_z(r)$, in particular, by function (26).

Let us discuss some other features of dispersion relation (30) and its solution (31). Recall that dispersion relation (30) is a direct consequence of exact dispersion relation (25). It follows from solution (31) that, for $r_p \longrightarrow R$, there are waves with the frequencies $\omega = \omega_{p2}$ and there are no waves with the frequencies $\omega = \omega_{p1}$. Looking at formulas (21), however, one may decide that the converse is true. The reason is that, for $r_p = R$, the relation $\omega = \omega_{p1}$ for an internal wave follows not from dispersion relation (25) but rather from differential equation (6), which is identically satisfied for $\varepsilon_1 = 0$. In other words, differential equation (6) contains more information than the dispersion relation derived by the method of matching solutions. As for the dispersion relation $\omega = \omega_{p2}$ (whose presence in the case $r_p \longrightarrow R$ appears at first glance to be strange because the thickness of a plasma with the electron plasma frequency ω_{p2} is zero, i.e., there is no plasma at all), it corresponds to a surface wave localized at the waveguide boundary. The structure of such "boundary" surface waves will be considered below.

Another distinctive feature of dispersion relation (30) is that it is not symmetric in the two electron plasma frequencies. As a consequence, for $k_z \longrightarrow 0$, solution (31) yields $\omega \approx \omega_{p2}$ rather than $\omega \approx \omega_{p1}$ (this asymmetry was pointed out above). This is attributed to the specific properties of cylindrical geometry, in which the point $r = 0$ is a singular point. In the planar case, the dispersion relation is symmetric in the electron plasma frequencies. If, in cylindrical geometry, the inner plasma terminate at a certain finite distance from the waveguide axis (i.e., if there were a vacuum axial region in a cylindrical waveguide), then, as will be shown below, a surface wave with $\omega \approx \omega_{p1}$ would also exist in the limit $k_z \longrightarrow 0$.

For a plane waveguide that is formed by two metal plates at $x = -L_1$ and $x = L_2$ and in which $\omega_p(x) = \omega_{p1}$ at $x < 0$ and $\omega_p(x) = \omega_{p2}$ at $x > 0$, the dispersion relation has the form

$$\frac{\varepsilon_1}{\chi_1}\frac{1 + \exp(-2\chi_1 L_1)}{1 - \exp(-2\chi_1 L_1)} = \frac{\varepsilon_2}{\chi_2}\frac{1 + \exp(2\chi_2 L_2)}{1 - \exp(2\chi_2 L_2)}.$$

For $k_z \longrightarrow \infty$, the solution to this dispersion relation coincides with that to dispersion relation (28). For $k_z \longrightarrow 0$, we have $\varepsilon_1 L_2 + \varepsilon_2 L_1 = 0$, which yields

$$\omega = \sqrt{\frac{\omega_{p1}^2 L_2 + \omega_{p2}^2 L_1}{L_1 + L_2}}.$$

We can see that the dispersion relation and its solutions are both symmetric in the two electron plasma frequencies. Also, if there is only one boundary between two plasmas of different densities, then there is a single surface wave, as is the case in cylindrical geometry.

In the case $\omega_{p2} = 0$, in which solution (31) is invalid, dispersion relation (30) requires separate consideration. In this case, ($\omega_{\min} = 0$), the dispersion of waves at small k_z is described by the formula

$$\omega = \frac{\omega_{p1}}{\sqrt{2}} k_z r_p \sqrt{\ln\frac{R}{r_p}}. \tag{32}$$

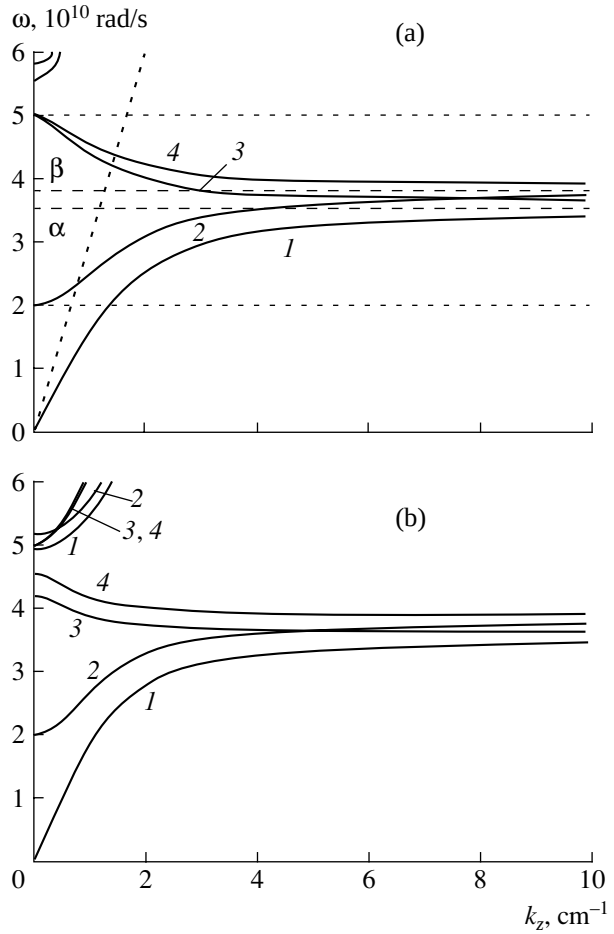

Fig. 3. Dispersion curves of the surface waves in a waveguide with a two-step plasma density profile in a zero external magnetic field: (*1*) $\omega_{p1} = 5$ and $\omega_{p2} = 0$, (*2*) $\omega_{p1} = 5$ and $\omega_{p2} = 2$, (*3*) $\omega_{p1} = 0$ and $\omega_{p2} = 5$, and (*4*) $\omega_{p1} = 2$ and $\omega_{p2} = 5$. The curves were calculated for (a) $R = 1.5$ cm and $r_p = 0.75$ cm and (b) $R = 2.2$ cm and $r_p = 1.1$ cm (in this case, inequality (40) is satisfied).

We can see that, as k_z increases, the frequency approaches the value $\omega_{p1}/\sqrt{2}$.

On the whole, we can conclude that, under conditions (14), the solutions to dispersion relation (25) (and, accordingly, to the boundary-value problem given by Eq. (6) and boundary conditions (8)) differ qualitatively from those to dispersion relation (24) (and, accordingly, to the problem given by Eq. (5) and boundary conditions (8)). Physically, this is explained by the fact that, under conditions (14), there is no more than a finite number of surface waves in a plasma waveguide in the absence of an external magnetic field. As for the internal plasma waves occurring in such a waveguide, they are closer to waves with a continuous spectrum (see formulas (19), (20)) than they are to conventional discrete waveguide E_{ls} modes in an infinitely strong external magnetic field. The mathematical structure of plasma waves (both surface and internal) in a zero external magnetic field is far more complicated than that of plasma waves in a waveguide in an infinitely strong external magnetic field.

Now, we analyze the results of numerically solving dispersion relation (25), which describes the frequency spectra of waves in a plasma waveguide in a zero external magnetic field. First, we consider the results obtained for a waveguide with the following parameters: $R = 1.5$ cm, $r_p = 0.75$ cm, $\omega_{p1} = 5 \times 10^{10}$ rad/s, and $\omega_{p2} = 0$. In Fig. 3a, the dispersion curve of the only possible surface wave in this waveguide is shown by curve *1*. For small k_z values, the dispersion curve is described by formula (32), and, for large wavenumbers, it asymptotically approaches the value $\omega_{p1}/\sqrt{2} \approx 3.536 \times 10^{10}$ rad/s (dashed line α). If we choose the above values of the waveguide radii and of the frequency ω_{p1} and set $\omega_{p2} = 2 \times 10^{10}$ rad/s, we arrive at dispersion curve *2*. In the frequency range $\omega < \omega_{p2} = \omega_{\min}$, there are no waves at all. For small k_z values and for $\omega_{p2} < \omega_{p1}$, dispersion curve *2* is described by formula (31); as k_z increases, the curve asymptotically approaches solution (28), $\omega \approx 3.808 \times 10^{10}$ rad/s, from below (dashed line β). Dispersion curves *1* and *2* correspond to waves with a normal dispersion.

Further, we keep the above values of the waveguide radii and interchange the positions of the two plasma species; i.e., we set $\omega_{p1} < \omega_{p2}$. Recall that, for an infinitely strong external magnetic field, the wave pattern in a waveguide in which the two plasma species are interchanged remains qualitatively the same. For $\omega_{p1} = 0$ and $\omega_{p2} = 5 \times 10^{10}$ rad/s, the dispersion curve of a surface wave is shown by curve *3* in Fig. 3a. For small k_z values, the dispersion curve is described by formula (31) and, as k_z increases, the curve asymptotically approaches the value $\omega_{p2}/\sqrt{2} \approx 3.536 \times 10^{10}$ rad/s (dashed line α). For $\omega_{p1} = 2 \times 10^{10}$ rad/s and for the above value $\omega_{p2} = 5 \times 10^{10}$ rad/s, the dispersion curve is represented by curve *4*, which is seen to behave like curve *3* but lies somewhat above the latter because, at large k_z values, it asymptotically approaches the limit given by solution (28) and shown by dashed line β. Dispersion curves *3* and *4* correspond to waves with an anomalous dispersion.

Figure 3a also shows dispersion curves of the electromagnetic waves (E_{01} modes) of a plasma waveguide in a zero external magnetic field. These dispersion curves, which were obtained by the relevant numerical calculations, lie in the upper left of the figure above the inclined dashed line corresponding to the light line $\omega = k_z c$. Since we are not interested here in electromagnetic waves, we do not even identify to which of the above four plasma configurations in question these dispersion curves correspond.

7. DETERMINATION OF THE SPECTRA OF INTERNAL PLASMA WAVES IN THE ABSENCE OF AN EXTERNAL MAGNETIC FIELD

In Fig. 3a, the dashed lines $\omega = \omega_{p1}$ and $\omega = \omega_{p2}$ serve not merely as a graphical illustration of the characteristic frequencies but describe the dispersion of the actual internal plasma waves whose eigenfrequencies and eigenfunctions are given by relationships (19). However, the solutions $\omega = \omega_{p1}$ and $\omega = \omega_{p2}$ cannot be derived from dispersion relation (25) because it has no solutions describing waves with eigenfrequencies and eigenfunctions (19). Recall that solution (19), instead of being derived as a solution to the eigenvalue problem in a mathematically precise way, was in fact constructed artificially.

We regularize the problem given by Eq. (6) and boundary conditions (8) in such a way that the solutions describing internal plasma waves with eigenfrequencies and eigenfunctions (19) can indeed be its eigensolutions, i.e., that they represent certain sets of eigenvalues and the corresponding eigenfunctions. To do this, we assume that the external magnetic field is nonzero. In this case, the transverse dielectric function of the plasma is described not by formula (3) but by the expression

$$\varepsilon_\perp(r) = 1 - \frac{\omega_p^2(r)}{\omega^2 - \Omega_e^2},$$

where Ω_e is the electron gyrofrequency. As for the longitudinal dielectric function, it is, as before, given by formula (2). For $\Omega_e \neq 0$, plasma dielectric tensor (1) becomes far more complicated: its off-diagonal elements $\varepsilon_{r\varphi} = -\varepsilon_{\varphi r}$ become nonzero (for $\Omega_e \ll \omega$, they are proportional to Ω_e), which implies that the E and H modes of the waveguide are coupled to each other. The mode coupling effect is proportional in magnitude to Ω_e/c [1, 8]. Since we are going to take the limit $\Omega_e \longrightarrow 0$, we ignore the mode coupling and immediately set $\varepsilon_{r\varphi} = 0$. From Eqs. (4), which remain valid in this case, we obtain, instead of Eq. (6), the following more general equation:

$$\frac{d}{dr}\left(r\frac{\varepsilon_\perp(r)}{\chi_\perp^2}\frac{dE_z}{dr}\right) - r\varepsilon_\parallel(r)E_z = 0, \qquad (33)$$

where $\chi_\perp^2 = k_z^2 - \varepsilon_\perp(r)\omega^2/c^2$ and the dielectric functions $\varepsilon_\parallel(r)$ and $\varepsilon_\perp(r)$ were defined above. Equation (33) is also supplemented with boundary conditions (8). To take the limit $\Omega_e \longrightarrow 0$ in the problem given by Eq. (33) and boundary conditions (8) is not a trivial matter.

Let us solve the problem given by Eq. (33) and boundary conditions (8) for the case in which the electron plasma frequency is described by formula (21). We integrate Eq. (33) over r in the vicinity of the point $r = r_p$ to obtain, instead of matching conditions (23), the conditions

$$\{E_z\}_{r_p} = 0, \quad \left\{\frac{\varepsilon_\perp}{\chi_\perp^2}\frac{dE_z}{dr}\right\}_{r_p} = 0.$$

Substituting solution (26) into these matching conditions yields the following dispersion relation for determining the eigenfrequencies of a plasma waveguide in a finite external magnetic field:

$$q_1\frac{\varepsilon_{\perp 1}}{\chi_{\perp 1}^2}\frac{I_1(q_1 r_p)}{I_0(q_1 r_p)} = q_2\frac{\varepsilon_{\perp 2}}{\chi_{\perp 2}^2}\frac{I_1(q_2 r_p)K_0(q_2 R) + K_1(q_2 r_p)I_0(q_2 R)}{I_0(q_2 r_p)K_0(q_2 R) - K_0(q_2 r_p)I_0(q_2 R)}, \qquad (34)$$

$$q_{1,2}^2 = \chi_{\perp 1,2}^2\frac{\varepsilon_{\parallel 1,2}}{\varepsilon_{\perp 1,2}}.$$

Recall that Eq. (34) is valid only for a weak external magnetic field such that the coupling between the E and H modes is unimportant.

Although, for $\Omega_e = 0$, Eq. (34) coincides exactly with dispersion relation (25), it has in addition some other, essentially different solutions. It is these solutions in which we are interested now. Since we are going to take the limit $\Omega_e \longrightarrow 0$, we assume that $\Omega_e < \omega, \omega_{pj}$, where ω_{pj} is any of the nonzero electron plasma frequencies of the plasma species of the piecewise constant plasma filling. For $\omega < k_z c$, the signs of the quantities

$$q_j^2 = \chi_{\perp j}^2\frac{\varepsilon_{\parallel j}}{\varepsilon_{\perp j}}$$

are determined by the signs of the ratios of the dielectric functions ($\chi_{\perp j}^2 > 0$):

$$S_j = \frac{\varepsilon_{\parallel j}}{\varepsilon_{\perp j}} = \frac{(\omega^2 - \omega_{pj}^2)(\omega^2 - \Omega_e^2)}{(\omega^2 - \Omega_e^2 - \omega_{pj}^2)\omega^2} \approx \frac{(\omega^2 - \omega_{pj}^2)}{(\omega^2 - \Omega_e^2 - \omega_{pj}^2)}. \qquad (35)$$

In the frequency range

$$\omega_{pj}^2 < \omega^2 < \omega_{pj}^2 + \Omega_e^2 \qquad (36)$$

we have $S_j < 0$, in which case the quantities q_j^2 change from zero to minus infinity. For $q_j^2 < 0$, the following relationships are satisfied: $I_l(q_j) = I_l(i|q_j|) = CJ_l(|q_j|)$ and $K_l(q_j) = K_l(i|q_j|) = CN_l(|q_j|)$, where C are complex constants and $J_l(x)$ and $N_l(x)$ are Bessel and Neumann functions. Consequently, in frequency range (36), solution (26) describes an internal wave.

For $\Omega_e \ll \omega, \omega_{pj}$, the inequalities $|\varepsilon_{\perp j}| < \Omega_e^2/\omega_{pj}^2 \ll 1$ hold in frequency range (36); therefore, dispersion relation (34) can be represented as

$$D_j(|q_j|) = C_j\varepsilon_{\perp j}, \quad j = 1, 2, \tag{37}$$

where the constants C_j are finite in frequency range (36) for any Ω_e value and the dispersion functions D_j are given by the formulas

$$D_j(|q_j|) = \begin{cases} J_0(|q_1|r_p), & j = 1, \\ J_0(|q_2|r_p)N_0(|q_2|R) - J_0(|q_2|R)N_0(|q_2|r_p), & \\ j = 2. & \end{cases} \tag{38}$$

In this case, it follows from dispersion relations (37) and (38) and solution (26) that, in the limit $\Omega_e \longrightarrow 0$, the boundary-value problem given by Eq. (33) and boundary conditions (8) for a waveguide in which the piecewise constant plasma filling is described by formulas (21) has the following eigenvalues and the corresponding eigenfunctions:

$$\omega = \omega_s = \omega_{p1} + \xi_s(\nu),$$

$$E_z(r) = E_s(r) = \begin{cases} J_0\left(\mu_{0s}\frac{r}{r_p}\right), & 0 \le r < r_p, \\ 0, & r_p < r < R, \end{cases} \tag{39a}$$

$$s = 1, 2, \ldots,$$

$$\omega = \omega_s = \omega_{p2} + \zeta_s(\nu),$$

$$E_z(r) = E_s(r)$$

$$= \begin{cases} 0, & 0 \le r < r_p, \\ J_0\left(\tilde{\mu}_{0s}\frac{r}{R}\right)N_0(\tilde{\mu}_{0s}) - N_0\left(\tilde{\mu}_{0s}\frac{r}{R}\right)J_0(\tilde{\mu}_{0s}), & \\ r_p < r < R, & \end{cases} \tag{39b}$$

$$s = 1, 2, \ldots.$$

Here, $\nu_j = \Omega_e^2/\omega_{pj}^2$, the functions $\xi_s(x)$ and $\zeta_s(x)$ approach zero as $x \longrightarrow 0$, μ_{0s} is the root of the equation $J_0(x) = 0$, $\tilde{\mu}_{0s}$ is the root of the equation $J_0(\lambda x)N_0(x) - N_0(\lambda x)J_0(x) = 0$, and $\lambda = r_p/R$. In a waveguide with a piecewise constant plasma filling, the structure of any other internal plasma wave (see relationships (19)) is analogous to that given by formulas (39). It follows from formulas (39) that, for $\Omega_e \longrightarrow 0$, all the eigenfrequencies are the same, $\omega_s = \omega_{pj}$, and there are an infinite number of different eigenfunctions corresponding to the same eigenfrequency. In this sense, it is possible to speak of an arbitrary transverse structure of the field of internal plasma waves in a plasma waveguide in a zero external magnetic field.

8. SOME DISTINCTIVE FEATURES OF THE SURFACE WAVES IN THE ABSENCE OF AN EXTERNAL MAGNETIC FIELD

We turn now to surface waves in a waveguide with a piecewise constant plasma filling (21) in a zero external magnetic field. In discussing the dispersion curves shown in Fig. 3a, we used formulas (31) and (32), which were obtained from exact dispersion relation (25) in the potential approximation, i.e., under condition (29). For the dispersion curves illustrated in Fig. 3a, inequality (29) fails to hold. Nevertheless, these two formulas provide a qualitatively correct description of the dispersion of the surface waves. However, in a waveguide with higher electron plasma frequencies ω_{pj} and with a larger radius R, the situation is qualitatively different, especially when a lower density plasma species in the waveguide is surrounded by a higher density plasma species, $\omega_{p2} > \omega_{p1}$. From Fig. 3a and formula (31), we can see that, in the limit $k_z \longrightarrow 0$, the frequency of the surface wave is equal to ω_{p2}. This is always true for $\omega_{p2} < \omega_{p1}$. However, for $\omega_{p2} > \omega_{p1}$ and under the inequality

$$\omega_{p2}^2 > \mu_{01}^2\frac{c^2}{R^2} + p(r_p)\omega_{p1}^2, \tag{40}$$

the frequency of the surface wave in the limit $k_z \longrightarrow 0$ is lower than ω_{p2}. Moreover, the dispersion of this wave in the long-wavelength range can become normal. In condition (40), we have used the positive parameter $p(r_p)$, which, usually, differs insignificantly from unity but cannot be calculated analytically in the general case. Inequality (40) indicates that the electron plasma frequency of a denser plasma species is higher than the cutoff frequency of an internal electromagnetic wave in a waveguide filled with a lower density plasma.

Figure 3b shows the dispersion curves of the surface and internal waves in a plasma waveguide in the absence of an external magnetic field. In the figure, the electron plasma frequencies are the same as those in Fig. 3a and the waveguide radii are somewhat larger, namely, $R = 2.2$ cm and $r_p = 1.1$ cm. For a plasma waveguide in which $\omega_{p1} = 5 \times 10^{10}$ rad/s and $\omega_{p2} = 0$, the dispersion curves of a surface and an internal wave are shown by the lower and the upper curves *1*, respectively. Curves *2* show the dispersion curves of the same waves for $\omega_{p1} = 5 \times 10^{10}$ rad/s and $\omega_{p2} = 2 \times 10^{10}$ rad/s. In both cases, we have $\omega_{p2} < \omega_{p1}$; hence, the dispersion curves in question are, on the whole, similar to the corresponding curves in Fig. 3a. For a waveguide in which $\omega_{p1} = 0$ and $\omega_{p2} = 5 \times 10^{10}$ rad/s, the dispersion curves of a surface and an internal wave are shown by the lower and the upper curves *3*, respectively. Curves *4* are the dispersion curves of the same waves for $\omega_{p1} = 2 \times$

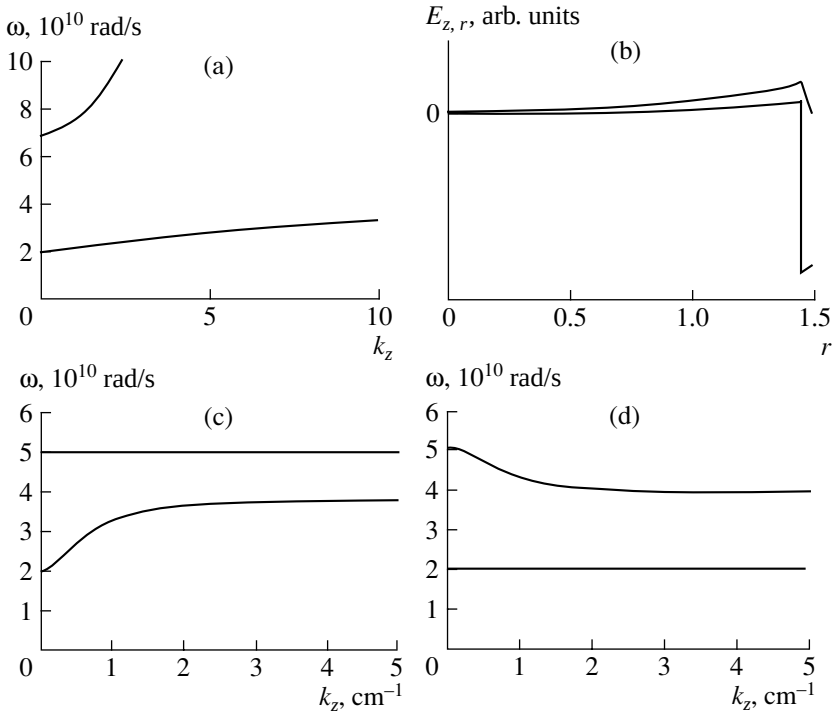

Fig. 4. Some particular cases of surface plasma waves in a zero external magnetic field: (a) the dispersion curve of a boundary surface wave (the lower curve), (b) the structure of the electric field components E_z (upper curve) and E_r (lower curve) in a boundary surface wave, and (c, d) the dispersion curves of the surface waves in a waveguide with two plasma species and with a vacuum axial region. In plot (c), the inner plasma species is denser than the outer plasma species; in plot (d), the converse situation is shown.

10^{10} rad/s and $\omega_{p2} = 5 \times 10^{10}$ rad/s. Since, in this case, the condition $\omega_{p2} > \omega_{p1}$ holds and inequality (40) is satisfied, the dispersion curves in question differ from the corresponding curves in Fig. 3a. Thus, as $k_z \longrightarrow 0$, the frequencies of the surface waves approach a frequency lower than the electron plasma frequency ω_{p2}. As for the cutoff frequencies of the electromagnetic waves, they, on the contrary, become exactly equal to ω_{p2} (on the scale adopted in Fig. 3b, the upper dispersion curves *3* and *4* for the electromagnetic waves coincide almost entirely with one another). For brevity, we do not present here a more detailed analysis of the coupling between electromagnetic and surface waves in the case in which inequality (40) is satisfied by a larger margin.

To conclude the analysis of a waveguide in which the piecewise constant plasma filling is given by formulas (21) and the external magnetic field is absent, we consider the following two particular cases. In the above discussion of dispersion relation (30) and its solution (31), we have introduced the notion of the boundary surface waves. Such waves, with the frequency $\omega \approx \omega_{p2}$, exist in a waveguide in which a plasma of small (and even infinitely small) thickness is adjacent to a metal wall. In order to give a clearer insight into the physical meaning of these waves and their structure, we consider numerical results obtained for a waveguide with the parameters $\omega_{p1} = 5 \times 10^{10}$ rad/s, $\omega_{p2} = 2 \times 10^{10}$ rad/s, $R = 1.5$ cm, and $r_p = 1.45$ cm. Figure 4a shows the dispersion curve of the boundary surface wave in such a waveguide, and Fig. 4b illustrates the structure of the electric field components $E_z(r)$ and $E_r(r)$ of this wave that were calculated at the point ($k_z = 2.1086$ cm^{-1}, $\omega = 2.1409 \times 10^{10}$ rad/s) of the dispersion curve. The shorter the distance from the interface between the two plasma species to the waveguide wall ($r_p \longrightarrow R$), the closer the dispersion curve to the straight line $\omega = \omega_{p2}$ and the narrower the plasma region near the wall, $r_p < r < R$, where the field is localized. Moreover, in the limit $r_p \longrightarrow R$, we have $|E_z(r)/E_r(r)|_{\max} \longrightarrow 0$. In this limit, the field distribution can be described by the relationships

$$E_z(r) = 0, \quad E_r(r) = \begin{cases} 0, & 0 < r < R - \delta \\ \infty, & R - \delta < r < R, \end{cases}$$
$$\delta \longrightarrow +0,$$

which clearly conveys the physical meaning of the boundary surface wave.

Also, in discussing dispersion relation (30), we have pointed out the fact that it is not symmetric in the two electron plasma frequencies and, in particular, that for $k_z \approx 0$ it has no solutions describing waves with the frequency $\omega \approx \omega_{p1}$ (recall that the electron plasma frequencies are numbered in accordance with formulas (21)).

As was mentioned above, the reason for this is that, in cylindrical geometry, the point $r = 0$ is a singular point. If we assume that there is no plasma at the waveguide axis, then we arrive at new solutions describing new surface waves. Figures 4c and 4d show dispersion curves for two waveguides with the same radii $R = 1.5$ cm and $r_p = 0.75$ cm but with different piecewise constant plasma fillings: $\omega_{p1} = 5 \times 10^{10}$ rad/s and $\omega_{p2} = 2 \times 10^{10}$ rad/s (Fig. 4c) and $\omega_{p1} = 2 \times 10^{10}$ rad/s and $\omega_{p2} = 5 \times 10^{10}$ rad/s (Fig. 4d). The inner plasma species occupies the region $r \in [r_1, r_p]$, where $r_1 = 0.1$ cm; i.e., there is a vacuum axial region in the waveguide. We can see that, although the radius of the vacuum region is small, new branches arise in the frequency spectra, namely, the branch $\omega \approx \omega_{p1} = 5 \times 10^{10}$ rad/s in Fig. 4c and the branch $\omega \approx \omega_{p1} = 2 \times 10^{10}$ rad/s in Fig. 4d. Cylindrical waveguides possess the following fundamental property: in the long-wavelength range, there can never be branches $\omega \approx \omega_p(r = 0)$, where $\omega_p(r = 0)$ is the electron plasma frequency at the waveguide axis. If this frequency is equal to zero, then, in the long-wavelength limit, there are no waves with frequencies $\omega \longrightarrow 0$. We emphasize that these conclusions do not refer to waveguides in a strong external magnetic field.

9. WAVEGUIDE WITH A THREE-STEP PLASMA FILLING

We turn now to the investigation of a waveguide with a three-step plasma filling—a case that is more complicated than the previous one but is more important from a practical point of view. Specifically, we assume that the function $\omega_p(r)$ is given by the relationships

$$\omega_p(r) = \begin{cases} \omega_{p0} = \text{const}_0, & 0 < r < r_1, \\ \omega_{p1} = \text{const}_1, & r_1 < r < r_2, \\ \omega_{p2} = \text{const}_2, & r_2 < r < R. \end{cases} \quad (41)$$

We focus primarily on a waveguide in a zero external magnetic field. We solve Eq. (6) for adjacent waveguide regions filled with different plasma species and match the solutions at the surfaces $r_{1,2}$ with the help of conditions (23) to obtain the following dispersion relation:

$$\begin{aligned} &\frac{Q_2 I_0(\chi_1 r_2) - Q_1 I_1(\chi_1 r_2)}{Q_0 I_0(\chi_1 r_1) - Q_1 I_1(\chi_1 r_1)} \\ &= \frac{Q_2 K_0(\chi_1 r_2) + Q_1 K_1(\chi_1 r_2)}{Q_0 K_0(\chi_1 r_1) + Q_1 K_1(\chi_1 r_1)}, \\ &Q_0 = \frac{\varepsilon_0}{\chi_0}\frac{I_1(\chi_0 r_1)}{I_0(\chi_0 r_1)}, \quad Q_1 = \frac{\varepsilon_1}{\chi_1}, \\ &Q_2 = \frac{\varepsilon_2}{\chi_2}\frac{I_1(\chi_2 r_2)K_0(\chi_2 R) + I_0(\chi_2 R)K_1(\chi_2 r_2)}{I_0(\chi_2 r_2)K_0(\chi_2 R) - I_0(\chi_2 R)K_0(\chi_2 r_2)}, \end{aligned} \quad (42)$$

$$\varepsilon_j = 1 - \frac{\omega_{pj}^2}{\omega^2}, \quad \chi_j^2 = k_z^2 - \frac{\omega^2}{c^2}\varepsilon_j, \quad j = 0, 1, 2.$$

In the limit $k_z \longrightarrow \infty$, dispersion relation (42) transforms into the relation

$$\begin{aligned} &(\varepsilon_0 + \varepsilon_1)(\varepsilon_1 + \varepsilon_2) \\ &= -(\varepsilon_1 - \varepsilon_0)(\varepsilon_2 - \varepsilon_1)\exp(-2k_z(r_2 - r_1)). \end{aligned} \quad (43)$$

For $r_2 \neq r_1$, this dispersion relation has the solutions

$$\omega = \sqrt{\frac{\omega_{p0}^2 + \omega_{p1}^2}{2}}, \quad \omega = \sqrt{\frac{\omega_{p1}^2 + \omega_{p2}^2}{2}}, \quad (44)$$

which are analogous to solution (28) and stem from the interaction between neighboring plasma species. For $r_2 - r_1 \longrightarrow 0$, dispersion relation (43) yields other eigenfrequencies:

$$\omega = \sqrt{\frac{\omega_{p0}^2 + \omega_{p2}^2}{2}}, \quad \omega = \omega_{p1}. \quad (45)$$

The first of relations (45) is analogous to relation (44). The second is an analogue of the dispersion relation for a boundary surface wave. Note that this second relation is valid over the entire wavenumber range such that $k_z(r_2 - r_1) \ll 1$.

Figure 5 illustrates the results of solving dispersion relation (42) numerically for $R = 3$ cm, $r_1 = 1$ cm, and $r_2 = 2$ cm. The figure shows the dispersion curves of only two surface waves that, in the case at hand, occur at the two interfaces between three different plasma species. The three electron plasma frequencies were taken to be 0, 2×10^{10}, and 5×10^{10} rad/s, and all their possible combinations were considered. The triples of the values of the electron plasma frequencies (in units of 10^{10} rad/s) arranged in order of increasing distance from the waveguide axis are presented at the top of each frame of Fig. 5. Figure 6 presents the dispersion curves of surface waves in the same waveguide but with electron plasma frequencies that differ somewhat from those in Fig. 5, namely, 1×10^{10}, 3×10^{10}, and 5×10^{10} rad/s. Figures 5 and 6 clearly demonstrate all the above regular features of the behavior of solutions to the problem given by Eq. (6) and boundary conditions (8) in the case of a piecewise constant function $\omega_p(r)$.

We again stress the following fundamental property of the spectra of surface waves in a waveguide with a piecewise constant plasma filling in a zero external magnetic field: in the long-wavelength limit $k_z \longrightarrow 0$, there are no branches corresponding to waves whose frequency is equal to the electron plasma frequency at the waveguide axis. This property, which is fully confirmed by Figs. 5 and 6, holds not only for waveguides in the absence of an external magnetic field but also for waveguides in a weak external magnetic field. An anal-

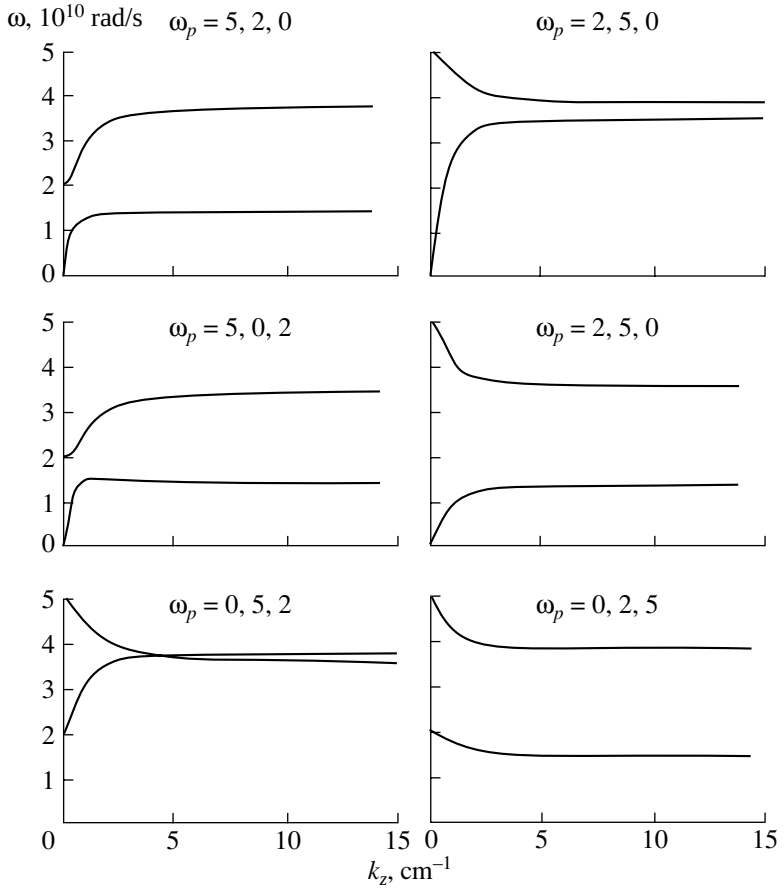

Fig. 5. Dispersion curves of the surface waves in a waveguide with two plasma species and with a vacuum axial region in a zero external magnetic field (ω_p is given in units of 10^{10} rad/s).

ysis shows that the external magnetic field can be regarded as sufficiently weak under the inequality (see conditions (13))

$$\Omega_e < \omega_{\min}. \tag{46}$$

In this case, the surface plasma waves generally possess the same features as those in a zero external magnetic field. Under the inequality

$$\Omega_e > \omega_{\max}, \tag{47}$$

the external magnetic field is strong and slow waves in a plasma waveguide are fully analogous to waves in a plasma waveguide in an infinitely strong external magnetic field.

Function (41) models a so-called annular plasma filling, which is important for experimental investigations. Let us consider two more examples of waveguides with annular plasma filling that are frequently used in experiments. Figure 7 illustrates the results calculated numerically for a plasma waveguide with the parameters $R = 3$ cm, $r_1 = 1$ cm, $r_2 = 2$ cm, $\omega_{p0} = \omega_{p2} = 0$, and $\omega_{p1} = 5 \times 10^{10}$ rad/s in a zero external magnetic field. The dashed lines show the dispersion curves of surface waves in the absence of the plasma background, $\omega_{p0} = \omega_{p2} = 0$, and the solid lines show those of the same surface waves in the case of a uniform plasma background, $\omega_{p0} = \omega_{p2} = 10^{10}$ rad/s. The presence of the plasma background is seen to seriously affect the structure of the spectrum: there is no surface wave in the low-frequency range. Note that the results illustrated in Fig. 7 do not contradict the fact that, in the limit $k_z \longrightarrow 0$, the frequency spectrum does not contain a branch corresponding to a wave whose frequency is equal to the electron plasma frequency at the waveguide axis. For the case to which Fig. 7 refers, we have $\omega_{p0} = \omega_{p2}$, and, in the long-wavelength limit $k_z \longrightarrow 0$, a wave with the electron plasma frequency near the waveguide wall (in Fig. 7, this frequency is ω_{p2}) is inevitably present in the spectrum.

In a waveguide in an infinitely strong external magnetic field, the presence of the background plasma affects the spectra of slow waves in another way: additional branches corresponding to internal waves with a frequency $\omega < \omega_{p0} = \omega_{p2}$ appear in the low-frequency range (as is the case in Fig. 2). The effect of the background plasma on the frequency spectra in a plasma waveguide in a strong external magnetic field was investigated in detail in [9].

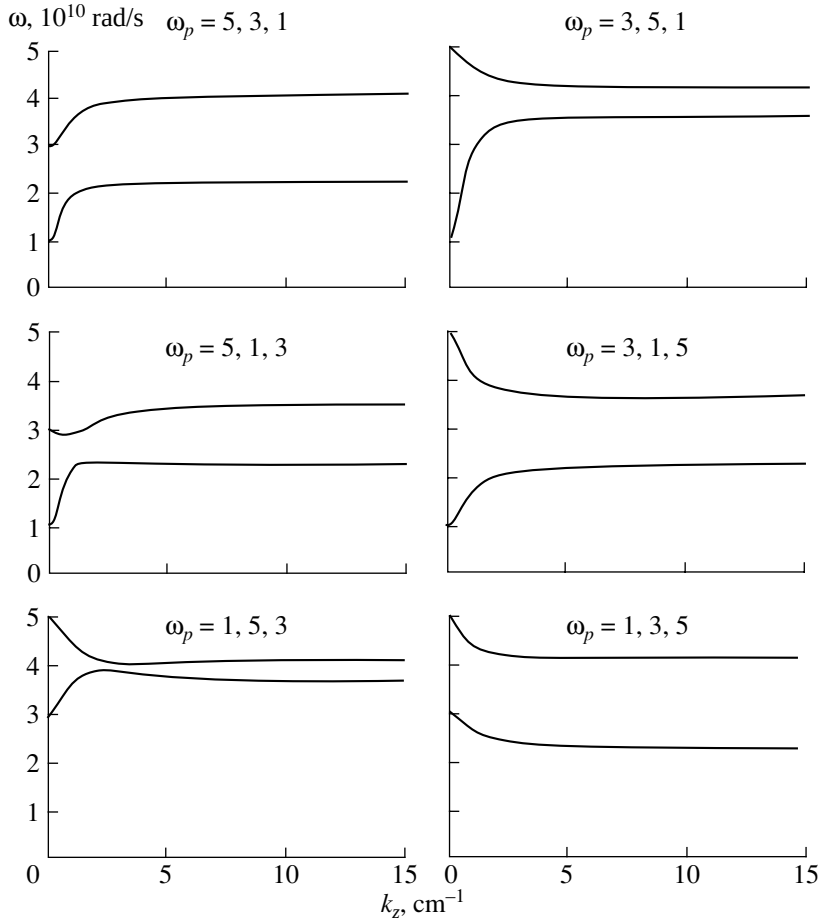

Fig. 6. Dispersion curves of the surface waves in a waveguide with a three-step plasma density profile in a zero external magnetic field for different combinations of the densities of neighboring plasmas (ω_p is given in units of 10^{10} rad/s).

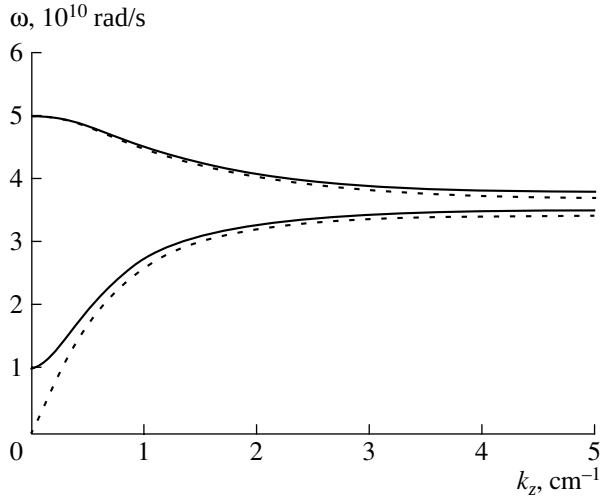

Fig. 7. Characteristic dispersion curves of the surface waves in a waveguide with an annular plasma filling in a zero external magnetic field. The dispersion curves in the absence of the plasma background are shown by the dashed lines, and those for a uniform plasma background are shown by the solid lines.

10. PLASMA FILLING WITH SMOOTH PLASMA BOUNDARIES

When the plasma boundaries in the waveguide are not sharp, slow plasma waves have far more complicated properties, especially in a weak external magnetic field. The waves in such a plasma were considered in our earlier paper [5]. Above, we have already mentioned these waves in discussing formulas (16)–(18) and solution (20). Now, we are going to investigate these waves in more detail: a task that is of considerable physical interest and of great importance in solving problems of microwave electronics [8, 10].

We begin with a model problem that has an analytic solution and permits a simple limiting transition to the case of a plasma with a sharp boundary. We go over to plane waveguide geometry (i.e., switch from the coordinate r to the coordinate x) and restrict ourselves to the potential approximation ($c \longrightarrow \infty$). We assume that the external magnetic field is absent and that the plasma

distribution over the region $x \in (-\infty, +\infty)$ is given by the formulas

$$\omega_p^2(x) = \begin{cases} \omega_p^2 = \text{const}, & x < -L \\ (\omega_p^2/2)(1 - x/L), & -L \le x \le L \\ 0, & x > L. \end{cases} \quad (48)$$

A limiting transition to the case of a plasma with a sharp boundary is obvious: it is necessary to reduce L in formulas (48) to zero. For convenience, we nondimensionalize the coordinate and introduce the following notation:

$$\xi = \frac{x}{L}, \quad \kappa = k_z L, \quad \alpha = \frac{\omega_p^2 - 2\omega^2}{\omega_p^2}. \quad (49)$$

In the region of constant plasma density, the electric field component E_z satisfies the equation

$$\frac{d^2 E_z}{d\xi^2} - \kappa^2 E_z = 0, \quad \xi < -1, \quad \xi > 1. \quad (50)$$

In the region where the plasma density varies, the corresponding equation has the form

$$\frac{d}{d\xi}\left((\xi - \alpha)\frac{dE_z}{d\xi}\right) - \kappa^2(\xi - \alpha)E_z = 0, \quad -1 \le \xi \le 1. \quad (51)$$

The solutions to Eq. (50) that are bounded at infinity are given by the formulas

$$E_z(\xi) = \begin{cases} A\exp(-\kappa\xi), & \xi > 1 \\ B\exp(\kappa\xi), & \xi < -1, \end{cases} \quad (52)$$

where A and B are constants. The solutions to Eq. (51) are expressed in terms of the modified Bessel functions I_0 and K_0 of the argument $z = \kappa(\xi - \alpha)$:

$$E_z(\xi) = CI_0(\kappa(\xi - \alpha)) + DK_0(\kappa(\xi - \alpha)). \quad (53)$$

In discussing formula (18), in which the field component in question diverges logarithmically, we have pointed out that the frequency ω should be regarded as complex. Consequently, the argument in solution (53) is also complex: $z = x + iy$. For small absolute values of the complex argument, the function K_0 has a logarithmic singularity [11],

$$K_0(z) = -\ln(z)I_0(z) + \ldots = -(\ln\sqrt{x^2 + y^2} + i\arctan(y/x))I_0(z) + \ldots, \quad z = x + iy, \quad (54)$$

while the function I_0 has no singularity. At a certain point of the interval $-1 < \xi < 1$ on the real axis ξ, we have $x = 0$ ($\xi = \mathrm{Re}\,\alpha$) and $y \neq 0$. In this case, in moving along the real axis from the point $\xi = 1$ to the point $\xi = -1$, the arctangent function in formula (54) changes by $\pm\pi$, depending on the sign of y. Consequently, if solution (53) is used near the boundary $\xi = 1$, then the solution near the boundary $\xi = -1$ should be written as

$$E_z(\xi) = CI_0(\kappa(\alpha - \xi)) + DK_0(\kappa(\alpha - \xi)) \pm i\pi DI_0(\kappa(\alpha - \xi)). \quad (55)$$

We insert solutions (52), (53), and (55) into the matching conditions,

$$\{E_z(\xi = \pm 1)\} = 0, \quad \left\{\frac{dE_z}{d\xi}(\xi = \pm 1)\right\} = 0 \quad (56)$$

and eliminate the constants A, B, C, and D to obtain the following dispersion relation for determining the complex frequencies ω:

$$\frac{I_0[\kappa(1-\alpha)] + I_1[\kappa(1-\alpha)]}{I_0[\kappa(1+\alpha)] + I_1[\kappa(1+\alpha)]} = \frac{K_0[\kappa(1-\alpha)] - K_1[\kappa(1-\alpha)]}{K_0[\kappa(1+\alpha)] - K_1[\kappa(1+\alpha)] \pm i\pi\{I_0[\kappa(1+\alpha)] + I_1[\kappa(1+\alpha)]\}}. \quad (57)$$

Note that the last two of conditions (56) imply that the normal components of the electric induction vector should be continuous; this follows from the continuity of the plasma dielectric function $\varepsilon_\perp(x)$ at $\xi = \pm 1$, the plasma distribution being given by formulas (48). Note also that dispersion relation (57) can be derived only from solution (53); in this case, however, it is necessary to use the following familiar formulas of the theory of analytic continuation [11]:

$$I_\nu(e^{im\pi}z) = e^{i\nu m\pi}I_\nu(z), \quad K_\nu(e^{im\pi}z) = e^{-i\nu m\pi}K_\nu(z) - i\pi\frac{\sin\nu m\pi}{\sin\nu\pi}I_\nu(z). \quad (58)$$

In the long-wavelength limit

$$|\kappa| = |k_z|L \ll 1, \quad (59)$$

dispersion relation (57) transforms to

$$\frac{1}{1+\alpha} \mp i\pi\kappa = \frac{1}{1-\alpha}. \quad (60)$$

Taking into account inequality (59) and using the expression for α (see formulas (49)), we obtain from dispersion relation (60) the sought-for expression for the complex frequency:

$$\omega = \frac{\omega_p}{\sqrt{2}}\left(1 - i\frac{\pi}{4}|k_z|L\right). \quad (61)$$

For $L = 0$ (i.e., for a sharp plasma boundary), formula (61) determines the well-known frequency of a surface wave at the boundary of a plasma half-space. The surface wave also exists in the case of a smooth plasma boundary ($L \neq 0$); moreover, under condition (59), it is damped only weakly. Presumably, this damping is caused by the conversion of the surface wave into local internal waves (see solution (20)) at the plasma resonance point $\omega = \omega_p(x)$.

In long-wavelength limit (59), the surface waves can be investigated analytically not only for a plasma density distribution given by formulas (48) but in a more general case as well. Let the transverse dielectric function $\varepsilon(x)$ of the plasma be continuous and constant at $x < x_1$ ($\varepsilon = \varepsilon_1$) and at $x > x_2$ ($\varepsilon = \varepsilon_2$). When integrating the equation (see Eq. (15))

$$\frac{d^2E_z}{dx^2} + \frac{d\ln\varepsilon}{dx}\frac{dE_z}{dx} - k_z^2E_z = 0 \qquad (62)$$

over the region $x \in [x_1, x_2]$ in the long-wavelength limit $|k_z(x_2 - x_1)| \ll 1$, we can ignore the term $k_z^2E_z$. As a result, we obtain the following general solution (see formulas (16), (17)):

$$E_z = \begin{cases} A\exp(-k_zx), & x > x_2 \\ C + D\int\limits_{x_1}^{x}\dfrac{dx'}{\varepsilon(x')}, & x_1 \le x \le x_2. \\ B\exp(k_zx), & x < x_1. \end{cases} \qquad (63)$$

We match functions (63) in a conventional manner and eliminate the constants A, B, C, and D to arrive at the dispersion relation

$$\frac{1}{\varepsilon_1} + \frac{1}{\varepsilon_2} = -k_z\int\limits_{x_1}^{x_2}\frac{dx}{\varepsilon(x)} = -k_zVp\int\limits_{x_1}^{x_2}\frac{dx}{\varepsilon(x)} - i\pi\left|k_z\left(\frac{d\varepsilon}{dx}\right)^{-1}_{x_0}\right|, \qquad (64)$$

where the symbol Vp denotes the principal value of the integral and x_0 is a point at which $\varepsilon(x) = 0$. Dispersion relation (64) and formulas (48) immediately yield relation (61).

It follows from formulas (52) that the quantity $\lambda \sim k_z^{-1}$ determines the characteristic transverse spatial scale on which the surface wave is localized. Therefore, inequality (59) implies that the scale on which the plasma density varies is short in comparison to the transverse scale on which the wave field is localized, $L \ll \lambda$. However, this is obviously a natural condition for the existence of a surface wave. When inequality (59) fails to hold, the surface wave ceases to exist, or, more precisely, it degenerates into an internal wave whose field is localized just in the region where the plasma is inhomogeneous. When the inequality opposite to inequality (59) is satisfied, dispersion relation (57) reduces to

$$W\exp(W) = z, \quad z = \pm\frac{1}{2}i, \quad W = 2\kappa(1-\alpha). \qquad (65)$$

The function $W(z)$ defined by this dispersion relation is known as the Lambert function, which was thoroughly investigated and tabulated [12]. Dispersion relation (65) yields the following expression for the frequency of the wave that is damped at the slowest rate:

$$\omega = \frac{\omega_p}{2\sqrt{|k_z|L}}(0.54 - 0.36i). \qquad (66)$$

This expression implies that $|\omega| \ll \omega_p$ and that the imaginary part of the frequency is on the order of its real part. Since the inequality opposite to inequality (59) is satisfied, the wave field is localized in the region where the plasma is inhomogeneous (as if there were metal walls at $x = \pm L$). Such strongly damped internal (unnatural) oscillations of an inhomogeneous plasma were studied in [13, 14].

In the long-wavelength limit, the damping of surface waves by plasma density variations is weak. This indicates that, in deriving the dispersion relations $\omega = \omega(k_z)$, the damping can be ignored to a first approximation. On the other hand, by taking into account weak damping, it is possible to eliminate divergences in the components of the electric field of surface waves (see formulas (17) and (18)) and, thereby, to overcome difficulties in numerically solving the boundary-value problem given by Eq. (6) and boundary conditions (8) for a smooth plasma density profile in a waveguide. The difficulties in carrying out integration were overcome in the following way: First, Eqs. (4) were solved over the interval from zero to $r^* - h/2$, where $\varepsilon_\perp(r^*) = 0$ and h is the mesh spacing of the difference grid. Second, the same equations were solved in the interval from $r^* + h/2$ to R. The equations were integrated under the assumptions $E_z(r^* + h/2) = E_z(r^* - h/2)$ and $B_\varphi(r^* + h/2) = B_\varphi(r^* - h/2)$; this is equivalent to the integration over the vicinity of the singular point r^* in terms of the Cauchy principal value. Recall that, in the case of a strong external magnetic field, numerical solution of the boundary-value problem given by Eq. (5) and boundary conditions (8) presents no difficulty. In conclusion, we consider the results of numerical calculation of the frequency spectra of waves in a waveguide with a thin-walled annular plasma—an important issue in plasma microwave electronics.

Figure 8 shows the profiles of the function $\omega_p(r)$ for which the calculations were carried out. We investigated four plasma density profiles: a step profile in the absence of the plasma background (Fig. 8a), a Gaussian profile in the absence of the plasma background (Fig. 8b), a step profile in the presence of the plasma background (Fig. 8c), and a Gaussian profile in the presence of the plasma background (Fig. 8d). In all four

cases, the waveguide radius was $R = 2.05$ cm, the mean radius of a thin-walled annular plasma was $r_p = 1.05$ cm, and the maximum electron plasma frequency (see conditions (13)) was $\omega_{max} = 22 \times 10^{10}$ rad/s. In the case of a step profile, the plasma thickness was $\Delta_p = 0.1$ cm, the maximum electron plasma frequency in the presence of the plasma background being $\omega_{min} = 6.96 \times 10^{10}$ rad/s. The Gaussian profile $\omega_p^2(r) = \omega_{max}^2 \exp(-(r - r_p)^2/\delta_p^2)$ was chosen ($\delta_p = 0.0564$ cm) so that the line density of a thin-walled annular plasma was the same in all the cases under analysis. For the profiles chosen, long-wavelength limit (59) implies that $\delta_p k_z \sim \Delta_p k_z \ll 1$; it is this inequality that is satisfied over almost the entire wavenumber range $k_z < \omega_{max}/c$, which is important for plasma microwave electronics. Note that the cases of a step plasma density profile (Figs. 8a, 8c) can be investigated analytically by the method of dispersion relations (see Section 9, Eq. (42)). Here, we present only the results of numerical solution in finite differences of the boundary-value problem given by Eq. (5) and boundary conditions (8) and that given by Eq. (6) and the same boundary conditions. A comparison of numerical results with the solutions to the dispersion relations (in the cases of a step plasma density profile) confirms the efficiency and reliability of numerical methods used in our simulations. The parameters of the plasma waveguides (such as the waveguide radii, the electron plasma frequencies, and the plasma thicknesses) that were chosen for simulations correspond to those in actual physical experiments [15].

Figure 9 depicts the dispersion curves for a waveguide free of the plasma background. In the figure, the dispersion curves of the slow plasma waves and of the E- and H-type fast electromagnetic waves are shown. The straight line emanating from the origin of the coordinates is the light line $\omega = k_z c$. Figures 9a and 9c were calculated for an infinitely strong external magnetic field and for a step and a Gaussian plasma density profile, respectively. It can be seen that the dispersion curves in the figures are essentially identical. In other words, in the case of a strong external magnetic field, the dispersion curves are insensitive to the shape of the plasma density profile. This conclusion stems from the internal nature of the wave field within the plasma and is valid only for thin-walled annular plasma columns with the same line densities.

Figures 9b and 9d display the dispersion curves calculated for a zero external magnetic field and for a step and a Gaussian plasma density profile, respectively. In both figures, the lower curves, which are the dispersion curves of a low-frequency slow plasma wave, are seen to have essentially the same shape. This indicates that the dispersion of such waves is insensitive to the shape of the plasma density profile, in agreement with dispersion relation (61), which was obtained in the long-wavelength limit. It is of course necessary to take into account that formula (61) was derived in the potential approximation for a plasma half-space rather than for a waveguide plasma. Moreover, the lower curves in Figs. 9b and 9d are identical to the corresponding curves in Figs. 9a and 9c. This indicates that the dispersion of a long-wavelength low-frequency slow plasma wave in a waveguide with a thin-walled annular plasma is independent of the strength of the external magnetic field [16].

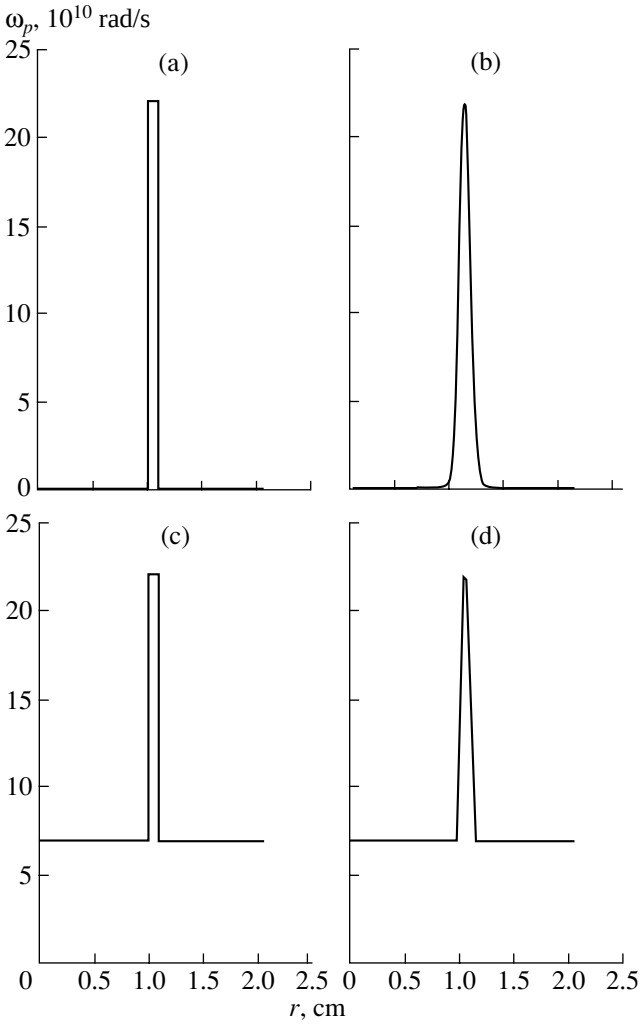

Fig. 8. Density profiles of a thin-walled annular plasma for which the simulations were performed: (a) a step profile in the absence of the plasma background, (b) a Gaussian profile in the absence of the plasma background, (c) a step profile in the presence of the plasma background, and (d) a Gaussian profile in the presence of the plasma background.

In Fig. 9b, we can also see the dispersion curve of a high-frequency slow plasma wave (the upper curve). For small k_z values, this curve describes an electromagnetic wave ($\omega/k_z > c$). As k_z increases, the wave becomes slower and, as $k_z \longrightarrow \infty$, its frequency approaches $\omega_p/\sqrt{2}$, the wave dispersion being anomalous. Waves of this type have been discussed in detail in Section 9. In order for the two surface plasma waves—

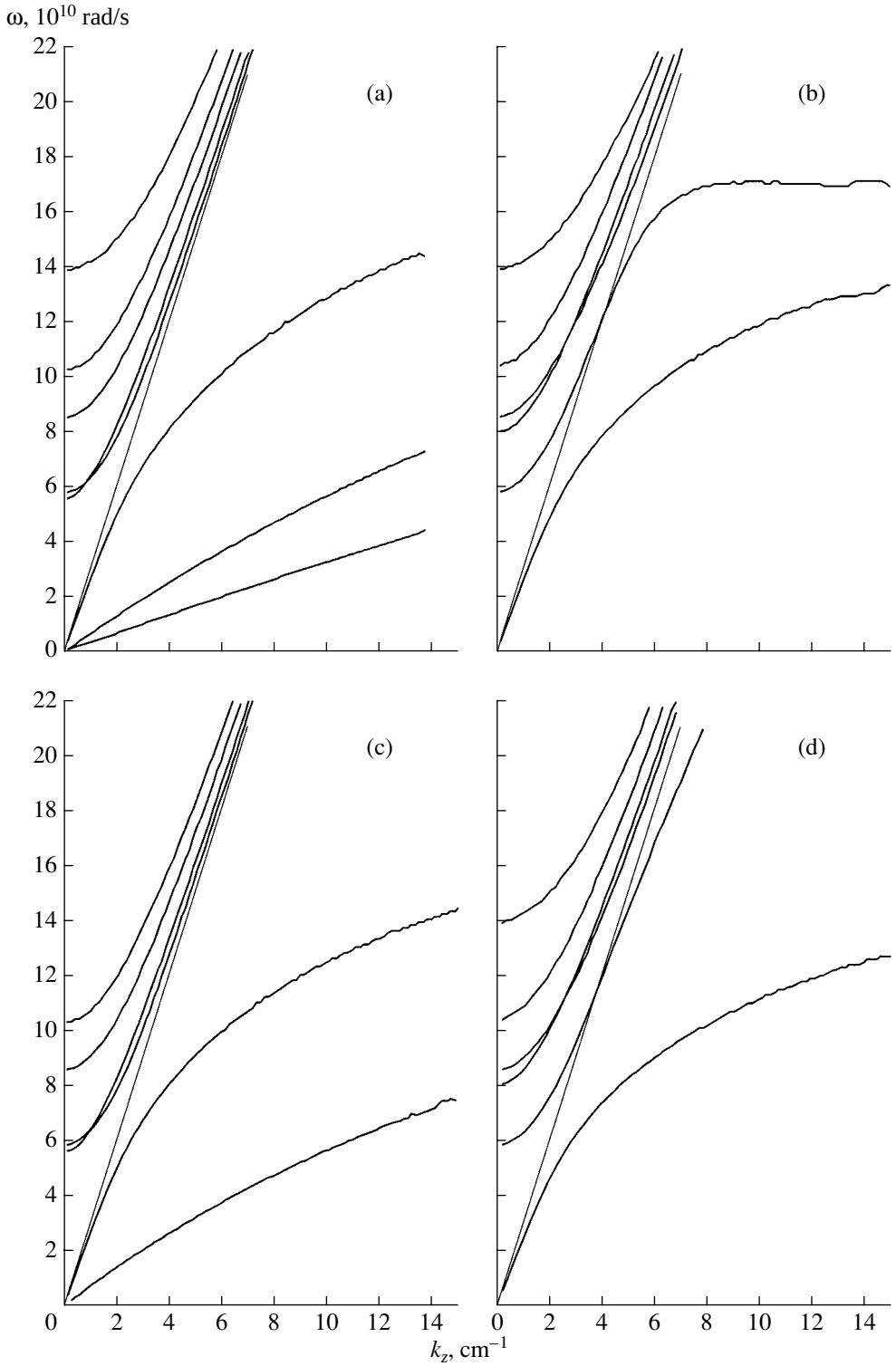

Fig. 9. Dispersion curves of the waves in a waveguide with (a, b) a steplike and (c, d) a Gaussian annular plasma in (a, c) an infinitely strong and (b, d) an infinitely weak external magnetic field in the absence of the background plasma.

low-frequency and high-frequency—to exist simultaneously, the plasma in the waveguide should have two free surfaces (boundaries). In particular, for a high-frequency plasma wave, it is of fundamental importance that there be the inner boundary $r = r_p - \Delta_p/2$. In Fig. 9d, there is no dispersion curve of a high-frequency slow plasma wave. More precisely, the long-wavelength electromagnetic branch of this dispersion curve is

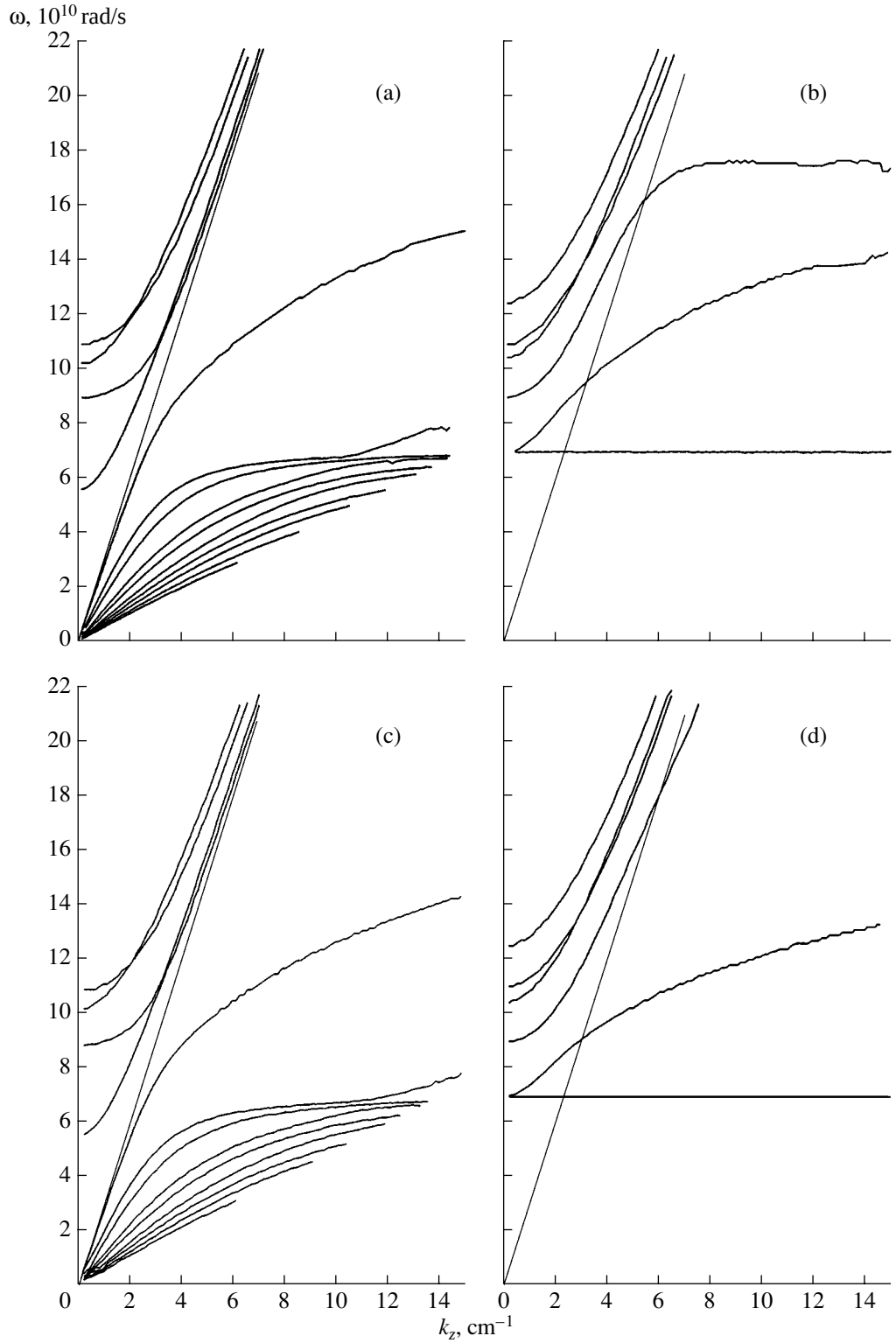

Fig. 10. Dispersion curves of the waves in a waveguide with (a, b) a steplike and (c, d) a Gaussian annular plasma in (a, c) an infinitely strong and (b, d) an infinitely weak external magnetic field in the presence of the background plasma.

present, but there is no indication that the wave is slowed and its dispersion becomes anomalous. Hence, in a plasma with a Gaussian density profile, a high-frequency slow plasma wave cannot exist. The reason is that such a wave is generated by opposite electric charges induced on the boundaries of the annular

plasma column [16]. Moreover, the penetration depth of the wave field into the plasma should exceed the transverse size of the region where the surface charges are localized. In the case of a step plasma density profile, the surface charges are localized in an infinitely thin region. For a Gaussian profile, this is not the case in the long-wavelength range, while short-wavelength plasma waves should be considered with allowance for their strong damping.

The dispersion curves for a waveguide with a thin-walled annular plasma and a background plasma are shown in Fig. 10, which demonstrates the same regular features of the frequency spectrum as those in the previous figure. A new feature is the appearance of internal waves in the plasma background in a strong external magnetic field (see Figs. 10a, 10c, and also Fig. 2) and the disappearance of a low-frequency slow plasma wave with a frequency $\omega < \omega_{min}$ in a zero external magnetic field (see Figs. 10b, 10d, and also Figs. 3, 6).

In our opinion, it is of interest to investigate, in both its theoretical and practical respects, the problem of how the dispersion of waves in a plasma waveguide is influenced by the shape of the plasma density profile. For a waveguide filled entirely with a plasma, this problem was investigated in [5] (see also [8]). A much more complicated case of an annular plasma requires a separate study. Note that in this case the Gaussian plasma density profile is not optimal in the sense that it does not permit a limiting transition to a step profile. In subsequent papers, we will continue our work on the effect of the shape of the plasma density profile on the dispersion properties of plasma waveguides, including those in a finite external magnetic field.

ACKNOWLEDGMENTS

We are grateful to A.V. Timofeev and A.V. Zvonkov, who proposed to write the final section of this paper, and to I.N. Kartashov for his help in carrying out numerical simulations. This study was supported in part by the RF Ministry of Education (project no. E02-3.2-447); the RF Ministry of Industry, Science, and Technologies (project no. NSh-1962.2003.2); and the program Universities of Russia (project no. UR.01.03.073).

REFERENCES

1. A. F. Alexandrov, L. S. Bogdankevich, and A. A. Rukhadze, *Principles of Plasma Electrodynamics* (Vysshaya Shkola, Moscow, 1978; Springer-Verlag, Berlin, 1984).
2. V. S. Vladimirov, *Equations of Mathematical Physics* (Nauka, Moscow, 1971; Dekker, New York, 1971).
3. A. N. Tikhonov and A. A. Samarskii, *Equations of Mathematical Physics* (Nauka, Moscow, 1972; Pergamon Press, Oxford, 1964).
4. Yu. N. Dnestrovskij, D. P. Kostomarov, G. P. Pereverzev, and A. V. Pogosyan, Fiz. Plazmy **1**, 623 (1975) [Sov. J. Plasma Phys. **1**, 344 (1975)].
5. M. V. Kuzelev, R. V. Romanov, and A. A. Rukhadze, Fiz. Plazmy **27**, 260 (2001) [Plasma Phys. Rep. **27**, 243 (2001)].
6. A. S. Il'inskiĭ, V. V. Kravtsov, and A. G. Sveshnikov, *Mathematical Models in Electrodynamics* (Vysshaya Shkola, Moscow, 1991).
7. V. V. Nikol'skiĭ and T. I. Nikol'skaya, *Electrodynamics and Wave Propagation* (Nauka, Moscow, 1989).
8. M. V. Kuzelev, A. A. Rukhadze, and P. S. Strelkov, *Plasma Relativistic Microwave Electronics* (MGTU im. N.É. Baumana, Moscow, 2002).
9. M. V. Kuzelev and A. A. Rukhadze, Fiz. Plazmy **25**, 471 (1999) [Plasma Phys. Rep. **25**, 426 (1999)].
10. M. V. Kuzelev and A. A. Rukhadze, Fiz. Plazmy **26**, 250 (2000) [Plasma Phys. Rep. **26**, 231 (2000)].
11. *Handbook of Mathematical Functions*, Ed. by M. Abramowitz and I. A. Stegun (Dover, New York, 1965; Nauka, Moscow, 1979).
12. A. E. Dubinov, I. D. Dubinova, and S. K. Saĭkov, *Lambert W Function* (SarFTI, Sarov, 2004).
13. A. V. Timofeev, in *Reviews of Plasma Physics*, Ed. by M. A. Leontovich (Atomizdat, Moscow, 1979; Consultants Bureau, New York, 1986), Vol. 9.
14. V. A. Mazur, A. B. Mikhailovskiĭ, A. L. Frenkel', and I. G. Shukhman, in *Reviews of Plasma Physics*, Ed. by M. A. Leontovich (Atomizdat, Moscow, 1979; Consultants Bureau, New York, 1986), Vol. 9.
15. M. V. Kuzelev, O. T. Loza, A. A. Rukhadze, *et al.*, Fiz. Plazmy **27**, 710 (2001) [Plasma Phys. Rep. **27**, 669 (2001)].
16. M. V. Kuzelev, Fiz. Plazmy **28**, 544 (2002) [Plasma Phys. Rep. **28**, 501 (2002)].

Translated by I.A. Kalabalyk

Plasma Physics Reports, Vol. 31, No. 2, 2005, pp. 167–177. Translated from Fizika Plazmy, Vol. 31, No. 2, 2005, pp. 192–202.

PLASMA DYNAMICS

Studies of the Structure and Dynamics of the Radiating Plasma of a Micropinch Discharge

A. N. Dolgov, V. K. Lyapidevskiĭ, D. E. Prokhorovich, A. S. Savelov, and G. Kh. Salakhutdinov

Moscow Engineering Physics Institute (State University), Kashirskoe sh. 31, Moscow, 115409 Russia

Received May 16, 2003; in final form, March 17, 2004

Abstract—Space-resolved X-ray spectra and electron emission spectra from a micropinch discharge are measured with the help of tracking detectors. Results from measurements of the discharge optical emission with a high temporal and spatial resolution are also presented. © *2005 Pleiades Publishing, Inc.*

In this paper, we present the results from experimental studies of micropinch discharges by untraditional diagnostic methods. The experiments were carried out in a low-inductance vacuum spark (LIVS) facility (the parameters and design of the facility are described in [1]) at discharge currents of up to 150 kA. The working medium was iron plasma.

The most widespread method for determining the spectrum of X-ray emission is to measure the extinction curve [2]. The determination of the emission spectrum from the extinction curve is a rather complicated problem and, in some cases, requires prior information about the spectrum. In the present study, X-ray spectra were measured with the help of nuclear photoemulsions that allowed us to detect X-ray photons from the tracks of secondary electrons. This method ensures much higher accuracy than the extinction curve method; moreover, it allows one to reveal the fine structure of the spectrum, which cannot be measured by the filter method.

Another advantage of the tracking method is that it allows one to measure X-ray spectra from different regions of the emitting plasma by forming a plasma image (e.g., with the help of a pinhole camera) in the detector.

In this study, thick photoemulsions were also used as tracking detectors in a magnetic analyzer of electrons [3]. To study the particle emission spectra from a short-lived hot plasma, X-ray films are most frequently used as particle detectors. The main difficulty in using these films is that it is necessary to know their absolute spectral sensitivity, i.e., the dependence of the film blackening on the number of incident particles per unit area of the detector surface throughout the entire energy range under study. For this purpose, fragmentary experimental data on separate spectral intervals and the calculated spectral sensitivities are usually used. This can introduce substantial errors into the measurement results.

The use of a tracking detector, first, increases the sensitivity of measurements (because, in this case, it is possible to detect individual electrons); second, it allows one to determine the energy of the detected electron from the measured track length; and, third, it substantially increases the reliability of the calibration of the spectrometric system as a whole.

To take the advantages of the tracking method, it is necessary to know the main spectral characteristic of the nuclear photoemulsion—the instrumental line shape, i.e., the response of the detector to the flux of monoenergetic electrons throughout the entire energy range under study. Since the energy of an individual electron (either primary or secondary) can be conveniently determined by counting the number of grains in its track [4], the instrumental line shape in our case describes the distribution of the primary or secondary electrons over the number of developed grains in the track, provided that the recorded particles (electrons or X-ray photons) are monoenergetic.

In our measurements, we used a 200-μm-thick P-type (relativistic) nuclear photoemulsion without a substrate. The photoemulsion efficiently detected particles with a relatively low ionizing power, such as hard X-ray photons and high-energy electrons.

The instrumental line shape for X-ray emission was measured in the photon energy range from a few to 160 keV. For this purpose, the photoemulsion was exposed to the emission of gamma-active isotopes and the characteristic X-ray emission of foils of different elements. The photoabsorption of monoenergetic photons is accompanied by the formation of a series of monoenergetic groups (lines) of photoelectrons emitted from the *K* and *L* shells of Ag and Br ions that enter into the composition of the emulsion microcrystals. It was found that the yield ratio of the different groups of photoelectrons only slightly depends on the energy of X-ray photons in the energy range of 10–150 keV. Moreover, in the exposed photoemulsion, the groups of photoelectrons corresponding to the characteristic Ag

1063-780X/05/3102-0167$26.00

and Br emission, as well as Compton and Auger electrons, were observed.

The results obtained show that the leading role in the interaction of X-ray emission in the photon energy range of $h\nu > 10$ keV (which is of interest to us) with a photoemulsion is played by photoabsorption. The contribution from Compton absorption turns out to be negligibly small. The Auger electrons leave tracks of a few grains in a nuclear photoemulsion; in this case the beginning of the track coincides with the beginning of the primary photoelectron track. Such an elongated track can be erroneously interpreted as the track of an electron with a somewhat higher energy.

The part of the response function that corresponds to photoelectrons can be represented in the form

$$K(n, \bar{n}(E)) = A\left[\exp\left(-\frac{(n-\bar{n})^2}{2\sigma^2}\right)\right.$$
$$+ 0.33\exp\left(-\frac{(n-\bar{n}-\Delta n_1)^2}{2\sigma^2}\right) \quad (1)$$
$$\left. + 0.11\exp\left(-\frac{(n-\bar{n}-\Delta n_2)^2}{2\sigma^2}\right)\right],$$

where n is the number of the developed grains in a secondary electron track; $\bar{n}(E)$ is the position of the most intense photopeak for secondary electrons with an energy E; $\sigma = 1.5$ is the rms deviation; A is the normalizing coefficient; and $\Delta n_1 = 3$ and $\Delta n_2 = 6$ are the shifts of the second and third photopeaks relative to the most intense photopeak, respectively.

The photoabsorption of monoenergetic X-ray photons with an energy E_{ph} is accompanied by the generation of photoelectrons from the K and L shells of Ag and Br atoms with energies

$$E = E_{ph} - E_{K,L}, \quad (2)$$

where $E_{K,L}$ is the electron binding energy at the K or L shell ($E_{K(\mathrm{Ag})} = 25.5$ keV, $E_{K(\mathrm{Br})} = 13.5$ keV, and $E_{L(\mathrm{Ag})} = 3.5$ keV) [5].

To determine the instrumental line shape with respect to electrons, the photoemulsion was irradiated by electrons with energies 40, 60, 80, and 100 keV. The distributions of the tracks of primary electrons with the above energies over the number of grains were approximated by a Gaussian distribution, and the position of the maximum of the distribution for a given electron energy and the distribution width (which determines the energy resolution) were then found. The results obtained from the photoelectron tracks and the primary electron tracks agree well with one another. This allows us to derive a general calibration relationship between the electron energy and the number of grains in an electron track:

$$\bar{n}(E) = \frac{E}{\omega} - n_0\frac{E}{E+E_0}, \quad (3)$$

where $\omega = 1.67$ keV/grain is the energy spent by an electron on the formation of a developed grain, $n_0 = 17$, and $E_0 = 28.5$ (the energy is measured in kiloelectronvolts) [6].

The procedure of recovering the energy distributions of the electrons and X-ray photons from the measured instrumental electron spectra was described in detail in [7, 8]. In the present study, we used a somewhat simpler procedure of recovering the spectrum of primary electrons. The experimental distribution of the number of tracks over the number of grains in them, $N_{(n)}$, was first determined. The energy range of the recorded electrons (from $E_{\min}$ to $E_{\max}$) was then divided into intervals ΔE_i, and the parameter

$$\Psi_i(n) = \int_{\Delta E_i} K(n, E)dE/\Delta E_i \quad (4)$$

was calculated for each interval. Thereafter, the set of the algebraic equations

$$\sum_{n=n_{\min}}^{n_{\max}}\left(N(n) - \sum_{i=1}^{m}\Psi_i(n)\Delta N_i\right)\Psi_{k(n)} = 0, \quad (5)$$
$$k = 1, 2, \ldots, m,$$

was solved. Here, $m < n_{\max} - n_{\min}$ is the number of the above spectral intervals and ΔN_i is the sought number of primary electrons within the energy interval ΔE_i. This set allowed us to find the linear combination ΔN_i corresponding to the minimal deviation of the calculated distribution of the number of tracks over the number of grains in them from the experimentally determined value of $N_{(n)}$. The obtained spectrum of primary electrons, which had the form of a histogram

$$\varphi(E) = \frac{\Delta N_i}{\Delta E_i} \quad (6)$$

was then approximated by a continuous function. The error in determining the energy spectrum was statistical in character and was governed by the number of primary electrons in the above spectral intervals.

X-ray emission from different regions of a micropinch discharge was recorded on a nuclear photoemulsion using a pinhole camera with a 100-μm-diameter hole covered by a 100-μm beryllium foil. An image of the radiating plasma was simultaneously produced on an X-ray film with the help of a similar pinhole camera. The extinction curve of the X-ray emission from of the discharge plasma was measured with a multichannel scintillation spectrometer [9], and the energy spec-

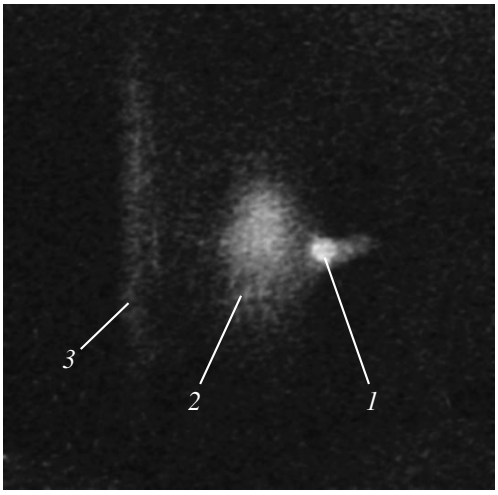

Fig. 1. X-ray ($h\nu > 3$ keV) pinhole image of the discharge region: (*1*) hot spot, (*2*) electrode plasma, and (*3*) electrode surface.

trum was then determined by the method of effective energies [10].

X-ray pinhole images vary from shot to shot; however, they always contain three characteristic spatially separated regions (Fig. 1): a hot spot (micropinch), the electrode plasma, and the surface of the external electrode (cathode). Figure 2 shows the measured emission spectra from different regions of the same discharge.

Let us note the main features of the measured spectra. The X-ray spectra have a characteristic inflection in the energy range $h\nu \approx 10$–15 keV. For comparison, the dotted line shows the thermal spectra with temperatures of 3 and 10 keV. In the photon energy range of 10–30 keV, the shape of the spectrum is approximately the same for all of the emitting regions of the discharge. This means that the energy spectra of the electrons accelerated in the micropinch plasma and electrode plasma are similar to the spectrum of the electrons bombarding the electrode surface.

Figure 2b shows the integrated (over the entire discharge gap) X-ray spectrum restored from the extinction curve measured with the help of a scintillation spectrometer. This spectrum is very similar to the spectrum obtained with the help of a nuclear photoemulsion.

The measured X-ray spectrum lies in the photon energy range $h\nu = 10$–30 keV. At lower energies, the accuracy of measurements with the help of a nuclear photoemulsion is substantially aggravated. On the side of higher energies (at least up to 300–400 keV), there are no fundamental restrictions on the spectral measurements. In this case, the 30-keV upper bound was determined by the exposure conditions of the nuclear photoemulsion. These conditions (the material and thickness of the foil, the hole diameter of the pinhole camera, and the distance between the source and detector) were, in turn, determined by the desire, on the one hand, to compare the results obtained by the nuclear photoemulsion and scintillation spectrometer methods and, on the other hand, to facilitate the process of adjusting the recording system (i.e., to provide the possibility of comparing the structure produced in the nuclear photoemulsion with images of the emitting

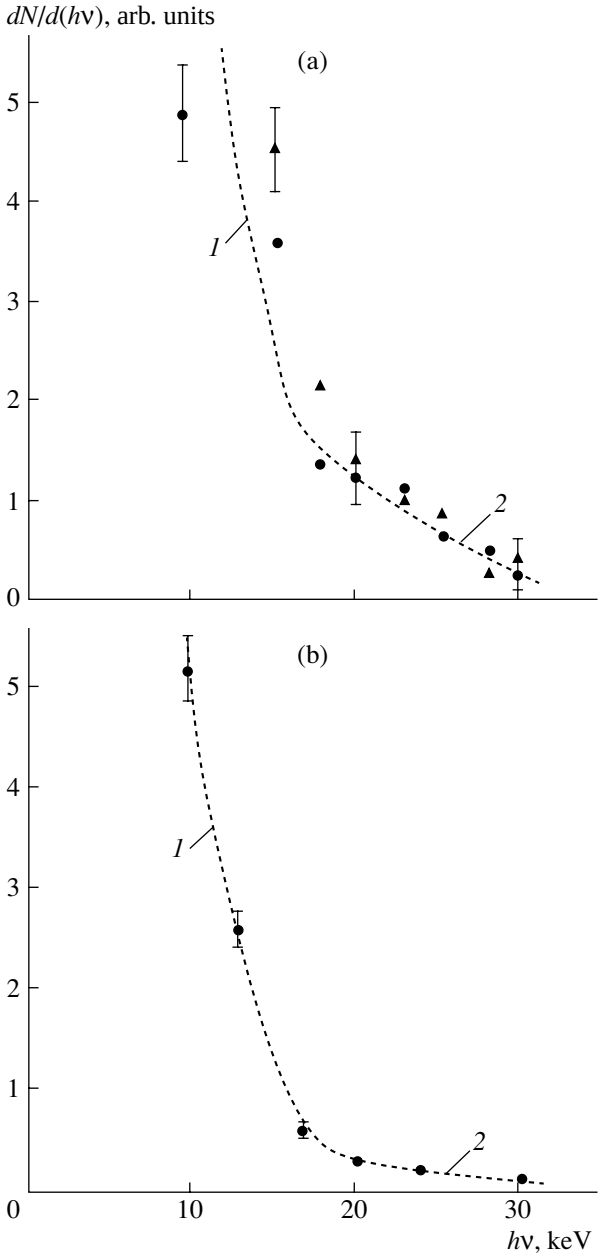

Fig. 2. X-ray spectra (a) measured with the help of a nuclear photoemulsion for different regions of a micropinch discharge (the triangles and circles refer to the hot spot and the electrode surface, respectively) and (b) recovered from the extinction curve obtained by the attenuation filter method with the help of a scintillation spectrometer. Segments *1* and *2* of the fitting dotted lines correspond to electron temperatures T_e of ≈3 and ≈10 keV, respectively.

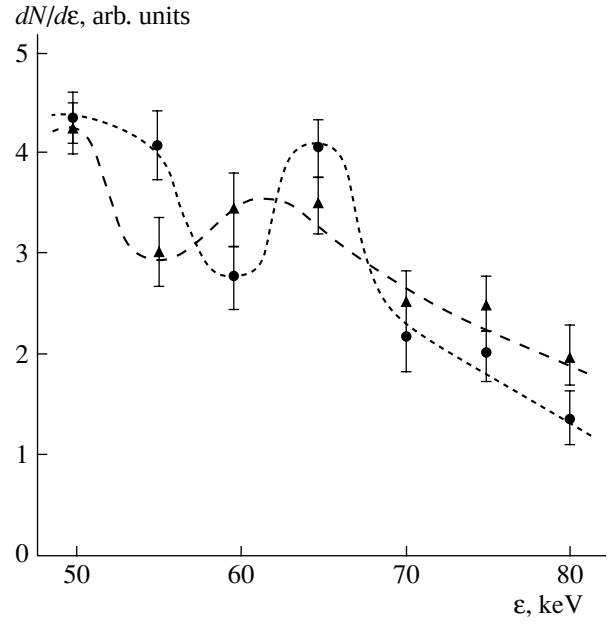

Fig. 3. Characteristic electron spectra obtained in two different discharges.

plasma produced on an X-ray film in each discharge in the same spectral range). Under chosen exposure conditions, most of the photoemulsion sensing area was occupied by the tracks of electrons with relatively low energies and it was impossible to analyze and measure the parameters of the longer tracks of high-energy electrons.

The spectrum of the fast electrons emitted from the discharge plasma was measured with the help of a compact permanent-magnet analyzer and a nuclear photoemulsion [3]. The entrance slit of the analyzer was placed coaxially with an orifice in the external electrode in the immediate vicinity of it. The exposure was produced in a single-shot mode.

Figure 3 shows two typical electron spectra in the energy range of 50–80 keV. The difference between these spectra indicates that there is a random shot-to-shot scatter in the acceleration conditions in the micropinch plasma. The spectra are nonmonotonic, which is probably due to either the specific dynamics of the acceleration process or the presence of several different acceleration mechanisms. The shapes of the spectra agree qualitatively with the data from [11].

In order to confirm that the time evolution of the acceleration processes in the discharge is determined by the process of micropinching, we also recorded X-ray emission in the photon energy range of $h\nu >$ 3 keV and electron emission in the energy range of 50–80 keV by scintillation detectors with a time resolution of no worse than 10 ns [12]. The X-ray and electron beams were spatially separated into two synchronized recording channels with the help of a magnetic analyzer. Our experiments unambiguously show that the formation of a micropinch region [13] is always accompanied by the generation of intense high-energy electron beams. It was earlier shown that, in a micropinch discharge, there are also electron acceleration mechanisms that are not related to the micropinch formation [1].

Table

Element	Ag	Br	C	D	N
Content, g/cm^3	1.83	1.36	0.28	0.28	0.09

The method for recovering the X-ray spectrum from the measured distribution of the ranges of the secondary electrons generated in the interaction of X-ray photons with a nuclear photoemulsion allows one to record X-ray photons with energies of $h\nu \geq 5$ keV [5]. For photons with energies of $h\nu \leq 5$ keV, the electron tracks consist of only one or two developed grains; as a result, the energy spectrum can hardly be determined from the distribution of tracks over the number of grains [7].

In the present study, X-ray spectra in the photon energy range of 1–20 keV were measured by the filter method (see [14] for details). In our case, the nuclear emulsion itself served as a filter. This allowed us to obtain information about the spatial structure of X-ray sources.

The element composition of the 50-μm-thick P-type photoemulsion used the this series of experiments is given in the table.

To measure the distribution of the recorded photons over the photoemulsion depth, the photoemulsion was divided into identical 8.8-μm-thick horizontal layers with an area of 300 μm^2. The number of photons passed through each layer was determined from the number of the developed grains. Using these data, we constructed the extinction curves from which the X-ray spectrum from the discharge plasma was evaluated. The plasma emission transmitted through the entrance window covered by a 100-μm beryllium foil formed images in the nuclear photoemulsion with the help of five identical pinhole cameras with 350-μm-diameter holes made in a 180-μm lead foil and covered by 200-, 400-, 600-, 800-, and 1000-μm beryllium foils. Among five images obtained with different foils, we chose one image in the upper layer of which the number of tracks was about 100. The extinction curve of X-ray emission was then constructed for different regions of the plasma image (the hot spot, the electrode plasma, and the electrode surface).

From the measured extinction curves, we determined the plasma temperature T_e. It was assumed that the emission spectrum was thermal and was completely determined by one parameter—the temperature T_e:

$$\frac{dN}{dE} \sim \exp\left(-\frac{E}{T_e}\right), \quad E = h\nu. \tag{7}$$

The choice of a one-parameter model of the spectrum is based on our earlier results on the recording of X-ray emission from the plasma of a micropinch discharge [13, 15]. These results show that such an approach is quite justified in the photon energy range of 1–20 keV.

The temperature T_e was determined by minimizing the deviation S of the measured extinction curve from that calculated for the plasma emission spectrum with a temperature T_e:

$$S^2(T_e) = \sum_{i=1}^{f} \frac{(N_i^{\text{ex}} - N_i^{\text{th}}(T_e))^2}{\sigma_i^2}, \quad (8)$$

$$N_i^{\text{ex}} = N_i - N_i^b, \quad (9)$$

$$\sigma_i^2 = N_i + N_i^b, \quad (10)$$

where N_i is the total number of tracks in the ith layer (signal + background), N_i^b is the number of background tracks in the ith layer, and f is the number of points in the extinction curve (the superscript "ex" and "th" refer to experiment and calculation, respectively).

The expected number of tracks in the ith layer was calculated from the following formulas:

$$N_i^T(T_e) = \sum_k N_k(E) \frac{dN}{dE}(E_k, T_e), \quad (11)$$

$$N_k(E) = N_0 K_0(E) K_{(E)}^{i-1}(1 - K(E)), \quad (12)$$

$$K_0(E) = \exp\left[-\sum_j \mu_j(E)\rho_j x_j\right], \quad (13)$$

$$K(E) = \exp\left[-x\sum_l \mu_l(E)\rho_l\right], \quad (14)$$

where N_0 is the total number of the photons that are emitted into the solid angle at which the working area of the photoemulsion is seen; $\mu_j(E)$, $\rho_j(E)$, and x_j are the photoeffect cross section, specific density, and effective thickness of the entrance window and foil for the elements that enter into the composition of the entrance window and foil; $\mu_L(E)$ and $\rho_L(E)$ are the photoeffect cross section and specific density of the photoemulsion components; and $K_0(E)$ and $K(E)$ are the fractions of the photons that have not interacted with the entrance window, the foil, and the photoemulsion. The data on the photoeffect cross section μ_E were taken from [16].

The summation over k was performed in the electron energy range of 1–20 keV. The extension of the energy range toward smaller energies does not influence the calculated values of $N_i^T(E)$, since the low-energy photons are completely absorbed in the entrance window and foil. The extension of the energy range toward higher energies also does not influence the results of calculations, since the fraction of high-energy photons in the emission spectrum is small. The main contribution comes from photons with energies of 3–10 keV.

To find the error in determining T_e, we performed a series of calculations with different sets of N_i and N_i^b obtained by processing different regions of the image of the radiating plasma within the same discharge.

The size of the micropinch region was estimated by measuring the width of the edge fuzziness of the micropinch image. We observed two groups of micropinches with sizes of ≤5 μm and ≈150 μm and temperatures of 1.8 ± 0.3 and 1.1 ± 0.3 keV, respectively. The characteristic electron temperature of the plasma was 2.4 ± 0.3 keV at the electrode surface and 1.3 ± 0.3 keV near the electrode (see Fig. 4). Note that the effective temperature characterizes the energy of fast electrons bombarding the cold peripheral plasma.

The available literature data show that the optical and X-ray emissions from a micropinch plasma correlate well with one another [17]. This led us to the idea of investigating the spatiotemporal characteristics of the visible and near UV emission from a micropinch discharge by using a small-size FÉR-7 streak camera. An apparent advantage of this device (in addition to the nanosecond time resolution) is that it can operate in a continuous mode (in contrast, e.g., to photography with pulsed laser illumination).

An optical scheme for investigating the visible plasma glow is shown in Fig. 5.

The radiation of adjusting He–Ne laser *1* (λ = 633 nm) with an initial beam diameter of ~3 mm was expanded to a diameter of ~15 mm by two-lens expander *2*; as a result, interelectrode gap *3* was entirely covered by the laser beam. Lens *4* and diaphragm *5* served to cut off the scattered radiation. Two-prism system *7* allowed one to obtain 90°-rotated longitudinal slit images of the radiating plasma at different distances from the discharge axis. The necessity of the image rotation was related to the vertical orientation of the entrance slit of the streak camera. Otherwise, it would be necessary to rotate the streak camera itself by 90° in the vertical plane, which would obviously be inconvenient from the operational standpoint. Slit images were cut off by vertical slit *8* and, after passing through lens *9*, which magnified the slit image by a factor of about 4 in order to improve the spatial resolution, got onto the entrance of the FÉR-7 streak camera. By shifting lens system *7* in the horizontal plane, it was possible to either vary the distance from the discharge axis when obtaining longitudinal streak images of the plasma glow in different cross sections parallel to the discharge axis or choose the position of the transverse cross section between the anode and cathode when obtaining transverse streak images.

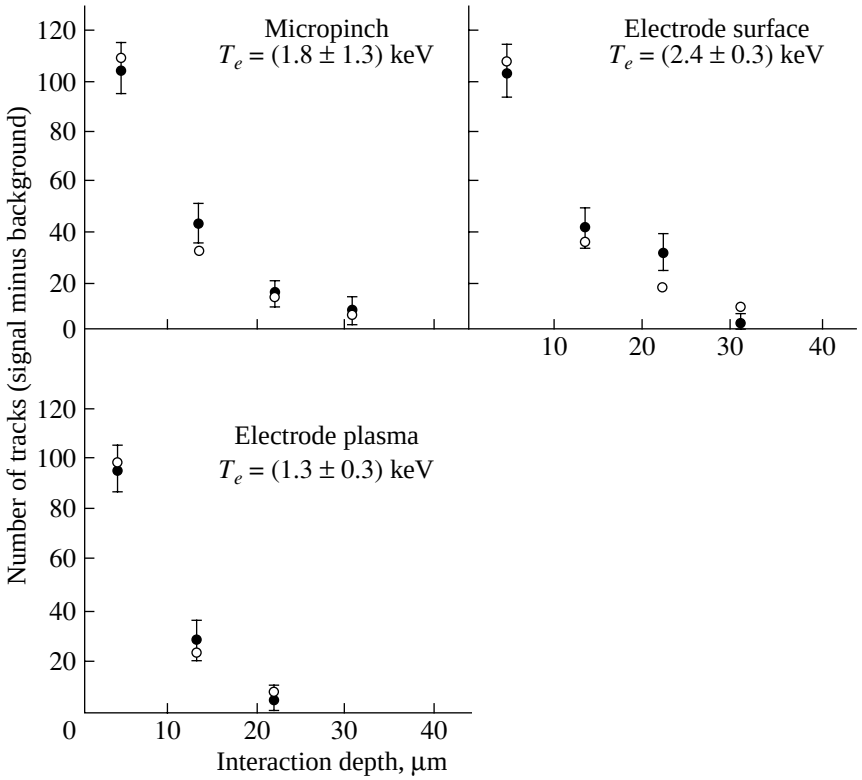

Fig. 4. Measured (closed circles) and calculated (open circles) extinction curves of a nuclear photoemulsion for X-ray emission from different discharge regions.

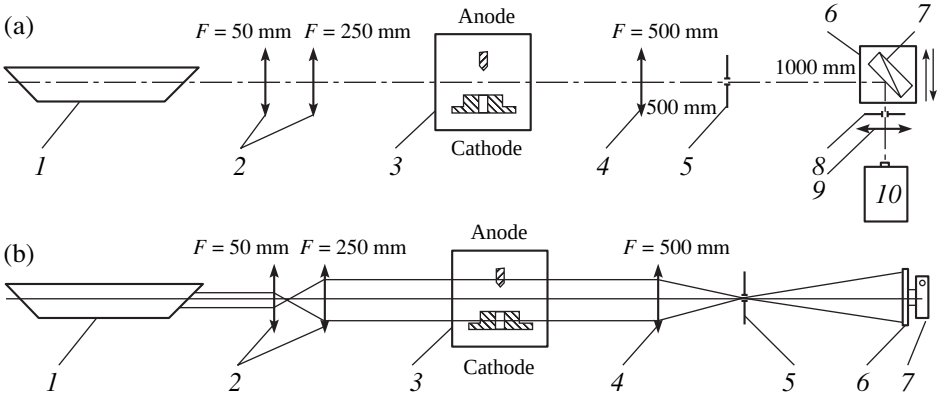

Fig. 5. Schematics of (a) the optical system for studying the plasma emission with the help of an FÉR-7 streak camera: (*1*) adjusting He–Ne laser (λ = 633 nm), (*2*) two-lens expander, (*3*) electrode system of a micropinch discharge, (*4*) lens (*F* = 500 mm), (*5*) diaphragm, (*6*) optical bench, (*7*) two-prism system, (*8*) 0.5-mm slit, (*9*) lens (*F* = 500 mm), and (*10*) FÉR-7 and (b) the system for laser shadowgraphy of LIVS discharges: (*1*) ILGI-503 nitrogen laser (λ = 337 nm), (*2*) two-lens expander, (*3*) electrode system of a micropinch discharge, (*4*) quartz lens (*F* = 500 mm), (*5*) diaphragm, (*6*) interference filter (λ = 337 ± 5 nm), and (*7*) photographic camera.

An analysis of the streak images obtained with a slit oriented along the discharge axis allowed us to study the spatiotemporal evolution of the plasma glow throughout the entire interelectrode gap (Fig. 6). At a discharge current amplitude of I_{max} = 150 kA, the pattern of the processes occurring at the discharge axis and near it (up to a radius of ~0.75 mm) is fairly reproducible: the brightest plasma glow is observed within the

time intervals 1.0–1.2, 1.4–1.8, and 2.0–2.4 μs at a distance of 2.75–3.85 mm from the cathode surface (the first two intervals are marked in Fig. 6 as regions *B* and *C*, respectively). In region *C*, at a distance of about 3.30 mm from the cathode surface, a fine double-hump temporal structure of the plasma glow with a time interval of 40–60 ns between the humps is observed. This structure disappears as either of the electrodes is approached. Moreover, regions *B* and *C* are displaced toward both the cathode and the anode with initial velocities of $V_0 \approx 5 \times 10^6$ cm/s and $V_0 \approx 3.5 \times 10^6$ cm/s, respectively. The propagation velocities of these regions decrease as the electrodes are approached. In addition to the axial propagation, we also observed the radial propagation of the above glow regions with velocities of $V_0 \approx 1.5 \times 10^6$ cm/s in the middle of the gap and near the cathode and $V_0 \approx 4 \times 10^6$ cm/s near the anode.

In the electrode regions, the character of the plasma glow is nearly the same as in the middle of the gap, but its brightness is much lower.

At distances from the discharge axis larger than 1.0 mm, the glow pattern described above is smeared out: regions *B* and *C* merge together and form a smoothly varying glow in the time interval 1.5–3.7 μs, on the background of which spikes with a duration 300–400 ns can spontaneously arise.

An interesting result is the observation of a fine double-hump temporal structure of the plasma glow at the discharge axis (with a time interval of ~50 ns between the humps) at the instant when the discharge current reaches its first maximum. This structure disappears with increasing distance from the place where the constriction develops and the micropinch forms.

Streak images obtained with a slit oriented perpendicularly to discharge axis give an idea of the dynamics of the radial distribution of the plasma glow. An analysis of these streak images show that, in the cross section in which the constriction develops, the compression of the plasma near the instant at which the discharge current reaches its first maximum proceeds in two stages divided by a time interval of ~70 ns.

To obtain information about the spatiotemporal plasma dynamic in the interelectrode gap of the LIVS facility, we developed a system for optical shadowgraphy (Fig. 5b).

The radiation of nitrogen laser *1* with an initial beam diameter of ~3 mm was expanded with the help of expander *2* consisting of two quartz lenses with focal lengths of 50 and 250 mm (the positions of the focal points of the lenses coincided with one another). As a result, the diameter of the laser beam increased by a factor of about 5, which was sufficient to entirely cover interelectrode gap *3*. The radiation passed through the plasma was gathered by quartz lens *4*, in the focal point of which diaphragm *5* was placed. The diaphragm completely transmitted the radiation that was not deflected

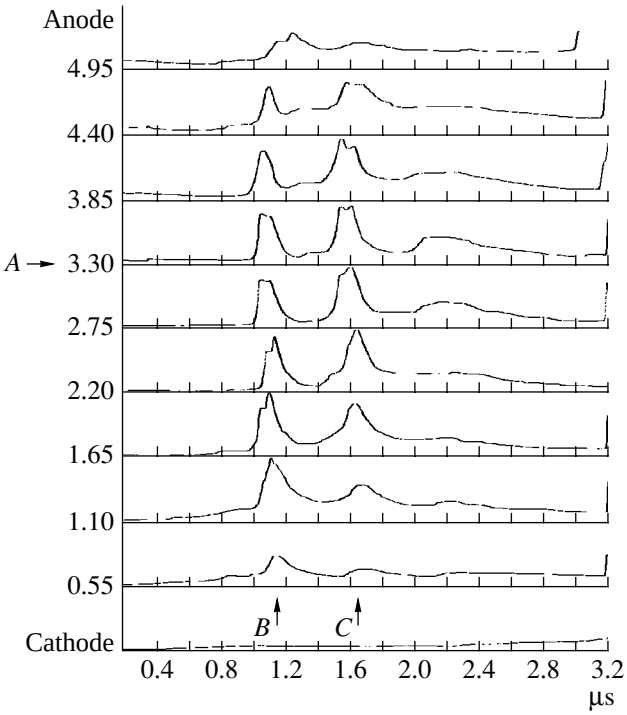

Fig. 6. Densitograms of streak images obtained with a detector slit oriented along the discharge: (*A*) cross section corresponding to the region in which the constriction develops and the micropinch forms, (*B*) contraction of the current-carrying shell toward the axis, and (*C*) formation of the constriction. The distance from the cathode is plotted on the vertical axis.

by the plasma. By varying the diameter of the diaphragm orifice, it was possible to substantially reduce the parasitic effect of the spontaneous plasma emission. For this purpose, we also used interference filter *6*, tuned to the laser wavelength ($\lambda = 337 \pm 5$ nm). The images of the discharge region were recorded on the MIKRAT 300 film with the help of a ZENIT photographic camera operating in the released-shutter mode. By choosing the optimal distances between the elements of the optical system and by varying the diameter of the diaphragm orifice *5*, we achieved a contrast shadow pattern with a minimal background illumination from the spontaneous plasma emission.

The LIVS discharge was photographed starting from the instant of discharge initiation up to the stage of plasma decay. The amplitude of the discharge current was varied in the range I_{max} = 40–150 kA. During each discharge, one shadow image was taken at a definite instant. To increase the reliability of the results obtained (taking into account variations in the plasma behavior in each discharge), the shadow image statistics (over about five images) was gathered for the above instant.

Images produced by the laser radiation in the absence of a discharge and by the background plasma emission are presented in Figs. 7a and 7b, respectively.

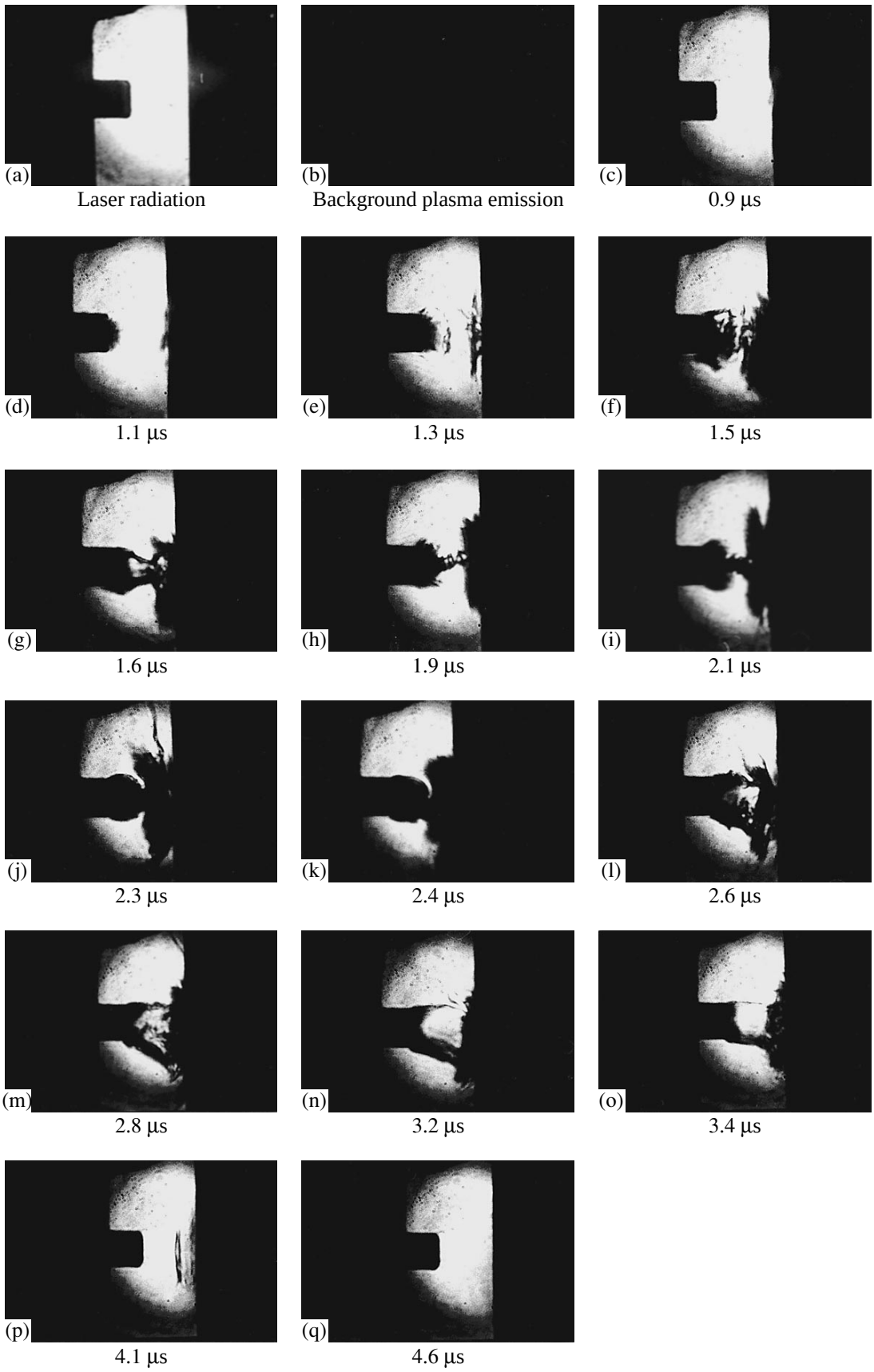

Fig. 7. Series of shadow images of the LIVS discharge region at I_{max} = 150 kA.

By the instant $\tau = 1.1$ μs, which corresponds to the time interval between the instant of discharge initiation and the instant of triggering the nitrogen laser, localized plasma structures consisting of the ionized vapor of the electrode material appear near the electrodes (Fig. 7d): a round "cap" of width 0.5 mm near the anode and a similar structure with a diameter and width of about 4 mm near the cathode. The propagation of the electrode plasmas toward one another (Fig. 7e) with velocities of $\sim 10^6$ cm/s results in their collision in the central region of the interelectrode gap at the instant $\tau = 1.5$ μs (Fig. 7f), their compression toward the discharge axis (Fig. 7g), and the formation of a plasma column with a diameter of about 1 mm (Figs. 7h, 7i). The column is subject to the onset of sausage instability (the $m = 0$ mode) over a time interval $\tau = 1.8$–2.0 μs near the maximum of the discharge current. In some shots, the onset of kink instability (the $m = 1$ mode) was also observed. Starting from $\tau = 2.1$–2.2 μs (Figs. 7j, 7k), the plasma channel expands with a velocity of $\sim 10^6$ cm/s. By the instant $\tau \approx 2.6$ μs, a funnel-shaped plasma structure expanding toward the cathode is formed in the discharge gap (Figs. 7l, 7m, 7n, 7o). This structure disappears by the end of the first half-period of the discharge current, $\tau = 4.0$ μs (Fig. 7p). Thereafter, there are no distinct plasma structures with appreciable electron density gradients in the discharge region (Fig. 7q).

On the whole, shadow images of the interelectrode gap taken at different energies deposited in the discharge are qualitatively the same as those obtained at the maximum amplitude of the discharge current ($I_{max} = 150$ kA). A decrease in the current amplitude is accompanied by the shrinking of the region with appreciable (for probing radiation) electron density gradients: this region is mainly concentrated near the discharge axis.

A comparative analysis of shadow images of the discharge gap and streak images of the emitting plasma of a LIVS discharge allows us to draw the following conclusions:

At the axis of the discharge and near it, region *B* corresponds to the compression of the current-carrying shell toward the axis and region *C* corresponds to the onset of the sausage instability of the plasma column, which results in the formation of micropinches (this stage manifests itself in the appearance of a fine double-hump temporal structure of the plasma glow). Thereafter, the plasma in the interelectrode gap decays. The fact that the above regions are smeared out as the distance from the discharge axis increases may be related to the propagation of the different plasma regions in the axial and radial directions with velocities of $\sim 10^6$ cm/s. The same (on the order of magnitude) plasma propagation velocities in both the longitudinal and transverse (with respect to the discharge axis) directions were recorded by particle diagnostics in [18].

CONCLUSIONS

(i) Direct evidence that there are two successive compressions of the constriction region in a micropinch discharge (as predicted by the model of radiative compression for currents above the critical one [19]) has been obtained for the first time in experiments with a continuous recording of plasma emission with high temporal and spatial resolution. Note that, in streak images, the plasma surrounding the micropinch (rather than the micropinch itself) is probably observed. Previously, the hypothesis about the presence of two compressions (a slow compression followed with a fast one) have been invoked to explain the discrepancy among the results from different diagnostics: multiframe photographing of the micropinch plasma with the help of pulsed laser illumination, measurements of the derivative of the discharge current, and recording of the X-ray emission from multiply charged ions [20]. In accordance with the above hypothesis, the first two diagnostics allow one to observe the first compression, while the latter allows one to observe the formation of a hot dense plasma, which is a consequence of the second compression.

In this study, it has been found that the development of a constriction in the plasma column results in the formation of a contracted glowing region that propagates along the discharge axis toward both the cathode and anode with an initial velocity of $\sim 10^6$ cm/s. The propagation velocity of the glowing region decreases as the electrodes are approached. Such a pattern can be interpreted as the plasma outflow from the constriction region or the formation of a shock wave in this region [21].

(ii) Space-resolved measurements of the X-ray spectra from the three regions of a micropinch discharge (the micropinch itself, the electrode plasma, and the electrode surface) with the help of tracking detectors in the photon energy range of 10–30 keV have shown that these spectra are clearly nonequilibrium and closely coincide with one another. This indicates that the energy spectra of the accelerated electrons in the micropinch plasma and electrode plasma are similar to the spectra of the electrons bombarding the electrode surface. Simultaneous measurements of X-ray emission in the photon energy range of $h\nu > 3$ keV and electron emission in the electron energy range of 50–80 keV in the axial direction with the help of scintillation detectors have shown that the formation of a micropinch is accompanied by the generation of high-energy electrons. In other words, it is shown experimentally for the first time that the region where the micropinch forms is a source of superthermal electrons propagating in the axial direction and bombarding the electrode plasma and electrode surface.

Measurements of the spectrum of high-energy electrons with the help of a magnetic analyzer and tracking detectors have shown that the spectrum is nonmonotonic. This is probably due to either the specific dynam-

ics of the micropinch plasma or the presence of several different acceleration mechanisms. The reliability of the previous measurements of the spectra of high-energy electrons with the help of a photofilm in the multipulse exposure mode has been confirmed. Therefore, our results support the conclusion that the high-energy electrons in a micropinch discharge in the vapor of high-Z elements are generated in electrostatic fields and that the electron emission spectrum is threshold in character; i.e., it changes substantially when passing from subcritical to supercritical currents.

(iii) Space-resolved measurements of X-ray spectra in the photon energy range of $h\nu \approx 1$–20 keV by the filter method and with the help of tracking detectors have made it possible to estimate not only the electron temperature in the micropinch but also its size. Two groups of micropinches were observed with characteristic sizes of ≤ 5 μm and ≈ 150 μm and temperatures of 1.8 ± 0.3 and 1.1 ± 0.3 keV, respectively. According to the theoretical model [22], the regime of strong radiative compression terminates when the plasma is compressed to the radius (in cm)

$$r = 10^9 I^2 / T_e^{3.5}, \quad (15)$$

where the discharge current I is in MA and the plasma electron temperature T_e is in keV. At a current of 150 kA, temperatures of 1.8 keV and 1.1 keV correspond to the minimum possible micropinch sizes (i.e., the sizes at which radiative compression terminates) of ~1 μm and ~15 μm, respectively. A micropinch size of ~150 μm corresponds to the so-called first compression. Due to an increase in radiative losses, the first compression is followed by the second compression [19]. The first of the recorded micropinches is apparently formed in the regime of strong radiative compression, whereas the second micropinch is formed in the regime of the spontaneous heating of the pinch plasma between the first and the second compressions because of a decrease in the number of charged particles per unit length and the development of anomalous plasma resistivity in the constriction region [23].

The above theoretical model was previously used to explain the specific features of the X-ray spectra of multicharged ions measured in different micropinch experiments by the method of high-resolution diffraction spectroscopy. However, in those studies, the effect of polarization of the emitted radiation, which is now being actively discussed in the literature (see, e.g., [24]), was not taken into account; this can throw doubt on the correctness of the interpretation of the data obtained. Thus, the experimentally observed relation between the limiting values of $T_e^{\max}$ and $r_{\min}$ in a micropinch with allowance for the Bennet equilibrium condition

$$n_i = \frac{\mu_0 I^2}{8\pi^2 T_e (1+z) r^2} \quad (16)$$

(where n_i is the ion density of the micropinch plasma and z is the average degree of ionization) can be regarded as a first direct confirmation of the fact that the higher the micropinch temperature, the higher the micropinch plasma density. For the two observed micropinches, the plasma densities differ by approximately three orders of magnitude; this should inevitably manifest itself in the line emission spectrum from multiply charged ions [25].

REFERENCES

1. M. A. Gulin, A. N. Dolgov, N. N. Kirichenko, and A. S. Savelov, Zh. Éksp. Teor. Fiz. **108**, 1309 (1995) [JETP **81**, 719 (1995)].
2. N. G. Basov, Yu. A. Zakharenkov, N. N. Zorev, *et al.*, Itogi Nauki Tekh., Ser. Radiotekhnika **26** (1) (1982).
3. V. V. Kushin, V. K. Lyapidevskiĭ, N. V. Maslennikova, and G. Kh. Salakhutdinov, in *Proceedings of the Second All-Union School on Solid Tracking Detectors and Autoradiography, Odessa, 1989*, Abstracts of Papers, p. 44.
4. G. I. Kazarinov, V. V. Kushin, V. K. Lyapidevskiĭ, and I. V. Posysaeva, Prib. Tekh. Éksp., No. 4, 211 (1980).
5. N. A. Klyachin, V. V. Kushin, V. K. Lyapidevskiĭ, and N. B. Khokhlov, in *Diagnostic Methods in Plasma Studies* (Énergoatomizdat, Moscow, 1983), p. 59.
6. V. V. Averkiev, M. A. Gulin, A. N. Dolgov, *et al.*, Preprint No. 014-90 (Moscow Engineering Physics Institute, Moscow, 1990).
7. V. Ya. Arsenin, S. M. Knopova, V. V. Kushin, *et al.*, in *Hardware and Software for Automatic Systems of Nuclear Physics Experiments* (Énergoatomizdat, Moscow, 1982), p. 25.
8. V. V. Kushin, V. K. Lyapidevskiĭ, and L. B. Samoĭlov, in *Experimental Methods in Medium- and Low-Energy Nuclear Physics* (Énergoatomizdat, Moscow, 1986), p. 3.
9. V. V. Averkiev, A. N. Dolgov, V. K. Lyapidevskiĭ, *et al.*, Prib. Tekh. Éksp., No. 2, 173 (1991).
10. S. A. Zverev, M. P. Kalashnikov, V. K. Lyapidevskiĭ, *et al.*, Preprint No. 96 (Lebedev Physical Institute, USSR Acad. Sci., Moscow, 1980).
11. A. A. Gorbunov, M. A. Gulin, A. N. Dolgov, *et al.*, Pis'ma Zh. Éksp. Teor. Fiz. **50**, 320 (1989) [JETP Lett. **50**, 355 (1989)].
12. V. V. Averkiev, A. N. Dolgov, V. A. Kaplin, *et al.*, Prib. Tekh. Éksp., No. 5, 158 (1992).
13. V. V. Averkiev, A. N. Dolgov, V. K. Lyapidevskiĭ, *et al.*, Fiz. Plazmy **18**, 724 (1992) [Sov. J. Plasma Phys. **18**, 374 (1992)].
14. M. A. Gulin, A. N. Dolgov, N. N. Kirichenko, *et al.*, Prib. Tekh. Éksp., No. 6, 82 (1996).
15. A. N. Dolgov, N. N. Kirichenko, V. K. Lyapidevskiĭ, *et al.*, Fiz. Plazmy **19**, 97 (1993) [Plasma Phys. Rep. **19**, 50 (1993)].
16. M. A. Blokhin and N. G. Shveĭtser, *Handbook of X-ray Spectroscopy* (Nauka, Moscow, 1982).
17. H. Chuaqui, M. Favre, E. S. Wyndham, *et al.*, Phys. Plasmas **2**, 3910 (1995).

18. A. N. Dolgov, D. E. Prokhorovich, and A. S. Savelov, in *Proceedings of the XXX Zvenigorod Conference on Plasma Physics, Zvenigorod, 2003*, p. 126.
19. V. V. Vikhrev, V. V. Ivanov, K. N. Koshelev, and Yu. V. Sidel'nikov, Dokl. Akad. Nauk SSSR **262**, 1361 (1982) [Sov. Phys. Dokl. **27**, 153 (1982)].
20. V. A. Veretennikov, S. N. Polukhin, O. G. Semenov, and Yu. V. Sidel'nikov, Fiz. Plazmy **7**, 1199 (1981) [Sov. J. Plasma Phys. **7**, 656 (1981)]; V. A. Veretennikov, A. I. Isakov, O. N. Krokhin, *et al.*, Preprint No. 59 (Lebedev Physical Institute, USSR Acad. Sci., 1983).
21. A. N. Dolgov, Fiz. Plazmy **22**, 629 (1996) [Plasma Phys. Rep. **22**, 569 (1996)].
22. E. V. Aglitskiĭ, P. S. Antsiferov, K. N. Koshelev, and A. M. Panin, Fiz. Plazmy **12**, 1184 (1986) [Sov. J. Plasma Phys. **12**, 683 (1986)].
23. P. V. Sasorov, Fiz. Plazmy **18**, 275 (1992) [Sov. J. Plasma Phys. **18**, 143 (1992)].
24. E. O. Baronova, V. V. Vikhrev, A. E. Gureĭ, *et al.*, Fiz. Plazmy **24**, 25 (1998) [Plasma Phys. Rep. **24**, 21 (1998)].
25. K. N. Koshelev, Yu. V. Sidel'nikov, V. V. Vikhrev, and V. V. Ivanov, in *Spectroscopy of Hot Multicharged-Ion Plasma* (Nauka, Moscow, 1991), p. 163.

Translated by A.S. Sakharov

Plasma Physics Reports, Vol. 31, No. 2, 2005, pp. 178–183. Translated from Fizika Plazmy, Vol. 31, No. 2, 2005, pp. 203–208.

NONLINEAR PHENOMENA

Coulomb Explosion in a Cluster Plasma

V. Yu. Bychenkov* and V. F. Kovalev**

**Lebedev Institute of Physics, Russian Academy of Sciences, Leninskiĭ pr. 53, Moscow, 117924 Russia*
e-mail: bychenk@sci.lebedev.ru
***Institute for Mathematical Modeling, Russian Academy of Sciences, Miusskaya pl. 4a, Moscow, 125047 Russia*
e-mail: kovalev@imamod.ru

Received April 22, 2004; in final form, June 11, 2004

Abstract—The energy spectra of particles in a cluster plasma produced during the Coulomb explosion of spherically symmetric clusters with an arbitrary initial density distribution are investigated. A relationship is found between the energy spectrum of the ions and the density profile of the atoms in the cluster. © *2005 Pleiades Publishing, Inc.*

At present, high-intensity ultrashort laser pulses are widely used in experiments on the interaction of high-power laser radiation with cluster plasmas [1]. A characteristic feature of cluster plasma is its ability to strongly (almost entirely) absorb laser radiation [2]. This property makes it possible to build high-brightness X-ray sources [3]. Moreover, the expansion of clusters results in ion acceleration to high energies [1, 4–6]. In the case of deuteron clusters, ion–ion collisions produce fusion neutrons [7]; this provides an opportunity to create subnanosecond neutron sources for use in materials science, defectoscopy, etc.

If the laser field is strong enough, it almost instantaneously knocks electrons out of a cluster, thereby creating conditions for the subsequent Coulomb explosion of a positively charged microplasma. The ions of the exploding clusters are accelerated to high energies and give rise to a macroplasma with a high effective ion temperature. So far, the Coulomb explosion of a cluster and the spectrum of the accelerated ions have been described in the simplest "ideal cluster" model, in which the exploding cluster is treated as an exploding homogeneous spherical bunch with a given initial radius r_c and which predicts a square-root ion energy spectrum $\sqrt{\varepsilon}$ with a sharp energy cutoff at the maximal energy $\varepsilon_{max} \propto r_c^2$ [5, 6, 8]. Similar energy spectra were obtained in three-dimensional particle-in-cell simulations [5] and also were observed in experiments on the interaction of high-power laser radiation with cluster targets [9]. At the same time, in some experiments, ion energy spectra were found to differ from the above square-root spectrum with a sharp energy cutoff. This difference may be attributed to, e.g., the radial nonuniformity of the ion density in a cluster or to the initial spread in the cluster radii. Such a nonuniformity can lead to a smoothing of the energy spectrum of the accelerated ions (see [8, 9] for details). Currently, there are no reliable data on the relation of the initial density distribution in the clusters to the methods for producing them and to the parameters of the laser prepulse, which virtually always precedes the main laser pulse in actual experiments and affects the initial cluster density profile. In the present paper, we develop a theory of cluster plasma for clusters with an arbitrary initial ion density distribution and establish the relation between this distribution and the ion energy spectrum. Obviously, the ideal cluster model implies that the atomic density in a cluster is uniform and that the contrast of the laser pulse intensity is very high. The latter requirement is needed in order to prevent the cluster from expanding under the action of the prepulse, but it is hard to achieve in practice [10]. In connection with this, Kaplan *et al.* [11] investigated the expansion dynamics of an individual cluster with an initially nonuniform density in terms of the test ion model. In cluster plasma theory, however, the question of how to describe the ion energy spectrum as a function of the initial ion density profile has remained open. A discussion of this question is the main objective of our paper.

Let us consider a cluster affected by a high-power laser pulse such that the kinetic energy $mc^2a^2/2$ acquired by an electron in a strong laser field is much higher than the energy ZNe^2/r_c of its Coulomb interaction with the cluster and the amplitude $\max\{1, a\}(c/\omega_0)$ of its oscillations is much larger than the characteristic cluster radius r_c. Here, m and e are the mass and charge of an electron, c is the speed of light, $a = eE_0/(m\omega_0 c)$ is the dimensionless amplitude of the vector potential of the electromagnetic field with the electric field strength E_0 and frequency ω_0, Z is the ion charge number, and N is the number of atoms in the cluster. We assume that the laser field is strong enough to ionize the cluster and to knock the electrons out of it. The subsequent Coulomb explosion will occur as an expansion of the cluster into vacuum, provided that the pressure of the surrounding electron gas $n_e mc^2a^2/2$ is much lower than the

1063-780X/05/3102-0178$26.00

characteristic pressure e^2Z^2Nn/r_c of the expanding cluster. Here, n_e is the electron density in the intercluster space and n is the atomic density in the cluster. In what follows, we will assume that these conditions are met and will study the parameters of the plasma produced during Coulomb explosions of spherically symmetric clusters.

We describe the expansion dynamics of an individual spherically symmetric cluster under the action of Coulomb repulsive forces by the one-dimensional collisionless cold hydrodynamic equations for the ions and Poisson's equation for the electrostatic field E:

$$\partial_t n + r^{-2}\partial_r r^2 nu = 0, \quad \partial_t u + u\partial_r u = ZeE/M, \qquad r^{-2}\partial_r r^2 E = 4\pi Zen, \tag{1}$$

where M is the mass of an ion and u is the radial expansion velocity of the cluster. This set of equations is well known in the theory of charged plasma (see, e.g., [12]). At the same time, an analogous set of equations in which the right-hand side of Poisson's equation has the opposite sign describes the dynamics of particles moving in a self-consistent gravitational field (see, e.g., [13], Section 81).

The initial conditions for Eqs. (1) specify the spatial profiles of the ion density and velocity, $n|_{t=0} = n_c(r)$ and $u|_{t=0} = U(r)$ (and, consequently, of the electric field $E|_{t=0} = (4\pi Ze/r^2)\int_0^r dr r^2 n_c(r)$), at the time $t = 0$. The boundary conditions for the electric field imply that it vanishes at $r = 0$ and decreases to zero at infinity, $r \longrightarrow \infty$.

With such initial conditions, Eqs. (1) can be solved analytically in Lagrangian variables [13, 14] or in hodograph variables [15]; they can also be solved by using the energy and charge conservation laws [11, 16]. For initially immobile ions ($U = 0$), the solution to Eqs. (1) has the form

$$t\sqrt{\frac{2w(h)}{h^3}} = \frac{1}{2}\ln\frac{1+q}{1-q} + \frac{q}{1-q^2}, \qquad w(h) = \int_0^h dy y^2 \omega_L^2(y),$$
$$u(t,r) = q\sqrt{\frac{2w(h)}{h}}, \quad E(t,r) = r^{-2}w(h), \qquad r = \frac{h}{1-q^2}, \tag{2}$$
$$n(t,r) = n_c(h)(1-q^2)^3 \times\left[1 - \frac{3t}{2}q(1-q^2)\sqrt{\frac{2w(h)}{h^3}}\left(1 - \frac{h^3\omega_L^2(h)}{3w(h)}\right)\right]^{-1},$$

where $\omega_L(r) = (4\pi Z^2e^2n_c(r)/M)^{1/2}$. Here and below, we work in dimensionless variables in which the time is normalized to the inverse ion Langmuir frequency $\omega_L(0)$ calculated in terms of the initial density $n_c(0)$ at the center of the cluster; the coordinates r and h, the Langmuir frequency $\omega_L(0)$, the densities n and n_c, the velocity u, and the variable w are expressed in units of r_c, $\omega_L(r)$, $n_c(0)$, $\omega_L(0)r_c$, and $\omega_L^2(0)r_c^3$, respectively; and the electric field E is in units of $4\pi Zen_c(0)r_c$. Given the initial cluster density profile, the function $q(t, h)$ is determined from the first of relationships (2). Substituting the function $q(t, h)$ so obtained into the remaining relationships yields an implicit solution for an expanding cluster.

It should be noted that the condition for the nonnegative function $n(t, r) \geq 0$ to be finite at an arbitrary time is not satisfied for an arbitrary initial density distribution. Specifically, at a time $t = t_s$ determined from the condition

$$1 - \frac{3t_s}{2}q(t_s,h)(1-q^2(t_s,h))\sqrt{\frac{2w(h)}{h^3}} \times\left(1 - \frac{h^3\omega_L^2(h)}{3w(h)}\right) = 0, \tag{3}$$

the density given by the last of relationships (2) becomes infinite at a certain radius; in other words, the density has a singularity at $t = t_s$. In this case, the radial derivative of the ion velocity, $\partial u/\partial r$, also becomes infinite, which corresponds to the breaking of the Coulomb explosion wave, followed by the ion multistream motion at $t > t_s$. For a smooth initial density profile whose curvature passes through zero as r increases, such as, e.g., the Gaussian density profile $n_c(r) = \exp(-r^2)$, the radius of the spherical surface at which the explosion wave breaks corresponds to the vanishing of each of the derivatives $\partial_u r$ and $\partial_{uu} r$ at a fixed time t and is determined from Eq. (3) and the equation

$$3\left(1 - \frac{h^3\omega_L^2(h)}{3w(h)}\right) - q^2\left[\frac{h^3\omega_L^2(h)}{w(h)} + \frac{h^6\omega_L^4(h)}{w^2(h)} - 4\frac{h^3\omega_L^2(h)}{w(h)} - 2\frac{h^4\partial_h(\omega_L^2(h))}{w(h)}\right] = 0. \tag{4}$$

When the initial density profile does not have an inflection point, as is the case, for instance, with the parabolic profile $n_c(r) = (1 - r^2)\theta(1 - r)$, where $\theta(r)$ is the Heaviside step function, the Coulomb explosion wave breaks at the cluster's outer boundary. In this case, since the density of the cluster equals zero at its outer boundary, $\omega_L^2(1) = 0$, the time at which the solution becomes multivalued is determined by the root of an algebraic equation for the quantity $q_s \equiv q(t_s, 1)$:

$$t_s = \frac{2}{3\sqrt{2w(1)}}\frac{1}{q_s(1-q_s^2)},$$
$$\frac{1}{2}\ln\frac{1+q_s}{1-q_s} + \frac{1}{1-q_s^2}\left(q_s - \frac{2}{3q_s}\right) = 0. \quad (5)$$

The solution $q_s \approx 0.6232$ to this equation gives the following universal formula for the time at which the solution becomes multivalued: $t_s \approx 1.237/\sqrt{w(1)}$. For all similar clusters having the same total number of ions and differing only in the manner in which the density decreases monotonically with radius, the value of the quantity $w(1)$ is the same, $w(1) = 1/3$; i.e., a singularity arises at the time $t_s \approx 2.142$.

Hence, the description of cluster expansion on the basis of solution (2) to Eqs. (1) on time scales longer than t_s becomes meaningless; hence, the discontinuity that arises at the explosion front should be described by means of a kinetic approach. The onset of the discontinuity is similar to the onset of a singularity in a self-gravitating gas [15, 17, 18]. Such discontinuities are also subjects of the gas dynamics of simple waves in which some portions of the density profile are decreasing in the propagation direction of the wave. It is only for some idealized density distributions (such as radially nondecreasing density profiles $n_c(r)$ with a cutoff at a certain radius $r = r_c$) that the discontinuities do not arise. In particular, this is the case for an initial step density profile (an ideal cluster) [6, 8].

In spite of the presence of a singularity, which, in the hydrodynamic limit, corresponds to a spherical shock wave, Kaplan *et al.* [11] extended the hydrodynamic solution to the problem of the Coulomb explosion of a cluster beyond the instant at which the singularity arises. In contrast to that paper, we will not go beyond the limits of single-stream hydrodynamics and will consider how the accelerated ions are distributed over energies, which is an important problem for experiments with cluster plasmas. Integrating the ion energy distribution function $dN/d\varepsilon = 4\pi r^2 n(t, r)/(d\varepsilon/dr)$ over energy gives the total number of ions in the cluster. Accordingly, solution (2) yields

$$\frac{dN}{d\varepsilon} = \left(\frac{dN}{d\varepsilon}\right)^+ + \left(\frac{dN}{d\varepsilon}\right)^-,$$
$$\left(\frac{dN}{d\varepsilon}\right)^\pm = \begin{cases} N^\varepsilon\theta(d\varepsilon/dr) \\ -N^\varepsilon\theta(-d\varepsilon/dr), \end{cases} \quad (6)$$
$$N^\varepsilon = -2\pi\frac{h^4 n_c(h)}{qw(h)}\left[\frac{3t}{2}(1-q^2)^2\sqrt{\frac{2w(h)}{h^3}}\left(1-\frac{h^3\omega_L^2(h)}{3w(h)}\right) + q\left(1-\frac{h^3\omega_L^2(h)}{w(h)}\right)\right]^{-1},$$

where N is expressed in units of $n_c(0)r_c^3$, and ε is normalized to $M\omega_L^2(0)r_c^2/2$. The fact that distribution function (6) is the sum of two terms is related to the possible nonmonotonic dependence of ε on r: the superscript plus and minus signs indicate the contributions of the particles whose energy increases and decreases with r, respectively. Depending on the shape of the profile $n_c(r)$, there may be several radial regions with different signs of the derivative $d\varepsilon/dr$. For clusters with a parabolic and an exponential initial density profile, examples of such regions occurring at $t_s > t > 0$ will be presented below. At the points at which the radial derivative of the ion velocity vanishes, a singularity arises in N^ε and, accordingly, in the energy spectrum $dN/d\varepsilon$. This singularity, however, is integrable. For instance, if the singular point ε_m of the spectrum arises at a nonzero second derivative of the velocity, then, in the vicinity of this point, we have $dN/d\varepsilon \propto 1/\sqrt{\varepsilon_m - \varepsilon}$. For a monotonic velocity profile (e.g., for an ideal cluster), the ion energy spectrum is nonsingular. Let us present the solution and the ion energy spectrum that correspond to this case.

For an ideal cluster such that $n_c = n_c(0)\theta(r_c - r)$, solution (2) has the form

$$u = \sqrt{\frac{2}{3}}\sqrt{\frac{r_f - 1}{r_f}}\frac{r}{r_f}, \quad n = \theta\left(1 - \frac{r}{r_f}\right)r_f^{-3}, \quad E = (r/3)r_f^{-3}, \quad r \le r_f. \quad (7)$$

Here, the radius of the front of an expanding plasma, $r_f(t)$, is given by the same formula as that in the model of a test ion occurring at the spherical surface of an expanding cluster [6]:

$$t\sqrt{\frac{2}{3}} = r_f\sqrt{1-\frac{1}{r_f}} + \frac{1}{2}\ln\frac{1+\sqrt{1-1/r_f}}{1-\sqrt{1-1/r_f}}, \quad (8)$$

i.e., we have $r_f \approx 1 + t^2/6$ for $t \ll 1$ and $r_f \approx \sqrt{2/3}t$ for $t \gg 1$. These formulas imply that the velocity of the cluster ions and the electric field within the cluster increase linearly with r and reach their maxima at $r = r_f$; ahead of the front ($r \ge r_f$), the electric field decreases monotonically with radius, $E = (1/3)r^{-2}$. The ion density profile in the cluster keeps its initial shape: it continues to have the form of a step, whose width and height, however, change with time. The expansion front velocity $v_f = \dot{r}_f$ increases with time, $v_f = \sqrt{(2/3)(1-1/r_f)}$, and approaches its limiting value $v_m = \sqrt{2/3}$. Formula (7) for the ion energy spectrum yields a square-root dependence on energy $\varepsilon = Mu^2/2$ [5],

$$\frac{dN}{d\varepsilon} = 3\pi(1-1/r_f)^{-3/2}\sqrt{\frac{3\varepsilon}{2}}\theta\left[\frac{2}{3}(1-1/r_f) - \varepsilon\right], \quad (9)$$

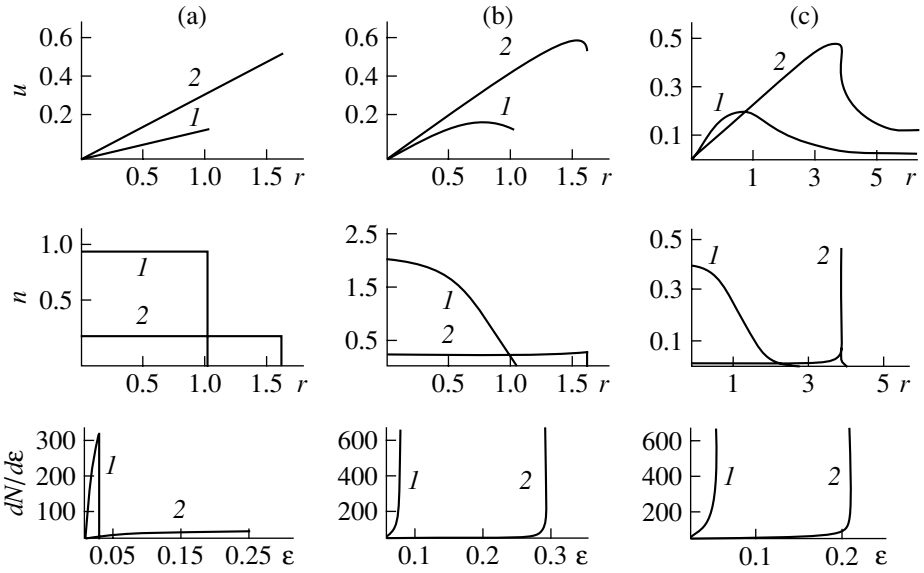

Fig. 1. Radial profiles of the ion velocity (top) and ion density (middle) and the ion energy spectrum (bottom) in clusters with the same total number of particles and with different initial profiles of the atomic density, (a) $n_c = \theta(1 - r)$, (b) $n_c(r) = 2.5(1 - r^2)\theta(1 - r)$, and (c) $n_c(r) = (4/3\sqrt{\pi})e^{-r^2}$, in the initial stage of expansion, $t = 0.2t_s$ (curves *1*), and in its final stage, $t = 0.99t_s$ (curves *2*) (at a time close to the instant at which the front of the Coulomb explosion wave breaks in the cases of decreasing density profiles).

with a cutoff at the front, i.e., at $\varepsilon_f = Mv_f^2/2$. The maximal cutoff energy is $\varepsilon_{\max} = M\omega_L^2(0)r_c^2/3$.

In order to illustrate solution (2) and spectrum (6), Fig. 1 presents the radial profiles of the ion density and ion velocity and also the ion energy spectra for different initial radial profiles of the cluster density: a step profile (an ideal cluster), a quadratic profile $n_c(r) \propto 1 - r^2$, and an exponential profile $n_c(r) \propto \exp(-r^2)$, the total number of particles in the cluster being the same. In contrast to the case of a step ion density profile, the velocity, density, and energy spectrum of the ions in an expanding cluster with a decreasing density profile behave in a qualitatively different manner. Thus, since the ions in the inner regions of an expanding cluster catch up with the peripheral ions, the ion density progressively equalizes in such a way that the ions are then accumulated at the outer boundary of the cluster. Over a finite time, a monotonically decreasing ion density evolves to a comparatively uniform profile in the form of a step but with a sharp increase in the ion density at the front of the expanding cluster. For a decreasing initial density profile, the ion energy spectrum differs from a square-root one (characteristic of an ideal cluster) and exhibits a sharp peak near the cutoff energy.

In actual experiments, the ion energy spectrum is smoother than the theoretical spectrum $dN/d\varepsilon$ because of the spread in the cluster radii. Moreover, in the case of clusters produced during the cooling of a gas jet, this spread is quite large [8] and the distribution of clusters over their dimensions is close to a Gaussian distribution, $G(r_c) \propto r_c \exp[-(r_c - r_0)^2/d^2]$, with $d \sim r_0$. Accordingly, the averaged ion energy distribution is determined by the convolution

$$\left\langle \frac{dN}{d\varepsilon} \right\rangle = \int_0^\infty \frac{dN}{d\varepsilon} G(r_c)\,dr_c, \quad \int_0^\infty G(r_c)\,dr_c = 1. \qquad (10)$$

Figure 2 shows averaged ion energy distributions (10) calculated for $d = r_0$ and for the same initial density profiles as those in Fig. 1. We can see that the height and width of the spectral peak, as well as its position at a fixed time, depend on the atomic density distribution within the cluster. It would be worthwhile to verify this result experimentally.

Let us now discuss the "temperature" of the cluster plasma, i.e., the ion energy averaged over an ensemble of clusters, $\langle \bar{\varepsilon} \rangle$. In order to find the cluster plasma temperature, we first use the definition of the mean energy in an individual cluster, $\bar{\varepsilon} = (1/N)\int_0^{\varepsilon_m} (dN/d\varepsilon)\varepsilon\,d\varepsilon$ (where the upper limit of integration, ε_m, is determined by the maximal velocity), and then average this energy over cluster radii with the help of the above distribution function $G(r_c)$. For example, for an ideal cluster such that $d = r_0$ and for $t \gg 1$, we have $\bar{\varepsilon} = (3/5)\varepsilon_{\max}$ and $\langle \bar{\varepsilon} \rangle = 0.9798M\omega_L^2(0)r_0^2/2$. The time evolution of the cluster plasma temperature $\langle \bar{\varepsilon} \rangle$ calculated in units of $M\omega_L^2(0)r_0^2/2$ for $d = r_0$ is shown in Fig. 3 for the above three density distributions in the cluster. It can be seen

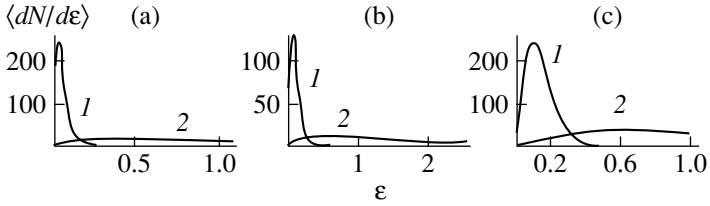

Fig. 2. Ion energy distribution functions (10) in cluster plasmas with different initial profiles of the atomic density, (a) $n_c = \theta(1 - r)$, (b) $n_c(r) = 2.5(1 - r^2)\theta(1 - r)$, and (c) $n_c(r) = (4/3\sqrt{\pi})e^{-r^2}$, at the times $t = 0.2t_s$ (curves *1*) and $t = 0.99t_s$ (curves *2*).

that the cluster plasma temperature increases with time. On long time scales, the temperature has a tendency to saturate. For decreasing density profiles, this feature requires further investigation because, in order for the model used here to be capable of correctly describing such time scales (on which a singularity arises), it should be extended to include the ion multistream motion. For clusters with different initial density profiles, the cluster plasma temperature exhibits qualitatively the same behavior but has somewhat different numerical values. In particular, for the initial density profiles n_c = const, $n_c(r) = 2.5(1 - r^2)$, and $n_c(r) = (4/3\sqrt{\pi})e^{-r^2}$, the ion temperature ratios at $t = 2$ are equal, respectively, to 1 : 1.548 : 0.314; in other words, sharply decreasing density profiles ensure maximal cluster plasma temperatures, whereas, in the case of smooth profiles, the temperature is substantially lower.

The above analysis has shown that the problem of investigating the spectrum of accelerated ions during a spherically symmetric Coulomb explosion of a cluster admits an analytic solution in the hydrodynamic approximation. For monotonically decreasing profiles of the atomic density in a cluster, the ion trajectories eventually become self-intersecting, which corresponds to the onset of a singularity in the solution. In this case, the solution obtained and, accordingly, the ion spectra calculated from it are valid only over a finite time. The behavior of the solution after the time at which it has become singular (i.e., the ion motion has become multistream) should be investigated by means of a kinetic approach. This is the subject of our further studies. Note that the radial position of the maximum in the ion energy spectrum and the radius at which the ion density becomes singular are separated in space. This permits us to suggest that the evolution of the ions to multistream motion will not eliminate the peak in the ion spectrum but rather will change the peak shape. In addition, it is important to point out a qualitative agreement between our results, which have been obtained in the hydrodynamic approximation, and the characteristic features of the expansion of clusters that were observed experimentally and were revealed numerically. Thus, the ion energy spectrum measured by Zweiback *et al.* [8] has a pronounced peak and decreases gradually in the high energy range, as do the spectra shown in Fig. 2. It is also possible that the discrepancies between the results calculated numerically by Nishihara *et al.* [5] and those obtained in the ideal cluster model (such as a local increase in the ion density leading to the appearance of a peak in the ion density profile or the formation of a local region where the ion spectrum is concave upward and is peaked near the energy cutoff) can be attributed to the fact that, in the initial stage of the cluster evolution, the ion density distribution near the cluster boundary is smeared out by the electrons that escape from the cluster under the action of a strong laser field. The behavior of the cluster plasma parameters that has been revealed in the present paper can be checked experimentally and is of practical interest for experiments on the interaction of high-power short laser pulses with cluster media.

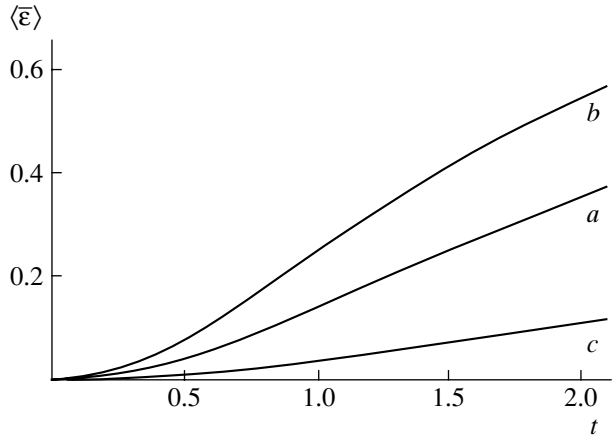

Fig. 3. Normalized ion temperature $2\langle\bar{\varepsilon}\rangle/M\omega_L^2(0)r_0^2$ in cluster plasmas with different initial profiles of the atomic density in the cluster: (*a*) $n_c = \theta(1 - r)$, (*b*) $n_c(r) = 2.5(1 - r^2)\theta(1 - r)$, and (*c*) $n_c(r) = (4/3\sqrt{\pi})e^{-r^2}$.

ACKNOWLEDGMENTS

We are grateful to V.Ya. Gol'din, N.V. Zmitrenko, and A.V. Shil'kov for their interest in this work and for fruitful discussions of the results obtained. This study

was supported in part by the Russian Foundation for Basic Research (project nos. 03-02-16428 and 02-01-00185), INTAS (grant nos. 2001-0233 and 2001-0572), and ISTC (grant no. 2289).

REFERENCES

1. T. Ditmire, J. Zweiback, V. P. Yanovsky, *et al.*, Nature (London) **398**, 489 (1999).
2. T. Ditmire, R. A. Smith, J. W. G. Tisch, and M. H. R. Hutchinson, Phys. Rev. Lett. **78**, 3121 (1997); K. Kondo, A. B. Borisov, C. Jordan, *et al.*, J. Phys. B **30**, 2707 (1997).
3. T. Ditmire, T. Donnelly, R. W. Falcone, and M. D. Perry, Phys. Rev. Lett. **75**, 3122 (1995); S. Dobosz, M. Leziys, M. Svhmidt, *et al.*, Phys. Rev. A **56**, R2526 (1997); E. Parra, I. Alexeev, J. Fan, *et al.*, Phys. Rev. E **62**, R5931 (2000).
4. M. Lezius, S. Dobosz, D. Normand, and M. Schmidt, Phys. Rev. Lett. **80**, 261 (1998).
5. K. Nishihara, H. Amitani, M. Murakami, *et al.*, Nucl. Instrum. Methods Phys. Res. A **464**, 98 (2001).
6. V. P. Krainov and M. B. Smirnov, Phys. Rep. **370**, 237 (2002).
7. J. Zweiback, R. A. Smith, T. E. Cowan, *et al.*, Phys. Rev. Lett. **84**, 2634 (2000).
8. J. Zweiback, T. E. Cowan, J. H. Hartley, *et al.*, Phys. Plasmas **9**, 3108 (2002).
9. S. Sakabe, S. Shimizu, M. Hashida, *et al.*, Phys. Rev. A **69**, 023203 (2004).
10. I. Yu. Skobelev, A. Ya. Faenov, A. I. Magunov, *et al.*, Zh. Éksp. Teor. Fiz. **121**, 88 (2002) [JETP **94**, 73 (2002)].
11. A. E. Kaplan, B. Y. Dubetsky, and P. L. Schkolnikov, Phys. Rev. Lett. **91**, 143401 (2003).
12. R. C. Davidson, *Theory of Nonneutral Plasmas* (Benjamin, New York, 1974; Mir, Moscow, 1978).
13. K. P. Stanyukovich, *Unsteady Motions of Continuous Media* (GITTL, Moscow, 1955).
14. A. I. Khasanov, in *Dynamics of Continuous Media* (Inst. of Hydrodynamics, Siberian Division, USSR Acad. Sci., Novosibirsk, 1977), Vol. 30, p. 123.
15. A. V. Gurevich and K. P. Zybin, Zh. Éksp. Teor. Fiz. **94**, 3 (1988) [Sov. Phys. JETP **67**, 1 (1988)].
16. I. Last, I. Schek, and J. Jortner, J. Chem. Phys. **107**, 6685 (1997).
17. Ya. B. Zel'dovich, Astrofizika **6**, 319 (1970).
18. V. I. Arnol'd, Tr. Sem. Im. I.G. Petrovskogo, No. 8, 21 (1982).

Translated by I.A. Kalabalyk

Plasma Physics Reports, Vol. 31, No. 2, 2005, pp. 93–103. Translated from Fizika Plazmy, Vol. 31, No. 2, 2005, pp. 115–125.

TOKAMAKS

Toroidal Alfvén Eigenmodes in a Tokamak with a Population of High-Energy Large-Orbit Ions

A. B. Mikhaĭlovskiĭ[1, 2], E. A. Kovalishen[1, 2], M. S. Shirokov[1, 3], and S. V. Konovalov[1, 4]

[1] *Nuclear Fusion Institute, Russian Research Centre Kurchatov Institute, pl. Kurchatova 1, Moscow, 123182 Russia*

[2] *Moscow Institute of Physics and Technology, Institutskiĭ pr. 9, Dolgoprudnyĭ, Moscow oblast, 141700 Russia*

[3] *Moscow Engineering Physics Institute (State University), Kashirskoe sh. 31, Moscow, 115409 Russia*

[4] *Naka Fusion Research Establishment, Japan Atomic Energy Research Institute, Ibaraki 3111-0193, Japan*

Received April 28, 2004

Abstract—The effect of the density gradient of high-energy ions moving in large magnetic drift orbits is studied analytically in the context of the problem of toroidal Alfvén eigenmodes (TAEs) in a tokamak. It is found that, when the population of such ions is not too small, this effect can substantially modify standard TAEs and give rise to new types of TAEs, which are called TAEs-H, TAEs-H^+s, and TAEs-H^-s. The continual dissipation of TAEs is investigated with allowance for the effect in question. It is shown that the dissipation acts to dampen all the TAE types under consideration. © *2005 Pleiades Publishing, Inc.*

1. INTRODUCTION

The study of Alfvén eigenmodes in a tokamak is of interest in connection with the problem of instabilities driven by their interaction with high-energy ions (see [1], Sections 29–31, and the literature cited therein). Earlier, it was found that, in discharges with a monotonic safety factor profile (i.e., with a positive shear), the most important of such modes are toroidal Alfvén eigenmodes (TAEs) and kinetic toroidal Alfvén eigenmodes (KTAEs) (see [1, 2] and the references therein). That these types of modes do indeed exist is confirmed by experimental investigations, in particular, those conducted in the TFTR [3], DIII-D [4], JT-60U [5], and JET [6] tokamaks.

In recent years, experiments have been carried out not only with discharges with a positive shear but also with reversed-shear discharges, i.e., those with a nonmonotonic safety factor profile [7]. Observations of discharges with reversed shear revealed the generation of so-called Alfvén cascades (ACs) [8, 9], i.e., Alfvén waves whose properties differ considerably from those of TAEs and KTAEs. Berk *et al.* [10] (see also [11]) suggested that ACs are a new type of Alfvén eigenmodes and that an important role in their formation is played by the Berk–Breizman–Sharapov (BBS) effect—the effect of the density gradient of high-energy ions moving in large magnetic drift orbits. The mechanism underlying this effect was explained in [12, 13], in which it was suggested that it is attributed to the drift motion of the electrons neutralizing the electric charge of high-energy ions and that it is unrelated to the resonant interaction of these ions with the waves. (This interaction, which, in particular, gives rise to the so-called "energetic particle modes," was investigated in [14] and in some earlier papers cited there.) To simulate MHD modes with allowance for the effect in question, a specially developed MISHKA-H computer code was developed [13].

The effect of the density gradient of high-energy large-orbit ions is typical not of reversed-shear discharges alone; it may also manifest itself in discharges with positive shear. This is why it is of interest to examine its role in the problem of TAEs. This subject will be taken up in the present paper. It should be noted that the first step in this direction was made in [15] in considering TAEs in the case in which the shear s is less than the inverse aspect ratio ϵ: $s < \epsilon$. In contrast to [15], we assume here that $s > \epsilon$. However, setting $s > \epsilon$, we nevertheless use the low shear approximation ($s < 1$). Thus, the shear lies within the range

$$\epsilon < s < 1. \tag{1.1}$$

The TAEs were first investigated analytically by Rosenbluth *et al.* [16], who calculated, among other things, the frequency of these modes and their damping by continual dissipation in the case corresponding to condition (1.1), in which we are interested here. Breizman and Sharapov [2] derived the expression for the frequency of TAEs in a simpler way than it was done in [16]. They considered the spatial structure of the TAEs and obtained an expression for their energy. Our analysis can be regarded as a generalization and extension of the analyses carried out in [2, 16] to the scope of problems outlined above, including the BBS effect. We show, in particular, that this effect can give rise to new types of TAEs and clarify how they are influenced by continual dissipation. In our examination, the BBS effect is characterized by the parameter H, introduced through Eq. (2.8). For this reason, the BBS effect will also be referred to as the H effect.

1063-780X/05/3102-0093$26.00 © 2005 Pleiades Publishing, Inc.

Our paper is organized as follows. In Section 2, we present the basic equations. In Section 3, we derive the dispersion relation for TAEs with allowance for the BBS effect and without allowance for continual dissipation. Section 4 presents an analysis of this dispersion relation. In Section 5, we consider the spatial structure and energy of the perturbations under consideration. In Section 6, we take into account the continual dissipation, and, in Section 7, we analyze its role in the perturbations in question. In Section 8, we discuss the results obtained. Finally, in Appendix A, we present the derivation of the basic equations, and in Appendix B, we explain some aspects of solving the perturbed equations.

2. BASIC EQUATIONS AND THEIR PRELIMINARY TRANSFORMATIONS

2.1. Basic Equations

The derivation of the basic equations for TAEs in the absence of high-energy ions can be found in Section 29.1 of [1]. The basic equations for our problem can be derived by incorporating the effect of the density gradient of high-energy ions into those equations. This will be done in Appendix A. The resulting set of basic equations has the form

$$(L_m^{(0)} + L_m^{(h)})\phi_m - \frac{\tilde{\epsilon}}{4q^2R^2}\frac{\partial^2\phi_{m-1}}{\partial r^2} = 0, \quad (2.1)$$

$$(L_{m-1}^{(0)} + L_{m-1}^{(h)})\phi_{m-1} - \frac{\tilde{\epsilon}}{4q^2R^2}\frac{\partial^2\phi_m}{\partial r^2} = 0. \quad (2.2)$$

Equations (2.1) and (2.2) differ from Eqs. (29.16) and (29.17) of [1] only in that they contain the terms with $L_m^{(h)}$ and $L_{m-1}^{(h)}$, which account for the effect at hand. According to Appendix A, in the approximation $m \gg 1$, which will be used below, we have

$$L_m^{(h)} = L_{m-1}^{(h)} = \frac{\omega\kappa_h\Omega_h m}{rv_A^2}\frac{n_h}{n_c}\frac{M_h}{M_i}. \quad (2.3)$$

The notation introduced here is explained in Appendix A.

By analogy with [1, 2], we switch from the coordinate r to the new radial variable

$$x = nq(r) - m + 1/2. \quad (2.4)$$

Carrying out the same manipulations as in Section 29.2 of [1], we reduce Eqs. (2.1) and (2.2) to the form

$$\frac{d}{dx}\left[\left(\frac{g\tilde{\epsilon}}{4} + x - x^2\right)\frac{d\phi_m}{dx}\right] - \frac{1}{s^2}\left(\frac{g\tilde{\epsilon}}{4} + x - x^2\right)\phi_m - H\phi_m - \frac{\tilde{\epsilon}}{4}\frac{d^2\phi_{m-1}}{dx^2} = 0, \quad (2.5)$$

$$\frac{d}{dx}\left[\left(\frac{g\tilde{\epsilon}}{4} - x - x^2\right)\frac{d\phi_{m-1}}{dx}\right] - \frac{1}{s^2}\left(\frac{g\tilde{\epsilon}}{4} - x - x^2\right)\phi_{m-1} - H\phi_{m-1} - \frac{\tilde{\epsilon}}{4}\frac{d^2\phi_m}{dx^2} = 0, \quad (2.6)$$

where s is the shear and

$$g = \frac{1}{\tilde{\epsilon}}\left(\frac{4q^2R^2\omega^2}{v_A^2} - 1\right), \quad (2.7)$$

$$H = -\frac{r_m\kappa_h\Omega_h}{4ms^2\omega}\frac{n_h}{n_c}\frac{M_h}{M_i}. \quad (2.8)$$

In what follows, we will consider a standard case, namely, that in which the density of high-energy ions is radially decreasing: $\kappa_h < 0$. In this case, we also set $\Omega_h > 0$ to obtain

$$\operatorname{sgn} H = \operatorname{sgn}\omega. \quad (2.9)$$

The frequency range $\omega > 0$ corresponds to perturbations propagating in the direction of the equilibrium magnetic field, and the range $\omega < 0$ refers to perturbations propagating in the opposite direction.

Equation (2.7) gives

$$\omega^2 = \frac{v_A^2}{4q^2R^2}(1 + \tilde{\epsilon}g). \quad (2.10)$$

Consequently, in our formulation of the problem, which goes back to the formulation developed in [1, 2], the procedure of finding the frequency of the eigenmodes reduces to that of calculating the parameter g.

2.2. Simplification of the Basic Equations in Inertialess Regions

Assuming that $s \ll 1$, we first consider Eqs. (2.5) and (2.6) in inertialess regions, i.e., those in which the terms with $g\tilde{\epsilon}$ can be ignored. In these regions, we also ignore toroidal effects, i.e., the terms with ϵ. In our problem, there are three singular points on the x axis, $x = (0, \pm 1)$; there also are two singular points at minus and plus infinity, $x \longrightarrow \pm\infty$. As in [1, 2], the inertialess region of primary interest for us is the vicinity of the point $x = 0$, i.e., the Alfvén gap region: it is only in this region that the behavior of the perturbation should be considered in order to determine the real part of the oscillation frequency ω. In this region, Eqs. (2.5) and (2.6) reduce to

$$x\frac{d^2\phi_m}{dx^2} + (1-x)\frac{d\phi_m}{dx} - \frac{x}{s^2}\phi_m - H\phi_m = 0, \quad (2.11)$$

$$x\frac{d^2\phi_{m-1}}{dx^2} + (1+x)\frac{d\phi_{m-1}}{dx} - \frac{x}{s^2}\phi_{m-1} + H\phi_{m-1} = 0. \quad (2.12)$$

Note that the x-dependent coefficients of the first derivatives $d\phi_m/dx$ and $d\phi_{m-1}/dx$ in Eqs. (2.11) and (2.12) are correction terms (see [1, 2] for details). In the terminology of [1, 2], the inertialess region is merely the external region of the mode.

In the vicinity of the point $x = 1$, it is sufficient to know the behavior of the mth field harmonic and in the vicinity of the point $x = -1$, it is sufficient to know the behavior of the $m-1$th harmonic. In analogy with Eqs. (2.11) and (2.12), we obtain from Eqs. (2.5) and (2.6) the set of equations

$$(x-1)\frac{d^2\phi_m}{dx^2} + x\frac{d\phi_m}{dx} - \frac{x-1}{s^2}\phi_m + H\phi_m = 0, \quad (2.13)$$

$$(x+1)\frac{d^2\phi_{m-1}}{dx^2} - x\frac{d\phi_{m-1}}{dx} - \frac{x+1}{s^2}\phi_{m-1} - H\phi_{m-1} = 0. \quad (2.14)$$

We must also know the behavior of the mth and $(m-1)$th harmonics of the perturbed field in regions far from the singular points in question. In these regions, Eqs. (2.5) and (2.6) have the form

$$\frac{d}{dx}\left[x(1-x)\frac{d\phi_m}{dx}\right] - \frac{1}{s^2}x(1-x)\phi_m - H\phi_m = 0, \quad (2.15)$$

$$\frac{d}{dx}\left[x(1+x)\frac{d\phi_{m-1}}{dx}\right] - \frac{1}{s^2}x(1+x)\phi_{m-1} + H\phi_{m-1} = 0. \quad (2.16)$$

Equations (2.13)–(2.16) differ from the corresponding equations of [16] in that they contain the terms with H.

2.3. Simplification of the Basic Equations in Inertial Regions

We distinguish between three inertial regions: the main region, which is the vicinity of the point $x = 0$, and two dissipative regions, which are the vicinities of the points $x = \pm 1$. In the main inertial region, we ignore the terms with x/s^2 and H and also corrections on the order of x. Equations (2.5) and (2.6) can then be reduced to Eqs. (29.35) and (29.36) of [1]:

$$\frac{d}{dz}\left[(g+z)\frac{d\phi_m}{dz}\right] - \frac{d^2\phi_{m-1}}{dz^2} = 0, \quad (2.17)$$

$$\frac{d}{dz}\left[(g-z)\frac{d\phi_{m-1}}{dz}\right] - \frac{d^2\phi_m}{dz^2} = 0, \quad (2.18)$$

where

$$z = 4x/\tilde{\epsilon}. \quad (2.19)$$

In dissipative regions, we ignore not only the correction terms containing the combination $x \mp 1$ and the terms containing $(x \mp 1)/s^2$ and H but also toroidal effects. In this case, Eqs. (2.5) and (2.6) yield the equations

$$\frac{d}{dx}\left[\left(\frac{g\tilde{\epsilon}}{4} + 1 - x\right)\frac{d\phi_m}{dx}\right] = 0, \quad (2.20)$$

$$\frac{d}{dx}\left[\left(\frac{g\tilde{\epsilon}}{4} + 1 + x\right)\frac{d\phi_{m-1}}{dx}\right] = 0. \quad (2.21)$$

Accounting for the terms with ϕ_{m+1} in Eq. (2.20) and for the terms with ϕ_{m-2} in Eq. (2.21) leads to corrections on the order of $m\tilde{\epsilon}$.

3. DERIVATION OF THE DISPERSION RELATION WITHOUT ALLOWANCE FOR CONTINUAL DISSIPATION

According to Appendix B, the solution to Eqs. (2.11) and (2.12) is represented in terms of confluent hypergeometric functions (cf. [1], Eqs. (29.28), (29.29)):

$$\phi_m = D_m \exp\left(-\frac{|x|}{s}\right) U\left[\frac{1}{2} - \frac{\hat{s}}{4}\operatorname{sgn} x, 1, \frac{2|x|}{s}\right], \quad (3.1)$$

$$\phi_{m-1} = D_{m-1} \exp\left(-\frac{|x|}{s}\right) U\left[\frac{1}{2} + \frac{\hat{s}}{4}\operatorname{sgn} x, 1, \frac{2|x|}{s}\right], \quad (3.2)$$

where D_m and D_{m-1} are constants and the parameter $\hat{s}$ is defined by the relationship

$$\hat{s} = s(1-2H). \quad (3.3)$$

For $|x|/s \ll 1$, the asymptotic behavior of solutions (3.1) and (3.2) is given by the expressions

$$\phi_m = -\pi^{-1/2} D_m\left[\ln\left(\frac{2|x|}{s}\right) + \gamma - 2\ln 2 - \frac{\pi^2\hat{s}}{8}\operatorname{sgn} x\right], \quad (3.4)$$

$$\phi_{m-1} = -\pi^{-1/2} D_{m-1}\left[\ln\left(\frac{2|x|}{s}\right) + \gamma - 2\ln 2 + \frac{\pi^2\hat{s}}{8}\operatorname{sgn} x\right], \quad (3.5)$$

where γ is Euler's constant. For $H = 0$, solutions (3.4) and (3.5) pass over to solutions (29.33) and (29.34) of [1].

Consider perturbations with

$$g^2 < 1. \quad (3.6)$$

According to expression (2.10), such perturbations occur in the Alfvén gap region (see [16] for details). In this case, in accordance with [1, 2], the solutions to

Eqs. (2.17) and (2.18) have the form (cf. [1], formulas (29.42), (29.43))

$$\phi_m = \frac{C_m}{2}\ln\left|z^2 + 1 - g^2\right| - \frac{gC_m - C_{m-1}}{(1-g^2)^{1/2}}\arctan\left[\frac{z}{(1-g^2)^{1/2}}\right] + \text{const}, \quad (3.7)$$

$$\phi_{m-1} = \frac{C_{m-1}}{2}\ln\left|z^2 + 1 - g^2\right| + \frac{gC_{m-1} - C_m}{(1-g^2)^{1/2}}\arctan\left[\frac{z}{(1-g^2)^{1/2}}\right] + \text{const}, \quad (3.8)$$

where C_m and C_{m-1} are the constants that are important for further analysis and "const" stands for those whose role is unimportant. For $|z| \gg 1$, solutions (3.7) and (3.8) take the form (cf. [1], formulas (29.44), (29.45))

$$\phi_m = C_m\ln|z| - \frac{\pi}{2}\frac{gC_m - C_{m-1}}{(1-g^2)^{1/2}}\operatorname{sgn} z + \text{const}, \quad (3.9)$$

$$\phi_{m-1} = C_{m-1}\ln|z| + \frac{\pi}{2}\frac{gC_{m-1} - C_m}{(1-g^2)^{1/2}}\operatorname{sgn} z + \text{const}. \quad (3.10)$$

In writing formulas (3.7)–(3.10), we have corrected for misprinted formulas (29.42)–(29.45) from [1].

Asymptotic expressions (3.9) and (3.10) coincide with expressions (3.4) and (3.5) when the parameter g satisfies the relationship

$$\sqrt{1-g^2}\left(1 - \frac{\pi^2\hat{s}^2}{16}\right) = -\frac{\pi}{2}g\hat{s}, \quad (3.11)$$

which plays the role of the dispersion relation. For $H = 0$, this relationship gives

$$g = -1 + \delta, \quad (3.12)$$

where δ is a small positive quantity equal to

$$\delta = \pi^2 s^2/8. \quad (3.13)$$

Relationships (3.12) and (3.13) characterize standard TAEs [1, 2].

Relationship (3.11) can be converted into the form

$$1 - g^2 = \frac{(\pi\hat{s}/2)^2}{[1 + (\pi\hat{s}/4)^2]^2}. \quad (3.14)$$

In transforming relationship (3.11) into relationship (3.14), the operation of squaring was used, which generally introduces redundant roots. Consequently, the solutions obtained with the help of relationship (3.14) should be tested against relationship (3.11).

From relationship (3.14) we obtain

$$g = \pm\frac{\left|1 - (\pi\hat{s}/4)^2\right|}{1 + (\pi\hat{s}/4)^2}. \quad (3.15)$$

In using this relationship, the roots should also be tested in the above manner.

4. TYPES OF TOROIDAL ALFVÉN EIGENMODES IN THE PRESENCE OF THE *H* EFFECT

According to relationship (3.3), we have

$$\hat{s} < 0 \quad (4.1)$$

for

$$H > 1/2. \quad (4.2)$$

In this case, the perturbations under consideration have very different properties from the standard TAEs. Thus, in the interval

$$\frac{1}{2} < H < \frac{1}{2}\left(1 + \frac{4}{\pi s}\right) \quad (4.3)$$

dispersion relation (3.11) has no solutions with $g < 0$, which correspond to standard TAEs (cf. relationships (3.12), (3.13)). Instead, it has solutions with

$$g = 1 - \delta, \quad (4.4)$$

where

$$0 < \delta < 1. \quad (4.5)$$

For $|\hat{s}| \ll 1$, the parameter δ is small, $\delta \ll 1$, and, according to dispersion relation (3.11), it is determined by relationship

$$\delta = \pi^2\hat{s}^2/8. \quad (4.6)$$

The solutions that correspond to H values within interval (4.3) and are characterized by relationships (4.4)–(4.6) will be referred to as TAEs-H solutions.

For large positive values of the parameter H, namely, those above the upper limit of interval (4.3),

$$H > \frac{1}{2}\left(1 + \frac{4}{\pi s}\right), \quad (4.7)$$

the only solutions to dispersion relation (3.11) are those with $g < 0$, in which case relationship (3.15) gives

$$g = -\frac{(\pi\hat{s}/4)^2 - 1}{1 + (\pi\hat{s}/4)^2}. \quad (4.8)$$

In the limit $sH \gg 1$, this result can be represented in the form of relationship (3.12) with

$$\delta = 8/(\pi s H)^2. \quad (4.9)$$

The perturbations characterized by relationships (4.8), (3.12), and (4.9) will be called TAEs-H$^+$s.

For moderately large negative H values and for positive H values lying in the interval $0 < H < 1/2$, i.e., for

$$-\frac{1}{2}\left(\frac{4}{\pi s} - 1\right) < H < 1/2, \quad (4.10)$$

we are dealing with perturbations with $g < 0$, which are analogous to standard TAEs. In this case, relationship (3.15) gives

$$g = -\frac{1-(\pi\hat{s}/4)^2}{1+(\pi\hat{s}/4)^2}. \quad (4.11)$$

For small $\hat{s}$ values, relationship (4.8) passes over to relationship (3.12) with the parameter δ given by formula (4.6). When

$$H < -\frac{1}{2}\left(\frac{4}{\pi s} - 1\right), \quad (4.12)$$

we see from relationship (3.15) that dispersion relation (3.11) has solutions with $g > 0$; in this case, the parameter g is given by formula (4.11). For $|H|s \gg 1$, relationship (4.11) reduces to relationship (4.4) with δ satisfying relationship (4.9). The relevant perturbations will be called TAEs-H$^-$s.

5. SPATIAL STRUCTURE AND ENERGY OF PERTURBATIONS

5.1. Internal Dimension of Perturbations

From solutions (3.7) and (3.8) it is clear that the quantity $(1-g^2)^{1/2}$ is a characteristic spatial scale of the internal layer in the z space. Using relationships (2.19) and (2.4), we find that, in ordinary space, this characteristic dimension, denoted by $\Delta^{\text{in}}_{\text{TAE}}$, is determined by the relationship

$$\Delta^{\text{in}}_{\text{TAE}} = \frac{\tilde{\epsilon} r_m}{4|m|s}(1-g^2)^{1/2}. \quad (5.1)$$

From relationship (3.14) we see that, for the perturbations under analysis, the relationship generally means

$$\Delta^{\text{in}}_{\text{TAE}} = \frac{\pi}{8}\frac{\tilde{\epsilon} r_m}{|m|s}\frac{|\hat{s}|}{1+(\pi\hat{s}/4)^2}. \quad (5.2)$$

For $H = 0$, this gives the following shear-independent dimension [1, 2]:

$$\Delta^{\text{in}}_{\text{TAE}} = \frac{\pi\tilde{\epsilon} r_m}{8|m|}. \quad (5.3)$$

For finite H values satisfying the condition $|H| \ll 1/s$, i.e., for $|\hat{s}| \ll 1$, relationship (5.2) reduces not to relationship (5.3) but rather to the relationship

$$\Delta^{\text{in}}_{\text{TAE}} = \frac{\pi}{8}\frac{\tilde{\epsilon} r_m}{|m|}|1-2H|. \quad (5.4)$$

For $1 \ll |H| \ll 1/s$, we have

$$\Delta^{\text{in}}_{\text{TAE}} = \frac{\pi}{4}\frac{\tilde{\epsilon} r_m |H|}{|m|}, \quad (5.5)$$

so the dimension $\Delta^{\text{in}}_{\text{TAE}}$ increases linearly with H. For $|H|s \gg 1$, relationship (5.2) reads

$$\Delta^{\text{in}}_{\text{TAE}} = \frac{\tilde{\epsilon} r_m}{\pi|m||H|s^2}. \quad (5.6)$$

We recall that the parameter H is defined by Eq. (2.7) and rewrite relationship (5.6) as

$$\Delta^{\text{in}}_{\text{TAE}} = \frac{4}{\pi}\frac{\tilde{\epsilon}|\omega|}{|\kappa_h|\Omega_h}\frac{n_c}{n_h}. \quad (5.7)$$

In the limiting case in question, the dimension $\Delta^{\text{in}}_{\text{TAE}}$ is shear-independent (cf. formula (5.3)).

5.2. Perturbation Parity Invariant

By analogy with [1, 2], we introduce the parameter μ, which is called the perturbation parity invariant, through the relationship

$$\mu = \frac{C_{m-1}-C_m}{C_m+C_{m-1}} = \frac{D_{m-1}-D_m}{D_m+D_{m-1}}. \quad (5.8)$$

By matching the internal and external solutions, we obtain the following expression for μ:

$$\mu = \frac{\operatorname{sgn} g \operatorname{sgn}(1-\pi^2\hat{s}^2/16)-1}{\operatorname{sgn} g \operatorname{sgn}(1-\pi^2\hat{s}^2/16)+1}. \quad (5.9)$$

From this expression we see that each type of TAEs considered in Section 4 is characterized by only one of the two values of the parameter μ: either $\mu = 0$ or $|\mu| = \infty$. In the first case, we have $C_{m-1} = C_m$ and $D_{m-1} = D_m$ and, accordingly, are dealing with even parity modes. In the second case, we have $C_{m-1} = -C_m$ and $D_{m-1} = -D_m$, which corresponds to odd parity modes. The situation with particular types of TAEs may be described in the following way:

For $0 \le H < 1/2$ and for negative H values in interval (4.10) (which corresponds to solutions with $g < 0$, analogous to standard TAEs), expression (5.9) gives $|\mu| = \infty$ and, therefore, refers to odd parity modes,

$$C_{m-1} = -C_m. \quad (5.10)$$

For positive H values in interval (4.3) (which corresponds to TAEs-H with $g > 0$), we have $\mu = 0$ and are thus dealing with even parity modes,

$$C_{m-1} = C_m. \quad (5.11)$$

For large positive H values satisfying inequality (4.7) (which corresponds to TAEs-H$^+$s), we also have $\mu = 0$ and are again dealing with even parity modes (see equality (5.11)). Finally, for large negative H values satisfying inequality (4.12) (which corresponds to TAEs-H$^-$s with $g > 0$), the parameter μ is infinite, $|\mu| = \infty$, and refers to odd parity modes (see equality (5.10)).

5.3. Even- and Odd-Parity Components of the Electrostatic Potential

In place of the functions ϕ_m and ϕ_{m-1}, we introduce the functions $\phi_\pm$ through the relationships

$$\phi_\pm = \phi_m \pm \phi_{m-1}. \tag{5.12}$$

Based on what was said above about the parameter H, we take into account solutions (3.7) and (3.8) to find that, for standard TAEs and for TAEs-H$^-$s, the functions $\phi_\pm$ in the internal layer have the form

$$\phi_+ = -\frac{2(g+1)C_m}{(1-g^2)^{1/2}}\arctan\frac{z}{(1-g^2)^{1/2}}, \tag{5.13}$$

$$\phi_- = C_m \ln|z^2 + 1 - g^2|. \tag{5.14}$$

As for TAEs-H and TAEs-H$^+$s, we otherwise arrive at the function ϕ_+ of form (5.14) and at the function ϕ_- of form (5.13), with the replacement $g + 1 \longrightarrow g - 1$.

5.4. TAEs Energy for Finite H Values

According to [1, 2], we can begin with the following expression for the energy of the TAEs:

$$W = \frac{1}{4\pi}\frac{c^2}{v_A^2}\int\left(\frac{\partial\phi}{\partial r}\right)^2 d\mathbf{r}. \tag{5.15}$$

In terms of the poloidal harmonics ϕ_m and ϕ_{m-1} and radial variable z, this expression reads [1, 2]

$$W = \frac{8\pi|m|sR}{\tilde{\epsilon}}\frac{c^2}{v_A^2}\int\left[\left(\frac{d\phi_m}{dz}\right)^2 + \left(\frac{d\phi_{m-1}}{dz}\right)^2\right]dz. \tag{5.16}$$

Using the results obtained in Section 5.3, we obtain

$$W = \frac{16\pi|m|sR}{\tilde{\epsilon}}\frac{c^2}{v_A^2}|C_m|^2 I_W, \tag{5.17}$$

where

$$I_W = \int\frac{dz}{(z^2+1-g^2)^2}\begin{cases}(g+1)^2+z^2, & \mu = \infty,\\ (g-1)^2+z^2, & \mu = 0.\end{cases} \tag{5.18}$$

We can see that $I_W > 0$; consequently, in agreement with the initial expression (5.15), all the TAE types under consideration possess positive energy: $W > 0$.

We take the integral on the right-hand side of expression (5.18) to find

$$I_W = \frac{\pi}{\sqrt{1-g^2}}\begin{cases}(1-g)^{-1}, & \mu = \infty,\\ (1+g)^{-1}, & \mu = 0.\end{cases} \tag{5.19}$$

For standard TAEs ($H = 0$), this yields

$$I_W = 1/s. \tag{5.20}$$

Substituting relationship (5.20) into expression (5.16), we arrive at the result that was obtained in [2] and was also presented in [1]. As for TAEs-H with $|\hat{s}| \ll 1$, expression (5.19) leads, instead of relationship (5.20), to the relationship

$$I_W = 1/|\hat{s}|. \tag{5.21}$$

Using expression (5.19), we can also show that the energy of the TAEs-H$^+$s and TAEs-H$^-$s can appreciably exceed that of the standard TAEs: for the former two types of eigenmodes, the right-hand side of this expression is proportional to $(s|H|)^3$.

6. ACCOUNT OF CONTINUAL DISSIPATION FOR FINITE H VALUES

6.1. Solutions to the Perturbed Equations in the Vicinities of the Points $x = \pm 1$

In the vicinities of the points $x = \pm 1$, we are faced with inertialess equations (2.13) and (2.14) and inertial equations (2.20) and (2.21). We begin by working with Eqs. (2.13) and (2.14). The approach of Appendix B leads us to solutions analogous to solutions (3.1) and (3.2):

$$\phi_m = D_m^1\exp\left(-\frac{|1-x|}{s}\right)$$
$$\times\left\{U\left[\frac{1}{2}-\frac{\hat{s}}{4}\mathrm{sgn}(1-x),\,1;\,\frac{2|1-x|}{s}\right]\right. \tag{6.1}$$
$$\left.+\,\theta(1-x)G_m^1 M\left[\frac{1}{2}-\frac{\hat{s}}{4},\,1,\,\frac{2(1-x)}{s}\right]\right\},$$

$$\phi_{m-1} = D_{m-1}^{-1}\exp\left(-\frac{|1+x|}{s}\right)$$
$$\times\left\{U\left[\frac{1}{2}-\frac{\hat{s}}{4}\mathrm{sgn}(1+x),\,1;\,\frac{2|1+x|}{s}\right]\right. \tag{6.2}$$
$$\left.+\,\theta(1+x)G_{m-1}^{-1} M\left[\frac{1}{2}-\frac{\hat{s}}{4},\,1,\,\frac{2(1+x)}{s}\right]\right\}.$$

Here, M is a confluent hypergeometric function; $\theta(t)$ is the Heaviside step function defined as

$$\theta(t) = \begin{cases}1, & t > 0,\\ 0, & t < 0,\end{cases} \tag{6.3}$$

and D_m^1, D_{m-1}^{-1}, G_m^1, and G_{m-1}^{-1} are constants.

Now, we solve Eqs. (2.20) and (2.21). The technique of solving Eq. (2.20) can be illustrated as follows: We integrate Eq. (2.20) over x, make the standard replacement $\omega \longrightarrow \omega + i\Delta$ (where $\Delta > 0$), and take the limit $\Delta \longrightarrow 0$. As a result, we obtain

$$\frac{d\phi_m}{dx} = C_m^1\left[\frac{P}{g\tilde{\epsilon}/4 + 1 - x} - i\pi\ \mathrm{sgn}\,\omega\ \delta\left(\frac{g\tilde{\epsilon}}{4} + 1 - x\right)\right], \quad (6.4)$$

where the symbol P stands for the principal value of the integral and C_m^1 is a constant of integration. We again integrate over x to arrive at a solution similar to solution (3.9):

$$\phi_m = -C_m^1[\ln|1 - x| - i\pi\,\mathrm{sgn}\,\omega\theta(1 - x)] + \mathrm{const}, \quad (6.5)$$

where const is a constant of integration, which is unimportant for further analysis. Analogously to the derivation of solution (6.5), solving Eq. (2.21) yields

$$\phi_{m-1} = C_{m-1}^{-1}[\ln|1 + x| - i\pi\,\mathrm{sgn}\,\omega\theta(1 + x)] + \mathrm{const}, \quad (6.6)$$

where C_{m-1}^{-1} is a constant of integration.

Now, we expand the right-hand sides of solutions (6.1) and (6.2) in powers of the small argument and match the resulting expressions with solutions (6.5) and (6.6). This, in particular, yields the following expressions for the constants of integration G_m^1 and G_{m-1}^{-1} in solutions (6.1) and (6.2):

$$G_m^1 = G_{m-1}^{-1} = -\frac{\pi^{3/2}\hat{s}}{4} + i\pi^{1/2}\,\mathrm{sgn}\,\omega. \quad (6.7)$$

For $H = 0$, the results just given agree with those obtained in [16].

6.2. Matching the Solutions in the Vicinities of the Points $x = \pm 1$ with the Solutions in the Vicinity of the Point $x = 0$

In analogy with solutions (6.1) and (6.2), we modify solutions (3.1) and (3.2) by taking into account the contribution of the functions M:

$$\phi_m = D_m\exp\left(-\frac{|x|}{s}\right)\left[U\left(\frac{1}{2} - \frac{\hat{s}}{4}\mathrm{sgn}\,x,\ 1,\ \frac{2|x|}{s}\right) + \theta(x)G_m M\left(\frac{1}{2} - \frac{\hat{s}}{2},\ 1,\ \frac{2x}{s}\right)\right], \quad (6.8)$$

$$\phi_{m-1} = D_{m-1}\exp\left(-\frac{|x|}{s}\right)\left[U\left(\frac{1}{2} + \frac{\hat{s}}{4}\mathrm{sgn}\,x,\ 1,\ \frac{2|x|}{s}\right) + \theta(-x)G_{m-1}M\left(\frac{1}{2} - \frac{\hat{s}}{2},\ 1,\ -\frac{2x}{s}\right)\right]. \quad (6.9)$$

Here, G_m and G_{m-1} are constants. In order to determine them, we solve Eqs. (2.15) and (2.16) and match the solutions obtained with solutions (6.1) and (6.2) in the vicinities of the points $x = \pm 1$ and with solutions (6.8) and (6.9) in the vicinity of the point $x = 0$.

Solving Eqs. (2.15) and (2.16) in the quasiclassical Wentzel–Kramers–Brillouin (WKB) approximation (with $1/s^2$ being the large parameter), we arrive at the following expression for the mth harmonic:

$$\phi_m = \frac{E_m\exp[-(1 - x)/s]}{(1 - x)^{(1 + sH)/2}x^{(1 - sH)/2}} + \frac{F_m\exp[(1 - x)/s]}{(1 - x)^{(1 - sH)/2}x^{(1 + sH)/2}}, \quad (6.10)$$

where E_m and F_m are constants and x lies within the range $0 < x < 1$. An analogous result is obtained for the $m - 1$th harmonic in the range $-1 < x < 0$.

Assuming that the argument of the functions U and M on the right-hand side of solution (6.1) is large, we find

$$\phi_m = D_m^{-1}\left(\frac{s}{2}\right)^{(1 + sH)/2}\left\{\frac{\exp[-(1 - x)/s]}{(1 - x)^{(1 + sH)/2}} + \frac{G_m^1(s/2)^{-sH}}{\Gamma[(1 + sH)/2]}\frac{\exp[(1 - x)/s]}{(1 - x)^{(1 - sH)/2}}\right\}. \quad (6.11)$$

Matching solutions (6.11) and (6.10) gives

$$D_m^{-1} = E_m(s/2)^{-(1 + sH)/2}, \quad (6.12)$$

$$F_m = E_m\left(\frac{s}{2}\right)^{-sH}\frac{G_m^1}{\Gamma[(1 + sH)/2]}. \quad (6.13)$$

Taking into account expressions (6.12) and (6.13), we reduce Eq. (6.10) in the vicinity of the point $x = 0$ to

$$\phi_m = E_m\exp\left(\frac{1}{s}\right)\left\{\left(\frac{s}{2}\right)^{-sH}\frac{G_m^1}{\Gamma[(1 + sH)/2]}\frac{\exp(-x/s)}{x^{(1 + sH)/2}} + \exp\left(-\frac{2}{s}\right)\frac{\exp(x/s)}{x^{(1 - sH)/2}}\right\}. \quad (6.14)$$

On the other hand, for large values of the argument of the functions U and M on the right-hand side of solution (6.8), we find

$$\phi_m = D_m\left\{\left(\frac{s}{2}\right)^{(1+sH)/2}\frac{\exp(-x/s)}{x^{(1+sH)/2}} + \frac{G_m(s/2)^{(1-sH)/2}}{\Gamma[(1+sH)/2]}\frac{\exp(x/s)}{x^{(1-sH)/2}}\right\}. \quad (6.15)$$

Assuming that solution (6.14) coincides with solution (6.15), we obtain the relationship between E_m and D_m (in further analysis, however, this relationship will not be used) and the expression for the coefficient G_m:

$$G_m = \exp\left(-\frac{2}{s}\right)\left(\frac{s}{2}\right)^{2sH}\frac{\Gamma^2[(1+sH)/2]}{G_m^1}. \quad (6.16)$$

The coefficient G_{m-1} is found in an analogous way. It turns out that

$$G_{m-1} = G_m. \quad (6.17)$$

6.3. Dispersion Relation with Allowance for Continual Dissipation

For $|x|/s \ll 1$, solutions (6.8) and (6.9) lead to the following generalization of solutions (3.4) and (3.5):

$$\phi_m = -\pi^{-1/2}D_m\left[\ln|x| - \frac{\pi^2}{8}\left(\hat{s} + \frac{4}{\pi^{3/2}}G_m\right)\operatorname{sgn}x + \text{const}\right], \quad (6.18)$$

$$\phi_{m-1} = -\pi^{-1/2}D_{m-1}\left[\ln|x| + \frac{\pi^2}{8}\left(\hat{s} + \frac{4}{\pi^{3/2}}G_m\right)\operatorname{sgn}x + \text{const}\right]. \quad (6.19)$$

In deriving these solutions, we took into account the relationship

$$\theta(x) = (1 + \operatorname{sgn}x)/2. \quad (6.20)$$

Matching solutions (6.18) and (6.19) with solutions (3.9) and (3.10), we arrive at a dispersion relation of the form of (3.11) with the replacement

$$\hat{s} \longrightarrow \hat{s} + 4G_m/\pi^{3/2}, \quad (6.21)$$

where the coefficient G_m is given by formulas (6.16) and (6.7).

We are interested only in the imaginary (dissipative) part of the parameter G_m. We denote this part by $G_m^{(1)}$ and, from the above formulas, obtain

$$G_m^{(1)} = -i\operatorname{sgn}\omega\pi^{3/2}\hat{\Delta}/4, \quad (6.22)$$

where

$$\hat{\Delta} = \frac{4}{\pi^2}\exp\left(-\frac{2}{s}\right)\left(\frac{s}{2}\right)^{2sH}\frac{\Gamma^2[(1+sH)/2]}{1+(\pi\hat{s}/4)^2}. \quad (6.23)$$

In terms of $\hat{\Delta}$, replacement (6.21) reads

$$\hat{s} \longrightarrow \hat{s} - i\hat{\Delta}\operatorname{sgn}\omega. \quad (6.24)$$

In this case, instead of relationship (3.11), we arrive at the relationship

$$\sqrt{1-g^2}\left(1 - \frac{\pi^2\hat{s}^2}{16}\right) + \frac{\pi}{2}\hat{s}g = i\frac{\pi}{2}\left(g - \frac{\pi\hat{s}}{4}\sqrt{1-g^2}\right)\hat{\Delta}\operatorname{sgn}\omega. \quad (6.25)$$

With allowance for $\hat{\Delta}$, the eigenvalue g is complex, so we have

$$g = g_0 + i\operatorname{Im}g, \quad (6.26)$$

where g_0 is the real part of g. In these terms, relationship (6.25) implies that the quantity g_0 satisfies dispersion relation (3.11) with the replacement $g \longrightarrow g_0$ and yields the following expression for the imaginary part $\operatorname{Im}g$:

$$\operatorname{Im}g = -\frac{\pi}{2}\hat{\Delta}\sqrt{1-g_0^2} \times \frac{g_0 - (\pi\hat{s}/4)\sqrt{1-g_0^2}}{g_0(1-\pi^2\hat{s}^2/16) - (\pi\hat{s}/2)\sqrt{1-g_0^2}}\operatorname{sgn}\omega. \quad (6.27)$$

For $H = 0$, this expression gives

$$\operatorname{Im}g = -\pi s\exp(-2/s)\operatorname{sgn}\omega, \quad (6.28)$$

which coincides with the corresponding results obtained in [16].

7. ANALYSIS OF THE ROLE OF CONTINUAL DISSIPATION FOR FINITE H VALUES

In analogy with expression (6.26), we set

$$\omega \longrightarrow \omega_0 + i\operatorname{Im}\omega, \quad (7.1)$$

where ω_0 is the real part of the oscillation frequency ω. Using expression (2.10), we find that $\operatorname{Im}\omega$ is related to $\operatorname{Im}g$ by

$$\operatorname{Im}\omega = \frac{\tilde{\epsilon}v_A^2}{8q^2R^2\omega_0}\operatorname{Im}g. \quad (7.2)$$

Taking into account the relationship $|\omega_0| \approx v_A/2qR$ (see expression (2.10)) and using relationships (6.27) and (3.11), we obtain

$$\mathrm{Im}\,\omega = -\frac{\pi}{8}\frac{\tilde{\epsilon} v_A}{qR}\hat{\Delta}\sqrt{1-g_0^2}\frac{1}{1+\pi^2\hat{s}^2/16}. \quad (7.3)$$

We thus see that continual dissipation acts to dampen all the TAE types under investigation.

In accordance with [16], relationship (7.3) for standard TAEs ($H = 0$) has the form

$$\mathrm{Im}\,\omega = -\frac{\tilde{\epsilon} v_A s}{\pi qR}\exp\left(-\frac{2}{s}\right). \quad (7.4)$$

In contrast, for TAEs-H ($|\hat{s}| \ll 1$), relationship (7.3) becomes

$$\mathrm{Im}\,\omega = -\frac{\tilde{\epsilon} v_A |\hat{s}|}{\pi qR}\exp\left(-\frac{2}{s}\right). \quad (7.5)$$

8. DISCUSSION OF THE RESULTS

We have shown that TAEs are significantly modified by the effect of the density gradient of high-energy ions moving in large magnetic drift orbits (an effect that was mentioned in [10] and was called above the BBS effect). It is of course clear that, for this effect to be pronounced, the population of high-energy ions should not be too small; i.e., the parameter H, introduced here through Eq. (2.8), should be large enough in comparison to unity: $|H| \geq 1$. An approximate estimate of the required H values can be obtained from Eq. (2.8) by setting $M_h = M_i$, $r_m\kappa_h \simeq 1$, $s \simeq 0.3$, $m = 3$, $n_h/n_c \simeq 10^{-3}$, and $\Omega_h/\omega \simeq 10^3$ (cf. [13]). These parameter values yield $H \simeq 1$. Note that Eq. (2.8) gives $H \sim 1/s^2$; i.e., the parameter H increases substantially as the shear decreases. Consequently, for a sufficiently low shear, we have $H \gg 1$. Our analysis also makes use of the parameter sH. Since $sH \sim 1/s$, the situations with $|sH| \gg 1$, which have been examined above, can occur when the shear is sufficiently low.

The effect we have investigated is highly sensitive to the sign of the parameter H; i.e., in accordance with (2.9), it is sensitive to the propagation direction of the perturbations relative to the direction of the equilibrium magnetic field. We have shown that, depending on the sign and magnitude of the parameter H, high-energy ions can give rise not only to perturbations like standard TAEs but also to new types of TAEs, which have been called above TAEs-H, TAEs-H$^+$s, and TAEs-H$^-$s (see Section 4 for details). As in the case of standard TAEs, the frequencies of TAEs-H$^-$s lie in the lower part of the Alfvén gap, whereas the frequencies of TAEs-H and TAEs-H$^+$s lie in its upper part. These new types of TAEs also differ from standard TAEs in spatial structure and energy (see Section 5 for details). It is shown that all the TAE types under consideration possess positive energy. It is pointed out that, like standard TAEs, the TAEs-H$^-$s are odd parity modes; in contrast, the TAEs-H and TAEs-H$^+$s are of even parity. Note also that the question about the parity of TAEs was the subject of an experimental investigation by Kramer *et al.* [17]. In that paper, however, the BBS effect was not taken into account, so it would be interesting to examine this problem in further experiments.

In order to take into account the continual dissipation of TAEs at finite H values, we have developed an approach similar to that taken in [16]. Using this approach, we have derived dispersion relation (6.25), in which the continual dissipation is characterized by the parameter $\hat{\Delta}$, introduced through equality (6.23). It is shown that this dissipation acts to dampen all the TAE types under discussion.

The effect of the density gradient of a thermal plasma was studied in a recent paper by Konovalov *et al.* [18] in connection with the problem of Alfvén cascades in tokamaks. In the context of our analysis, it seems worthwhile to examine the effect of this gradient on the TAEs.

The analytic formulas that have been derived above display the regular features characterizing the role of the BBS effect in the behavior of the TAEs. The features that have been revealed, on the one hand, can serve as a basis for numerical analysis of these modes with the MISHKA-H code [13] and analogous MHD computer codes capable of describing the effects of high-energy large-orbit ions, and, on the other hand, they should be taken into account in developing ITER-type fusion reactors.

ACKNOWLEDGMENTS

We are grateful to S.E. Sharapov for useful discussions. This work was supported in part by the Russian Foundation for Basic Research (project no. 03-02-16294), the Russian Federal Program for State Support of Leading Scientific Schools (project no. 2024.2003.2), the Department of Atomic Science and Technology of the RF Ministry of Atomic Industry, and the U.S. Civilian Research and Development Foundation for the Independent States of the Former Soviet Union (CRDF) (grant no. BRHE REC-011).

APPENDIX A

Derivation of the Basic Equations

The derivation begins with the current continuity equation

$$\nabla_\parallel \tilde{j}_\parallel + \nabla_\perp \cdot \tilde{\mathbf{j}}_\perp = 0, \quad (A.1)$$

where $\tilde{j}_\parallel$ and $\tilde{\mathbf{j}}_\perp$ are the perturbed current densities along and across the equilibrium magnetic field $\mathbf{B}_0$ and

$\nabla_\parallel$ and $\mathbf{\nabla}_\perp$ are the longitudinal and transverse components of the gradient operator. In Eq. (A.1), the term $(\tilde{\mathbf{B}}_\perp/B_0)\mathbf{\nabla}_\perp j_{\parallel 0}$ (where $\tilde{\mathbf{B}}_\perp$ is the perturbed magnetic field and $j_{\parallel 0}$ is the equilibrium longitudinal current density) is ignored because it is unimportant for the problem under analysis (for details, see [1], Sections 4, 7).

The term with $\tilde{j}_\parallel$ in Eq. (A.1) can be expressed through the perturbed electrostatic potential ϕ by means of the same transformations as in Section 29.1 of [1]. The transverse current $\mathbf{j}_\perp$ is represented as a sum of the inertial current given by expression (29.5) from [1] and the current $\mathbf{j}_\perp^{(h)}$ of the electrons that drift in crossed fields and neutralize the electric charge of high-energy large-orbit ions, so we have (see [13] for details)

$$\mathbf{j}_\perp^{(h)} = -e_h n_h \mathbf{V}_E, \tag{A.2}$$

where $\mathbf{V}_E = c(\mathbf{B}_0 \times \mathbf{\nabla}\phi)/\mathbf{B}_0^2$ is the drift velocity in crossed fields, n_h and e_h are the density of high-energy ions and their electric charge, and c is the speed of light. In this case, Eq. (A.1) yields the following generalization of Eq. (29.8) from [1]:

$$\hat{L}\phi \equiv (\mathbf{B}_0 \cdot \mathbf{\nabla})\left(\frac{1}{\mathbf{B}_0^2}\mathbf{\nabla}_\perp^2(\mathbf{B}_0 \cdot \mathbf{\nabla})\phi\right) + \frac{\omega^2}{v_A^2}\mathbf{\nabla}_\perp^2\phi + \hat{L}^{(h)}\phi = 0, \tag{A.3}$$

where

$$\hat{L}^{(h)}\phi = -i\frac{\Omega_h \omega}{r v_A^2}\frac{\partial n_h}{\partial r}\frac{M_h}{M_i n_c}\frac{\partial \phi}{\partial \theta}. \tag{A.4}$$

Here, ω is the frequency of the mode (the perturbed quantities are assumed to depend on time as $\exp(-i\omega t)$), Ω_h and M_h are the gyrofrequency of high-energy ions and their masses, n_c is the density of the thermal plasma, M_i is the mass of the thermal ions, r is the radial coordinate, and θ is the poloidal angle.

Equation (A.3) is transformed under the assumption that the electrostatic potential depends on the radius as

$$\phi(r) = \exp(-in\zeta)\sum_m \phi_m(r)\exp(im\theta) + \text{c.c.}, \tag{A.5}$$

where ζ is the toroidal angle, n is the toroidal mode number, and m is a set of poloidal mode numbers. The operators $\mathbf{\nabla}_\perp^2$ and $\mathbf{B}_0 \cdot \mathbf{\nabla}$ are transformed according to the same rules as in Section 29.1 of [1]. In this case, the operator $L_m^{(0)}\phi_m$ in Eq. (2.1) has the form

$$L_m^{(0)}\phi_m = \frac{d}{dr}\left[\left(\frac{\omega^2}{v_A^2} - k_{\parallel m}^2\right)\frac{d\phi_m}{dr}\right] - \frac{m^2}{r^2}\left(\frac{\omega^2}{v_A^2} - k_{\parallel m}^2\right)\phi_m, \tag{A.6}$$

where

$$k_{\parallel m} = (m - nq)/qR, \tag{A.7}$$

q is the safety factor, and R is the major radius of the torus. The operator $L_{m-1}^{(0)}\phi_{m-1}$ is given by the same formula but with the replacement $m \longrightarrow m-1$. Applying the operator $\hat{L}^{(h)}$ to expression (A.5) for the potential ϕ yields expression (2.3) with $\kappa_h \equiv d\ln n_h/dr$. Accounting for the toroidal geometry leads to the terms with $\tilde{\epsilon}$ in Eqs. (2.1) and (2.2); here, $\tilde{\epsilon} = 5\epsilon/2$, with ϵ being the inverse aspect ratio.

APPENDIX B

Solution of the Perturbed Equations in the Inertialess Region

Equations (2.11) and (2.12) can be solved as follows. We assume that

$$\phi_m = \exp(-\alpha|x|)y(x). \tag{B.1}$$

Substituting representation (B.1) into Eq. (2.11) and requiring that the parameter α satisfy the relationship

$$\alpha = -\frac{1}{2}\text{sgn}\,x + \left(\frac{1}{4} + \frac{1}{s^2}\right)^{1/2} \tag{B.2}$$

yields the following equation for the function y:

$$x\frac{d^2y}{d^2x} + [1 - x(1 + 2\alpha\,\text{sgn}\,x)]\frac{dy}{dx} - (\alpha\,\text{sgn}\,x + H)y = 0. \tag{B.3}$$

Equation (B.3) has a solution of the form

$$y \sim U(a, b, t), \tag{B.4}$$

where U is a confluent hypergeometric function, $b = 1$, and

$$a = \frac{\alpha\,\text{sgn}\,x + H}{2\alpha\,\text{sgn}\,x + 1}, \tag{B.5}$$

$$t = (1 + 2\alpha\,\text{sgn}\,x)x. \tag{B.6}$$

For $s \ll 1$, relationship (B.2) gives the approximate expression

$$\alpha = 1/s - \text{sgn}\,x/2. \tag{B.7}$$

In this case, we have

$$a = \frac{1}{2}\left(1 - \frac{\hat{s}}{2}\text{sgn}\,x\right), \tag{B.8}$$

where $\hat{s}$ is given by relationship (3.3).

Taking into account representation (B.1) and relationships (B.4)–(B.8) leads to solution (3.1). Solution (3.2) is derived in an analogous way.

REFERENCES

1. A. B. Mikhailovskii, *Instabilities in a Confined Plasma* (IOP, Bristol, 1998).
2. B. N. Breizman and S. E. Sharapov, Plasma Phys. Controlled Fusion **37**, 1057 (1995).
3. K. L. Wong, R. J. Fonck, S. F. Paul, *et al.*, Phys. Rev. Lett. **66**, 1874 (1991).
4. W. W. Heidbrink, E. J. Strait, E. Doyle, *et al.*, Nucl. Fusion **31**, 1635 (1991).
5. H. Kimura, M. Saigusa, S. Moriyama, *et al.*, Phys. Lett. A **199**, 86 (1995).
6. A. Fasoli, D. Borba, G. Bosia, *et al.*, Phys. Rev. Lett. **75**, 645 (1995).
7. F. M. Levinton, M. C. Zarnstroff, S. H. Batha, *et al.*, Phys. Rev. Lett. **75**, 4417 (1995).
8. H. Kimura, Y. Kusama, M. Saigusa, *et al.*, Nucl. Fusion **38**, 1303 (1998).
9. S. E. Sharapov, D. Testa, B. Alper, *et al.*, Phys. Lett. A **289**, 127 (2001).
10. H. Berk, D. N. Borba, B. N. Breizman, *et al.*, Phys. Rev. Lett. **87**, 185002 (2001).
11. S. E. Sharapov, B. Alper, H. L. Berk, *et al.*, Phys. Plasmas **9**, 2027 (2002).
12. S. V. Konovalov, A. B. Mikhailovskii, S. E. Sharapov, *et al.*, Dokl. Akad. Nauk **385**, 44 (2002) [Dokl. Phys. **47**, 488 (2002)].
13. S. E. Sharapov, A. B. Mikhailovskii, and G. T. A. Huysmans, Phys. Plasmas **11**, 2286 (2004).
14. F. Zonca, S. Briguglio, L. Chen, *et al.*, Phys. Plasmas **9**, 4939 (2002).
15. A. B. Mikhailovskii, M. S. Shirokov, S. V. Konovalov, and V. S. Tsypin, Dokl. Akad. Nauk (2004) (in press).
16. M. N. Rosenbluth, H. L. Berk, J. W. Van Dam, and D. M. Lindberg, Phys. Fluids B **4**, 2189 (1992).
17. G. J. Kramer, S. E. Sharapov, R. Nazikian, *et al.*, Phys. Rev. Lett. **92**, 015001 (2004).
18. S. V. Konovalov, A. B. Mikhailovskii, M. S. Shirokov, and T. Ozeki, Phys. Plasmas **11**, 2303 (2004).

Translated by I.A. Kalabalyk